The University Of Sheffield.

The Biogeochemistry of the Active Layer and Shallow Permafrost in a High Arctic Fjord Valley, Svalbard

Eleanor Louise Jones

A thesis submitted for the degree of

Doctor of Philosophy

The University of Sheffield

Department of Geography

September 2019

Abstract

Rising air temperatures are exposing carbon in Arctic permafrost to decomposition by microorganisms. This is predicted to amplify the response of Earth's climate system to the anthropogenic forcing of climate. However, the timing and magnitude of this climate feedback are uncertain because of the complex effects of permafrost landscape sedimentation and hydrology upon microbial decomposition of the carbon. This thesis explores the influence of landscape development on biogeochemical processes in continuous permafrost in Svalbard. Fjord valley infills and raised beaches are landforms developed as a direct consequence of deglaciation. Biogeochemical analyses of permafrost cores and water from the active layer were undertaken for three contrasting wetlands situated on these landforms. Chapter 3 demonstrates that the accumulation of organic carbon in fjord valley infills regulates biogeochemical processes, with pyrite oxidation being most pronounced in the drier, organic-poor wetland. In contrast, in the saturated groundwater-fed, organic-rich wetland, there are signs of iron- and sulfate-reduction, pyrite and siderite precipitation and methanogenesis. Chapter 4 shows that the degradation of an ice-wedge polygon situated on intra-beach sediments results in the degraded polygon developing more oxidising conditions, with a decrease in iron reduction, and decreased preservation of pyrite and siderite. Chapter 5 shows that concentrations of carbon dioxide are substantially higher than concentrations of methane in the pore water, owing to microbial respiration using ferric iron and sulfate as electron acceptors. Where methane is detected, hydrogenotrophic methanogenesis is the dominant pathway of methanogenesis. In the degraded ice-wedge polygon, the degradation causes oxidation and a decoupling of the relationship between the concentration of methane and the content of organic carbon. This implies that the production of carbon dioxide during the aerobic respiration of peat becomes increasingly important as ice-wedge polygons degrade. As air temperatures continue to rise in the high Arctic, degradation of ice-wedge polygons and the resultant drainage of water from the landscape are likely to result in pyrite and siderite oxidation and aerobic respiration of organic carbon.

Acknowledgements

I would firstly like to thank my inspirational and insightful principal supervisor, Andy Hodson. Andy has been approachable, full of exciting ideas and has provided me with wonderful opportunities. I am grateful to my co-supervisors, Kelly Redeker and Steve Thornton. Kelly has been enthusiastic and diligent in his support of me and I owe him special thanks for training me in the use of flux chambers and the isotopic analysis of methane. Steve's expertise in sediment core geochemical analysis and pore water sampling has been essential in this research and I am thankful to Steve for helping me plan my lab and field work.

I have been fortunate to be welcomed as a guest in numerous labs during this PhD. I had a particularly enjoyable and productive time working with Peter Wynn at the Lancaster Environment Centre on processing water samples for analysis, and our discussions helped to shape this research. Allie Tessin, who was based at the University of Leeds, was generous in her help and guidance, inviting me to the lab in Leeds to share the pyrite line.

I truly appreciate field assistance from my brother, Gwilym Jones. Gwilym accompanied me on two summer field seasons, and his support was invaluable. I am thankful to all who supported me during my time at the University Centre in Svalbard (UNIS). Gunnar Mallon, Graham Gilbert, Brendan O'Neill, Ebbe Bak, Dotan Rotem, Yishai Weinstein, Sarah St Germain, Simon Norum and Knut Lindland Tveit are thanked for their assistance with coring permafrost. Thanks to the logistics staff at UNIS, who helped me plan the fieldwork and stay safe.

I was lucky to be part of the LowPerm team during this PhD and enjoyed discussions and collaborations arising from this. Thanks are due to Brendan O'Neill, Gunnar Mallon, Jacob Yde, Kai Finster and Hanne Christiansen. I am grateful to Ebbe Bak for sharing microbiological data for me to use in this thesis. Gunnar mentored me throughout the PhD and spent many days helping me to saw up the cores.

This research was facilitated by the many technical staff who helped me in the lab, analysed samples for me and were cheerful company: Alan Smalley, Rob Ashurst, David Finlayson, Joe Hufton, Andy Fairburn, Irene Johnson, Roscoe Blevins, Anthony Turner, Gerd-Irene Signeres, Stuart Thomson, Andy Hobson, Dave Hughes and Paul Blackbourne. Alina Marca analysed water isotopes. Thanks to students who helped me in the lab: Masters student and 'Permafrost Princess' Jade Rogers and Louise Boothroyd.

Thanks to my friends and colleagues at the University of Sheffield, particularly my pals in the A floor office, who sustained me through many challenges. I am grateful to Katherine Krawec for her thesis mentoring and friendship. Thank you to Rebekah and Alison for the shared laughter and support. Huge thanks to Alex, Kate and Max, who put me up in their spare room for my last month in Sheffield. Wholehearted thanks to my parents, Huw and Candice, and to Gwilym, for their love and support through it all.

This research was funded by a NERC PhD studentship and by an EU-JPI grant to Andy Hodson.

"...Mud, mud, glorious mud..."

(Flanders and Swann, 1957)

Table of Contents

List of Figures

List of Tables

Chapter 1. General Introduction

1.1 Motivation

Surface temperatures in the Arctic are increasing at double the rate of the lower latitudes (Cowtan & Way, 2014; Screen & Simmonds, 2010; Serreze et al., 2009). Numerous changes and feedbacks are occurring in the Arctic in reaction to this rapid warming (Hinzman et al., 2013). The extent of sea ice is decreasing, mass is being lost from glaciers and ice sheets (IPCC, 2013) and permafrost is warming and thawing (Smith et al., 2005; Osterkamp, 2007; Romanovsky et al., 2010a, 2010b; Smith et al., 2010). Permafrost, which is ground that remains at or below 0 °C for at least two consecutive years (French, 2013), contains approximately 50% of the global terrestrial belowground organic carbon stocks (1330 to 1580 Pg carbon; Tarnocai et al., 2009; Hugelius et al., 2014). This accounts for the largest individual constituent of the terrestrial carbon pool, and is more than double the amount of carbon in the present atmosphere (Tarnocai et al., 2009; McGuire et al., 2012; IPCC, 2013). As rapid climate change occurs in the high Arctic, rising permafrost temperatures and progressively deeper seasonal thaw (active layer) are exposing formerly frozen soil organic carbon to soil microbial decomposition (Romanovsky et al., 2010b; Schuur et al., 2015; Koven et al., 2011). This releases carbon dioxide and methane to the atmosphere and it is predicted that by the mid-2020s this will cause permafrost ecosystems to become a net source of carbon (Elberling et al., 2013; Lee et al., 2012; Schuur et al., 2015). Hence, permafrost thawing will amplify the response of Earth's climate system to the anthropogenic climate forcing. However, the size and timing of the permafrost carbon feedback is uncertain (IPCC, 2013). As future climate change will exacerbate economic and social burdens on the human population (Carleton & Hsiang, 2016), it is therefore crucial to resolve the uncertainty in estimates of future greenhouse gas emissions from permafrost regions.

1.2 Climate change and greenhouse gases

Greenhouse gases (GHGs), such as carbon dioxide (CO_2), methane (CH_4) and nitrous oxide (N_2O), have long residence times in the atmosphere and have high thermal absorption

capacities (Serrano-Silva et al., 2014). Since the Industrial Revolution, global mean surface temperature has increased at an alarming rate because of rising greenhouse gas (GHG) concentrations in the atmosphere (IPCC, 2013). The burning of fossil fuels has contributed a total of 375 ± 30 PgC to the atmosphere between 1750 and 2011 (IPCC, 2013) and is the main reason for increasing concentrations of carbon dioxide in the atmosphere (Rotty, 1983; Boden et al., 2011; IPCC, 2013). Changes in land use (mainly deforestation) are the second major source of anthropogenic carbon dioxide emissions to the atmosphere (IPCC, 2013). Since the start of the Industrial Revolution, the concentration of atmospheric carbon dioxide has increased dramatically (from ~280 to ~400 parts per million; Myhre et al., 2013). The current atmospheric carbon dioxide concentrations of over 400 ppm have probably not been experienced on Earth for 3 million years (Martínez-Botí et al., 2015).

The importance of methane as a well-mixed greenhouse gas is second only to carbon dioxide (Myhre et al., 2013). Since the start of the Industrial Revolution, globally averaged surface methane concentrations have increased (from ~720 to ~1800 parts per billion; Myhre et al., 2013). Natural and anthropogenic sources emit methane to the atmosphere (Dean et al., 2018). Between 50 and 65% of the current total methane emissions are anthropogenic (IPCC, 2013). The main anthropogenic causes of the increase in atmospheric methane concentration are the growth in the number of ruminants (Barnosky, 2008), extraction and use of fossil fuels, landfill emissions and rice paddy agriculture (IPCC, 2013). Natural sources of methane are estimated to have contributed between 33 and 54% of the global emissions since 1980 (Kirschke et al., 2013). The largest natural source of methane to the atmosphere is wetlands, and other natural sources include other land water systems (lakes, ponds, rivers, estuaries), geological sources, wild animals, wildfires, termites, terrestrial permafrost and oceanic sources (Saunois et al., 2016).

The most recent report by the Intergovernmental Panel on Climate Change (IPCC) stated a high level of confidence that warming would cause permafrost extent to decrease, with consequent thawing of currently frozen permafrost carbon (IPCC, 2013). However, there was a low level of confidence in the magnitude of carbon losses via carbon dioxide and methane emissions, with estimates ranging from 50 to 250 PgC lost in the period 2000 to 2100 under the highest Representative Concentration Pathway (RCP8.5) scenario. The sources of

uncertainty were cited by the IPCC report as the rate of thaw, the proportion and timing of carbon released following thaw, the potential for negative feedbacks from nutrients, spatial variability and the ratio of carbon dioxide to methane emitted. Consequently, the Coordinated Modelling Intercomparison Project Phase 5 (CMIP5) Earth System Models used in the report did not include the permafrost carbon feedback in their projections of future atmospheric greenhouse gas concentrations and global temperature increase. This clearly signals the need to resolve the uncertainty in the response of permafrost to current climate change and its contribution to future climate change.

1.3 The response of permafrost to climate change

Permafrost is found beneath approximately 22.79 x 10^6 km^2, or 24%, of the Northern Hemisphere land surface (Zhang et al., 2008). This is ~15% of the global exposed land area (Zhang et al., 2008). In the continuous permafrost zone, permafrost exists beneath the entire exposed land surface, except for widely scattered sites (Figure 1.1; van Everdingen, 2005). In the extensive discontinuous permafrost zone, permafrost underlies between 65 and 90% of the exposed land surface, and in the sporadic permafrost zone, permafrost underlies between 10 and 35% of the exposed land surface (van Everdingen, 2005). In the International Polar Year (2007-2009), improvements were made to the permafrost monitoring network in the Northern Hemisphere polar regions by drilling new boreholes for long-term ground temperature monitoring, resuming ground temperature measurements at previously abandoned sites and continuing to measure ground temperatures at existing permafrost observatory sites (Romanovsky et al., 2010b; Figure 1.1). The overall trend in the mean annual ground temperature (MAGT) is to decrease northward. This trend is modified by factors such as elevation, ocean currents, snow thickness, vegetation type, ground composition, and landforms (Romanovsky et al., 2010b). For instance, thicker snow cover is associated with a higher MAGT (Smith et al., 2010). In north-western Russia, northern Scandinavia and Svalbard, warm ocean currents cause the MAGT to be higher than in other locations with a similar latitude in the high Arctic (Romanovsky et al., 2010b). Overall, Northern Hemisphere permafrost has warmed since the late 1970s (Romanovsky et al., 2010b). The rates of

warming are higher for colder permafrost (<-2 °C), such as in Svalbard, than for warmer permafrost, due to latent heat effects (close to 0 °C).

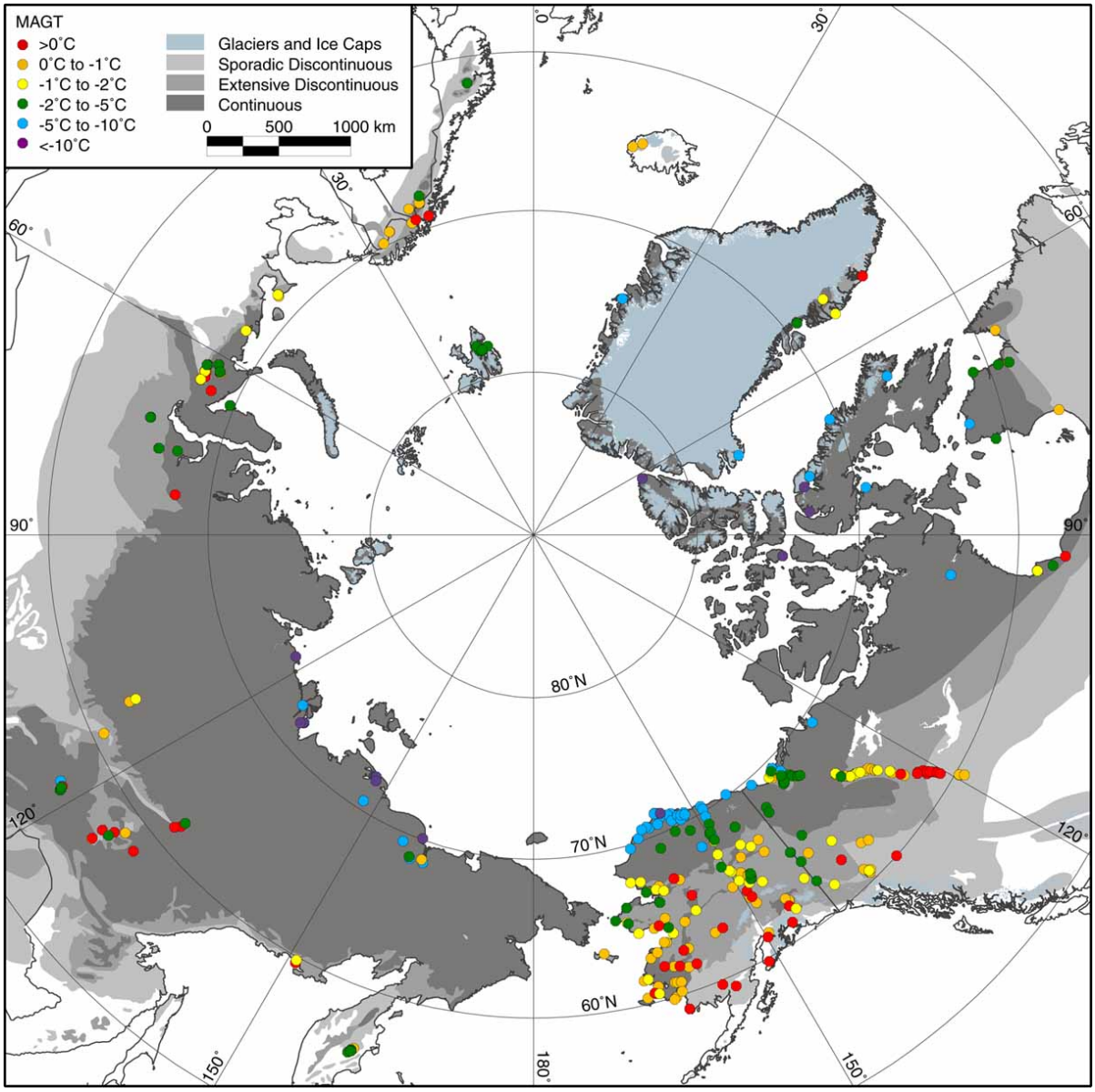

Figure 1.1 The mean annual ground temperature (MAGT) during the International Polar Year (2007-2009). The MAGT, at the depth of zero annual amplitude, is represented by coloured dots. The greyscale permafrost zones are after Brown et al. (1997). Modified after Romanovsky et al. (2010b).

Present-day permafrost is a product both of present-day climate and of past climates (Péwé, 1975). A large proportion of Arctic permafrost was formed in the late-Pleistocene, or even earlier (Brown, 1965; Gubin & Lupachev, 2008; Kanevskiy et al., 2011; Schirrmeister et al., 2011a). For instance, old permafrost, which is a remnant of paleoclimate, is found in the Yukon regions in Canada (Froese et al., 2008) and the Yedoma formations in Arctic and boreal

Alaska and north-eastern Russia (Reyes et al., 2010; Schirrmeister et al., 2011a, 2011b; Kanevskiy et al., 2011, 2014). However, younger permafrost has formed more recently, during the Holocene, following deglaciation and sub-aerial exposure (Humlum, 2005). Organic matter is accumulated in permafrost regions because organic matter decomposition is slowed by low temperatures and frequently saturated (thus reducing) conditions (Kaiser et al., 2007; Rodionov et al., 2007). Ice-rich, syngenetic permafrost forms when permafrost aggrades concurrently with sedimentation (French, 2013). Epigenetic permafrost forms when permafrost aggrades after sedimentation (French, 2013). Often, organic carbon in epigenetic permafrost has undergone some degradation before incorporation into the permafrost (Schuur et al., 2008), whereas syngenetic permafrost is more likely to contain relatively undecomposed organic matter that was promptly buried and frozen (Zimov et al., 2006; Sannel & Kuhry, 2009). Hence, the manner in which permafrost aggraded influences the quantity and quality of the organic matter available for decomposition upon thawing.

In addition to the style of permafrost aggradation, the hydrology of permafrost plays an important role in determining the quantity of organic matter accumulated. For example, in wetlands, oxygen diffusion into sediments is limited by water saturation (Dean et al., 2018). This means that net primary production exceeds decomposition, and so organic carbon accumulates in wetlands (Kolka et al., 2015). Furthermore, the hydrology of permafrost influences the type of greenhouse gas produced from decomposing organic matter in thawing permafrost. If the soil is well-drained, carbon dioxide is produced as organic carbon is decomposed aerobically (Liljedahl et al., 2012; Elberling et al., 2013). In contrast, under water-saturated, anaerobic conditions, organic carbon is decomposed anaerobically, producing carbon dioxide and/or methane (Lipson et al., 2012; Figure 1.2). The most substantial natural source of methane emissions globally is wetlands, which produce approximately one third of the total global methane emissions every year (Saunois et al., 2016). Approximately 34% of the total wetland methane emissions are from northern (Boreal and Arctic) wetlands (Wang, 1996; Bloom et al., 2010).

Limited diffusion of oxygen into sediments of the active layer under water-saturated conditions results in increased methane emissions (Riley et al., 2011). However, this picture may be complicated by the presence of alternative electron acceptors, such as nitrate,

manganese, iron and sulfate. The standard model developed for deep marine sediments indicates that, under anaerobic conditions, these alternative electron acceptors may be used preferentially in the microbial respiration of organic carbon, prior to the production of methane (Froelich et al., 1978). The alternative electron acceptors tend to be used by microorganisms in succession, according to their free energy yield (Froelich et al., 1978). The alternative electron acceptors are used as follows, in order of decreasing free energy yield: nitrate, manganese, iron and lastly sulfur (Froelich et al., 1978) . Generally, microbes do not respire using a specific alternative electron acceptor until the concentrations of the electron acceptors yielding a higher energy have substantially decreased (Tostevin & Poulton, 2019). Under steady state conditions, the result of this is a series of biogeochemical zones in which the use of each electron acceptor dominates (e.g., Figure 1.2; Burdige, 1993). This increases carbon dioxide production relative to methane production.

In reality, the Arctic cryosphere is a far more dynamic system than deep marine sediments and it does not exist in steady state; it is changing in response to past and present climate perturbations (Jakobsson et al., 2014), as well as in response to seasonal rainfall and temperature variations. Cycling (of electrons) occurs between different elements of the cascade represented in Figure 1.2. For instance, even in marine sediments in steady state, the re-oxidation of 70 to 90% of sulfide (produced by sulfate reduction) occurs, with the amount of re-oxidation increasing with an increased input of Fe(III) (Thamdrup et al., 1994). Experiments on salt marsh sediments indicate that this recycling can occur with sulfide acting as an electron donor for Fe(III)-reduction (Mortimer et al., 2011). Hence, the definition of biogeochemical zones in Figure 1.2 is only a proxy for process, as the concentrations of reactants and products relate to the difference between the rates of consumption and production, rather than the absolute rates of consumption and production. In addition, sediment microheterogeneity facilitates the existence of bacterial microniches, where isolated reducing conditions exist in confined areas of high organic matter (Stockdale et al., 2009, and references therein). Moreover, the biogeochemical zonation (Figure 1.2) is entangled with physical processes, such as hydrological input to and outflows from the active layer (Throckmorton et al., 2016) and annual freezing and thawing of the active layer. Finally, the speciation and availability of electron acceptors (dependent partly on substrate material and sedimentation) and organic carbon cause geochemical complexity that is not fully

represented by the conventional redox ladder illustrated in Figure 1.2 (Lovley & Chapelle, 1995; Bethke et al., 2011). For instance, the reduction of ferric iron was found to increase carbon dioxide production relative to methane production in an Arctic peat soil in Barrow, which is situated on the coastal plain of Alaska. Large quantities of siderite, which contains reduced iron and carbon, were found in these sediments. The pathway of decomposition of organic carbon was heavily influenced by the mineralogy of iron oxides (Herndon et al., 2017; Herndon et al., 2015). For example, ferrihydrite minerals suppressed methanogenesis, whereas the crystalline iron oxides did not decrease methane production (Herndon et al., 2015). In summary, there is a range of factors influencing methane and carbon dioxide production in the complex permafrost and active layer sediments of the Arctic cryosphere.

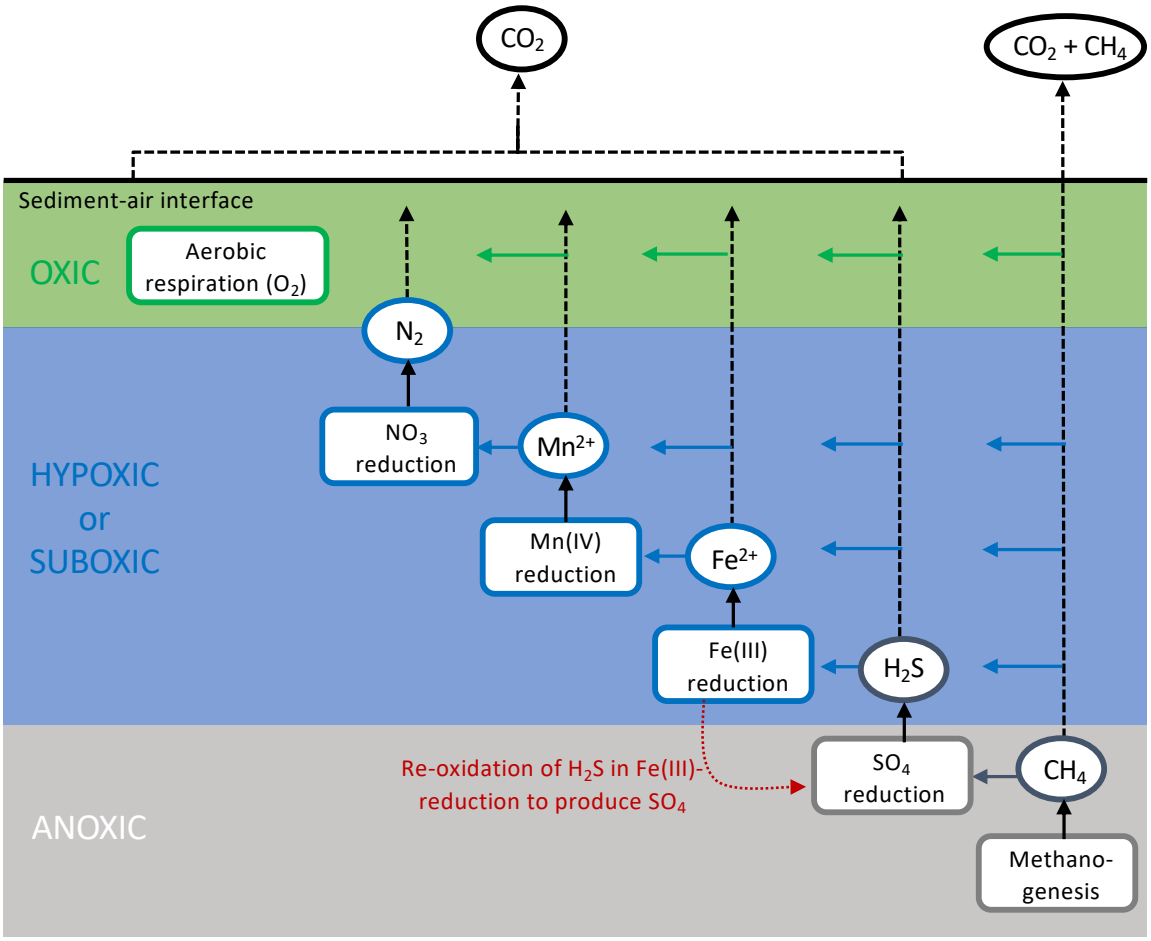

Figure 1.2 Conceptual diagram of the theoretical vertical sequence in water-saturated sediments of organic matter remineralisation (vertical arrows from rounded rectangles to ovals) and re-oxidation pathways (horizonal arrows). Re-oxidation of H_2S during Fe(III)-reduction to produce SO_4 shown by red dotted line and arrow. Above the sediment-air interface are arrows indicating the flux of greenhouse gases (CH_4 and CO_2) to the atmosphere. Modified after Bianchi et al. (2016).

Wetlands are more widespread in cool and/or wet climates than in hot and/or dry climates, due to the difference in the balance between evapotranspiration and precipitation (Mitsch & Gosselink, 2007). The water table of wetlands is usually near to or above the ground surface, but this may vary depending on the characteristics of the wetland (Woo & Young, 2006). Permafrost, particularly that with a high ice content, can act as an impermeable barrier that impedes the percolation of water and contributes to keeping wetland active layers saturated with water (Woo & Young, 2006). In the high Arctic, the formation of wetlands in polar deserts requires a reliable water supply, which could be from groundwater, streams and ponds, snowbanks or coastal water (Woo & Young, 2006). In addition, the topographical setting affects the development of a wetland; wetlands are more widespread in flat terrain or terrain depressions than in steep terrain (Mitsch & Gosselink, 2007). The high Arctic is

geomorphologically very active because many areas have only recently emerged from under the ice sheets (Woo & Young, 2006). Hence, high Arctic wetlands may be described by the landforms upon which they develop (e.g., raised beaches) in addition to their water source.

The hydrogeomorphology of a wetland can be described by a combination of climate, geomorphology and hydrology. Figure 1.3 shows that landscape geomorphology exerts an influence over the wetland hydrology, physiochemical environment and biota. The physiochemical environment of a wetland is influenced by its hydrology, with impacts on sediment and nutrient transport, oxygen availability and water chemistry. The build-up of sediments can in turn influence the hydrologic inflows and outflows (Mitsch & Gosselink, 2007). The physiochemical environment affects the wetland biota; for instance, reduced sediments favour microorganisms that are able to metabolise under anaerobic conditions, whereas oxidised sediments favour the survival of aerobic microorganisms (Mitsch & Gosselink, 2007). Finally, there are feedbacks between the various aspects of the system; for instance, plants build peat, trap sediment and retain nutrients, acting as ecosystem engineers (Mitsch & Gosselink, 2007, and references therein). The links shown here between climate, landscape geomorphology, hydrology, physiochemical environment and biota make it clear that there are many factors that could make the Arctic permafrost system heterogeneous with respect to GHG emissions.

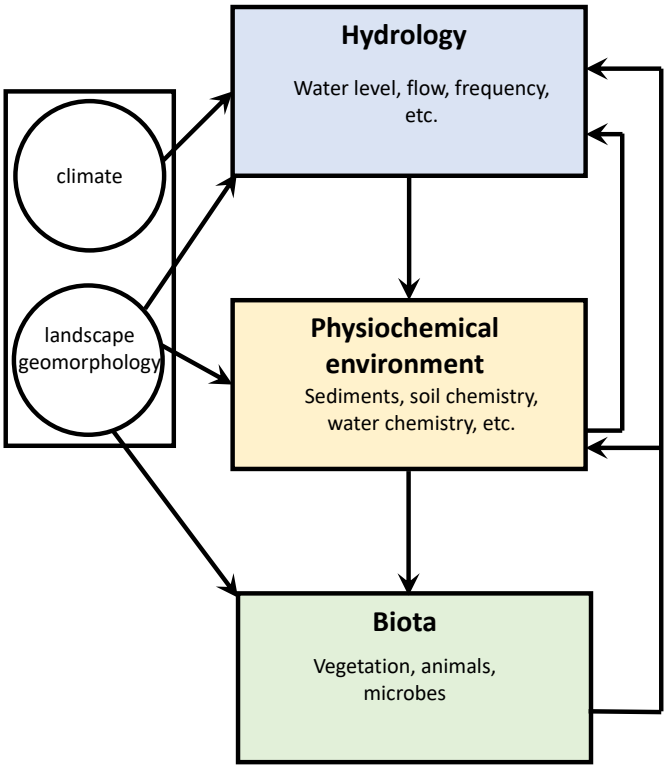

Figure 1.3 Conceptual diagram showing the interlinking effects of climate and basin geomorphology on landscape hydrology, physiochemistry and biota. After Mitsch and Gosselink (2007).

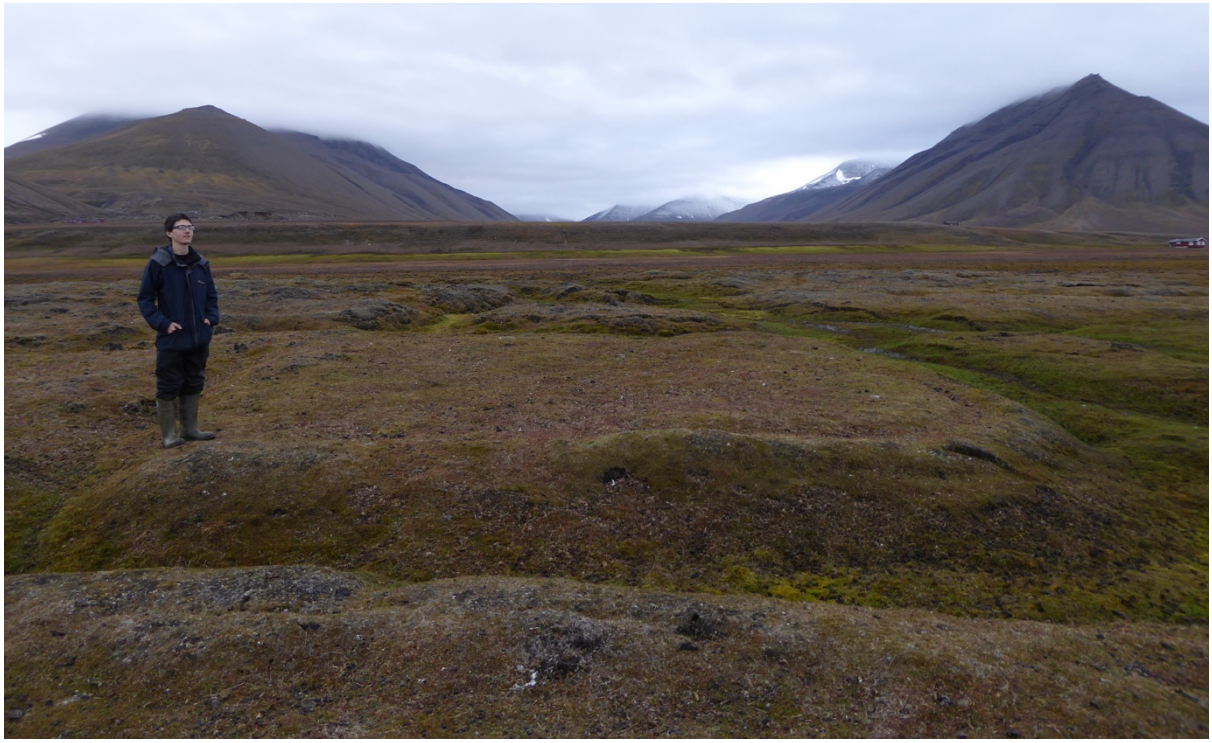

Figure 1.4 High-centred polygon at Revneset, Svalbard. Gwilym (pictured) is standing on the collapsed polygon rim.

Ice-wedge polygons, such as shown in Figure 1.4, are small-scale landforms that condition the environment within which wetlands form. Ice-wedge polygons are prevalent in permafrost regions (Christiansen et al., 2016) and 3% of the exposed land area in the Arctic is covered by ice-wedge polygon tundra (Minke et al., 2007). Ice-wedge polygons form alongside the development of ice-wedges, which are described further in Section 4.1. Low-centred ice-wedge polygons are commonly enclosed by raised rims that trap snow meltwater in the depressed polygon centre (Woo & Young, 2006). These landforms degrade in response to climate warming and their degradation influences landscape hydrology and the decomposition pathways of organic carbon. It is paramount, therefore, to study their impact on permafrost landscape hydrology, biology and greenhouse gas emissions.

The previous sections in this chapter described the heterogeneous nature of Arctic permafrost environments, with regard to the age of the permafrost, the type of aggradation (syngenetic/epigenetic), the landforms present, the hydrology and the geochemistry. Current research sampling does not adequately represent this heterogeneity (Metcalfe et al., 2018). Particularly well-studied permafrost locations include the coastal plain of Alaska, where detailed studies of the interactions between iron and organic carbon in permafrost have been conducted (e.g., Lipson et al., 2010; Herndon et al., 2015; Herndon et al., 2017). The Arctic Coastal Plain sediments were deposited in the Middle and Late Quaternary and mainly comprise near-shore marine, fluvial, alluvial and aeolian sediments (Meyer et al., 2010). Importantly, during the late Pleistocene, the Arctic Coastal Plain was not glaciated (Kaufman & Manley, 2004). The excellent biogeochemistry studies from Barrow must not be uncritically assumed to apply to permafrost regions that have a significantly different history of glaciation, sedimentation or permafrost aggradation. Simulations of the future permafrost carbon feedback cannot properly represent the diversity of permafrost environments without field and laboratory data from the full breadth of permafrost environments. Therefore, sampling of under-sampled permafrost environments is urgent. For instance, a study by Metcalfe et al., (2018) found that rapidly warming sites are poorly represented by current research sampling, but serve as early warning indicators of climatic change. The Svalbard archipelago is warming rapidly, but has relatively few field sampling locations and citations for many discipline areas, including biogeochemistry (Metcalfe et al., 2018). Further, the permafrost of Svalbard has a different history of glaciation, sedimentation and permafrost

aggradation from the coastal plain of Alaska, and thus is an ideal location for further study of permafrost biogeochemistry to confirm whether or not similar biogeochemical processes dominate this different, yet important, landscape.

1.4 Permafrost in Svalbard

As glaciers retreat, fjord valleys have rapid sedimentation and organic carbon burial rates, forming valley infills that are ideal for methanogenesis (Gilbert et al., 2017; Gilbert et al., 2018; Smith et al., 2015; Syvitski et al., 1986). In fact, over the past 10,000 years, almost one quarter of global marine sedimentation has occurred in fjords (Syvitski et al., 1987). In the lower elevation, coastal sites of Svalbard, glacial retreat and postglacial isostatic rebound have played a cardinal role in landscape evolution (Milne & Shennan, 2007). In western Svalbard (Figure 1.5), for instance, there were three glacial advances during the late Pleistocene (Weichselian) (Mangerud et al., 1998).

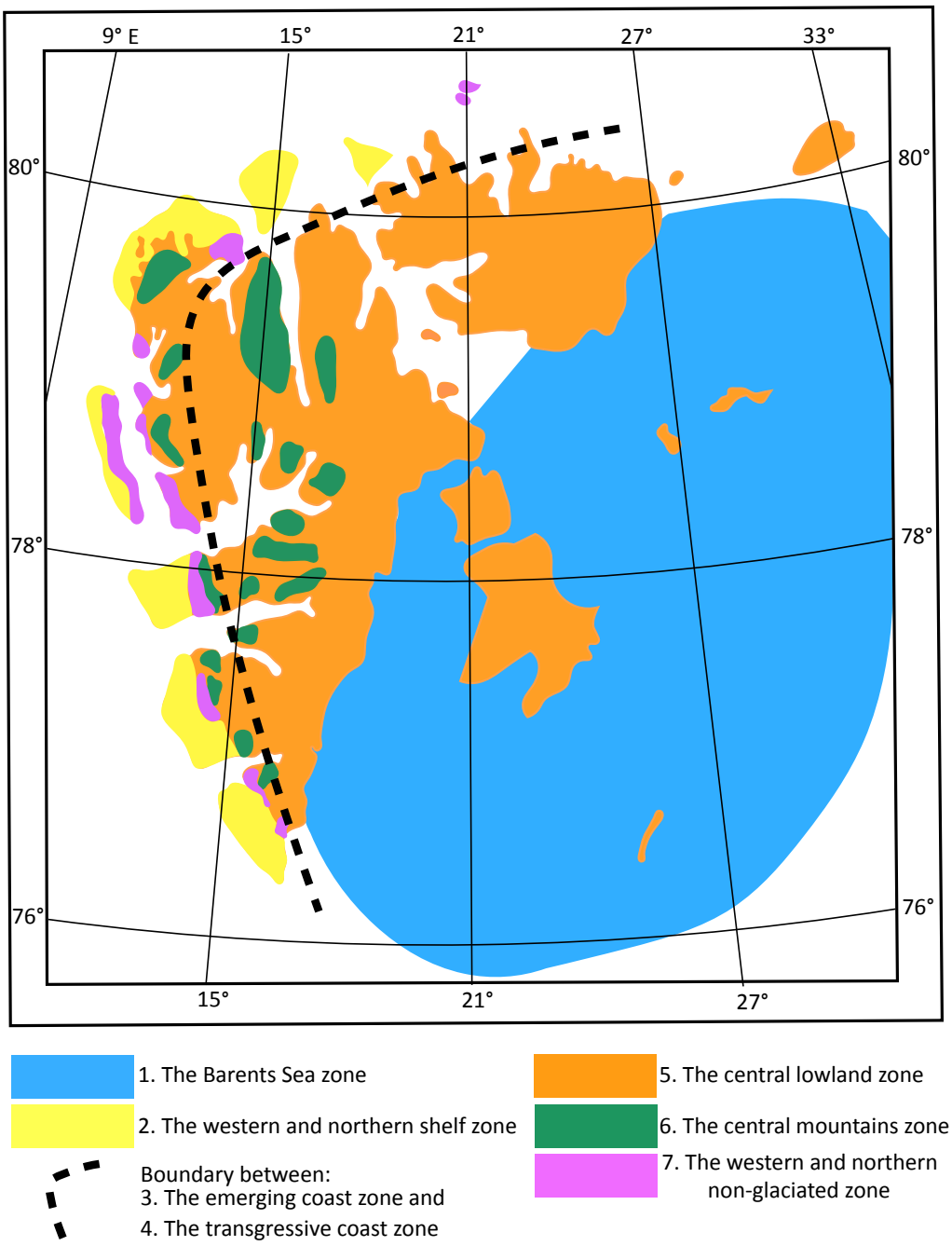

Figure 1.5 A schematic representation of permafrost zones in Svalbard. The Barents Sea was glaciated during the LGM and permafrost is absent, owing to a lack of subaerial exposure (Zone 1). Limited permafrost aggraded in areas that were not glaciated during the LGM, but were inundated by the sea in the Holocene (Zone 2). In the east, permafrost is younger and thinner owing to its recent subaerial exposure (Zone 3). In the north and west, coastal erosion and transgressions are occurring, but there is permafrost beneath the beaches (Zone 4). The present study is on land that deglaciated after the LGM (except areas covered by present-day glaciers), since which time permafrost has developed (Zone 5). Nunataks (LGM unglaciated mountains) contain permafrost up to 100,000 years old (Zone 6). Some areas were not glaciated during the LGM, but are above present sea level (Zone 7). Modified after Landvik et al. (1988).

In the most recent glaciation, the Last Glacial Maximum (LGM; 20 ka), the entire archipelago of Svalbard was covered by an ice sheet (Landvik et al., 1988; Landvik et al., 2005). Warm-based glaciers have basal ice at the pressure melting point (Benn and Evans, 2010). During the LGM, the valleys of western Spitsbergen were filled with warm-based, erosive ice streams, as indicated by the glacial striae up to 200 metres above sea level in central Spitsbergen (Humlum et al., 2003; Landvik et al., 2005; Humlum, 2005). Warm-based ice is a key factor in regulating the age of permafrost in Svalbard.

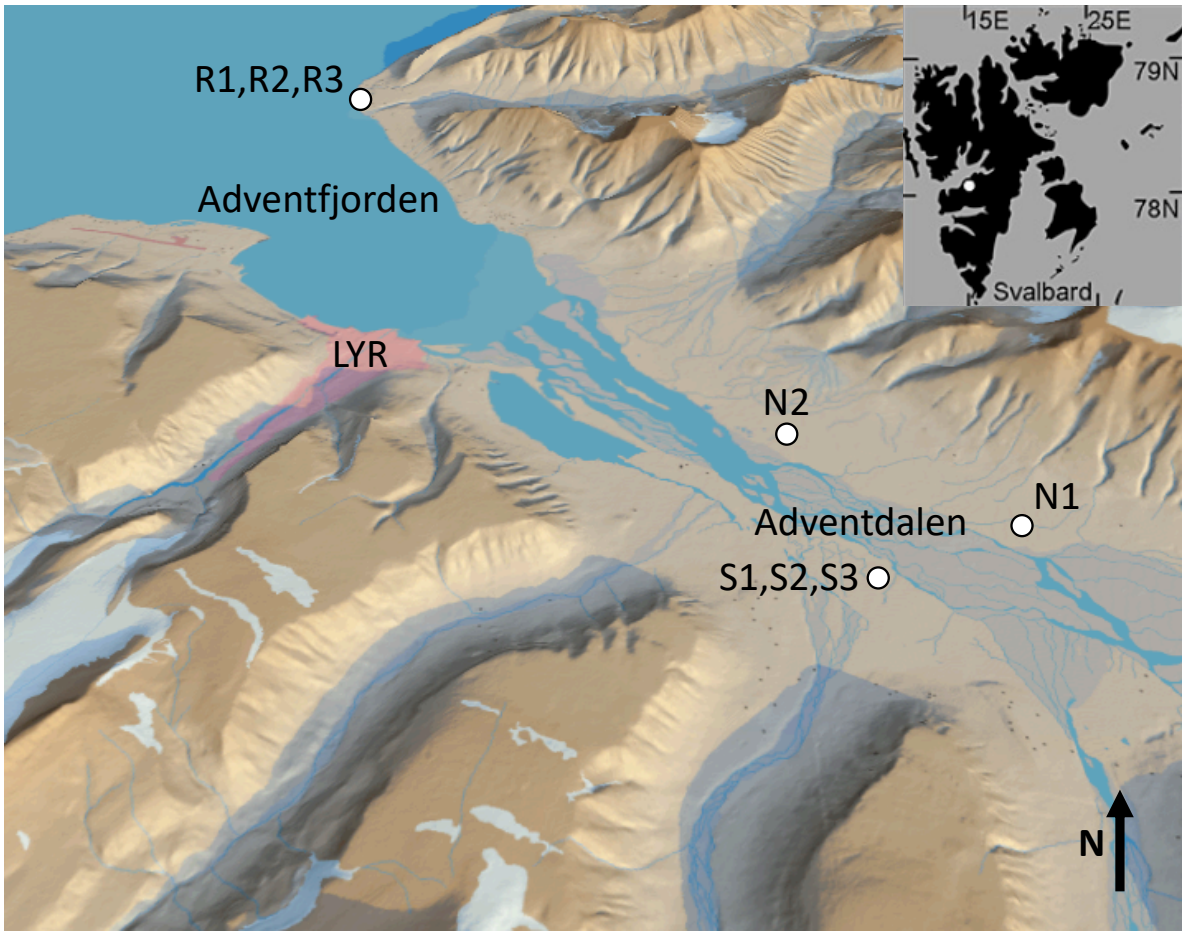

Figure 1.6 The Svalbard archipelago (inset) and Adventdalen, with a white circle indicating each site where ice-wedge polygons were sampled (Section 2.1 for further details).

After the LGM, the ice sheet retreated. Inner Adventfjorden (Figure 1.6) was ice-free by 10 ka; the evidence for this is a 10 ka raised beach at 62 metres above sea level in Bolterdalen (Lønne, 2005). Radiocarbon dating of driftwood from raised marine deposits provides evidence for the fall of relative sea level on western Spitsbergen (Salvigsen, 1984). Following deglaciation, a Gilbert-type delta prograded into Adventfjorden (Lønne & Nemec, 2004).

Despite the global eustatic sea-level rise (Fairbanks, 1989), the glacial isostatic rebound of Svalbard meant that relative sea level fell (Figure 1.7; Lønne & Nemec, 2004). The highest relative sea-level stand (the marine limit) is at 70 metres above sea level in outer Adventfjorden (Lønne & Nemec, 2004). The sea level fall was interrupted by still stands or transgressions (Forman et al., 2004). For instance, at Brøggerhalvøya, three barrier beaches below 45 metres above sea level indicate that there were three such events (Forman & Miller, 1984; Forman et al., 2004). Raised beaches are widespread across the coastline of the Svalbard archipelago (Forman et al., 2004; Salvigsen et al., 2005; Figure 1.8) and other high Arctic coasts (Funder et al., 2011; Nielsen et al., 2017; Dyke et al., 1997). Studies in Arctic Canada have found that peat commonly develops in the wetlands between raised beaches (Martini & Glooschenko, 1985). However, studies of coastal peat development on Svalbard are rare (e.g., Rozema et al., 2006) and there have not been any studies focussing on wetlands and peat development between raised beaches in Svalbard.

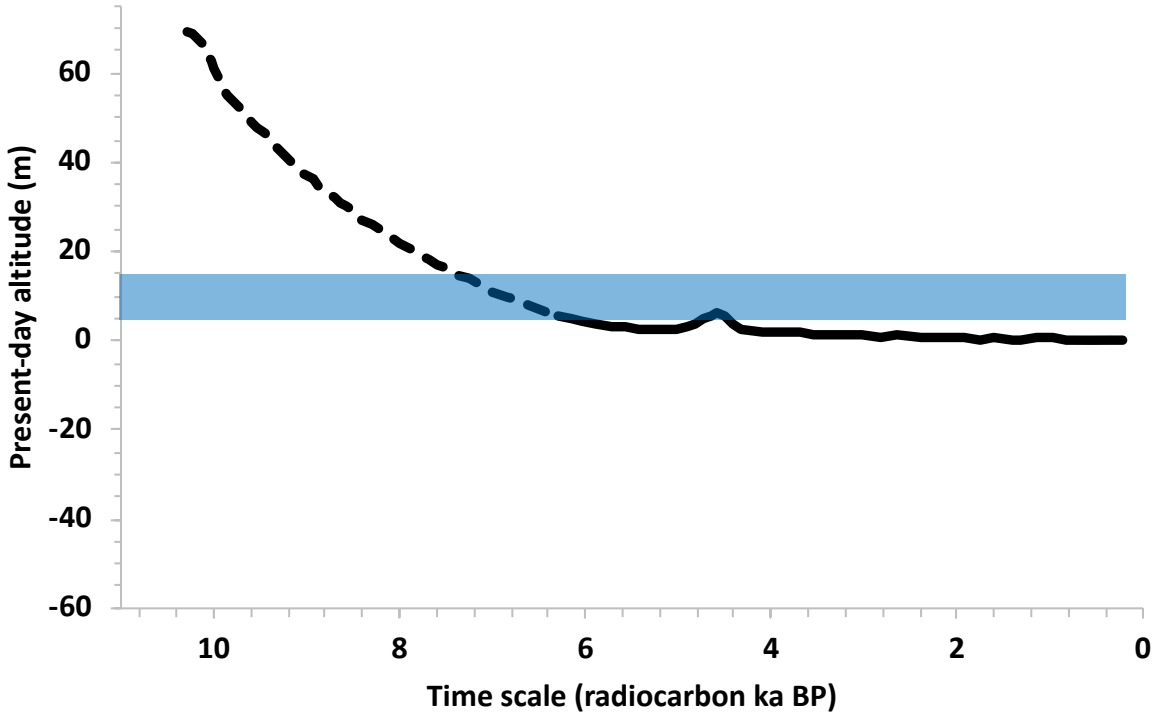

Figure 1.7 Sea level curve for Adventfjorden, based on data from Lønne & Nemec (2004).The solid black line is constrained by radiocarbon dates, and the dashed black line is hypothetical. The shaded blue rectangle represents an approximate estimate of the elevations of the cores presented later in this thesis. The position of the rectangle indicates that the core sediments presented in this thesis have an approximate age of between 4 and 8 radiocarbon ka BP.

Figure 1.8 Wetlands have formed between raised beaches in this photograph of a raised beach sequence at Bohemanflya, which is situated on the northwest side of Isfjorden, Svalbard. The raised beaches are linear features aligned approximately parallel to the coastline. Photo credit: A. Hodson.

During the Quaternary glaciations, with the exception of the high altitudes, warm-based glaciers caused permafrost in Svalbard to thaw (Landvik et al., 1988; Humlum et al., 2003; Humlum, 2005). In western Svalbard, permafrost aggradation began after the deglaciation (Haldorsen et al., 2010). The aggradation of permafrost in Svalbard since the LGM is linked to climatic variations over the Holocene (Humlum, 2005). Macrofossils and pollen in lake sediments (Birks, 1991), ice-rafted debris (IRD) in marine sediment cores (Hald et al., 2004), and recent instrumental records indicate three climatic phases since the LGM (Humlum, 2005). Between 9000 and 7500 years before present (B.P.), the post-LGM warming culminated in the maximum air temperatures for Svalbard in the Holocene (Birks, 1991; Humlum, 2005). Permafrost was probably discontinuous or absent on Svalbard below 300-500 metres above sea level (Humlum, 2005). After 4000 B.P., diatoms in marine sediment cores indicate that surface waters close to western Svalbard cooled (Koç et al., 1993). As permafrost aggradation can only occur once the ground is exposed to the cold air, glacial isostatic rebound influences the age of permafrost (Humlum, 2005). Pingos and ice wedges below the Holocene upper marine limit in Spitsbergen formed no earlier than 2650 B.P. and 2900 B.P. (Humlum, 2005), indicating that permafrost was established in the Late Holocene

near sea level (Humlum, 2005). The recent glaciation of Svalbard means that, compared to Siberia and the Alaskan North Slope, permafrost in Svalbard is young (Humlum et al., 2003).

1.5 Aims and objectives

The primary motivation for this research is the need of a deeper understanding of how past landscape development determines the biogeochemical processes in recently deglaciated permafrost landscapes. The aim of this thesis is to deduce the biogeochemical processes leading to the production of methane and carbon dioxide in the active layer and shallow permafrost sediments of polygonal ground in Adventdalen, Svalbard. The specific objectives are to:

1. Assess the variability of biogeochemical processes within two contrasting, yet complementary, ice-wedge polygonal wetlands in a fjord valley (Adventdalen).

2. Examine the influence of larger-scale landforms (fjord valley, raised beaches) and smaller-scale landforms (ice-wedge polygons) on biogeochemical processes and the concentrations of methane and carbon dioxide in active layer and shallow permafrost sediments in Svalbard.

3. Quantify the sources and sinks of methane in fjord valley (Adventdalen) and intra-beach sediments (Revneset).

1.6 Thesis structure

This thesis comprises the introduction (Chapter 1), the methodology (Chapter 2), three independent chapters of research material (Chapters 3 to 5) and a summary (Chapter 6). Chapter 1 introduces the research topic, reviews the key literature and presents the aims of the thesis. Chapter 2 presents the sampling locations and contains a detailed methodology applicable to Chapters 3 to 5. Chapter 6 provides a synthesis, suggests worthwhile future research and concludes the thesis.

Chapter 2. Methods

This chapter describes the methods applied in the research documented in this thesis. There are three main sections: Section 2.1 describes the sampling locations, Section 2.2 describes the collection and analysis of active layer and shallow permafrost cores and Section 2.3 describes sampling and analyses of water from the active layer. Microbiological data described in Chapter 5 were contributed by Ebbe Norskov Bak (Aarhus University) and Section 2.2.4 describes the core sampling, 16S sequencing and data analysis conducted by Ebbe.

2.1 Sampling locations

Adventdalen (78°19'N, 15°93'E) is a 12 km x 4 km valley, oriented NW-SE, in central Svalbard. The van Mijenfjord and Adventdalen Groups, which contain sedimentary rocks (sandstones, shales and carbonates), comprise the lithology of the Adventdalen catchment (Figure 2.1). These rocks contain carbonate and pyrite (Dallmann et al., 1999). The sandstones contain the iron-bearing mineral phases pyrite, siderite and glauconite (Svinth, 2013), plus shales (Riber & Lars, 2009). Also, there is a small amount of iron in biotite and chlorite (chamosite; Hodson et al., 2016).

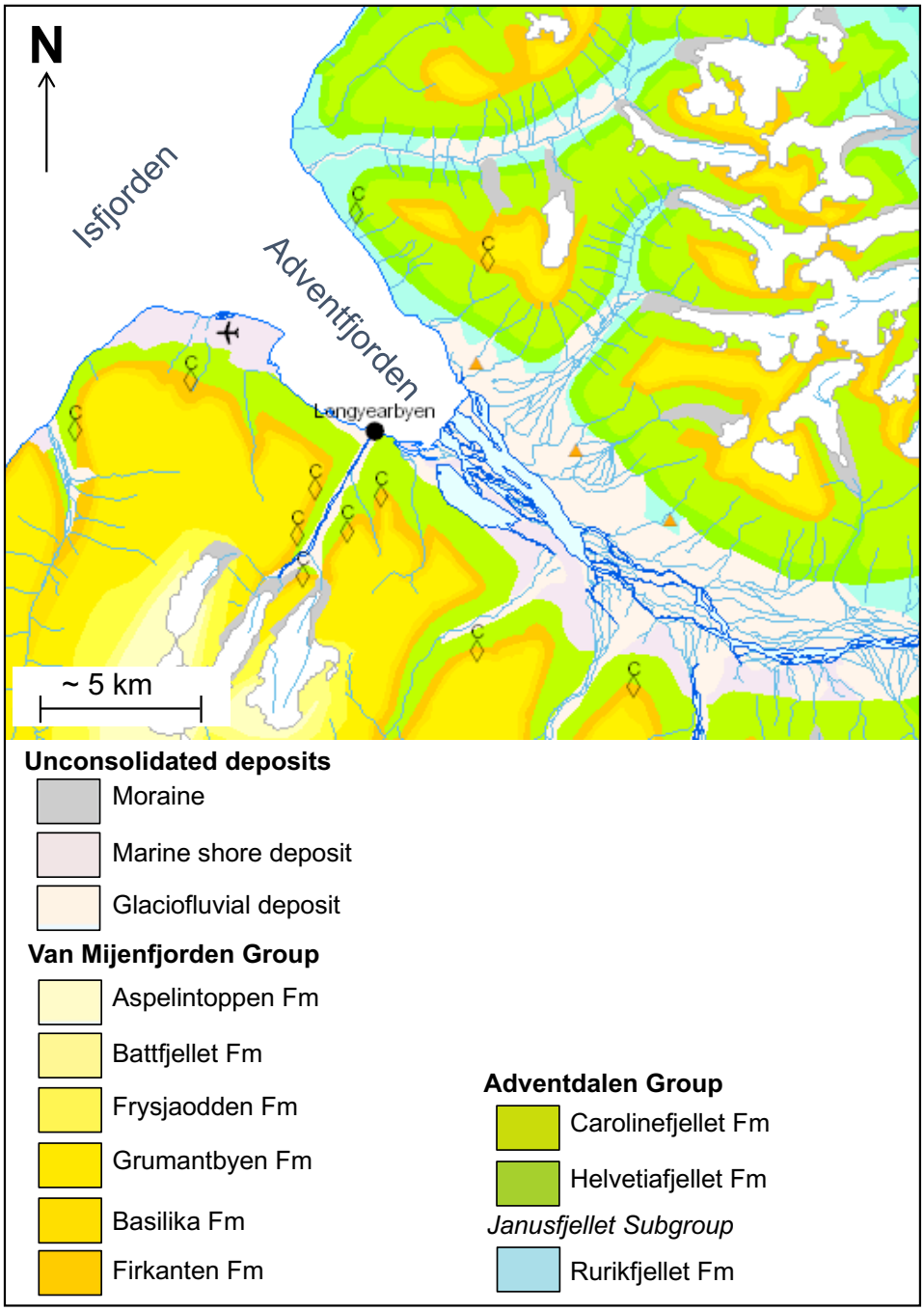

Figure 2.1 Geological map of the study area. The age of deposits ranges from the mid-Jurassic to the Quaternary. The formations of the Adventdalen Group (deposited mid-Jurassic to Lower Cretaceous) are the Rurikfjellet Formation (part of the Janusfjellet Subgroup; shale, siltstone and sandstone), the Helvetiafjellet Formation (sandstone, conglomerate and coal seams) and the Carolinefjellet Formation (shale, siltstone and sandstone). The formations of the Van Mijenfjorden Group (deposited Paleocene to Eocene) are the Firkanten Formation (sandstone, shale, coal seams), the Basilika Formation (shale, mudstone, siltstone), the Grumantbyen Formation (sandstone), the Frysjaodden Formation (shale, sandstone), the Battfjellet Formation (sandstone, siltstone, shale) and the Aspenlintoppen Formation (sandstone, siltstone, mudstone). Unconsolidated deposits of the Quaternary are present in areas across the map. Orange triangles represent pingos; rhombuses represent abandoned mines. Map based on data from the Norwegian Polar Institute (http://svalbardkartet.npolar.no).

Glacial retreat and postglacial isostatic rebound influence landscape evolution (Milne & Shennan, 2007). As a consequence, permafrost aggradation in many high Arctic fjord valleys has involved the freezing of reactive, fine-grained sediment originally deposited on the fjord floor via glacio-marine sedimentation and delta progradation throughout deglaciation (Haldorsen et al., 2010; Gilbert et al., 2018). During the Last Glacial Maximum, Adventdalen was filled with an erosive ice stream; this caused permafrost to thaw (Humlum, 2005; Humlum et al., 2003; Landvik et al., 2005). After retreat of the ice sheet, the glacial isostatic rebound of Svalbard meant that relative sea level fell, and a Gilbert-type delta prograded into Adventfjorden (Lønne & Nemec, 2004). In Adventdalen, below about 3 metres depth, the permafrost is epigenetic, as it formed after the progradation of the delta (Gilbert et al., 2018). At between 0 and 3 metres depth, the permafrost is syngenetic, as it aggraded concurrently with aeolian sedimentation (Gilbert et al., 2018). Although permafrost only aggraded after deglaciation, it is continuous in Svalbard, where it reaches a thickness of 80 to 100 metres near the coast (Brown et al., 1997; Humlum, 2005). The seasonally thawed surface permafrost is the 'active layer' (French, 2013). Active layer thicknesses in Svalbard can be from 0.4 to 6 metres (Christiansen, 2005). In Adventdalen, the active layer thickness is around 1 metre (Christiansen et al., 2010). This project will focus on 0 to 2 metres depth, which involves sampling the active layer and the shallow permafrost.

The climate of Svalbard is polar tundra (Kottek et al., 2006) and in Longyearbyen between 1981 and 2010, the mean annual air temperature (MAAT) was -4.6 °C (Førland et al., 2011). Between 1989 and 2011, MAAT increased by 1.25 °C per decade (Førland et al., 2011) and in 2018, the MAAT was -1.8 °C (eklima.met.no). The mean annual ground temperature (MAGT) ranges from -5.6 °C to -3.2 °C in the Adventdalen area (Christiansen et al., 2010) and the rising air temperatures have caused a recent increase in permafrost temperatures (Isaksen et al. 2007). The vegetation in the valley varies between 1.3 g m^{-2} and 27.2 g m^{-2} moss and 2.8 g m^{-2} and 9.6 g m^{-2} vascular plants, with the amount of moss dependent on the soil moisture (Sjögersten et al., 2006).

The study sites (Figure 1.6) were selected with the aim of sampling three different wetlands found in Adventdalen. Sites S1, S2 and S3 are collectively termed 'Ice-wedge South', sites N1 and N2 are collectively termed 'Ice-wedge North'. Together, Ice-wedge South and Ice-wedge

North are henceforth referred to as Adventdalen. Sites R1, R2 and R3 are collectively termed 'Revneset'.

Table 2.1 lists the sample locations with details of the sampling methods. The sites in Adventdalen are covered with Late Holocene loess (aeolian) deposits overlying alluvial and deltaic deposits (Cable et al., 2017; Gilbert et al., 2018). As aeolian deposits accumulated, permafrost aggraded syngenetically, and the permafrost beneath this aggraded epigenetically (following deposition of sediments, by downward freezing; Gilbert et al., 2018). The sites at Revneset are peat deposits, situated between raised beaches. All sites in Adventdalen are situated in areas of low-centred ice-wedge polygons, which are common in Adventdalen (Figure 2.2; Sørbel & Tolgensbakk, 2002). Revneset contains both low- and high-centred polygons, but only high-centred polygons and the troughs of low-centred polygons were sampled here (Figure 2.3). The approximate proportion of high- and low-centred polygons at Revneset was estimated by classifying the polygons along the Revneset coastline, between Hanaskogelva and the river immediately to the north draining Louisdalen, using aerial imagery from the Norwegian Polar Institute (Figure 2.4). 66% of classified polygons (92 polygons) were high-centred polygons and the remaining 34% were low-centred polygons (47 polygons). Ice-wedge North is a water-saturated wetland, mainly fed by springs, whereas Ice-wedge South is mainly precipitation-fed and only sporadically inundated by local snowmelt and rainfall. The primary water source to Revneset is summer precipitation, with a probable contribution from winter precipitation.

Table 2.1 Sampling locations, in UTM zone 33X. The sample types are cores of the active layer and shallow permafrost ('PF'), waters from the active layer extracted via Macro Rhizon samplers ('WM') and waters from the active layer extracted via the The Sheffield Spike ('TSS'). The polygon feature refers to whether the samples were extracted from a polygon centre ('c') or trough ('t').

Site Name	**Code**	**Latitude** (UTM)	**Longitude** (UTM)	**Sample Type (Date)**	**Polygon Feature**
Ice-wedge South	S1	8679400	521010	PF (15.06.15), WM (26.08.17 & 27.08.17)	c
	S2a	8679343	521042	PF (12.02.17)	c
	S2b	8679343	521042	PF (14.02.17)	c
	S3w	8679145	521223	TSS (28.08.17 & 10.09.17)	c
Ice-wedge North	N1	8680446	522541	PF (02.05.16)	c
	N2	8681819	519780	PF (15.04.14)	c
	N1w	8680446	522541	WM, TSS (31.08.17, 01.09.17 & 13.09.17)	c
	N2w	8681819	519780	TSS (02.09.17)	c
Revneset	R1a	8690378	512848	PF (30.04.16), WM (05.09.17)	c
	R1b	8690378	512848	PF (26.04.17)	c
	R2	8690380	512856	TSS (06.09.17)	t
	R3	8690404	512926	TSS (06.09.17)	t

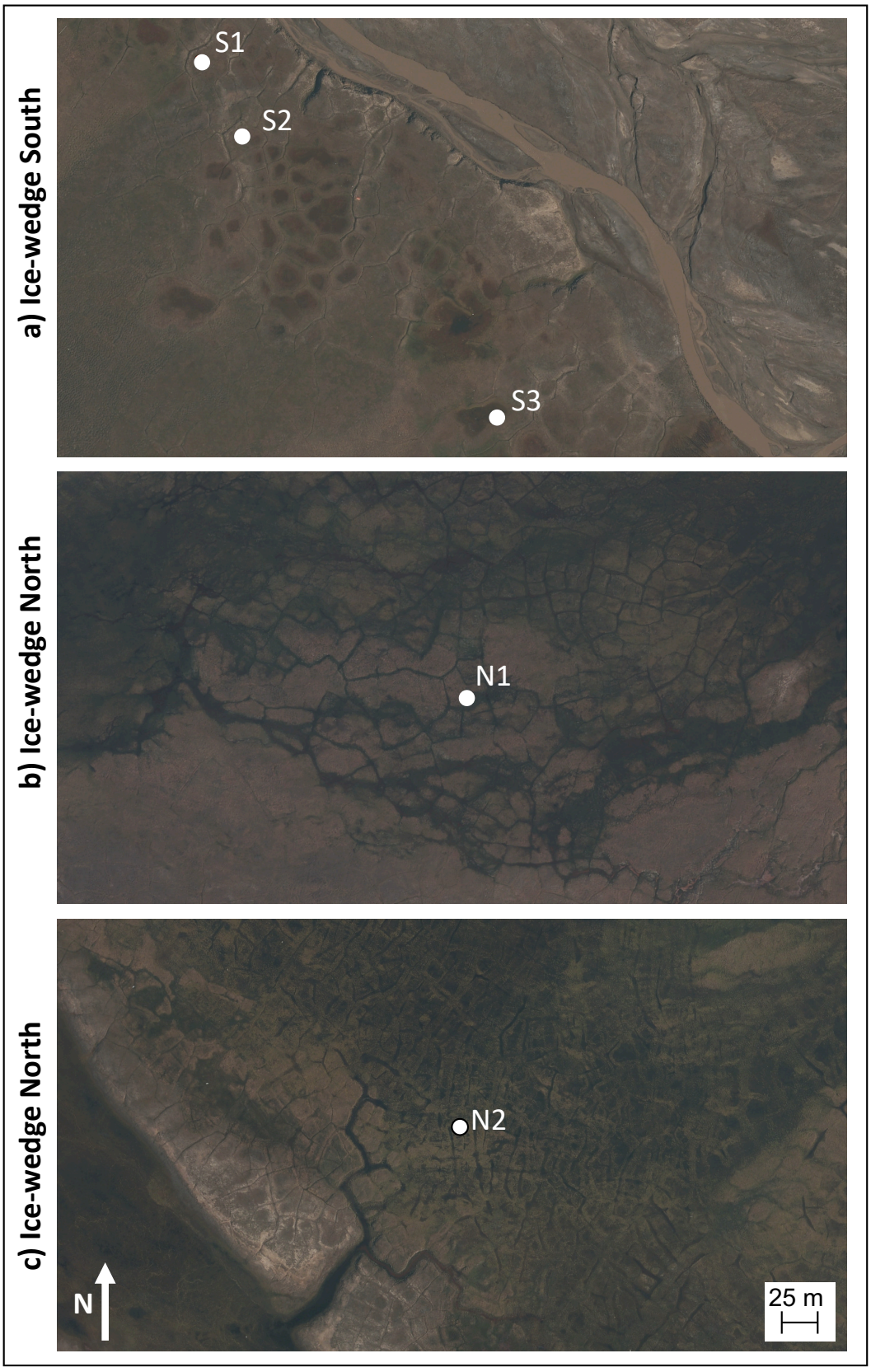

Figure 2.2 Aerial photographs of the Adventdalen sites, with the white circles representing the sampling locations in **a)** Ice-wedge South (S1, S2 and S3), **b)** Ice-wedge North (N1) and **c)** Ice-wedge North (N2). Scale bar is the same for all photographs. Courtesy of the Norwegian Polar Institute (https://toposvalbard.npolar.no/).

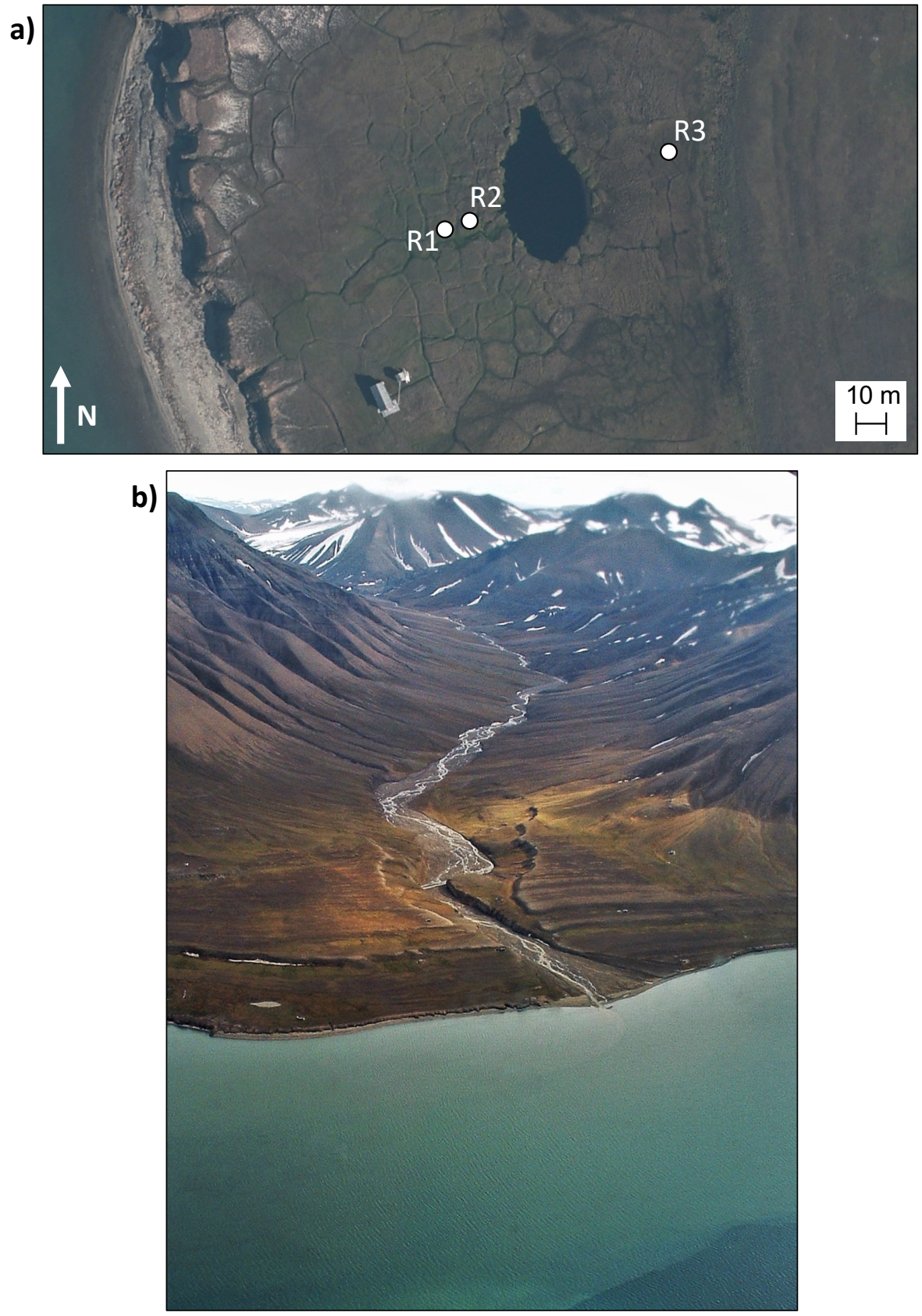

Figure 2.3 a) Aerial photograph of Revneset, with the sampling locations marked by white circles, courtesy of the Norwegian Polar Institute (https://toposvalbard.npolar.no/), and b) Aerial photograph of Revneset and Hanaskogdalen (the river valley). Credit: A. Hodson.

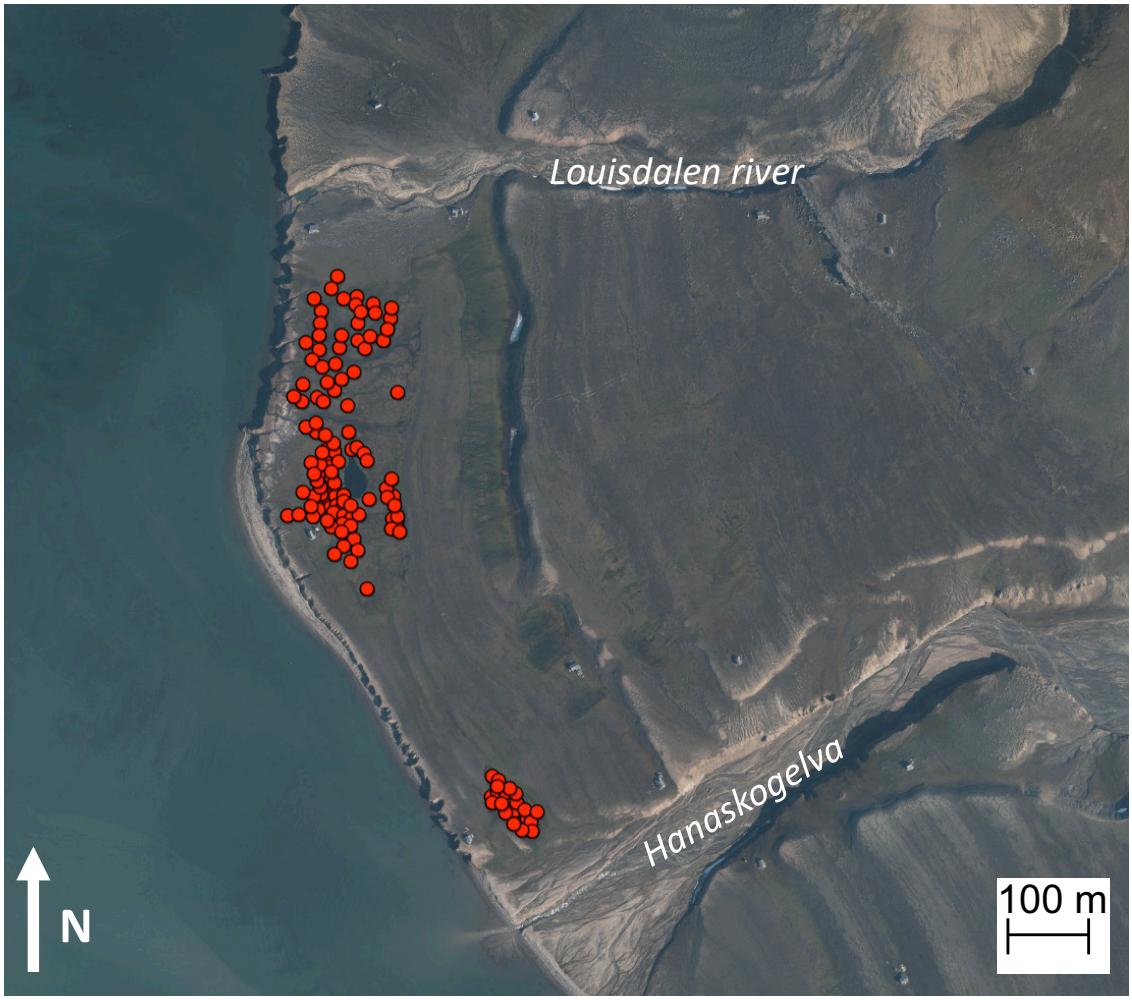

Figure 2.4 Aerial photograph of Revneset, showing the locations where polygons were classified either as high-centred or as low-centred on the basis of a visual inspection of the aerial photograph. Each classified polygon is marked by a red dot. Photograph courtesy of the Norwegian Polar Institute (https://toposvalbard.npolar.no/).

2.2 Sediment cores of the active layer and shallow permafrost

2.2.1 Coring and subdivision

Sediment cores of the frozen active layer and shallow permafrost were extracted in segments (5 cm diameter; between 5 and 50 cm length) using motorised hand drilling equipment (a Stihl BT 130 drilling engine, expandable drill string and cylindrical drill head; Figure 2.5). The core segments were extruded into individual Whirl Pak® bags, which were sealed and frozen during transport to the University of Sheffield, where they were stored at -18 °C. Coring was undertaken before the onset of thaw, when air temperatures were below 0 °C.

Cores were subdivided by sawing into 2 cm depth slices while frozen (Figure 2.5a). The freshly cut surfaces were scraped with a scalpel, and the outer 2 cm were removed with a hollow brass tube (3 cm diameter), to prevent contamination. The sawblade, scalpel and brass tube were cleaned with 70% isopropanol between slices.

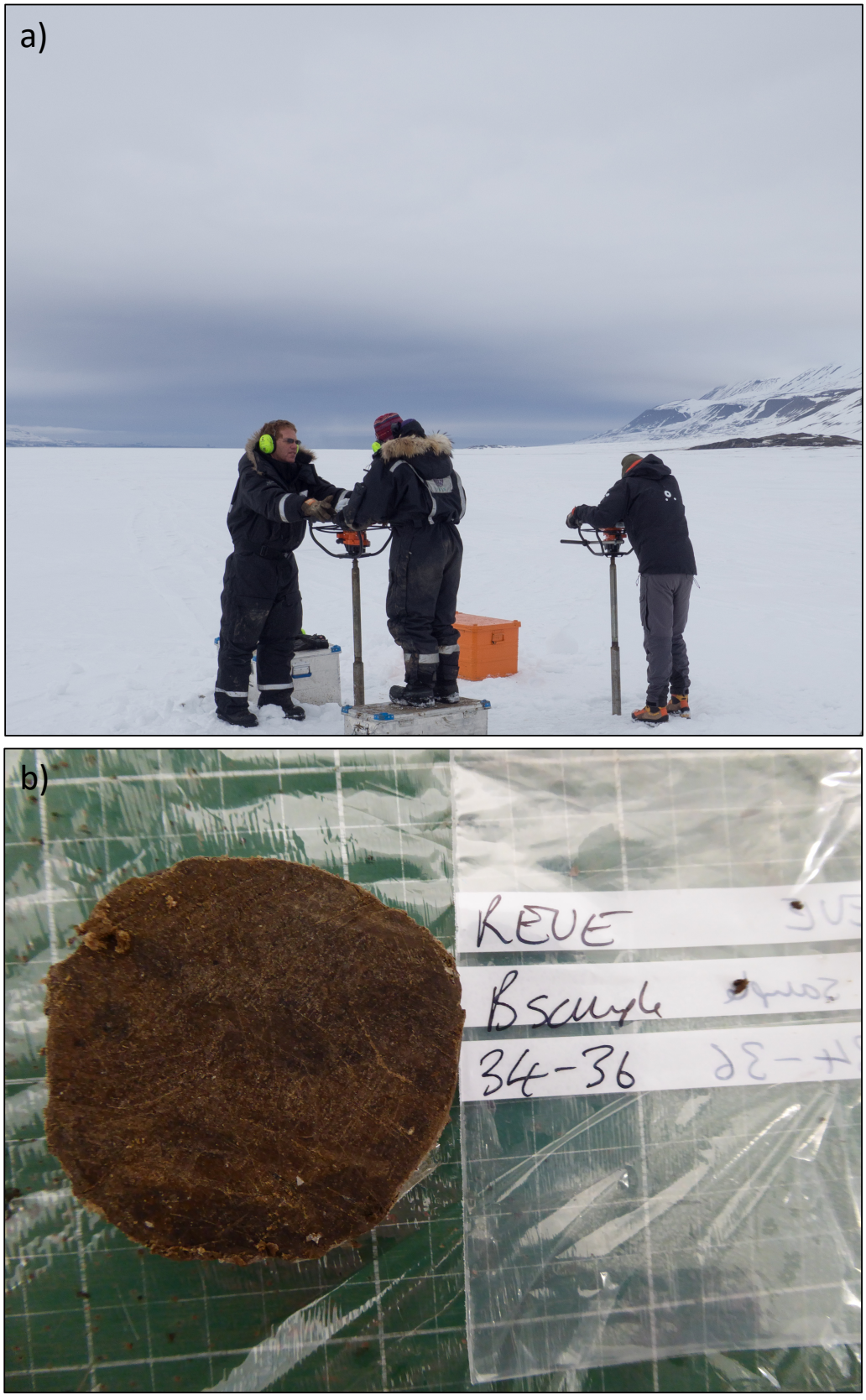

Figure 2.5 Photographs showing a) coring the active layer and shallow permafrost of Adventdalen in spring 2016, using body weight to force the drill down (Credit: Ebbe Bak), and **b)** a slice of core R1b from a depth interval of 34-36 cm. The squares on the green cutting board are 1 cm^2.

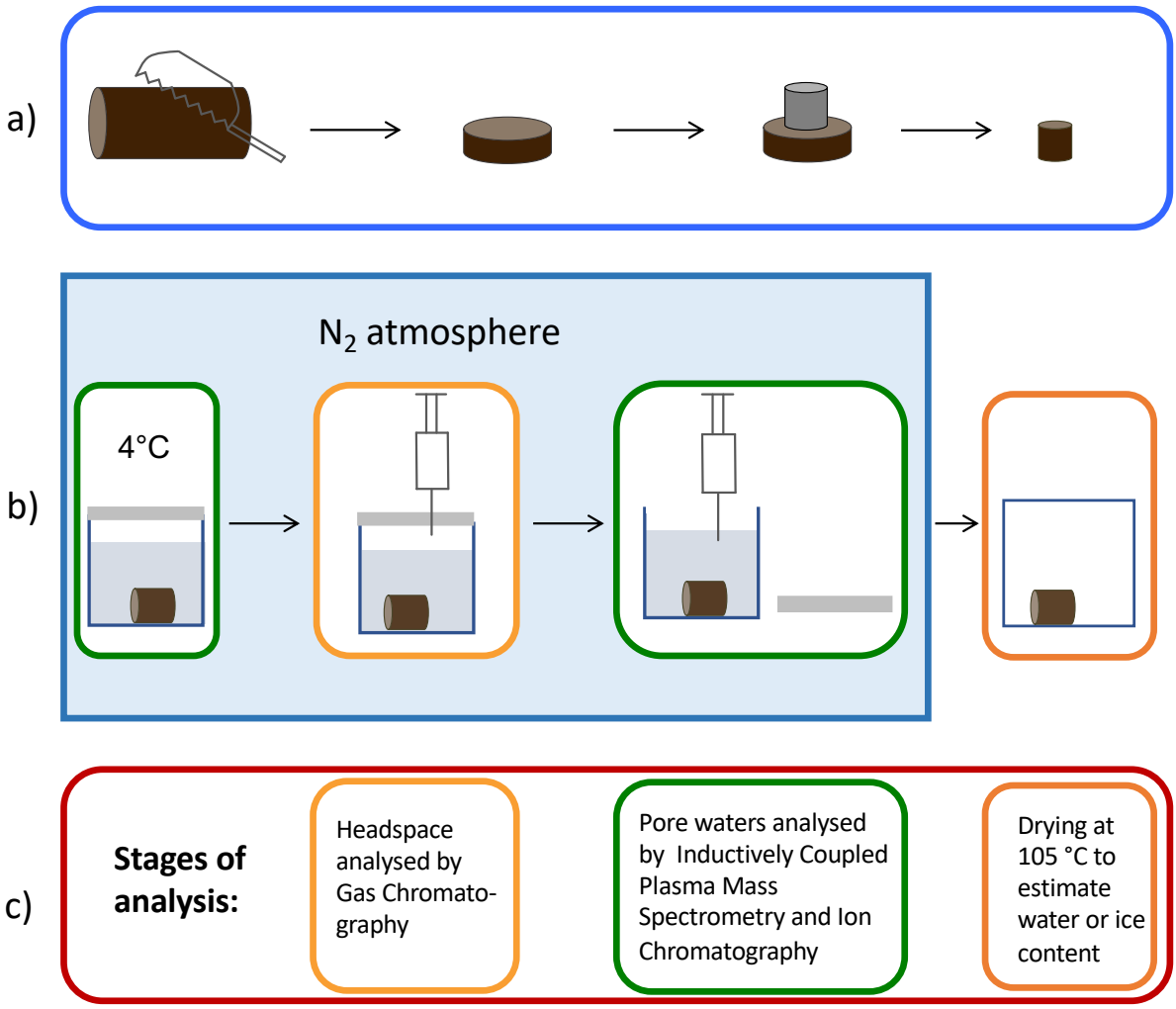

Figure 2.6 Schematic diagram illustrating a) subdivision of permafrost cores by sawing and removal of the outer 2 cm of each slice, b) equilibration of core samples with de-ionised water in vials with an N_2 headspace at 4 °C, followed by sampling of the headspace, sampling and filtering of the porewaters, and drying of the sediments, for c) analyses by gas chromatography, inductively coupled plasma-mass spectrometry and ion chromatography.

2.2.2 Pore water extractions

2.2.2.1 Glassware preparation

All glassware used in these extractions was decon washed and then acid-washed (10% HCL; 24-hour soak; 5x Milli-Q de-ionised water rinse) and dried. Pore water extractions were carried out in 22 mL vials, which firstly were weighed empty, then filled with Milli-Q de-ionised water, reweighed to determine their exact volume, and dried.

2.2.2.2 Sample preparation

A clean chisel and hammer were used to break the 3 cm diameter inner core samples into pieces. These pieces were added to the previously prepared 22 mL crimp top vials.

2.2.2.3 Pore water extraction

The pore water extraction method was adapted from a methodology developed by Spence et al. (2005). Vials containing samples were transferred to a Coy Vinyl Anaerobic chamber with a N_2 atmosphere (0 ppm oxygen). Each vial was weighed to determine the sample mass. Nitrogen-sparged de-ionised water (Milli-Q) was added to fill each vial. The vials were reweighed to determine the mass and volume of water added. Three mL of water were subsequently removed from the top of the vial to create a headspace. The vials were crimp-capped and stored for 5 days at 4 °C upside down with the crimp caps submerged in water (to prevent gas diffusion across the septa). This storage time allowed ample time for the de-ionised water to equilibrate with the pore waters (e.g., Spence et al., 2005; Figure 2.6b).

Five days after first saturating the sample, the sample vial headspace was analysed by Gas Chromatography with a flame ionisation detector (GC-FID) to determine the concentrations of methane and carbon dioxide. Firstly, 3 mL of oxygen-free nitrogen were injected into the headspace of each vial (to ensure that the vials did not become under pressured upon sampling). The vials were shaken for 30 seconds. Triplicate 1 mL samples were taken from each vial and analysed by GC-FID (Figure 2.6c). Section 2.2.2.4.2 provides information on the GC-FID analysis and calibration, and Section 2.2.2.5 provides details of the subsequent calculations.

Seven days after first saturation of the sample, the vials were centrifuged at 7750 rpm for 5 minutes and transferred to the anaerobic chamber. Each vial was de-capped and the supernatant water was removed using a Plastipak syringe attached to a wide bore needle. The water was filtered through a clean 0.22 µm nylon syringe filter (Perkin Elmer). The first 1 mL was filtered into a 1.5 mL borosilicate vial (Restek®) for later analysis by ion chromatography (IC). 5 mL were filtered into a 15 mL polypropylene centrifuge tube pre-

acidified with 50 µL nitric acid (Fisher Scientific Trace Metal Grade) for later analysis by Inductively Coupled Plasma Mass Spectrometry (ICP-MS).

The remaining sediments and water in the 22 mL vials were dried at 105 °C (Ernakovich et al., 2017; Kokelj & Burn 2003) for 24 hours and reweighed to determine the initial moisture content of the samples.

2.2.2.4 Post-sampling analyses

2.2.2.4.1 Major ions and metals

Major ions (Ca^{2+}, Mg^{2+}, Na^{+}, K^{+}, Cl^{-}, NO_3^{-}, SO_4^{2-}) were determined by ion chromatography (Dionex 3000 system; LOD = 0.02 mg L^{-1} for the lowest, undiluted analysis; precision <5% for the mid-range standards). The system comprised an autosampler, analytical pump, chromatography module and conductivity detector. The chromatography module contained an AS18 guard column, an AS18 analytical column for anion analysis and a CG12A guard column and CS12A analytical column for cation analysis. Each system had its own micromembrane suppressor. The anion system eluent was 34 mM potassium hydroxide at a flow rate of 0.2 mL/min. The cation system eluent was 28 mM methane sulphonic acid at a flow rate of 0.4 mL/min. The sample size was 10 µL. Dionex Chromeleon software collected data and controlled the autosampler.

Trace metals (Fe, Mn) were determined on a 5 mL sample acidified with 50 µL reagent grade HNO_3^{-} (Fisher Scientific Trace Metal Grade), using Inductively Coupled Plasma Mass Spectrometry or ICPMS (PerkinElmer Elan DRC II, MA, USA). The system used a nickel sampler and skimmer cones, a quartz torch and injector and a Meinhard spray chamber. The precision errors for repeat analyses of mid-range standards were < 5%, and the detection limits were 1.0 µg L^{-1}. Data acquisition was via Elan NT software. Sample introduction was via a Cetac ASX-150 and 4-line peristaltic pump set at 20 rpm, with one line used for adding the internal standard (^{103}Rh).

Analyte concentrations were corrected for blank analyses and corrected for the dilution during the pore water extraction

2.2.2.4.2 Methane and carbon dioxide

Methane and carbon dioxide concentrations in gas samples were determined using a GC-2014 Shimadzu Gas Chromatograph with a 30 m GS-Q, 0.53 mm internal diameter column and a 100 µL sample loop. Injection, flame ionisation detector (FID) and column temperatures were 60, 240 and 50 °C, respectively. The column temperature was kept at 50 °C isothermally for the three-minute run. Nitrogen was the carrier gas with a flow rate of 8.0 mL min^{-1}. A methaniser (nickel catalyst) at 380 °C converted CO_2 to CH_4 prior to detection by FID.

Sample concentrations were calculated based on a calibration constructed from serial manual dilutions of a certified 60% CH_4 40% CO_2 standard in N_2-flushed 120 mL Wheaton vials (linear over 0 to 140000 ppm methane and 0 to 90000 ppm carbon dioxide calibration range, $R^2 = 0.99$, n = 6). Standards and blanks were run daily, giving a coefficient of variation for both CH_4 and CO_2 of <1.3% (n = 22), and detection limits of 25 and 89 ppm for CH_4 and CO_2, respectively, equivalent to ~1.2 and ~25 µmol L^{-1} in the porewaters. Detection limits for methane and carbon dioxide were calculated from the mean plus three times the standard deviation of the blanks. For the samples and blanks, 1 mL of the headspace was sampled (in triplicate) with a gas-tight syringe and injected into the 100 µL sample loop.

2.2.2.5 Gas pore water calculations

Peak areas of methane and carbon dioxide were analysed using Shimadzu GC Solution Lite PostRun software. Peak areas were converted into gaseous concentrations (ppm) using the calibration described in Section 2.2.2.4.2. Mean concentrations of methane and carbon dioxide in the water blanks were subtracted from the concentrations in the sample vials. Sample vial headspace concentrations (ppm) were converted to partial pressures (x 10^{-6}). Partial pressures were converted to moles (n) of methane and carbon dioxide in the headspace, using the Ideal Gas Law (Equation 2.1):

$$n = \frac{PV}{RT} \tag{2.1}$$

where *n* is the number of moles of the gas in the headspace, *P* is the partial pressure of the gas in the headspace, *V* is the headspace volume (L), adjusted for the dilution effect of the 3 mL N_2 injected, *R* is the ideal gas constant (=0.08205 L atm mol^{-1} K^{-1}), and *T* is the temperature (room temperature; K).

For each vial, the quantity of dissolved methane was determined using the Bunsen coefficient (*B*) for 0‰ salinity and 4 °C (Equation 2.2; Wiesenburg & Guinasso, 1979):

$$CH_{4(aq)} = V_w \cdot P_{CH_4} \cdot \left(\frac{V_h}{V_w}\right) \cdot B \tag{2.2}$$

where $CH_{4(aq)}$ [mL] is the concentration of dissolved methane in the water, V_w [mL] is the water volume (total in vial during equilibration), P_{CH4} is the partial pressure of methane in the vial headspace, and V_h [mL] is the vial 'virtual' headspace after addition of 3 mL N_2. The quantity of methane was converted from mL to moles using the Ideal Gas Law (Equation 2.3):

$$CH_{4(aq)}\,[\mathrm{mol}] = \frac{\frac{CH_{4(aq)}\,[\mathrm{mL}]}{1000}}{R \cdot T} \tag{2.3}$$

The Analytical Expression for Temperature Dependence (Equation 2.4) was used to calculate a Henry's law constant (K_H [mol atm^{-1}]) at 4 °C, which describes the partitioning between aqueous and gaseous phases (Stumm & Morgan, 1996).

$$logK_{\mathrm{H}} = 108.3865 + 0.01985076\mathrm{T} - \frac{6919.53}{T} - 40.45154logT + \frac{669365}{T^2} \tag{2.4}$$

The partial pressure of CO_2 in the vial headspace was multiplied by K_H to determine the molar concentration of aqueous carbon dioxide ($CO_{2\,(aq)}$ [mol L^{-1}]). The concentration of $CO_{2\,(aq)}$ was multiplied by the volume of water in the vial to obtain the total quantity of $CO_{2\,(aq)}$ in the water.

The total quantity of methane in the vial was determined by summing the amount in the headspace and the amount dissolved in the water. The total quantity of carbon dioxide in the vial was determined by summing the amount in the headspace and the amount dissolved in

the water. It was assumed that all of the methane and carbon dioxide in the vial originated from the pore water. To calculate the concentration of methane in the sample pore water, the total methane (mol) was divided by the pore water volume (L). To calculate the concentration of carbon dioxide in the sample pore water, the total carbon dioxide (mol) was divided by the pore water volume (L).

2.2.3 Solid phase analyses

2.2.3.1 Organic carbon

Samples to be analysed for organic carbon were treated in the following manner. Samples were oven-dried (105 °C) and the <2 mm fraction was milled in a Retsch ball mill for 5 minutes at 15.0/s frequency. After milling, samples were transferred to Eppendorf™ microcentrifuge tubes. Ball mills were washed in de-ionised (Milli-Q) water and dried in the oven between samples. 90 mg of milled sample was weighed into an Eppendorf™ microcentrifuge tube and 500 µL of 6 M hydrochloric acid was added. The sample was stirred with a blunt needle and left to settle in a fume cupboard for 24 hours. The sample was centrifuged in a microcentrifuge at 13,000 rpm for 10 minutes, and the supernatant was removed with a 3 mL disposable pipette. De-ionised (Milli-Q) water was added to the sample tube (up to the 0.5 mL line), the sample was stirred, centrifuged, and the supernatant was removed by pipetting. Samples were dried for 24 hours at 105 °C. Samples to be analysed for total carbon were not treated with 6 M hydrochloric acid.

Between 25 and 50 mg of each sample were weighed into a tin capsule. Samples were analysed on an Elementar vario EL cube. Concentrations were checked with acetanilide standards (C_8H_9NO; Merck; n = 28, % C = 70.96 ±0.67, % N = 10.34 ±0.10), with 2 blanks and 2 acetanilide standards run every 15 samples**.**

2.2.3.2 Acid-volatile sulfur (AVS) and chromium-reducible sulfur (CRS)

Acid-volatile sulfur (AVS) and chromium-reducible sulfur (CRS) were determined at the University of Leeds. A two-step distillation method was applied to freeze-dried and milled sediment samples, using firstly 6 M HCl and then boiling 3 M $CrCl_2$ solution (Fossing & Barker

Jørgensen 1989; Canfield et al. 1986). In each extraction, H_2S was precipitated as Ag_2S, filtered, dried, and sulfide was determined gravimetrically. The stoichiometry of the phase was used to convert the mass to weight percent (FeS for AVS; FeS_2 for CRS).

2.2.3.3 Iron phases

Different operationally defined iron mineral phases were targeted with a four-step sequential extraction procedure applied to 100 mg freeze-dried and milled sediment samples. To extract (i) amorphous and nanoparticulate iron (oxyhydr)oxide phases (Fe_{ox1}), each sample was shaken for 24 hours with 10 mL ascorbate solution (50 g L^{-1} sodium citrate, 50 g L^{-1} sodium bicarbonate and 10 g L^{-1} of ascorbic acid; buffered at pH 7.5; Raiswell et al. 2008). For (ii) iron bound in carbonates (Fe_{carb}), the residual sample was shaken for 48 hours at 50 °C with 10 mL sodium acetate solution (1 M sodium acetate solution buffered with acetic acid to pH 4.5; Poulton & Canfield 2005). For (iii) crystalline iron (oxyhydr)oxides (Fe_{ox2}), the residual sample was then shaken for 2 hours with 10 mL dithionite solution (50 g L^{-1} sodium dithionate buffered to pH 4.8 with acetic acid and sodium citrate; Poulton & Canfield 2005). Lastly, for (iv) magnetite (Fe_{mag}), the residual sample was shaken with 10 mL ammonium oxalate solution (0.2 M ammonium oxalate/0.17 M oxalic acid buffered with ammonium hydroxide to pH 3.2) for 6 hours (Poulton & Canfield 2005). Extractions were performed at room temperature (except for Fe_{carb} at 50 °C) by continuous shaking. After centrifugation (4000 rpm for 4 minutes at 21 °C), the supernatant from each extraction was stored at 4 °C until analysis by atomic absorption spectroscopy (AAS).

2.2.4 Microbiological data collection and analysis (Aarhus University)

The cores analysed at Aarhus University by Ebbe Norskov Bak were cored as described in Section 2.2.1, but sample processing differed and was conducted as follows. The outer ≥ 5 mm were removed from the frozen cores with sterilized spoke shaves and the core ends were sawed off to remove potential contamination. The cores were divided into sections corresponding to successive 25 cm depth intervals from the surface downwards and were packed in separate sterile bags.

To check the efficiency of the Aarhus sampling decontamination procedure, one core section had an aqueous suspension of multifluorescent microspheres added to the sample bag immediately following extraction from the ground. The microspheres were mixed into the thawed surface material before the sample was returned to the cool box. Each layer removed with the spoke shave (~1 mm) was examined with a Leica DMRB microscope using the CY3-filter to record the density of the fluorescent microspheres. After removal of the outer 2 mm, the contamination level was reduced by more than 3 orders of magnitude and after 4 mm, no microspheres could be detected. Samples were kept frozen during transport to Aarhus University in Denmark.

Cores were subdivided by leaving them to thaw under anoxic conditions at 4°C overnight and homogenised by kneading the sample bags by hand. In the case of dry samples, sterile Milli-Q water was added to create a mud. Subsamples for DNA extraction were transferred to Oxygen 2 mL maximum recovery microtubes in duplicates and were frozen at -18 °C.

DNA extraction was done with bead beating, an enzymatic treatment and chemical lysis followed by pyrification using a modified method from the FastDNA Spin Kit for Soil (Qbiogene). Approximately 0.3 g sample was mixed with 300 µL extraction buffer in a Lysis matrix E tube and mechanically treated for 2x15 seconds at speed 4 and additional 15 seconds at speed 4.5 with a FastPrep Instrument. 50 µL of a mixture of lysozyme, Lipase Type 7, pectinase and β-glucuronidase and 50 µL of a mixture with Proteinase K, Protease Type 9 and Pronase was added. All enzyme mixtures were at a concentration of 1mg mL^{-1} for each compound. 75 µL of 20% SDS was added and the mixture was incubated for 65 °C for two hours. Following this, the standard procedure for the FastDNA Spin Kit for Soil was followed.

A mixed library was prepared according to the 16S Metagenomic Sequencing Library Preparation guide (Illumina, 2013) with the following modifications. Initially, 20 cycles of PCR were performed with the Bac 341F (5’ CCTACGGGNGGCWGCAG 3’) and the Bac 805R (5’ GACTACHVGGGTATCTAATCC 3’) primers for bacteria and 25 cycles of PCR were performed with the Archa344Fmod (5’ ACGGGGYGCAGGCGCGA 3’) and the Arch 915R (5’ GTGCTCCCCCGCCAATTCCT 3’) primers for archaea to amplify the highly variable V3-V4 regions of the 16S rRNA genes. Additionally, 10 cycles of PCR were run to attach the adapters,

followed by another 8 cycles to add index barcodes using Nextera Index primers. The PCR reactions were performed with the 2x KAPA HiFI Hotstart mix and denaturation at 95 °C, annealing at 55/60 °C for bacteria and archaeal primers, respectively, and elongation at 72 °C. The PCR products were cleaned between each PCR run with AMPure XP beads and length and quantity of the DNA were checked with gel-electrophoresis and Qubit HS. The DNA was pooled to a mixed library and analyzed with Illumina MiSeq to get 2x300 bp paired end-reads.

Each of the four datasets (bacterial and archaeal for day 0 and day 362) were analyzed separately for amplicon sequence variants (ASVs) using DADA2 (ver.1.12.1; Callahan et al., 2016) in R (ver. 3.6.0). The analysis from the two time points were gathered according to the target kingdom and chimeras were removed using DADA2. Sequences were classified taxonomically with IDTaxa from the Decipher Package (ver. 2.12.0; Murali et al., 2018) using the SILVA SSU r132 database as the reference. The sequence table, the taxonomy table and the metadata were gathered in phyloseq objects for bacteria and archaea, respectively. The data were then inspected and processed using phyloseq (ver. 1.28.0; McMurdie & Holmes, 2013). For each section of the three replicate cores from Ice-wedge South, the average ASV abundance was estimated by combining the relative abundance from the 16S microbiome analysis with the cell densities from the qPCR analysis. Heatmaps were made with ampvis2 (ver. 2.4.11; Andersen et al., 2018).

2.3 In-situ sampling

During the summer of 2017 (between 26/08/17 and 13/09/17), *in-situ* sampling of water from the active layer was conducted at Adventdalen and Revneset with two types of sampler: Macro Rhizon soil moisture samplers (Van Walt Ltd) and a custom-made stainless steel active layer water sampler ("The Sheffield Spike").

2.3.1 Macro Rhizon sampling

To obtain blank measurements, 3 Macro Rhizon soil moisture samplers (Van Walt Ltd) were soaked in de-ionised (Milli-Q) water for 5 minutes, and subsequently flushed with 10 mL de-

ionised (Milli-Q) water. Following this, de-ionised (Milli-Q) water was sampled through the Macro Rhizons for later analysis by IC and ICP-MS.

Macro Rhizon soil moisture samplers were installed at Revneset, Ice-wedge South and Ice-wedge North (Table 2.1). Active layer depths were 65 cm in S1, 63 cm in N1, 65 cm in N2 and 36 cm in R1. At Ice-wedge South and Ice-wedge North, Macro Rhizons were installed at depths of 9 cm, 30 cm and 60 cm. At Revneset, Macro Rhizon samplers were installed at depths of 9 cm, 20 cm and 30 cm, due to the shallower active layer depth at this site. At each site, triplicate samplers were installed at each depth, with a total of 9 Macro Rhizon samplers per site.

To install Macro Rhizon samplers, a gouge auger was inserted at 45° (measured using a clinometer), twisted 360° and removed. A narrow hole was created at the base of the augered hole with an insertion tool (a PVC pipe with a steel pin at the end). With the insertion tool in place (to prevent collapse of the surrounding soil into the hole), the Macro Rhizon was flushed with 10 mL de-ionised (Milli-Q) water (from a 500 mL polyethylene bottle). After removal of the insertion tool from the ground, the Macro Rhizon was inserted immediately (with the stopcock open). A 30 mL syringe was attached to the Macro Rhizon and the plunger was drawn to its full extent, producing a low-pressure zone, which required a wooden spacer to maintain (Figure 2.7). The first 2 mL (~3x the sampler volume) collected in the syringe were discarded, and the syringe was re-vacuumed. Between each insertion, soil was cleaned from the auger using a spatula and nearby standing/flowing water.

On the day of installation, samples for analysis of major ions and metals were collected. There was no need to pre-filter, as the pore size of the Macro Rhizons was 0.2 µm. Samples for later determination of major ions were collected in 1 mL Eppendorf tubes (with no headspace in the tubes). 5 mL samples for later determination of trace metals were collected in 15 mL Corning centrifuge tubes, pre-acidified with 50 µL nitric acid (AnalaR 65% Normapur, VWR, IL, USA). If the flow rate of water into the syringe was rapid enough, samples were collected the same day in 50 mL centrifuge tubes for later analysis of $\delta^{34}S\text{-}SO_4^{2-}$ and $\delta^{18}O\text{-}SO_4^{2-}$ and in 2 mL Eppendorf tubes for later analysis of $\delta^{18}O\text{-}H_2O$ and $\delta D\text{-}H_2O$. Otherwise, Macro Rhizon

samplers were revisited in subsequent days to allow time for water to collect overnight before sampling. All samples were stored at 4 °C until analysis.

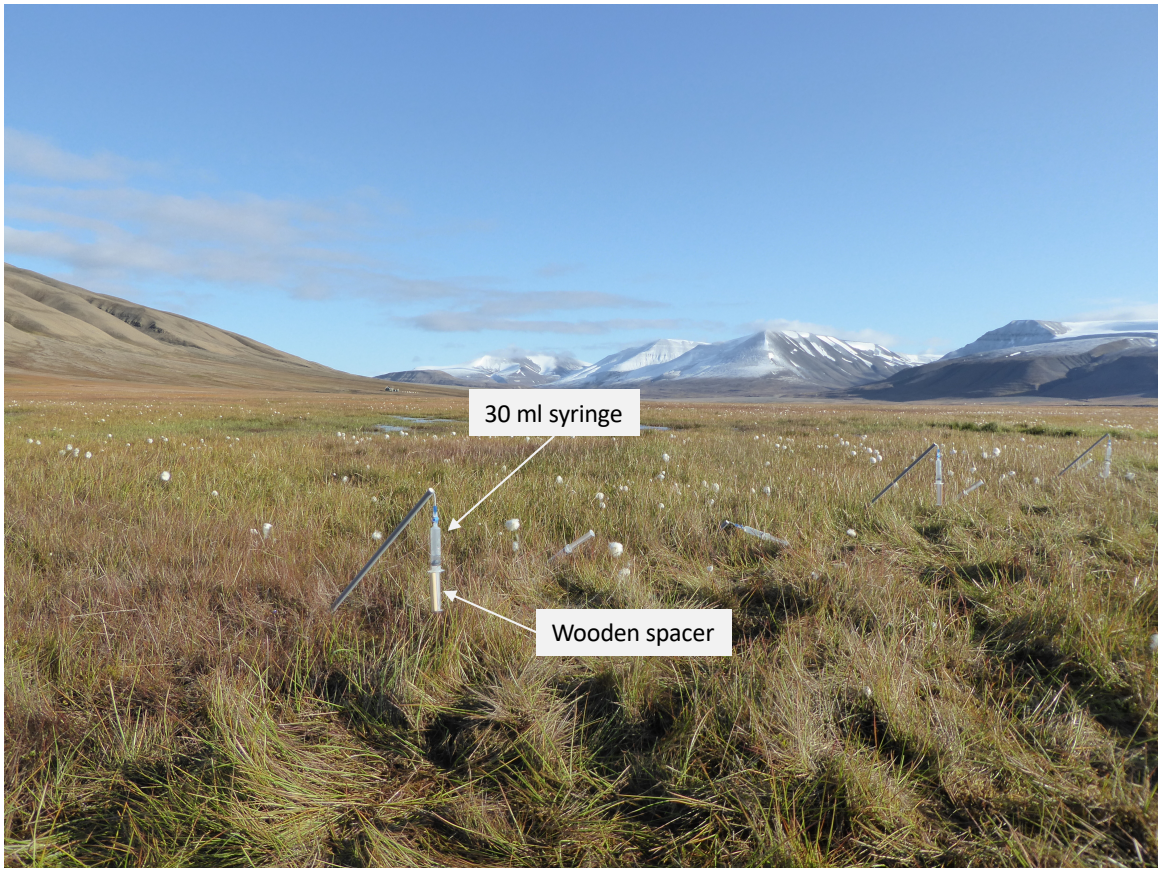

Figure 2.7 Macro Rhizon samplers installed in Ice-wedge North. Samplers were installed at three different depths, each with a syringe attached at the top.

2.3.2 Stainless steel active layer water sampler ("The Sheffield Spike")

A stainless-steel sampler (henceforth referred to as The Sheffield Spike, TSS; Figure 2.8) for water from the active layer was made with the aim of obtaining a higher depth resolution profile of the chemistry of water from the active layer. A 6 mm outer diameter (1.5 mm wall thickness) stainless steel pipe was inserted into an 8 mm outer diameter (1 mm wall thickness) stainless steel pipe. A collar was positioned near the top of the pipes, to allow a screw threaded T-bar to be attached for pushing the pipe into the ground. The pipe base was attached to a pointed stainless-steel tip. The outer pipe was slightly (5 cm) shorter than the inner pipe, leaving the base of the inner pipe exposed. Five sets of 3mm diameter holes were drilled through the inner pipe at 1 cm intervals down the exposed portion of the pipe. To

avoid blocking of the sample holes with sediments, a stainless-steel mesh (100 µm pore size) was glued (Araldite® epoxy resin) over the holes.

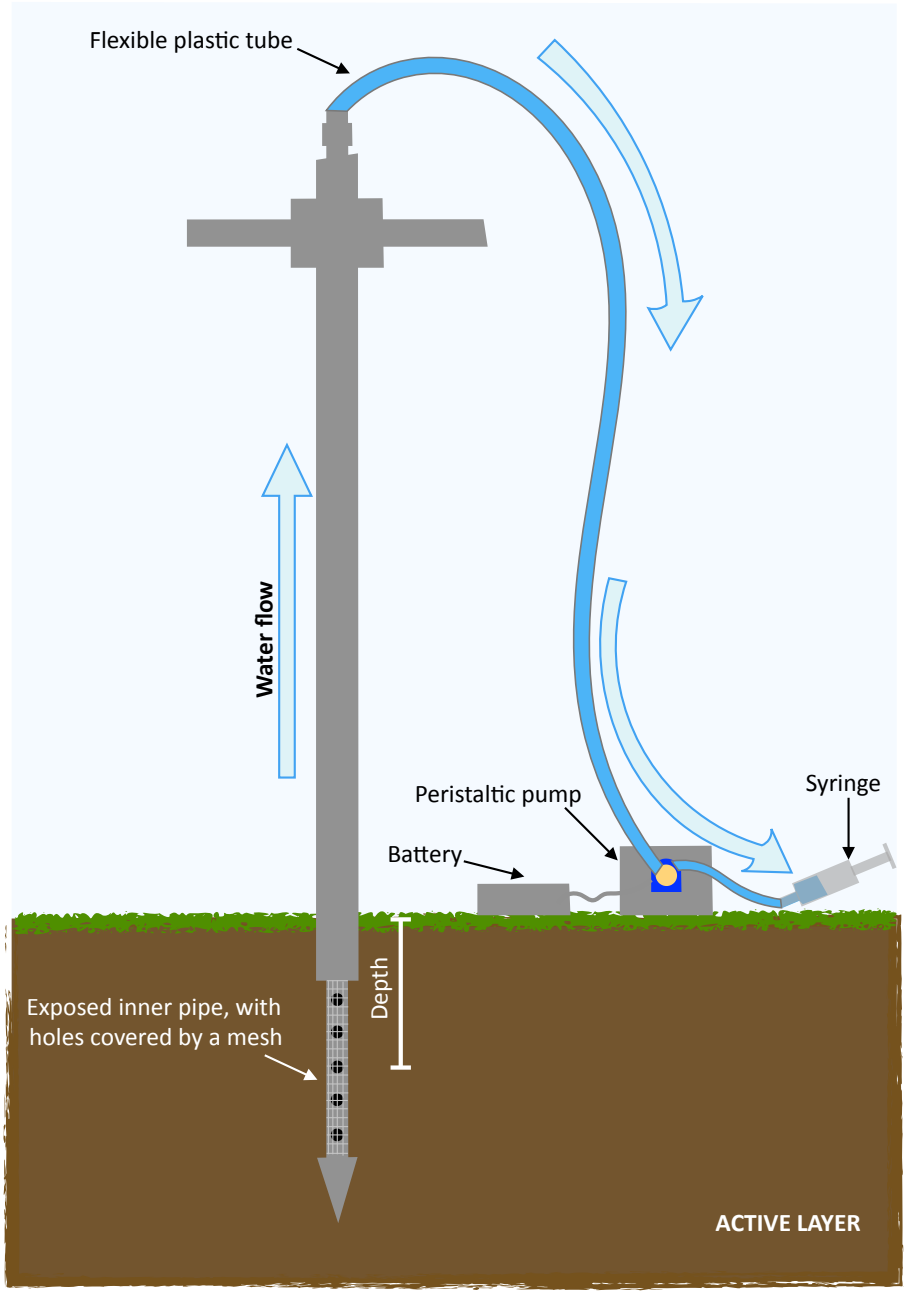

Figure 2.8 Schematic diagram illustrating the use of The Sheffield Spike to collect samples of water from the active layer.

The Sheffield Spike was soaked in and flushed with de-ionised (Milli-Q) water for 5 minutes. A peristaltic pump (Williamson Pumps Ltd; ~200 mA; pump rate in pure water 100 mL in 3 min) was attached via flexible plastic tubing to the top of The Sheffield Spike and was powered

by a 9-volt sealed lead acid battery. Blank samples of de-ionised (Milli-Q) water were taken for later analysis of trace metals, major ions and volatile fatty acids.

At each site, at each depth, The Sheffield Spike was flushed with ~10 mL water from the active layer. A 50 mL syringe was attached to the pump and water was pumped from each depth in turn, starting at 5 cm, and moving The Sheffield Spike progressively downwards in 10 cm increments. Water samples were slowly injected directly via a syringe needle into two previously prepared N_2-flushed 12 mL crimp top vials per depth. During sample injection (Figure 2.9), an outflow needle was inserted into the septum, so that the vial could be completely filled with sample, with no headspace or overpressure. One vial was later analysed for methane concentrations ($CH_{4\,(aq)}$) and the other for $\delta^{13}C\text{-}CH_4$.

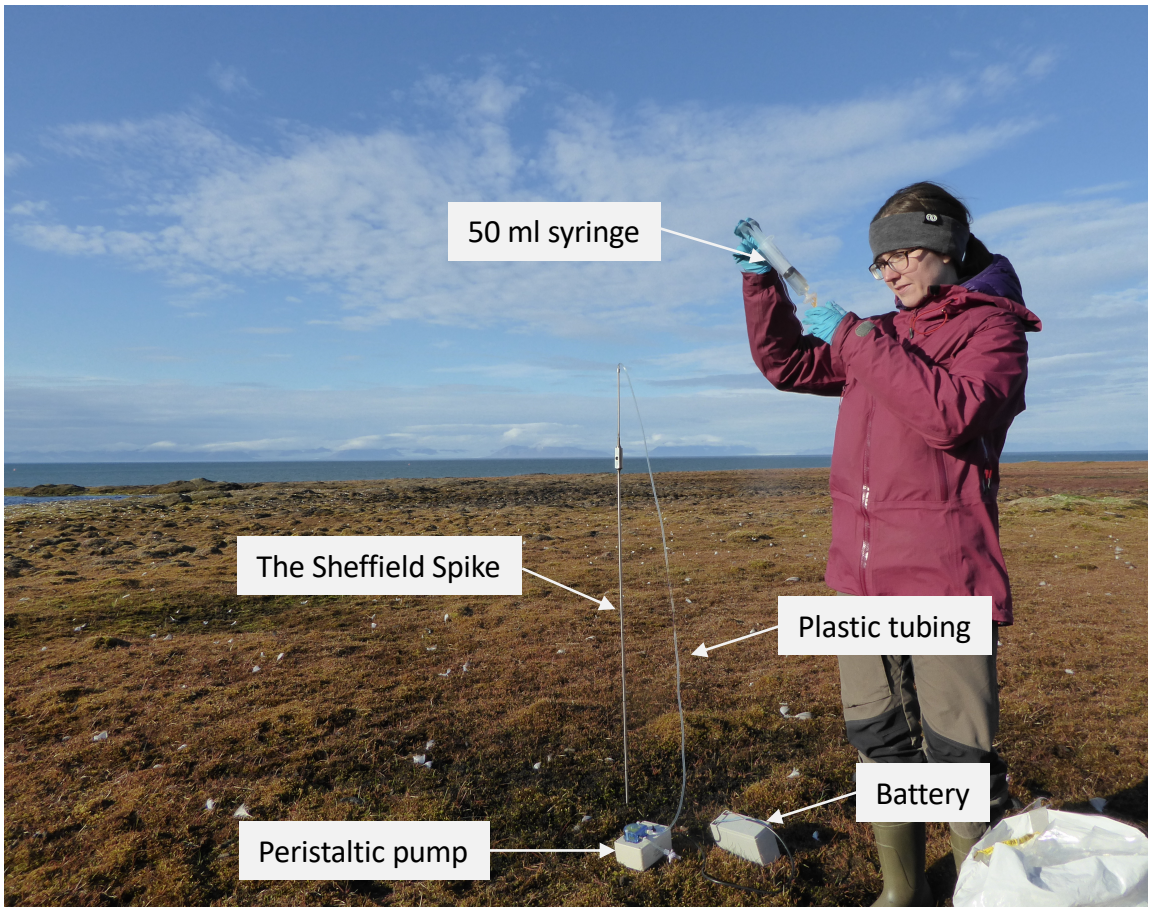

Figure 2.9 Using The Sheffield Spike at Revneset (site R3) on 6th September 2017 to pump water from the active layer. Credit: G. Jones.

Samples for later quantification of major ions, volatile fatty acids, $\delta^{18}O\text{-}H_2O$ and $\delta D\text{-}H_2O$ were filtered via a clean 0.22 µm nylon syringe filter (Perkin Elmer) into Eppendorf tubes (with no

headspace in the tubes). 5 mL samples for later quantification of trace metals were filtered into 15 mL Corning centrifuge tubes pre-acidified with 50 µL nitric acid (AnalaR 65% Normapur, VWR, IL, USA). A total of up to 60 mL water was pumped from each depth, which equates approximately to a sphere of 2.4 cm radius, if 100% porosity is assumed. Hence, even if porosity were only 30%, there should be no overlap between collection depths. All samples were stored at 4 °C until analysis.

2.3.3 Sample analysis

2.3.3.1 Volatile fatty acids (VFAs)

Eppendorf tubes containing the samples were centrifuged at 13 000 rpm for 5 minutes. 1 mL of supernatant was pipetted into a GC vial. The supernatant, blanks and standards were acidified with 15 µL analytical grade orthophosphoric acid to ensure that the acid/salt ratio (i.e. acetic acid versus acetate ions) was weighted towards the acid. Samples were analysed on a Thermo Scientific™ TRACE™ 1300 Gas Chromatograph, which was calibrated with dilutions of Acetic acid and a Volatile Acid Mix (46975-U, Sigma) composed of Acetic acid, Propionic acid, Isobutyric acid, Butyric acid, Isovaleric acid, Valeric acid, Isocaproic acid, Caproic acid and Heptanoic acid.

The R^2 for all calibrations was >0.99, and the detection limit, calculated as the mean of the blanks plus three times the standard deviation of the blanks (n = 5), was 4.22 µM for acetate.

2.3.3.2 Water isotopes

Samples were analysed at the University of East Anglia (UEA), using a Picarro 1102i analyser, by direct injection of 2.6 µL of water. Samples were measured together with 2 United States Geological Survey (USGS) standards: USGS 64444 and USGS 67400 and a UEA Norwich Tap Water (NTW) internal laboratory standard. Using the calibration line defined by the USGS standards, the true composition of the samples, relative to Vienna Standard Mean Ocean Water (VSMOW), was calculated. The differences in isotope values, known as δ, are defined as:

$$\delta_{\text{sample}} = \left[\frac{R_{sample}}{R_{standard}} - 1\right] \times 1000 \quad (2.5)$$

Sample is the sample value and standard is the reference value. *R* is the heavy/light ratio between the abundances of two isotopes (in this case, $^{18}O/^{16}O$ or $^{2}H/H$). δ is reported in parts per thousand (per mille, ‰). Enrichment in the heavy isotope is shown by a positive δ value, whereas a negative δ value indicates depletion. The standard, in this case, is VSMOW (Rohling, 2013). The same notation applies for sections 2.3.3.4 and 2.3.3.5, with different standards. The Global Meteoric Water Line (GMWL) was defined by Equation 2.6.

$$\delta^2H\text{-}H_2O = 8.17\delta^{18}O + 11.27 \quad (2.6)$$

The Local Meteoric Water Line (LMWL) was based on composite monthly precipitation data from 75 samples in the periods 1961-65 and 1972-75 collected at Isfjord Radio, which is approximately 50 km southwest of the study sites, and provided by the International Atomic Energy Agency (IAEA/WMO 2006). The LMWL ($R^2 = 0.91$) was defined by Equation 2.7.

$$\delta^2H\text{-}H_2O = 6.46\delta^{18}O - 5.98 \quad (2.7)$$

Deuterium excess ("d-excess") based on the GMWL was calculated according to Equation 2.8 (Rozanski et al., 1993).

$$\text{d-excess} = \delta^2H - 8.17\delta^{18}O \quad (2.8)$$

Hence, if d-excess > 11.27 this indicates a Deuterium excess, in comparison with the GMWL. Deuterium excess ("d-excess") based on the LMWL was calculated according to Equation 2.9.

$$\text{d-excess} = \delta^2H - 6.46\delta^{18}O \quad (2.9)$$

Hence, if d-excess > -5.98, this indicates a Deuterium excess, in comparison with the LMWL.

2.3.3.3 Concentrations of methane ($CH_{4\,(aq)}$) and carbon dioxide ($CO_{2\,(aq)}$)

Into each 12 mL crimp top vial containing a water sample, 5 mL of nitrogen gas was injected to displace (through an outflow needle) 5 mL of sample. This resulted in a 5 mL headspace. Samples were left at 4 °C for 2 hours to allow time for equilibration of dissolved gas with the headspace. The septum of each vial was pierced with a needle attached to a gas-tight syringe and 1 mL of headspace gas was sampled from each vial and injected into the GC-FID (Section 2.2.2.4.2). Post-GC calculations were conducted as in Section 2.2.2.5.

2.3.3.4 $\delta^{13}C\text{-}CH_4$

The ratio $^{13}C/^{12}C$, which was reported as the $\delta^{13}C$ isotopic composition of dissolved methane ($\delta^{13}C\text{-}CH_4$), was analysed at the University of York. A gas headspace equilibration technique (15 minutes) was employed, after which 6 mL of sample were injected into a 120 mL glass serum Wheaton vial (Viton-stoppered, He-flushed). The 2 mL sample loop was flushed with 6 mL of headspace and this was injected into a 25 m MolSieve column in an Agilent 7890B GC connected to an Isoprime100 Isotope Ratio Mass Spectrometer (IRMS). The definition in Equation 2.5 applies for the $\delta^{13}C$ of methane ($\delta^{13}C\text{-}CH_4$), and the reference was Vienna Pee Dee Belemnite (VPDB). For all samples with > 3 ng C, analytical precision errors were < 0.3‰.

2.3.3.5 Sulfate isotopes ($\delta^{34}S\text{-}SO_4$) and ($\delta^{18}O\text{-}SO_4$): sample preparation and analysis

Processing and analysis of the ratios $^{34}S/^{32}S$ (reported as $\delta^{34}S\text{-}SO_4$) and $^{18}O/^{16}O$ ($\delta^{18}O\text{-}SO_4$) of sulfate in water samples from the active layer was undertaken at Lancaster Environment Centre (LEC). The volume of sample required to obtain 350 µg barium sulfate for analysis by continuous flow isotope ratio mass spectrometry was calculated based on results from ion chromatography. Three types of resin were prepared for each sample: 4 mL of Supelite™ DAX-8 (for removal of dissolved organic matter), 1 mL of Dowex® 50 W-X8 (for removal of cations) and 1 mL of Dowex® 1X8 (for removal of anions). Each resin was mixed with de-ionised (Milli-Q) water to form a sludge and was loaded into an acid-washed syringe with a fritz in the base to retain the resin. The Dowex® 50 W-X8 and 1X8 resins were conditioned with 15 mL 1 M HCl, followed by repeated rinses (3-4 times) until the pH was neutral. The

SupeliteTM DAX-8 resin was conditioned with 15 mL methanol, followed by repeated rinses (3-4 times). The prepared resins were stacked (Figure 2.10).

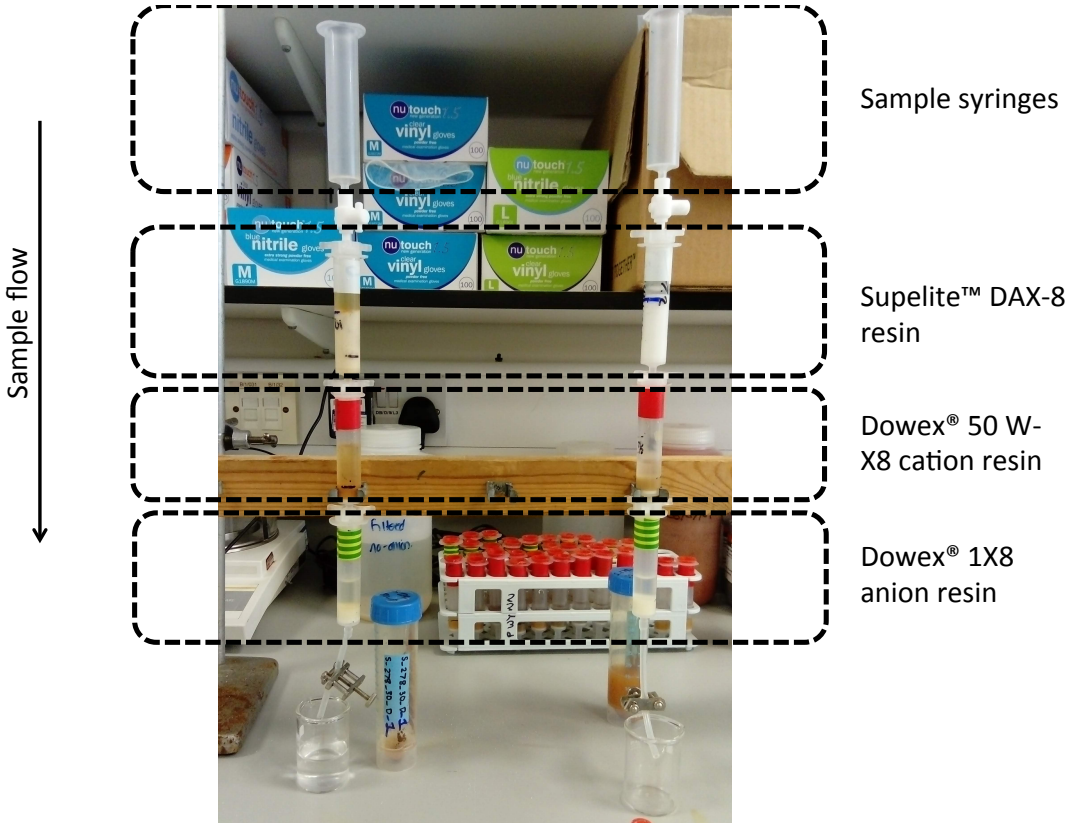

Figure 2.10 Two water samples flowing through resins in the laboratory.

The Dowex® AG2 X8 was blown dry and eluted by adding a 0.5 mL aliquot of 1 M HCl, leaving it for 20 minutes and then blowing the Dowex® AG2 X8 dry and collecting the acid in an Eppendorf. This was repeated twice more, resulting in 1.5 mL volume in the Eppendorf. 0.2 mL of 1 M $BaCl_2$ was added to the eluted sample, and the samples were left for 48 hours at 4 °C to allow the $BaSO_4$ to precipitate. Each sample was rinsed three times (centrifuged at 3500 rpm for 20 minutes, supernatant discarded, 1.5 mL de-ionised (Milli-Q) water added and mixed on a vortex, and repeated twice more, or more, until the pH was neutral). The supernatant was removed and the samples were dried at 40 °C.

The dry samples were weighed into tin or silver capsules for analysis of $\delta^{34}S\text{-}SO_4$ and $\delta^{18}O\text{-}SO_4$ respectively. Isotopic analysis was undertaken by Elemental Analyser (Elementar Pyrocube) linked to a continuous flow isotope ratio mass spectrometer (Isoprime 100 with dual inlet capability for injection of monitoring gases) and followed methods detailed in Wynn et al., 2015. Combustion of $BaSO_4$ within tin capsules yielded SO_2 for determination of $\delta^{34}S$.

Analytical conditions demanded the use of vanadium pentoxide as an oxidizing agent and a combustion temperature of 1050 °C. Pyrolysis of $BaSO_4$ at 1450°C within silver capsules and in the presence of carbon black, yielded CO for the determination of $\delta^{18}O$. $\delta^{34}S$ values were corrected against Vienna Cañon Diablo Troilite (VCDT) using within run analyses of international standards National Bureau of Standards (NBS)-127 and International Atomic Energy Agency (IAEA) SO-5. $\delta^{18}O$ values were corrected to VSMOW using within-run analyses of NBS-127 and IAEA-SO-6. Internal standard MLSG (a subglacial meltwater precipitate of $BaSO_4$) was used to monitor drift and precision within each run as well as external precision between analytical sequences. Within-run standard replication (1SD) was better than +/- 0.3‰ for both sulfur and oxygen isotope values.

2.3.3.6 Precipitation correction

Pre-melt snowpack chemistry data from Svalbard were compiled (Hodgkins et al., 1997; Wynn et al., 2006; Tye et al., 2007; Yde et al., 2008) in order to calculate the mean X/Cl ratios (where X is a major anion or cation). The following ratios in the snowpack were established: Na/Cl (= 0.82), K/Cl (= 0.02), Mg/Cl (= 0.10), Ca/Cl (= 0.08) and SO_4/Cl (= 0.11). By assuming that chloride behaves conservatively and is derived only from precipitation (*pd*), these ratios were used to calculate the fraction of each anion or cation in pore water (*pw*) derived from precipitation (fX_{pd}; Equation 2.10):

$$fX_{pd} = \left(\frac{X}{Cl}\right)_{snow} \cdot \left(\frac{Cl}{X}\right)_{pw} \quad (2.10)$$

The residual (fX_{npd}) represents the fraction of each anion or cation in pore water derived from weathering (Equation 2.11):

$$fX_{npd} = 1 - fX_{pd} \tag{2.11}$$

The δ^{34}S-SO_4 values were corrected for snow inputs, following Equation 2.12 (from Hindshaw et al., 2016) and using the mean snowpack δ^{34}S-SO_4 value of 17.5‰ from the compilation of pre-melt snowpack chemistry from Svalbard.

$$\delta^{34}S_{npd} = \frac{\left(\delta^{34}S_{pw} - f \cdot \delta^{34}S_{snow}\right)}{(1-f)} \tag{2.12}$$

Where *f* is the fraction of sulfate derived from snowmelt. δ^{18}O-SO_4 values were corrected in the same way as in Equation 2.12, using the mean snowpack δ^{18}O-SO_4 value of 9.28‰ from the compilation of pre-melt snowpack chemistry from Svalbard.

2.4 Data Analyses

Data analyses were performed in Microsoft Excel and R (R Core Team, 2017) and graphics were prepared with Excel or the ggplot2 R package. Prior to testing correlations between variables, Shapiro Wilk's method was used to test whether data were normally distributed. Many variables were not normally distributed and their relationships with one another were non-linear. Therefore, in correlation analysis, the Spearman correlation test (a test appropriate for non-normally distributed data) was selected for testing monotonous relationships between the variables because it is robust to skewed distributions and outliers (du Prel et al., 2010). The test ranks each variable from highest to lowest, assigning a '1' to the largest number in each variable group, and '2' to the second largest, and so on. The difference between the ranks is calculated and squared, and this is used to calculate the coefficient (ρ), which lies between -1 (a strong negative monotonic correlation) and +1 (a strong positive monotonic correlation). In a monotonic relationship, the value of the

dependent variable either never increases or never decreases as the independent variable increases.

The Grubbs test (Grubbs, 1950), which is a test to detect outliers in data with a normal distribution, was conducted on log-transformed data to ensure a normal distribution and one outlying observation from the $\delta^{13}C\text{-}CH_4$ dataset from Ice-wedge North ($\delta^{13}C\text{-}CH_4$ = -150.08‰) was removed from the dataset.

Chapter 3. Biogeochemical Processes in the Active Layer and Permafrost of a High Arctic Fjord Valley

3.1 Introduction

Permafrost is found beneath 24% of the land area of the Northern Hemisphere and stores immense quantities (1330 to 1580 Pg) of organic carbon (Hugelius et al., 2014; Tarnocai et al., 2009). Section 1.1 discussed that permafrost ecosystems are currently a net sink of carbon, owing to the drawdown of carbon dioxide exceeding emissions of methane and carbon dioxide (Kirschke et al., 2013; Parmentier et al., 2013; Schaefer et al., 2011). As rapid climate change occurs in the high Arctic, rising permafrost temperatures and progressively deeper active layers are exposing previously frozen soil organic carbon and facilitating microbial decomposition of this soil organic carbon (Romanovsky et al., 2010a; Schuur et al., 2015; Koven et al., 2011). This releases carbon dioxide and methane to the atmosphere and is predicted to cause permafrost ecosystems to become a net carbon source by the mid-2020s (Lee et al., 2012; Schuur et al., 2015; Elberling et al., 2013).

To predict the impact of permafrost thaw on biogeochemical cycling, it is necessary to understand the heterogeneity of biogeochemical processes in Arctic soils, both laterally and vertically. The distribution of stored organic carbon varies across the permafrost landscape, and with depth (Kuhry et al., 2010). Organic carbon accumulation and storage in permafrost is maximised in regions where waterlogged conditions dominate, as under these conditions, net primary production exceeds decomposition (Kolka et al., 2015). This is similar to peatlands, which have particularly large stores of organic carbon. Hydrology exerts a powerful influence on the type of gaseous products released from decomposing thawed permafrost organic carbon**.** For example, drained soil allows previously frozen organic carbon to decompose rapidly under oxic conditions, producing carbon dioxide (Liljedahl et al., 2012; Elberling et al., 2013), whereas water saturation limits the oxygen supply and enhances anaerobic respiration and methane production (Lipson et al., 2012; Olefeldt et al., 2013a; Turetsky et al., 2008). However, under anaerobic conditions, alternative electron acceptors such as nitrate, manganese, iron and sulfate may be used preferentially in the microbial

respiration of organic carbon, prior to the production of methane (Froelich et al., 1978). The use of alternative electron acceptors increases carbon dioxide production relative to methane, and hence the coupling between hydrology and the availability of alternative electron acceptors plays a crucial role in determining the magnitude of the permafrost carbon feedback.

Hodson et al. (2016) conducted hydrological monitoring demonstrating that waters draining through reactive, fine-grained sediments in the lower elevation coastal sites of Svalbard's Central Tertiary Basin (i.e. Adventdalen, the site of the present study) acquire reactive iron from pyrite oxidation. The authors found pyrite oxidation to be a process that exerts a major control upon the composition of fluvial runoff, as evidenced by the presence of high sulfate and cation concentrations. This process has also been observed in catchments close to Adventdalen (Bolterdalen and Longyeardalen; Rutter et al., 2011; Yde et al., 2008). This indicates that Adventdalen and the surrounding area has an abundance of alternative electron acceptors, such as ferric iron and sulfate, for the microbial oxidation of organic carbon. The abundance of ferric iron and sulfate in the waters draining through Adventdalen is important in the context of greenhouse gas emissions because Fe(III)- and sulfate-reduction are thermodynamically favourable to methanogenesis. Fe(III)-reduction has been found to suppress methanogenesis in the permafrost landscape of Barrow, Alaska (Lipson et al., 2012; Miller et al., 2015) and sulfate reduction has been observed to decrease methane production in wetlands (e.g., Pester et al., 2012). Hodson et al. (2016) used the highly correlated decrease in concentrations of sulfate and *Fe (all dissolved and colloidal iron that passed through a 0.45 μm filter) at low flow to infer removal by sulfate reduction and precipitation of pyrite (FeS_2), iron monosulfide (FeS) and perhaps elemental sulfur in waters draining through the Endalen alluvial sediment fan. However, the processes removing *Fe and sulfate from these waters were hypothesised to be limited by the paucity of organic matter (e.g., Raiswell & Canfield, 2012). The lack of organic matter has also been observed to limit the removal of *Fe and sulfate from pore water in fjord sediment cores in Svalbard (Wehrmann et al., 2014). It follows from these findings that it is necessary to test whether the accumulation of organic carbon in such environments results in enhanced removal of iron and sulfate from solution.

The objective of this chapter, therefore, is to determine how the vertical and lateral heterogeneity of organic carbon accumulation in Adventdalen influences the biogeochemical processes in the active layer and shallow permafrost sediments and pore water. This chapter presents and discusses the results of the geochemical analyses of the pore water and sediment from the cores of the active layer and shallow permafrost of Ice-wedge South and Ice-wedge North.

3.2 Results

Figure 3.1 (a-e) shows that the Ice-wedge North cores had a higher gravimetric water content than the Ice-wedge South cores. The gravimetric water content (g water g^{-1} dry sediment) for the two sites differed significantly according to Welch's t-test (Table 3.1). N2 had a mean gravimetric water content of 6.05 g g^{-1}, with no clear trend with depth, whereas the mean gravimetric water content in N1 was 2.79 g g^{-1} (maximum was 9.14 g g^{-1}) and was highest at the surface and below 90 cm depth. In S1, however, the mean water content was 0.57 g g^{-1}, with peaks near the surface, and at 105, 141 and 169 cm, and a maximum water content of 1.32 g g^{-1}. The mean gravimetric water content of S2a and S2b was similar (0.58 and 0.45 g g^{-1}, respectively). Both these cores had an increased water content near the surface.

The sedimentary organic carbon content for the two sites also differed significantly according to Welch's t-test (Table 3.1). Table 3.1 and Figure 3.1 show that Ice-wedge North had a higher organic carbon content than Ice-wedge South. The surface of N1 had a high organic carbon content (29.7%). In the permafrost, the organic carbon content was high, but variable (low at 30-70 cm depths, peaking at 100-140 cm depth). S1, however, had a more uniform and lower organic carbon content (mean of 2.38 wt.%), but with a peak near the surface (5.40%) and at 61 cm depth (4.65%).

Table 3.1 Results of Welch's t-tests comparing organic carbon, gravimetric water content, $Fe_{(aq)}$, sulfate, $CH_{4(aq)}$, CRS, Fe_{ox1}, Fe_{ox2}, Fe_{carb} and Fe_{mag} for Ice-wedge South and Ice-wedge North. t is the t statistic, df is the degrees of freedom, p is the significance level, S.D. is the standard deviation of the mean and n is the number of samples. Asterisks indicate level of significance: $p < 0.05$ (*); $p < 0.01$ (**); $p < 0.001$ (***).

Variable	t	df	p-value	Ice-wedge South			Ice-wedge North			Units of mean
				mean	S.D.	*n*	mean	S.D.	*n*	
Organic carbon	-7.9	60.8	***	2.30	0.86	30	12.5	9.94	60	Dry wt.%
Gravimetric water content	-7.4	72.5	***	0.53	0.34	113	4.6	4.68	73	$g\ g^{-1}$
$Fe_{(aq)}$	8.7	127.8	***	2.92	2.76	113	0.6	0.60	73	$mmol\ L^{-1}$
Sulfate	14.6	125.9	***	7.49	4.81	113	0.7	0.97	73	$mmol\ L^{-1}$
$CH_{4(aq)}$	-10.3	70.1	***	1.24	2.13	113	98.0	79.0	71	$\mu mol\ L^{-1}$
CRS	-3.1	6.2	*	0.01	0.01	9	0.1	0.04	7	Dry wt.%
Fe_{ox1}	-4.1	11.6	**	0.47	0.14	10	1.0	0.36	10	Dry wt.%
Fe_{ox2}	7.5	17.7	***	0.44	0.09	10	0.1	0.10	10	Dry wt.%
Fe_{carb}	-3.5	10.2	**	0.50	0.11	10	1.0	0.43	10	Dry wt.%
Fe_{mag}	5.1	17.4	***	0.76	0.17	10	0.3	0.21	10	Dry wt.%

The concentrations of $Fe_{(aq)}$ and sulfate differed significantly between the two sites, according to Welch's t-test (Table 3.1). Figure 3.2a and Figure 3.2b show that the $Fe_{(aq)}$ in N1 and N2 was < 3.0 mmol L^{-1}. In N1, peaks in aqueous iron were at 31, 67, 93 and 155 cm depth. In N2, the peaks were broader and at depths: 15-73cm, 109-139cm, and 197 cm. Figure 3.2f and Figure 3.2g show that while N2 had a sulfate concentration <1.3 mmol L^{-1}, N1 had up to 4.7 mmol L^{-1} in the peak at the active layer base. N1 had a clear trend in sulfate, increasing from the surface towards the base of the active layer, and then decreasing into the permafrost (with a small peak ~150 cm).

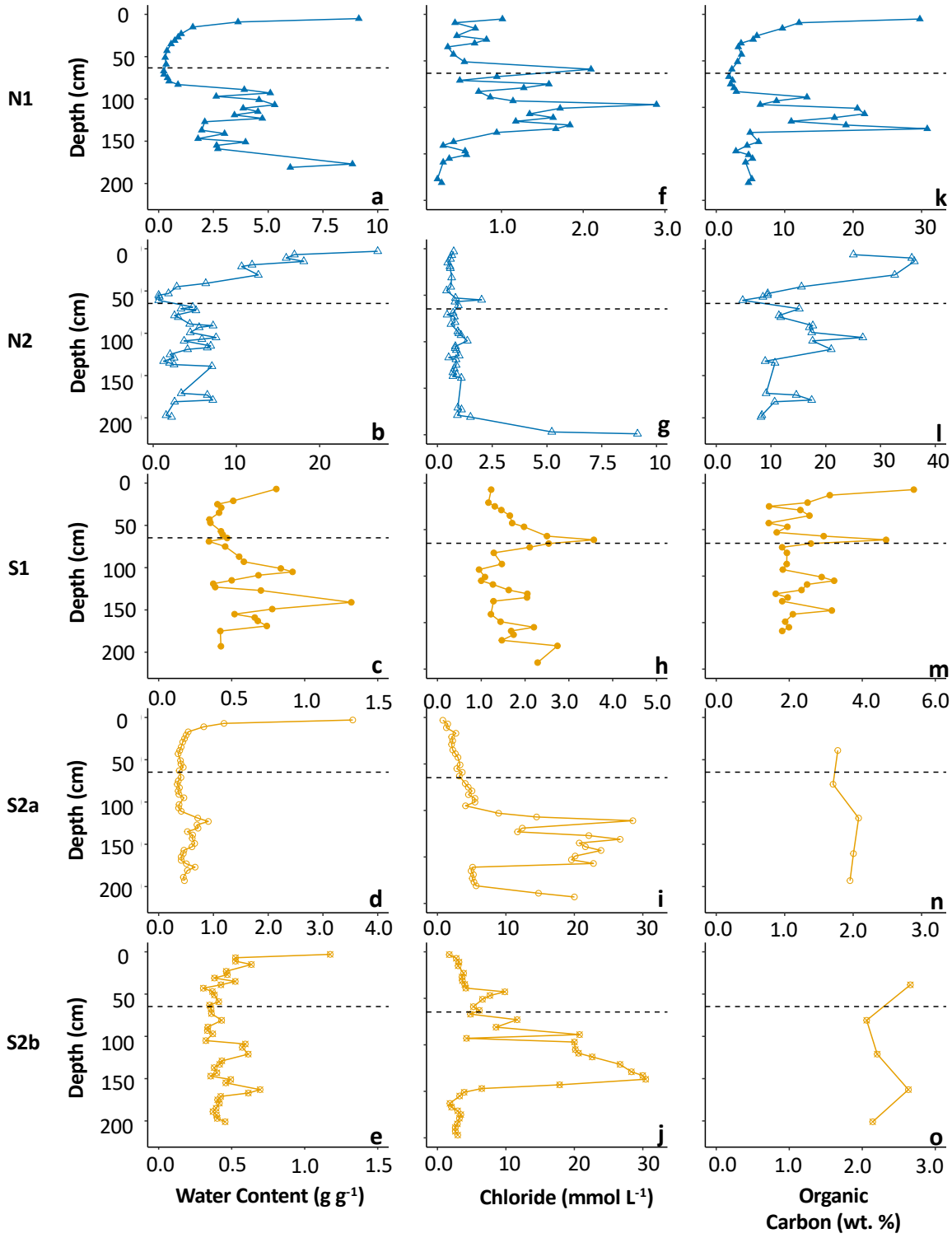

Figure 3.1 Depth profiles of water content (a-e), chloride concentration (f-j) and quantity of organic carbon (k-o) for N1, N2, S1, S2a and S2b. The horizontal dashed line on each plot represents the active layer depth in 2017.

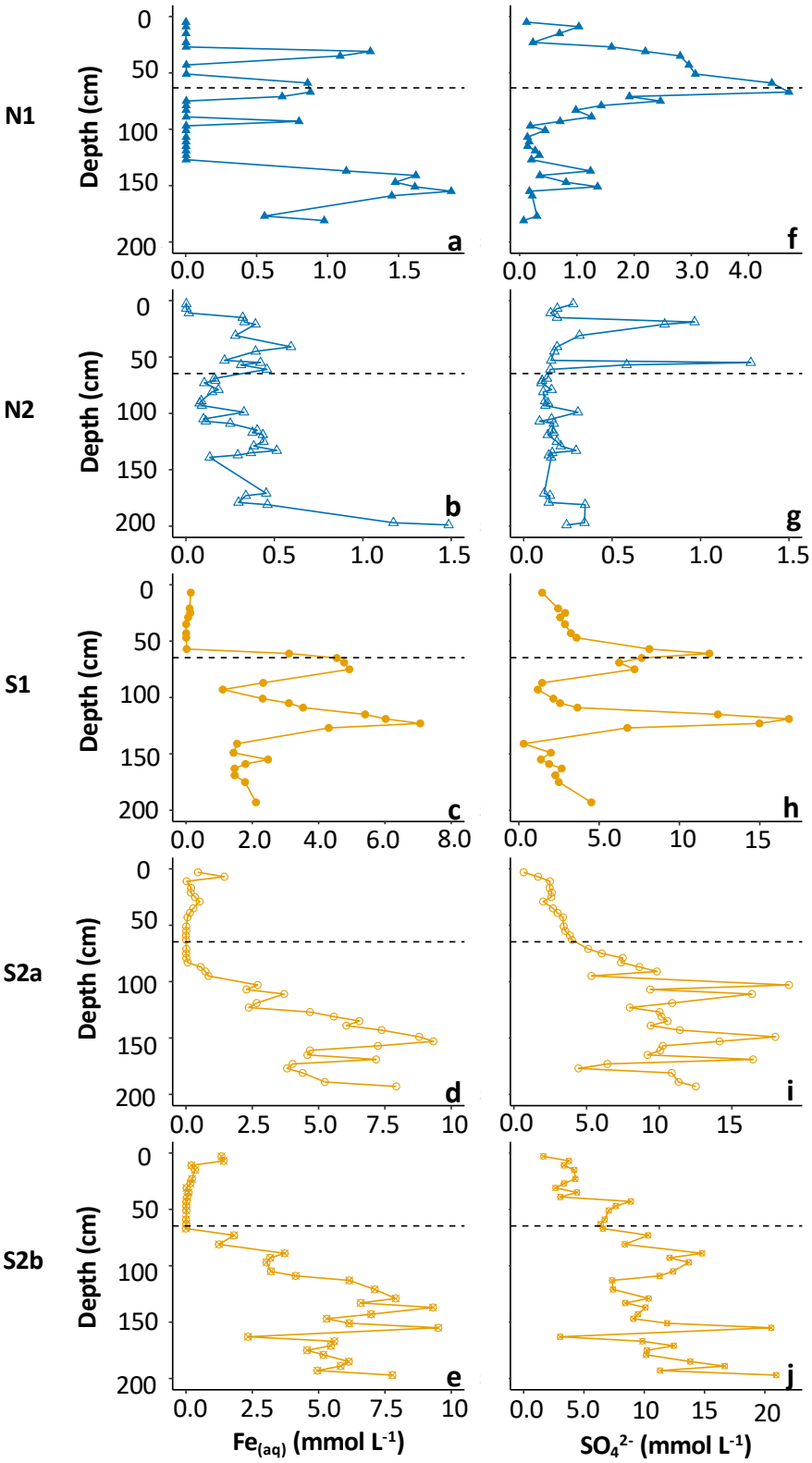

Figure 3.2 Depth profiles of $Fe_{(aq)}$ (a-e) and SO_4^{2-} (f-j) for N1, N2, S1, S2a and S2b. The horizontal dashed line on each plot represents the active layer depth in 2017.

Figure 3.2 (c-e) shows that the concentration of $Fe_{(aq)}$ was low (<1.5 mmol L^{-1}) in the active layer of all the Ice-wedge South cores. $Fe_{(aq)}$ in S1 peaked at 75 cm and 123 cm depth. The

$Fe_{(aq)}$ concentration in the permafrost of S2a and S2b had less distinct peaks, but increased with depth, reaching over 7.5 mmol L^{-1}. Figure 3.2(h-j) show that sulfate followed similar depth trends to $Fe_{(aq)}$ for all three Ice-wedge South cores, reaching >20 mmol L^{-1} in core S2b. The sulfate concentration in the active layer was higher than the $Fe_{(aq)}$ concentration.

Figure 3.3(a and f) shows that N1 had only low concentrations of calcium and magnesium in pore water (<6 mmol L^{-1}), with the highest values of both cations in the uppermost core sample. N2 had similarly low concentrations of calcium and magnesium (Figure 3.3b and g). S1 displayed distinct peaks in all cations at the base of the active layer and >1 m depth in the permafrost (Figure 3.3 and Figure 3.4, c and h). S2a and S2b show the greatest range in concentrations of calcium and magnesium (reaching ~15 mmol L^{-1}), with higher concentrations in the permafrost (Figure 3.3d, e, i and j). The concentration of potassium was generally <2.5 mmol L^{-1} in N2, S1, S2a and S2b (Figure 3.4), but reached >20 mmol L^{-1} in N1. The sodium concentration was <10 mmol L^{-1} in all the cores (Figure 3.4f-j).

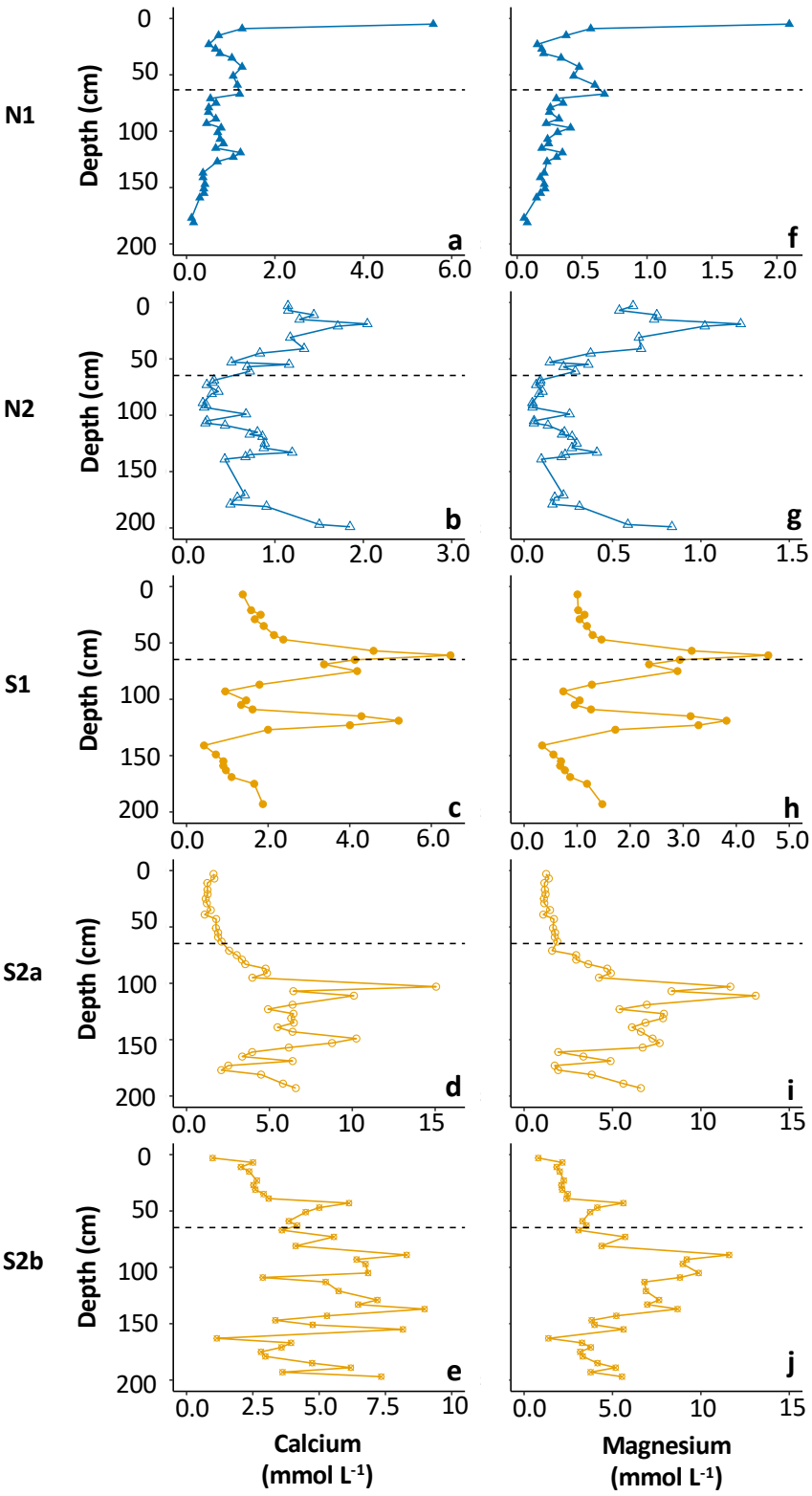

Figure 3.3 Depth profiles of calcium (a-e) and magnesium (f-j) for N1, N2, S1, S2a and S2b. The horizontal dashed line on each plot represents the active layer depth in 2017.

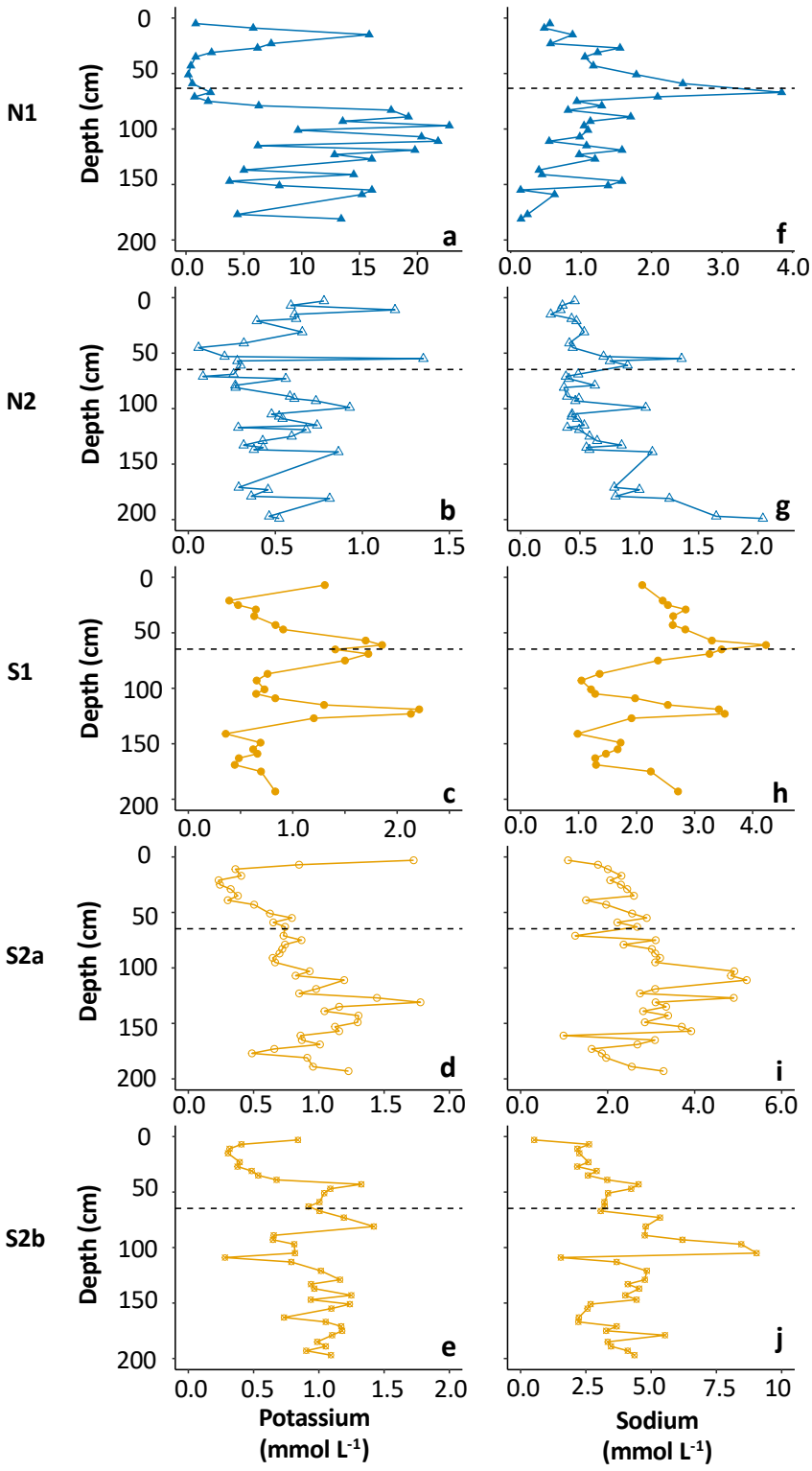

Figure 3.4 Depth profiles of potassium (a-e) and sodium (f-j) for N1, N2, S1, S2a and S2b. The horizontal dashed line on each plot represents the active layer depth in 2017.

Compared with the porewater $Fe_{(aq)}$ and sulfate profiles, the concentration of iron species was constant with depth in S1 (data not shown). Fe_{ox1} was <0.8 wt.%, Fe_{ox2} was <0.6 wt.%, Fe_{carb} was <0.8 wt.%, Fe_{mag} was <1 wt.%, CRS was <0.05 wt.%, and no AVS was detected in this

core (Table 3.2). The concentration of iron species was more variable down N1, with concentrations: Fe_{ox1} <1.6 wt.%, Fe_{ox2} <0.35 wt.%. Fe_{carb} was the dominant extracted iron phase at N1, reaching a maximum of 1.57 wt.% (Table 3.2). Overall, N1 had less Fe_{ox2} and Fe_{mag} than S1. Fe_{mag} at N1 was <0.71 wt. %. N1 contained an order of magnitude more CRS than S1 (Table 3.2). N1 had the highest CRS at 15 cm depth and at 115 cm depth, which tracked the organic carbon content. AVS was detected at 15 cm in N1, and also in all three samples measured between 114 and 156 cm.

Table 3.2 Summary statistics for the solid phase data of Ice-wedge South and Ice-wedge North, including AVS, CRS, Fe_{ox1}, Fe_{ox2}, Fe_{carb}, Fe_{mag} and organic carbon.

			Ice-wedge North		Ice-wedge South		
Unit			N1	N2	S1	S2a	S2b
AVS	dry wt.%	mean	0.02	na	0	na	na
		(min-max)	*(0.00-0.05)*	na	*(0-0)*	na	na
		n	*7*	na	*9*	na	na
CRS	dry wt.%	mean	0.12	na	0.02	na	na
		(min-max)	*(0.02-0.27)*	na	*(0.00-0.05)*	na	na
		n	*7*	na	*9*	na	na
Fe_{ox1}	dry wt.%	mean	0.97	na	0.44	na	na
		(min-max)	*(0.32-1.64)*	na	*(0.30-0.77)*	na	na
		n	*10*	na	*12*	na	na
Fe_{ox2}	dry wt.%	mean	0.13	na	0.44	na	na
		(min-max)	*(0.05-0.32)*	na	*(0.24-0.52)*	na	na
		n	*10*	na	*12*	na	na
Fe_{carb}	dry wt.%	mean	1.00	na	0.53	na	na
		(min-max)	*(0.38-1.57)*	na	*(0.39-0.73)*	na	na
		n	*10*	na	*12*	na	na
Fe_{mag}	dry wt.%	mean	1.58	na	4.11	na	na
		(min-max)	*(0.55-3.43)*	na	*(2.48-5.78)*	na	na
		n	*10*	na	*12*	na	na
Organic Carbon	dry wt.%	mean	8.55	16.7	2.41	1.9	2.34
		(min-max)	*(1.84-30.8)*	*(4.83-45.6)*	*(1.44-5.41)*	*(1.71-2.08)*	*(2.06-2.66)*
		n	*33*	*29*	*28*	*5*	*5*

Table 3.3 summarises the sulfate $\delta^{34}S\text{-}SO_4$ results obtained from samples of water from the active layer. Overall, the Ice-wedge South water was more depleted in ^{34}S than the Ice-wedge North water. At Ice-wedge South, the water $\delta^{34}S\text{-}SO_4$ was most enriched in ^{34}S at 30 cm depth, whereas the $\delta^{34}S\text{-}SO_4$ was more depleted in ^{34}S in depths 9 cm and 60 cm. The Ice-wedge North $\delta^{34}S\text{-}SO_4$ was increasingly depleted in ^{34}S with increasing depth.

Table 3.3 $\delta^{34}S\text{-}SO_4$ (‰) in water from the active layer in polygons S1 and N2.

Site	Depth (cm)	$\delta^{34}S\text{-}SO_4$			
		mean	*min*	*max*	*n*
S1	9	-6.90	*-6.95*	*-6.85*	*2*
S1	30	-2.23	*-3.74*	*-0.13*	*3*
S1	60	-6.78	*-8.37*	*-5.70*	*3*
N1	9	15.1	*3.33*	*25.3*	*3*
N1	30	5.19	*-0.98*	*11.4*	*2*
N1	60	-2.83	*-4.03*	*-2.16*	*3*

3.3 Discussion

The long-term biogeochemical evolution of this high Arctic floodplain has played a vital role in determining the biogeochemical processes and mineral precipitation within the active layer and permafrost sediments. Two sites with contrasting hydrological regimes displayed marked contrasts in the accumulation and decomposition of permafrost organic carbon. The quantity of organic carbon exerted a landscape-scale control on the active layer and permafrost biogeochemistry, regulating the consumption of alternative electron acceptors for the microbial oxidation of organic carbon. This indicates that the stabilization of the floodplain by vegetation (following deglaciation, e.g., Milner et al., 2009) caused the water-saturated areas of the floodplain to switch to iron- and sulfate-reduction, with net iron and carbon storage via increased pyrite (FeS_2) and siderite ($FeCO_3$) precipitation. In contrast, the drier areas stored far less organic carbon and were instead dominated by the biogeochemical signatures of the oxidation of pyrite.

3.3.1 Dominant weathering reactions

Previous work on waters draining glacial and periglacial sediments has demonstrated the relevance of pyrite oxidation coupled to both carbonate and silicate dissolution in the nearby Endalen, Bolterdalen and Longyeardalen catchments (Hodson et al., 2016; Rutter et al., 2011; Yde et al., 2008, respectively). The pore water profiles shown in Figure 3.1, Figure 3.2, Figure 3.3 and Figure 3.4 represent the following attributes of both the active layer and the underlying permafrost: (1) the *in situ* distribution of extractable or adsorbed solutes, reactive mineral phases, and gases, and (2) the products of additional rock-water-microorganism interactions following thaw. Across both sites, except for N1 where potassium dominated,

calcium and magnesium were the dominant cations (Figure 3.3 and Figure 3.4), indicating that carbonate dissolution prevails over silicate dissolution, despite a low carbonate content in the sediments (<0.8 dry wt.% at Ice-wedge South) and low volumetric carbonate contents (~0.3 to 1.8%, but up to 10.7%) in the Todalen and Endalen endmembers (Svinth, 2013). This contrasts with a study in a nearby unglaciated catchment (Fardalen) that found a relatively high proportion of silicate weathering, suggested to be the result of a combination of relatively rapid leaching of carbonate phases from the active layer and low rates of physical weathering in the sediments failing to expose fresh carbonates to weathering (Hindshaw et al., 2016). However, carbonate weathering has previously been shown to control the water chemistry of both glacial and non-glacial watersheds, even where the bedrock is predominantly silicate, with only trace amounts of carbonate (Horton et al., 1999; Blum et al., 1998). This strongly suggests that although the low carbonate content coupled with the potential for active layer leaching might limit the importance of carbonate weathering in Adventdalen to some degree, the reactivity of the carbonate phases (compared to silicates) compensated for these factors.

The weathering processes responsible for the acquisition of Ca^{2+} and Mg^{2+} are most likely to be represented by the following reactions (after Hindshaw et al., 2016; Tranter et al., 2002; and Yde et al., 2008):

(3.1) Carbonate dissolution with carbonic acid

$$\mathrm{Ca}_{1-x}\mathrm{Mg}_{x}CO_3 + CO_2 + H_2O \rightarrow (1-x)Ca^{2+} + xMg^{2+} + 2HCO_3^- \quad (3.1)$$

(3.2) Sulfide oxidation coupled to carbonate weathering

$$4\mathrm{FeS}_2 + 16\mathrm{Ca}_{1-x}(\mathrm{Mg}_x)\mathrm{CO}_3 + 15\mathrm{O}_2 + 14\mathrm{H}_2\mathrm{O} \rightarrow 4\mathrm{Fe(OH)}_3 + 16(1-x)\mathrm{Ca}^{2+} + 16x\mathrm{Mg}^{2+} + 16\mathrm{HCO}_3^- + 8{\mathrm{SO}_4}^{2-} \quad (3.2)$$

The covariance between ions is used here to focus on the dominant weathering processes in the entire active layer and permafrost. Evidence for carbonate weathering as a source of both Ca^{2+} and Mg^{2+} was provided by the strong positive correlation between these ions at Ice-wedge South (ρ = 0.95, $p < 0.0001$) and a regression slope close to unity (0.89). When

corrected for precipitation inputs of both cations, the slope remained unchanged (Figure 3.5), but the intercept decreased significantly towards zero (0.24 mmol L^{-1}), suggesting that dolomite represents a credible, common source for both ions.

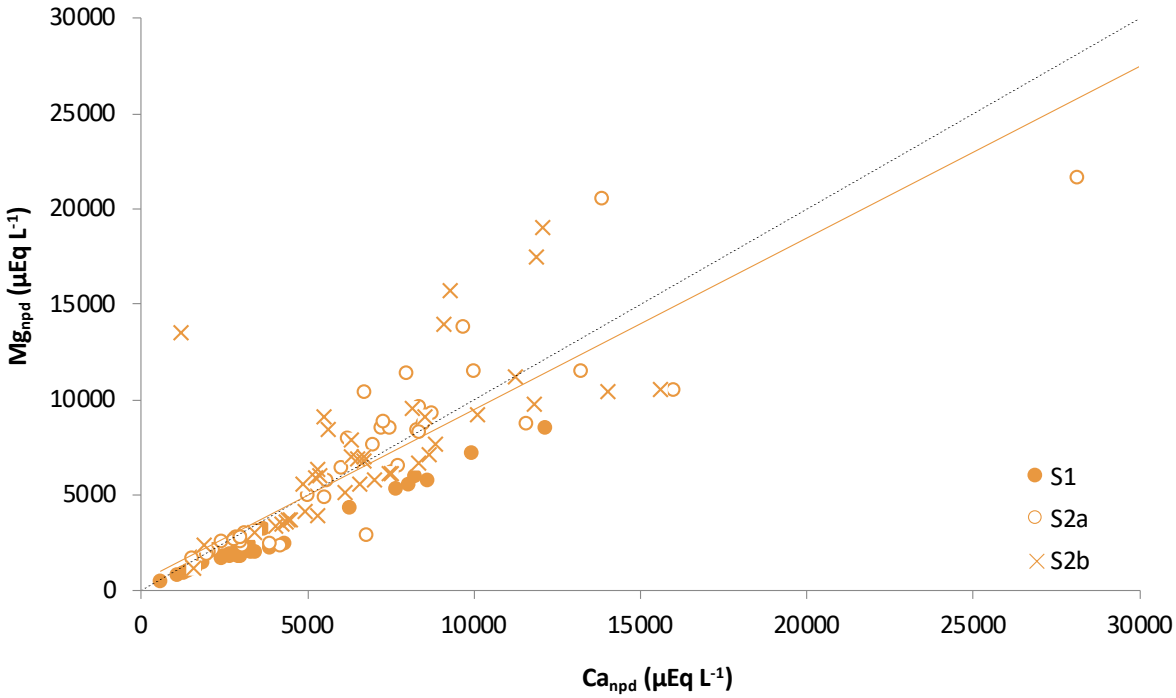

Figure 3.5 Non-precipitation-derived magnesium (Mg_{npd}) and non-precipitation-derived calcium (Ca_{npd}) in the three cores from Ice-wedge South. The dashed black line corresponds to a 1:1 relationship between Ca_{npd} and Mg_{npd} that represents dolomite dissolution. The solid orange line is a regression for all points from the three cores from Ice-wedge South (R^2 = 0.69).

Although $(Ca+Mg)_{npd}$ was strongly correlated with $(SO_4^{2-})_{npd}$ ($p<0.0001$, ρ = 0.81), the regression slope was 0.73, which suggests that some of the sulfate originated from other sources. The presence of silicates in the catchment indicates that sulfide oxidation coupled to silicate dissolution may play a role in making up the deficit. Since silicates in the catchment are mainly present as Na- and K-feldspars, they may be represented by the formulae: $NaAlSi_3O_8$ and $KAlSi_3O_8$ in the following reactions (Hindshaw et al., 2016; Tranter et al., 2002):

(3.3) Silicate dissolution with carbonic acid

$$NaAlSi_3O_8(s) + 2CO_2(aq) + 2H_2O(l) \rightleftharpoons Na^+(aq) + 2HCO_3^-(aq) + AlSi_3O_8(s) \quad (3.3)$$

(3.4) Sulfide oxidation coupled to silicate dissolution

$$16\mathrm{Na}_{1-x}\mathrm{K}_x\mathrm{Si}_3\mathrm{O}_8(\mathrm{s}) + 4\mathrm{FeS}_2(\mathrm{aq}) + 15\mathrm{O}_2(\mathrm{aq}) + 86\mathrm{H}_2\mathrm{O}(\mathrm{l}) \quad (3.4)$$

$$\rightleftharpoons$$

$$16(1-x)\mathrm{Na}^+(\mathrm{aq}) + 16x\mathrm{K}^+ + 8\mathrm{SO}_4^{2-}(\mathrm{aq}) + 4\mathrm{Al}_4\mathrm{Si}_4\mathrm{O}_{10}(\mathrm{OH})_8(\mathrm{s}) + 4\mathrm{Fe(OH)}_3(\mathrm{s}) + 32\mathrm{H}_4\mathrm{SiO}_4(\mathrm{aq})$$

When silicate and carbonate dissolution are both driven by sulfide oxidation, the total base cation (Ca^{2+}+Mg^{2+}+Na^++K^+) ratio to SO_4^{2-} tends towards unity when precipitation inputs are insignificant (Fairchild et al., 1994; Tranter et al., 2002; Wadham et al., 2010). However, this characteristic signature can be overprinted or masked by ion exchange reactions or mineral precipitation acting to remove base cations from solution. Prior to correction for precipitation inputs, the total base cation ratio to sulfate at Ice-wedge South was 0.98 (r^2 = 0.68). The standard correction for precipitation inputs resulted in a lower regression slope of 0.76 (r^2 = 0.70; Figure 3.6). Of the base cations, sodium was particularly affected by masking effects, with non-precipitation-derived inputs appearing negative, similar to Cable et al. (2017). This is indicative of ion exchange reactions or mineral precipitation (e.g. albite) and hence precludes the use of the non-precipitation-derived ion ratios to estimate the importance of sulfide oxidation coupled to silicate dissolution.

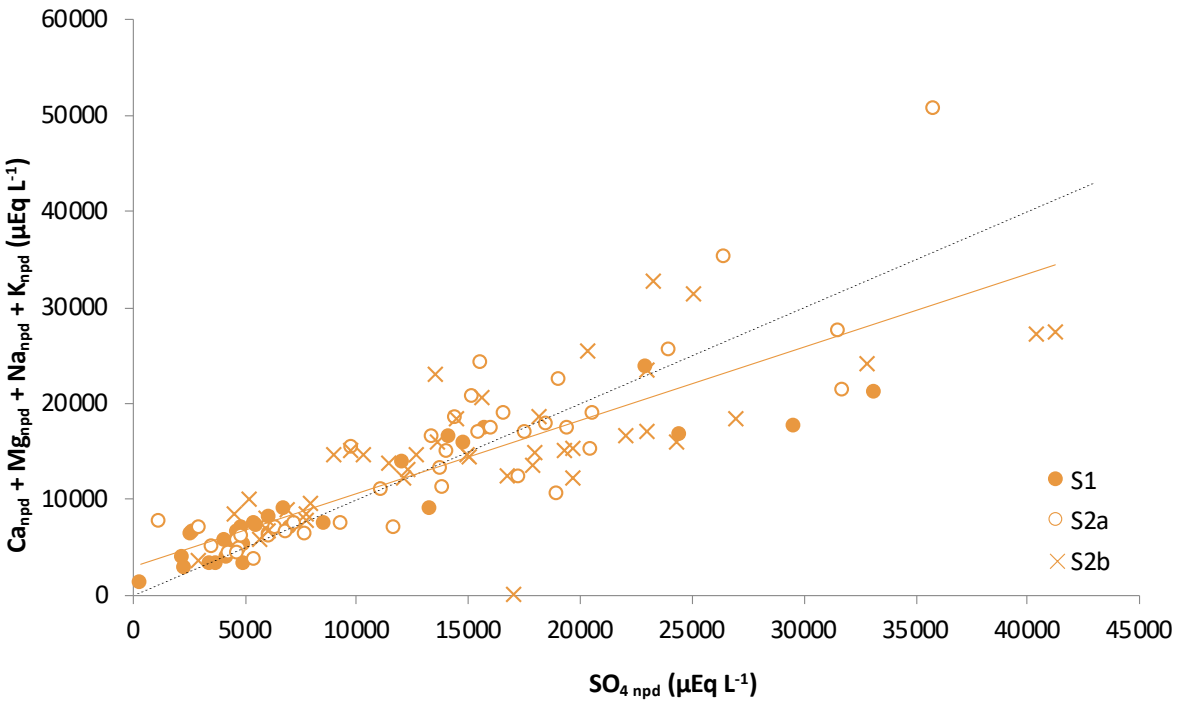

Figure 3.6 Total non-precipitation-derived base cations and non-precipitation-derived sulfate in the three cores from Ice-wedge South. The dashed black line corresponds to a 1:1 relationship between $SO_{4\ npd}$ and (Ca_{npd} + Mg_{npd} + Na_{npd} + K_{npd}) that represents sulfide oxidation coupled to silicate dissolution. The solid orange line is a regression for all points from the three cores from Ice-wedge South (R^2 = 0.70).

Since the concentration of SO_4^{2-} derived from pyrite oxidation was high and developed within a sometimes-anoxic environment, alternative processes of pyrite oxidation require identification. The reduction of solid-phase iron (oxyhydr)oxides (Equation 3.5), potentially produced by Equations 3.2 and 3.4, could provide the alternative mechanisms, resulting in the significant contribution of ferrous iron to the total cations in solution (Raiswell & Canfield, 2012; Hodson et al., 2016).

$$2Fe(OH)_3 + FeS_2 + 2H_2O \longrightarrow 3Fe^{2+} + 2SO_4^{2-} + 10H^+ \quad (3.5)$$

However, iron reduction need not be achieved in combination with sulfide oxidation (Equation 3.6).

$$4Fe(OH)_3 + CH_2O + 8H^+ \longrightarrow 4Fe^{2+} + 11H_2O + CO_2 \quad (3.6)$$

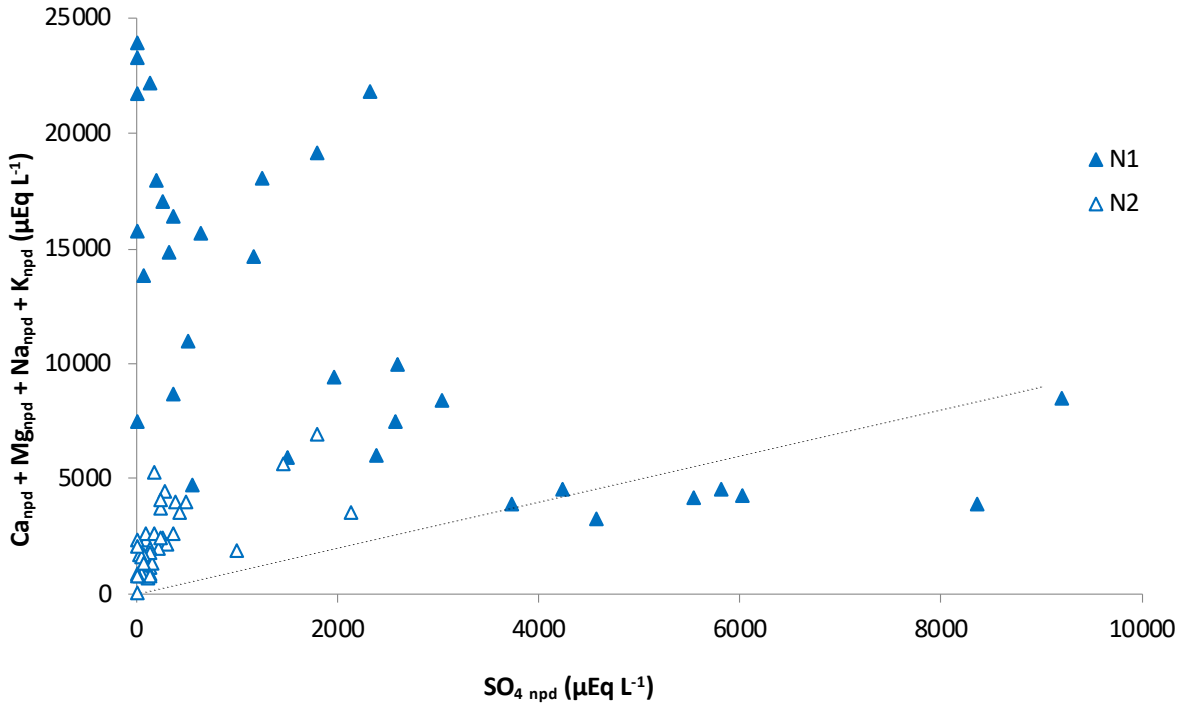

Figure 3.7 Total non-precipitation-derived base cations and non-precipitation-derived sulfate in the two cores from Ice-wedge North. The dashed black line corresponds to a 1:1 relationship between SO_{4npd} and (Ca_{npd} + Mg_{npd} + Na_{npd} + K_{npd}) that represents sulfide oxidation coupled to silicate dissolution.

In contrast to Ice-wedge South, Figure 3.7 shows that the Ice-wedge North pore waters generally do not plot on the 1:1 line, and there is no relationship between sulfate and total cations for these. Despite this, some samples from this site have a sulfate to chloride ratio greater than the snowpack sulfate to chloride ratio. This indicates that sulfide oxidation has enhanced the sulfate concentrations, as gypsum is absent from the bedrock, precluding this phase as a source of sulfate (Svinth, 2013). The absence of a 1:1 relationship between total cations and sulfate at this site therefore strongly suggests that the sulfate produced by sulfide oxidation is removed in part by sulfate reduction during respiration of organic matter (Equation 3.7; Wadham et al., 2004).

$$SO_4^{2-} + 2CH_2O \rightleftharpoons H_2S + 2HCO_3^- \quad (3.7)$$

The major ion ratios show that sulfide oxidation coupled to carbonate dissolution can contribute substantial quantities of sulfate to the sediment pore water at Ice-wedge South. In contrast, processes removing sulfate from the sediment pore water at Ice-wedge North preclude the use of major ion ratios to determine the significance of sulfide oxidation. In

addition, the evidence for iron- and sulfate-reduction indicates that microbially-mediated anaerobic oxidation of organic carbon produced bicarbonate and carbon dioxide.

3.3.2 Sources and sinks of sulfate

Sulfur and oxygen isotopic values of sulfate in waters provide compelling evidence for the identification of the sources and sinks of sulfate (e.g., Wynn et al., 2006, 2015; Turchyn et al., 2013; Hindshaw et al., 2016). Pre-melt snowpacks in Svalbard at Midtre Lovenbreen (Wynn et al., 2006) and near Ny Ålesund (Tye & Heaton, 2007) reveal a $\delta^{34}S$ range of +17 to +18‰ and a $\delta^{18}O$ range of +8.6 to +9.7‰ for the precipitation-derived sulfate contribution to the active layer pore water (i.e. $SO_4^{2-}{}_{pd}$). A study of dissolved organosulfur compounds in a raised peat bog showed that atmospheric sulfur in surface water sulfate is also taken up by plants (plant $\delta^{34}S$ was 0.1‰ and 4.2‰) and released when they decay, releasing humic organosulfur with $\delta^{34}S$ values reflecting the precipitation-derived origin of the sulfate (Bottrell et al., 2010). Other sources of sulfate to the pore water include the oxidative weathering of pyrite (OWP), as in Equations 3.2, 3.4 and 3.5. The mass weighted mean sulfide $\delta^{34}S$ values in the geological formations of the study region varies widely, from -40.6‰ in the Grumantbyen Formation to 1.78‰ in the Aspelintoppen Formation (Dixon, 2020; Table 3.4). In the geological formations measured closest to the sites, the range in mass weighted mean sulfide $\delta^{34}S$ values is narrower, from -13.8‰ in the Carolinefjellet Formation to -2.01‰ in the Firkanten Formation (Dixon, 2020). These nearby $\delta^{34}S$ values are therefore used to discriminate the rock-derived sulfate from the snowpack-derived sulfate.

Table 3.4 The mean quantity of sulfide (wt.%) in bedrock, the numerical mean sulfide $\delta^{34}S$ (‰) in bedrock and the mass-weighted mean sulfide $\delta^{34}S$ (‰) in bedrock (Dixon, 2020).

Formation	n	Mean S	Numerical mean $\delta^{34}S$	Mass weighted mean $\delta^{34}S$
		wt. %	‰	‰
Asplentoppen	4	0.09	0.44	1.78
Battfjellet	3	0.06	1.56	1.49
Frysjaodden (Gilsonryggen)	4	0.15	-4.98	1.34
Grumantbyen	3	0.10	-32.35	-40.60
Basilika	4	1.71	8.45	2.04
Firkanten (Endalen)	3	0.24	-6.22	-7.88
Firkanten (Todalen)	3	3.55	-0.76	-2.01
Carolinefjellet	3	0.15	-13.27	-13.79

The $\delta^{18}O$ of sulfate depends on the oxidation pathway; the oxygen atoms in the sulfate can originate either from atmospheric oxygen (+23.5‰) or from the surrounding water (-11‰ to -14‰ at our sites). In sulfate produced by OWP via Fe^{3+} (Equation 3.5), the oxygen atoms are derived solely from the surrounding water molecules. Experiments have demonstrated that there is no isotopic discrimination during the incorporation of oxygen atoms from water molecules into sulfate (Lloyd, 1968). In contrast, the incorporation of oxygen atoms from O_2 molecules into sulfate molecules during OWP via O_2 causes an isotopic fractionation of -8.7‰. Consequently, sulfate produced by OWP via O_2 is depleted in ^{18}O by -8.7‰ compared with atmospheric O_2, which is strongly enriched in ^{18}O at +23.7‰ (Bottrell and Tranter, 2002). However, during OWP via O_2, there can be isotopic exchange between water and oxygen atoms in sulfoxy anions of intermediate valency, obscuring the isotopic signal of atmospheric oxygen (Balci et al., 2007). Hence, even in OWP via O_2, three out of four oxygen atoms in the sulfate molecule could show an isotopic signal from water (Bottrell and Tranter, 2002).

To elucidate whether the sulfate in the samples from Adventdalen could derive from OWP only via O_2, the approach of Bottrell and Tranter (2002) was applied to the $\delta^{18}O$ values of sulfate from the waters in the active layer. This conservative approach assumed that only the final oxygen atom incorporated into sulfate will still carry an isotopic signature indicative of its source (water or atmospheric oxygen). Only if there is less than 25% of the oxygen in a

sulfate molecule derived from O_2 can it be certain that part of the sulfate was produced anoxically, by OWP via Fe^{3+}. Equation 3.8 uses the measured $\delta^{18}O$-H_2O water isotopic compositions (Table 3.5) to calculate a threshold sulfate $\delta^{18}O$ ($\delta^{18}O_{THRESH}$) for the formation of sulfate with one oxygen atom from O_2 and three from water (Bottrell and Tranter, 2002).

$$\delta^{18}O_{THRESH} = (23.7 - 8.7) \times 0.25 + 0.75 \times \delta^{18}O_{THRESH} \quad (3.8)$$

In a comparison of $\delta^{18}O$-SO_4^{2-} and $\delta^{18}O_{THRESH}$-SO_4^{2-}, only one sample from the Adventdalen active layer pore waters falls below the threshold for OWP via Fe^{3+} (Table 3.5), indicating that $SO_4^{2-}{}_{npd}$ in this sample must derive from OWP via Fe^{3+}. In the rest of the samples, $SO_4^{2-}{}_{npd}$ could have derived from OWP via Fe^{3+}, but the isotopic data do not require that and it is probable that $SO_4^{2-}{}_{npd}$ in the remaining samples instead derived from OWP via O_2. This is a surprising result, as these samples are from between 9 and 60 cm below the ground surface and it was anticipated that oxygen penetration would decrease with profile depth. However, it is possible that radial oxygen loss from the roots of wetland plants may have provided an oxygen source to this deeper pore water (e.g. Johnston et al., 2014). In addition, ice-wedge cracking provides a route for ingress of oxygenated rain and meltwater.

Table 3.5 Oxygen isotopes of weathering-derived sulfate ($\delta^{18}O\text{-}SO_4^{2-}{}_{npd}$) and water ($\delta^{18}O\text{-}H_2O$) compared to the threshold for anoxic oxidation of pyrite ($\delta^{18}O_{THRESH}$).

Site	Depth	$\delta^{18}O\text{-}SO_4^{2-}{}_{npd}$	$\delta^{18}O\text{-}H_2O$	$\delta^{18}O_{THRESH}$	OWP
	cm	‰	‰	‰	
S	9	-5.36	-11.4	-4.78	anoxic
S	9	-3.36	-11.3	-4.75	oxic
S	30	3.47	-12.3	-5.45	oxic
S	30	3.48	-12.3	-5.45	oxic
S	30	2.54	-12.4	-5.57	oxic
S	30	3.95	-12.1	-5.30	oxic
S	60	1.39	-12.0	-5.24	oxic
S	60	3.83	-13.1	-6.05	oxic
S	60	5.66	-12.4	-5.57	oxic
N	9	9.16	-13.0	-6.00	oxic
N	9	5.65	-13.0	-6.01	oxic
N	9	1.40	-13.0	-5.96	oxic
N	30	5.06	-13.7	-6.56	oxic
N	30	6.12	-13.5	-6.34	oxic
N	60	5.33	-14.1	-6.79	oxic
N	60	5.39	-14.1	-6.79	oxic
N	60	4.32	-13.8	-6.59	oxic
N	60	4.32	-13.5	-6.38	oxic

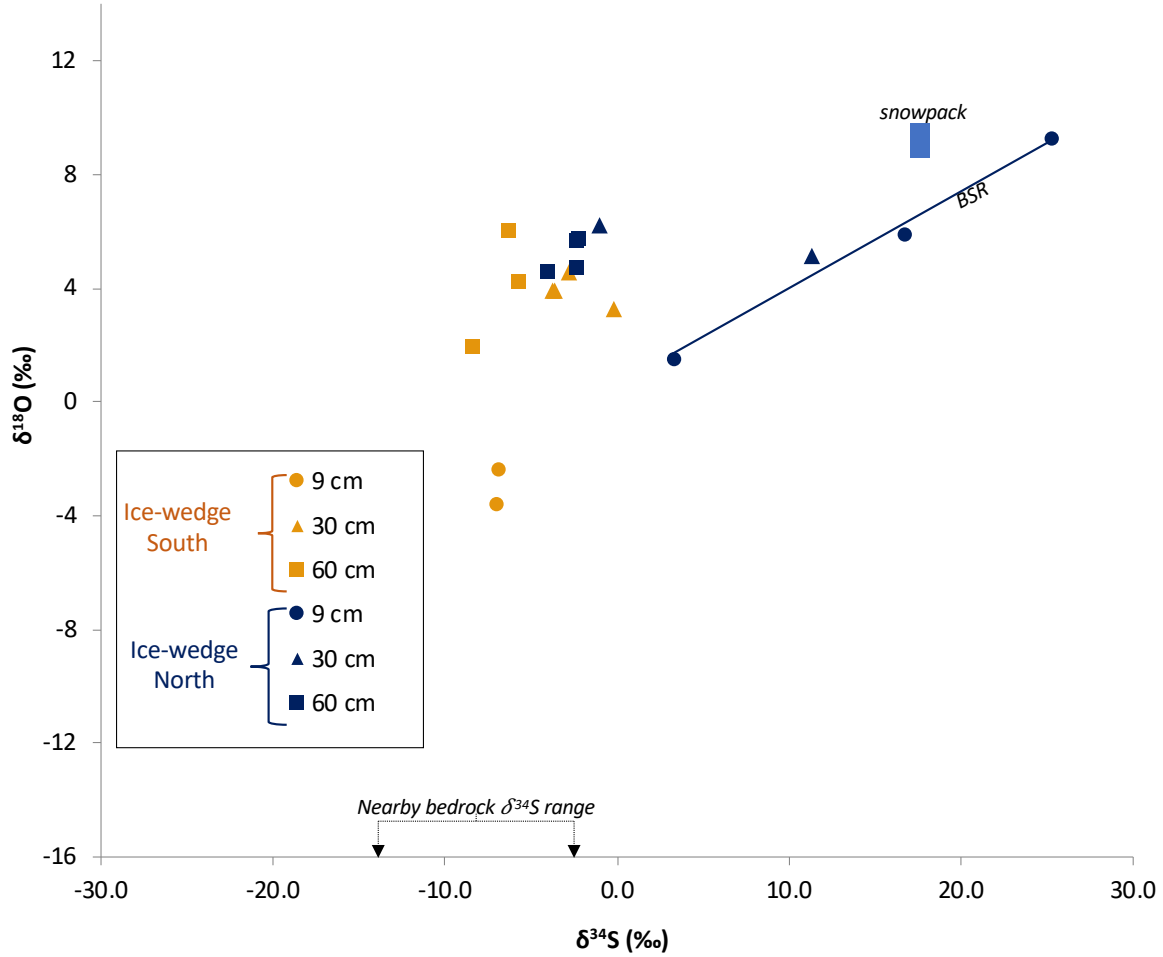

Figure 3.8 Water samples from the active layer of Ice-wedge South and Ice-wedge North in $\delta^{18}O\text{-}SO_4$ and $\delta^{34}S\text{-}SO_4$ isotope space. The blue box represents the isotopic range of pre-melt snowpacks in Svalbard at Midtre Lovenbreen (Wynn et al., 2006) and near Ny Ålesund (Tye & Heaton, 2007). The solid blue line is a regression line illustrating BSR (R^2 = 0.98). The nearby bedrock range is of the mass-weighted mean sulfide $\delta^{34}S$ in the Firkanten and Carolinefjellet Formations (Dixon, 2020).

Figure 3.8 shows how plotting sulfate $\delta^{18}O$ and $\delta^{34}S$ in sulfur isotopic space can provide a unique solution to elucidating the sulfate sources. The stoichiometric stage of pyrite oxidation results in sulfur isotopic fractionation between pyrite and sulfate ($\varepsilon_{SO4\text{-}pyrite}$) of -1.3‰ to -0.6‰ (Balci et al., 2007; Brunner et al., 2008; Pisapia et al., 2007). The mass-weighted mean sulfide $\delta^{34}S$ of the nearby Firkanten and Carolinefjellet Formations, combined with the sulfur isotopic fractionation during the stoichiometric stage of sulfide oxidation, indicates that any water sample with a $\delta^{34}S\text{-}SO_4^{2-}{}_{npd}$ value between -15.1‰ and -2.6‰ is likely to have derived all of its sulfur from the stoichiometric oxidation of pyrite. Figure 3.8 shows that half of the samples of pore water from Adventdalen contain $SO_4^{2-}{}_{npd}$ falling within this $\delta^{34}S\text{-}SO_4^{2-}{}_{npd}$ range, indicating that the stoichiometric oxidation of pyrite is an important process

contributing sulfate to active layer pore water in Adventdalen. This corroborates the evidence from $\delta^{18}O\text{-}SO_4^{2-}$ presented earlier.

Although all except for the most ^{34}S-enriched sample have a $\delta^{34}S$ range that falls between the range of the bedrock and snowpack $\delta^{34}S$ values (Figure 3.8), the origin of sulfate in these samples in ^{34}S and ^{18}O cannot be explained purely as a mixing of sulfate derived from these two sources. There are two lines of evidence for this, as follows. Firstly, if mixing between (relatively ^{34}S-enriched) precipitation-derived sulfate and (relatively ^{34}S-depleted) weathering-derived sulfate were solely responsible for the $\delta^{34}S$ values of pore water sulfate in the active layer, a negative linear correlation between the concentration and $\delta^{34}S$ values of weathering-derived sulfate would result. There is no such negative linear correlation in the pore water samples from Adventdalen ($R^2 < 0.2$). Secondly, a negative correlation between $\delta^{34}S\text{-}SO_4^{2-}$ and the sulfate-to-chloride molar ratio (SO_4^{2-}/Cl^-) would result from mixing between weathering-derived sulfate (high SO_4^{2-}/Cl^-, relatively ^{34}S-depleted) and precipitation-derived sulfate (low SO_4^{2-}/Cl^-, relatively ^{34}S-enriched). In fact, there is a positive correlation between $\delta^{34}S\text{-}SO_4^{2-}$ and SO_4^{2-}/Cl^- ($R^2 = 0.49$). Neither line of evidence supports mixing between snowmelt and pyrite oxidation as the sole reason for the $\delta^{34}S\text{-}SO_4^{2-}$ values observed in the samples from Adventdalen. Hence, these statistical tests indicate that sulfate removal from the pore water by bacterial sulfate reduction (BSR) may be a factor in enriching the remaining sulfate in these samples. In BSR, there is preferential reduction of the lighter isotopes of sulfur and oxygen, leading to isotopic enrichment of the residual sulfate. It is common for the product H_2S to be incorporated into iron sulfides or into organic matter (Brown, 1985, 1986; Blodau et al., 2007). This causes both $\delta^{34}S$ and $\delta^{18}O$ values in the remaining sulfate to increase, and so a positive correlation between them results (Mandernack et al., 2003). Since there is a positive correlation ($R^2 = 0.98$) between $\delta^{34}S$ and $\delta^{18}O$ in four samples from Ice-wedge North, it seems highly likely that BSR occurs in the pore water of the active layer at Ice-wedge North.

3.3.3 Iron and sulfur mineral precipitation

The $\delta^{34}S$ and $\delta^{18}O$ values of pore water sulfate in the active layer are indicative of sulfate reduction at Ice-wedge North. The sulfate concentration was relatively low at Ice-wedge

North (<4.7 mmol L^{-1}; Figure 3.2f and g), supporting the isotopic evidence for sulfate reduction. To produce a distinctive $\delta^{18}O$-$\delta^{34}S$ signature of sulfate reduction, the reduced sulfur must be sequestered in the solid phase (iron sulfide or carbon-bonded sulfur). The reactions of iron with hydrogen sulfide can be expressed with the following simplified equation scheme, where Equation 3.9 represents hydrogen sulfide reacting with iron oxides to form iron monosulfide (AVS) and sulfur, and Equation 3.10 represents the formation of the more stable pyrite (CRS) from the metastable iron monosulfide and sulfur (Raiswell & Canfield, 2012):

$$2FeOOH + 3H_2S \rightarrow 2FeS + S^0 + 4H_2O \quad (3.9)$$

$$FeS + S^0 \rightarrow FeS_2 \quad (3.10)$$

The AVS formed in Equation 3.9 is comprised mainly of the iron sulfide minerals mackinawite, greigite and amorphous FeS. These phases are usually only stable for short periods before their re-oxidation or further reduction to pyrite (Chesworth, 2008). Table 3.2 shows that the AVS concentrations in the Ice-wedge North sediments were low, but detectable, in just over half the tested samples, reaching a maximum of 0.05 dry weight percent (equivalent to 6.02 µmoles g^{-1} dry sediment; 115 cm depth). The low concentrations of AVS indicate that AVS is not a significant long-term store of the products of iron and sulfate reduction. The CRS includes pyrite, which is the most thermodynamically stable iron sulfide (Berner, 1967). Concentrations of CRS are higher than AVS, reaching 0.27 dry weight percent (equivalent to 22.4 µmoles g^{-1} dry sediment; 115 cm depth) at Ice-wedge North (Table 3.2).

The Ice-wedge North sediments contain abundant iron in the form of poorly crystalline ferrihydrite (Fe_{ox1}), crystalline goethite (Fe_{ox2}), magnetite (Fe_{mag}), siderite (Fe_{carb}) and pyrite (CRS). Ferrous iron in the porewaters is probably derived from the dissimilatory reduction of iron (oxyhydr)oxides (Equation 3.6), as well as the oxidation of allogenic and authigenic pyrite (Equation 3.5). In addition to reacting with hydrogen sulfide to form AVS or CRS, the dissolved ferrous iron reacts with bicarbonate ions to form siderite ($FeCO_3$; Fe_{carb}). Siderite tends to occur in reducing, CO_2-rich, hydromorphic environments, such as peatlands (Chesworth,

2008). Table 3.2 shows that Fe_{carb} reaches >1.5 dry wt.% in the sediments at Ice-wedge North, indicating that it is a more significant sink of ferrous iron than pyrite. As the precipitation of siderite dominates over the precipitation of pyrite, it is possible that an additional sink for the hydrogen sulfide is carbon-bonded sulfur (CBS), which has previously been shown to be an important sink for reduced sulfur in peat soils (Blodau et al., 2007; Spratt & Morgan, 1990). Although CBS was not measured in these cores, a strong positive correlation between organic carbon content and CRS (ρ = 0.9; Table 3.6) and also Fe_{carb} (ρ = 0.67; Table 3.6) indicates that where the organic carbon content is high, sulfate reduction, CRS precipitation and Fe_{carb} precipitation occur. Given the high concentration of sedimentary organic carbon, it seems likely that CBS exists and is forming here.

Table 3.6 Spearman rank correlation coefficients (ρ) and significance (p). Asterisks indicate level of significance: p < 0.05 (*); p < 0.01 (**); p < 0.001 (***); not significant (n.s.).

Core	Variable 1	Variable 2	ρ	p
S1	Chloride (mmol L^{-1})	Gravimetric water content (g g^{-1})	-0.63	***
S2a	Chloride (mmol L^{-1})	Gravimetric water content (g g^{-1})	0.15	n.s.
S2b	Chloride (mmol L^{-1})	Gravimetric water content (g g^{-1})	-0.38	*
N2	Chloride (mmol L^{-1})	Gravimetric water content (g g^{-1})	-0.33	*
N1	Chloride (mmol L^{-1})	Gravimetric water content (g g^{-1})	0.05	n.s.
N1 & S1	Organic Carbon	Sulphate	-0.68	***
	Organic Carbon	$Fe_{(aq)}$	-0.61	***
	$Fe_{(aq)}$ (mmol L^{-1})	Sulfate (mmol L^{-1})	0.56	***
	Organic Carbon (dry wt.%)	Fe_{CRS} (dry wt.%)	0.90	***
	Organic Carbon (dry wt.%)	Fe_{ox1} (dry wt.%)	0.75	***
	Organic Carbon (dry wt.%)	Fe_{ox2} (dry wt.%)	-0.85	***
	Organic Carbon (dry wt.%)	Fe_{carb} (dry wt.%)	0.67	**
	Organic Carbon (dry wt.%)	Fe_{mag} (dry wt.%)	-0.89	***

In contrast to Ice-wedge North, the $\delta^{34}S$ and $\delta^{18}O$ values of the sulfate in water from the active layer of S1 indicate primarily OWP via O_2, and some OWP via Fe^{3+}. Evidence for a mostly oxidised active layer at S1 is in the mostly low $Fe_{(aq)}$ concentration in the water from the active layer and the low water table (summer 2017). CRS and AVS concentrations at this site are low, corroborating the isotopic indications of an absence of sulfate reduction at this site. In addition, the siderite concentration is lower than at Ice-wedge North. Finally, Figure 3.2c and h show that aqueous iron and sulfate covary at this site, which is indicative of pyrite oxidation.

Across both sites, the quantity of sediment organic carbon exerts a strong control on biogeochemical processes and mineral precipitation. Firstly, Table 3.6 shows that organic carbon content is strongly positively correlated with pyrite (ρ = 0.90), siderite (ρ = 0.67) and ferrihydrite (ρ = 0.75). In addition, organic carbon content is negatively correlated with sulfate (ρ = -0.68) and aqueous iron (R = -0.61). This further supports the mechanisms discussed above, whereby in organic carbon-poor sediment, the oxidation of pyrite produces aqueous iron and sulfate that are not reduced to form authigenic pyrite and siderite, whereas in sediments rich in organic carbon, the dissolved iron and sulfate are reduced and form the minerals siderite and pyrite. Finally, sediment organic carbon content appears to influence the formation of crystalline iron (oxyhydr)oxides and magnetite. Organic carbon content is negatively correlated with Fe_{ox2} (ρ = -0.85) and Fe_{mag} (ρ = -0.89). A plausible explanation is a combination of cycling redox conditions and dissolved oxygen levels at Ice-wedge South which increase the crystallinity of ferrihydrite, coupled with an inhibition of the change from poorly crystalline ferrihydrite (Fe_{ox1}) to crystalline goethite (Fe_{ox2}) by organic compounds at Ice-wedge North (e.g., Herndon et al., 2017; Schwertmann & Murad, 1988; Amstaetter et al., 2012; Thompson et al., 2006). These significant relationships demonstrate that the quantity of sediment organic carbon exerts landscape-scale controls on the active layer and permafrost biogeochemistry.

3.3.4 Variations in pore water geochemistry due to physical processes

The biogeochemical processes discussed above are overprinted on a set of complex physical processes, including hydrological inputs to the active layer (precipitation, advection and ground ice melt; Throckmorten et al., 2016), hydrological outputs from the active layer (evaporation, freezing and advection) and the diffusion of ions from regions of high concentration to regions of low concentration. Each physical process influences the distribution of chemical constituents in the active layer and their signatures commonly overlap or mask one another. For instance, both evaporation of water and ion freeze-out from the active layer concentrate porewater chemistry and enrich the $\delta^{18}O$ and δD of the remaining water (Throckmorton et al., 2016).

Kokelj and Burn (2003, 2005) suggest that the near-surface permafrost may be a sink for soluble materials, relative to the active layer, owing to (1) leaching of soluble materials by advection of water through the active layer, (2) the migration of ions downwards along thermally-induced suction gradients in fine-grained alluvium ("cryosuction"), and (3) solute exclusion by downward freezing in sandy silt alluvium. Assuming that chloride behaves conservatively, without participating in dissolution or precipitation reactions, its concentration profile in each core can in principle be used to establish the net effect of the physical processes described above (Jessen et al., 2014). For example, a constant concentration of chloride with depth would indicate that active layer leaching, ion migration and solute exclusion are not important in the pore water chemical profiles. A variable concentration with depth would indicate that these processes are causing vertical solute transport (Jessen et al., 2014) and presumably causing concentration gradients which induce solute diffusion.

Table 3.7 Results from Welch's t-test, which was used to test whether the concentration of chloride was significantly different for permafrost (PF) versus active layer (AL) in each core. t is the t statistic, df is the degrees of freedom, p is the significance level, S.D. is the standard deviation of the mean and n is the number of samples. Asterisks indicate level of significance: $p < 0.05$ (*); $p < 0.01$ (**); $p < 0.001$ (***); not significant (n.s.).

Core	Variable	t	df	p	AL			PF			Units for mean
					mean	S.D.	*n*	mean	S.D.	*n*	
S1	chloride	0.59	11.42	n.s.	1.84	0.77	9	1.67	0.52	20	mmol L^{-1}
S2a	chloride	-6.44	28.01	***	2.39	0.81	14	12.60	8.31	28	mmol L^{-1}
S2b	chloride	-3.52	31.62	**	4.66	2.20	14	11.81	10.29	28	mmol L^{-1}
N1	chloride	-1.22	22.15	n.s.	0.75	0.52	10	1.01	0.67	23	mmol L^{-1}
N2	chloride	-1.62	31.10	n.s.	0.76	0.40	13	1.35	1.78	27	mmol L^{-1}

Figure 3.1(f-j) shows that the concentration of chloride varied with depth in all the cores, indicating that physical processes contributed to the pore water chemistry at specific depths. Welch's t-test shows that only cores S2a and S2b had a significantly higher concentration of chloride in the permafrost compared with in the active layer (Table 3.7). The lack of a significant difference between the chloride concentration of the active layer and permafrost chloride in the three other cores indicates that the active layer was not leached relative to the permafrost. The upper permafrost in Adventdalen has aggraded syngenetically (Cable et al., 2017), which means that the present-day permafrost is comprised of former active layers that have been incorporated into the permafrost with sedimentation and a rising permafrost

table. The rate of advection through the active layer has probably remained unchanged as permafrost has aggraded. In contrast to these cores, cores S2a and S2b have significantly more concentrated chloride in the permafrost compared with the active layer, and the chloride concentration in their active layer is greater than in the other cores. This indicates either that there is an additional source of chloride to these cores, or that the rate of advection is lower in these sediments, both in the current and former active layers. The additional chloride in these cores could originate by diffusion from the underlying deltaic sediments (5 metres below the top of permafrost). Nearby cores display an increase in chloride concentration from a mean of ~1 mmol L^{-1} in the loess sediments (down to 2 m below top of permafrost) to a mean of ~68 mmol L^{-1} in the deltaic sediments (5 to 10 m below top of permafrost) (Cable et al., 2017). Diffusion upwards from these marine sediments may enhance the pore water chloride concentration at shallower depths in some locations, although the reasons for the location-specific diffusion are not clear. The data do not enable enhanced chloride concentration due to upward diffusion to be distinguished from enhanced chloride concentration due to low advection rates. However, far greater rates of advection are likely at Ice-wedge North on account of the spring-fed hydrologic regime and high water content.

Solute exclusion by downward freezing results in the accumulation of solutes at the base of the active layer (Kokelj & Burn, 2005). S1, N1 and S2b show increased chloride in pore water at the base of the active layer (Figure 3.1f, h and j). This accumulation may be enhanced by the additional migration of chloride ions downwards along thermally-induced suction gradients. An additional effect of this would be that zones of solute enrichment correspond to locations of ice enrichment (Kokelj & Burn, 2005). Evaluation of the variation between chloride concentration and gravimetric water content for each core reveal that there was a significant ($p < 0.05$) weak to medium strength (ρ = -0.33 to -0.63) negative relationship between these two variables in cores S1, S2b and N2 (Table 3.7). The absence of this observation in the other cores indicates that it is solute exclusion by downward freezing, rather than cryosuction, that concentrates chloride in pore water at the base of the active layer. The medium strength negative correlation between water content and chloride concentration in core S1 suggests that evaporation contributes to the chloride concentration in this core, but the low ρ value suggests that this is not an important process. The weak

negative correlation between water content and chloride concentration in cores S2b and N2 implies a minor role for evaporation in concentrating chloride in the pore water, but the very low ρ values again suggest that this process is not important.

In summary, the active layer is not leached relative to the permafrost, except in cores S2a and S2b, where upwards diffusion of chloride from marine sediments may occur. Furthermore, three cores (S1, N1 and S2b) have experienced solute exclusion by downward freezing of the active layer, but cryosuction seems unimportant for vertical migration of ions in all cores. However, the variability in chloride concentration with depth confirms a complex contribution of physical processes in the observed pore water profiles. Despite the additional complexity of these physical processes, the use of covariances between ions has enabled the dominant biogeochemical processes in Adventdalen to be elucidated.

3.4 Conclusions

The evidence presented in this chapter demonstrates that the accumulation of organic carbon in the continuous permafrost of a deglaciated high Arctic valley regulates the biogeochemical processes across this landscape. Signals of pyrite oxidation were more pronounced in the dry, organic-poor sediments to the south of the Adventelva braided river, whereas the groundwater-fed, organic-rich sediments to the north of Adventelva displayed clear signs of iron- and sulfate-reduction, pyrite precipitation and siderite precipitation. As air temperatures continue to rise in the high Arctic and active layer depths increase, there are likely to be major changes in the iron, sulfur and carbon cycling in this valley, depending on how permafrost thaw impacts the geomorphology and hydrology of the ice-wedge polygonal terrain.

Chapter 4. Interacting Hydrogeomorphology and Biogeochemistry in a High Arctic Permafrost Setting

The previous chapter examined the biogeochemical processes occurring in low-centred ice-wedge polygons situated on fjord valley infill sediments. This chapter follows with a comparison of the biogeochemistry of a high-centred, degraded ice-wedge polygon situated between raised beaches and the biogeochemistry of low-centred ice-wedge polygons situated on fjord valley infill sediments.

4.1 Introduction

Low-relief wetlands cover a substantial area of the pan-Arctic landscape (<400 000 km^2; Walker et al., 2005). In the high Arctic, the formation of wetlands in the polar desert depends on a reliable water supply during the thaw season, as water-saturated surface conditions are required to form wetlands and peatlands (Martini & Glooschenko, 1985; Woo & Young, 2006). The water supply may be from groundwater, streams and ponds, snowbanks or coastal water. The geomorphology of the landscape directly affects its hydrology (Mitsch & Gosselink, 2007) and the topographical setting of a wetland governs the inflows and outflows of water (Woo & Young, 2006). Topographical settings that receive an ample supply of water include depressions that have water inputs from drainage and a high retention of water, valley bottoms that receive both surface and ground water inflows, any slope below a late-lying snowbank that receives sustained meltwater runoff for an extended period, and many streambanks and shorelines that experience frequent inundation (Woo & Young, 2006). In recently-glaciated regions of the high Arctic, the topography is modified by isostatic rebound, periglacial and fluvial processes, all of which control the setting in which wetlands develop (Woo & Young, 2006). Raised beaches, which are formed during postglacial isostatic rebound, are widespread along the coasts of Svalbard (e.g., Forman et al., 2004; Salvigsen et al., 2005) and other high Arctic coasts (Funder et al., 2011; Nielsen et al., 2017; Dyke et al., 1997). Studies in Arctic Canada have found that peat commonly develops in the wetlands between raised beaches (Martini & Glooschenko, 1985), and this peat becomes older and more developed further inland from the coast (Price & Woo, 1988). Studies of coastal peat

development on Svalbard are rare (e.g., Rozema et al., 2006) and there have not been any studies focussing on wetlands and peat development between raised beaches in Svalbard.

While postglacial isostatic rebound conditions the landscape in which wetlands and peatlands form, smaller-scale landforms, such as ice-wedge polygons, play a role in the site-specific hydrology (e.g., Liljedahl et al., 2012). In permafrost regions, the most easily identifiable landforms are ice-wedge polygons (Christiansen et al., 2016), and ~250 000 km^2 of the Arctic is covered by polygon tundra (Minke et al., 2007). There are two main types of ice-wedge polygon: low-centred and high-centred. The formation of ice-wedges occurs when plummeting temperatures during winter cause the ground to cool and contract, resulting in thermal contraction cracks (Leffingwell, 1915; Lachenbruch, 1962). Snowmelt infiltrates the cracks, and when the temperature drops, the water refreezes and expands, widening the cracks. As the tensile strength of ice is lower than that of sediment, in subsequent years, cracking recurs in the ice (Lachenbruch, 1962; Mackay, 1984). Over centuries to millennia, ice-wedges form, owing to the continued cycle of cracking, infilling and refreezing. The formation of ice-wedges causes deformation of the surrounding sediment, resulting in the distinctive surface microtopography of low-centred polygons, with elevated rims along the polygon edges (Liljedahl et al., 2016). The small-scale variations in the ground surface microtopography associated with ice-wedge polygons regulate the landscape hydrology (Liljedahl et al., 2012). For example, the rims of low-centred polygons serve as hydrologic barriers, resulting in the centres of low-centred polygons flooding temporarily or continuously during the summer (Liljedahl, 2011).

Ice-wedges are vulnerable to climate change (Jorgenson et al., 2015). In Alaska, for example, as air temperatures have risen, the degradation of ice wedges has increased over the past three decades (Jorgenson et al., 2006; Liljedahl et al., 2016; Raynolds et al., 2014). As the near surface permafrost thaws and ice-wedges melt, the result is differential ground subsidence (Liljedahl, 2011). This causes the troughs to subside and the polygon rims to collapse into the troughs, resulting in the polygons becoming flat-centred and then eventually high-centred. While many field studies have observed an increase in inundation and active layer thickness due to permafrost degradation (Olefeldt et al., 2013, and references therein), permafrost thaw can instead result in landscape drying, as drainage channels created by the loss of

ground ice take water away from wetlands (Godin et al., 2016). The complete transformation of low-centred polygons to high-centred polygons has hydrologic implications, which are that the centres of high-centred polygons are well-drained and the connected troughs form a drainage system, causing an overall landscape drying (Figure 4.1; Liljedahl et al., 2016).

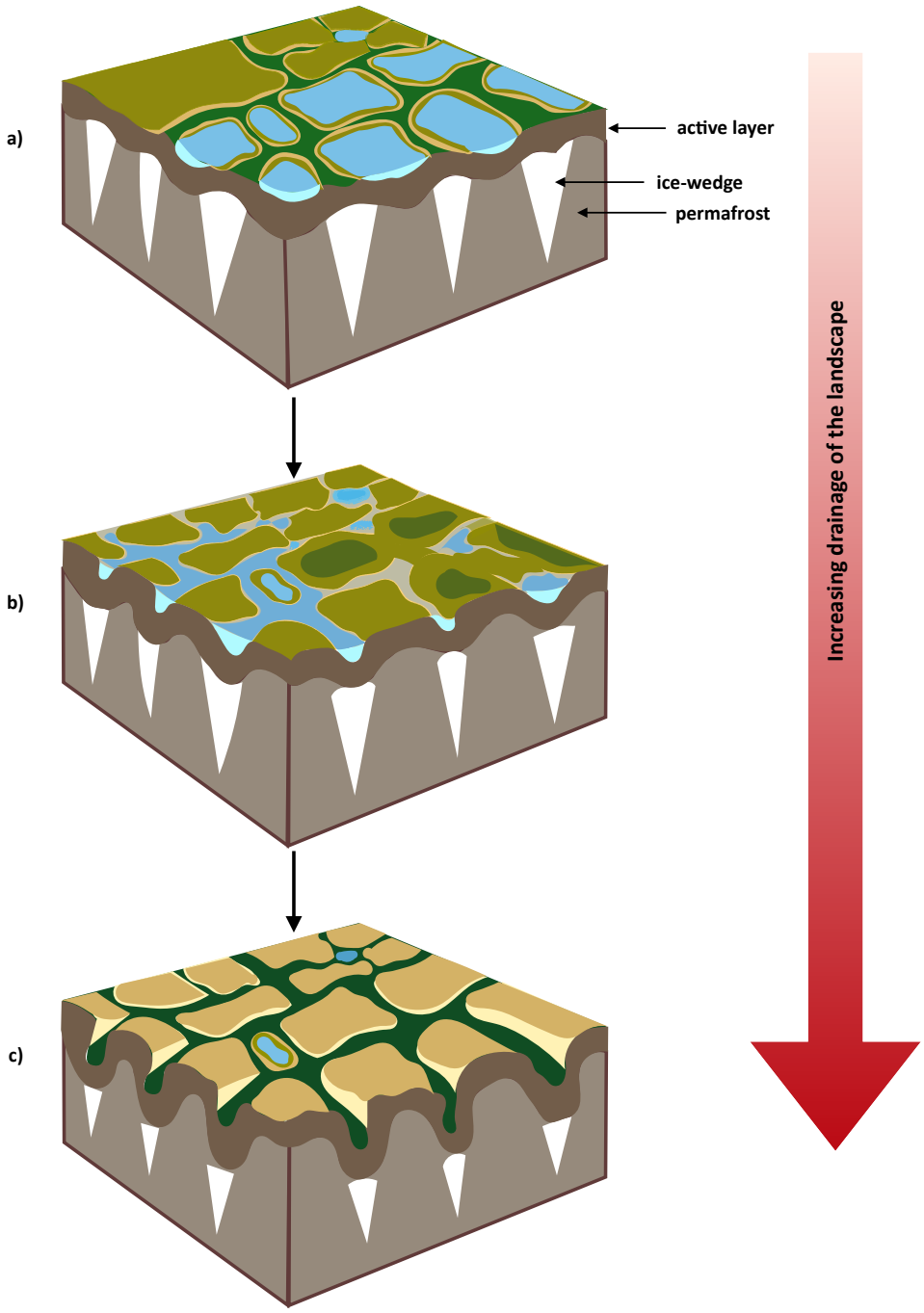

Figure 4.1 A schematic diagram of the hydrologic impacts of ice-wedge polygon degradation, showing the transformation from **a)** undegraded polygons, with inundated low-centred polygons, through **b)** an initial degradation stage, with the ice wedge tops melting and the troughs becoming disconnected from each other, around either low- or high-centred polygons and **c)** an advanced stage of degradation, with high-centred polygons and well-connected troughs that form a drainage network and cause an overall drying of the polygonal landscape. Figure modified after Liljedahl et al. (2016).

Ice-wedge polygon degradation influences the pathways of decomposition of organic carbon, with implications for the types of greenhouse gas released from thawing permafrost (Wainwright et al., 2015; Lara et al., 2015; Sachs et al., 2010). Low-centred polygons are linked with a higher summer methane flux, owing to their higher temperature, moister soil,

frequently higher proportion of vascular plants and higher concentrations of aqueous total organic carbon (Lara et al., 2015; Sachs et al., 2010; Wainwright et al., 2015). Numerous studies at the Barrow Environmental Observatory, Alaska, have observed decreases in methane emissions with permafrost degradation in ice-wedge polygon terrain. For instance, Vaughn et al. (2016) found that permafrost degradation caused local decreases in tundra methane emissions in ice-wedge polygon terrain. This was supported by findings from Wainwright et al. (2015), who used a multiscale zonation approach to show that low-centred polygons had a higher flux of methane than other polygon types. On Samoylov Island, in the southern central Lena River Delta, Sachs et al. (2010) also found higher methane fluxes from low-centred polygons than high-centred polygons. In comparison, there is less consensus on the effect of polygon degradation on carbon dioxide fluxes: while the lower soil moisture and decreased cover of vascular plants may result in increased carbon dioxide emissions (Wainwright et al., 2015), once plant growth in the peak growing season is accounted for, a net drawdown of carbon dioxide is observed in high-centred polygons (Lara et al., 2015). Finally, these studies have tended to focus on greenhouse gas emissions under ice-wedge polygon degradation, but further work is needed to elucidate the underlying biogeochemical processes leading to greenhouse gas emissions.

There is clear evidence that ice-wedge polygon degradation is increasing in response to rising air temperatures in Alaska. In contrast, by comparing aerial photographs from 1948 to 2015 of Adventdalen, Svalbard, Pirk et al. (2017a) found no striking ice-wedge degradation at Ice-wedge South. The absence of dramatic degradation at this site indicates that ice-wedge degradation has not yet been triggered by the gradual increase in air temperature. As temperature and precipitation in Svalbard are predicted to further increase (Førland et al. 2011) it becomes more likely that degradation of low-centred ice-wedge polygons in Svalbard will occur. The aim of this chapter is to characterise the dominant biogeochemical processes occurring in a high-centred polygon situated between raised beaches in Svalbard. The low-centred polygons of Ice-wedge North are discussed in this chapter as a reference site, providing a basis for comparison.

4.2 Results

The active layer depths at N1 and N2 (Ice-wedge North, low-centred polygons) were similar (63 and 65 cm, respectively; Table 4.1), yet the active layer at R1a and R1b (Revneset, high-centred polygon) was shallower (36 cm; Table 4.1). While the water table depth was shallow at both N1 and N2 (3 and 0 cm below the ground surface, respectively; Table 4.1), the water table depth at R1a and R1b was much lower (31 cm below the ground surface; Table 4.1). Figure 4.2a shows that the water from the active layer at each site formed a distinct group on a $\delta^{18}O$-$\delta^{2}H$ plot. The water from the active layer of Revneset was more enriched in ^{2}H and ^{18}O than the samples from Ice-wedge North. Figure 4.2b shows that the water from the active layer of Ice-wedge North had a greater d-excess relative to the GMWL than the water from the active layer of Revneset. Figure 4.2c shows that few samples from Revneset and Ice-wedge North have a d-excess relative to the LMWL, and some samples from both sites have a d-excess below -5.98, indicating enrichment of these samples in the heavy isotopes.

Table 4.1 Active layer and water table depths at the end of the thaw season in 2017 at Ice-wedge North (N1 and N2) and Revneset (R1a and R1b). Active layer depths are presented as a mean of three measurements within each polygon, with the minmum and maximum depth of each polygon active layer in brackets, and water table is one measurement, taken at the point of water sampling from the active layer.

Site	Date	Active layer depth (cm)	Water table depth below ground surface (cm)
N1	31/08/2017	63.3 (60.0-65.0)	3
N2	02/09/2017	64.7 (62.0-68.0)	0
R1a and R1b	05/09/2017	36.0 (34.0-39.0)	31

All the cores from Ice-wedge North and Revneset contained a high organic carbon content at specific depths (Figure 4.3). N2 had the highest organic carbon content at the surface (45 dry weight percent; Figure 4.3b), a minimum organic carbon content at 61 cm depth (5 dry weight percent), and a further peak in organic carbon content between 61 and 132 cm depth. N1 had a slightly lower organic carbon content (Figure 4.3a), but the trends with depth were similar to N2, in that the surface had a high organic carbon content (30 dry weight percent), the organic carbon content decreased with depth to 67 cm depth (1.84 dry weight percent), and between 83 and 147 cm depth, the organic carbon peaked again. R1a had a high organic carbon content at the surface (38 dry weight percent; Figure 4.3c), which decreased to a

minimum at 45 cm depth (13 dry weight percent), increased to a maximum between 45 and 109 cm depth, and finally was generally very low (~0.5 dry weight percent) below 109 cm depth. The profile from R1b was at a lower depth resolution, but clearly indicated a higher organic carbon content in the active layer and upper permafrost, compared to the lower permafrost (Figure 4.3d).

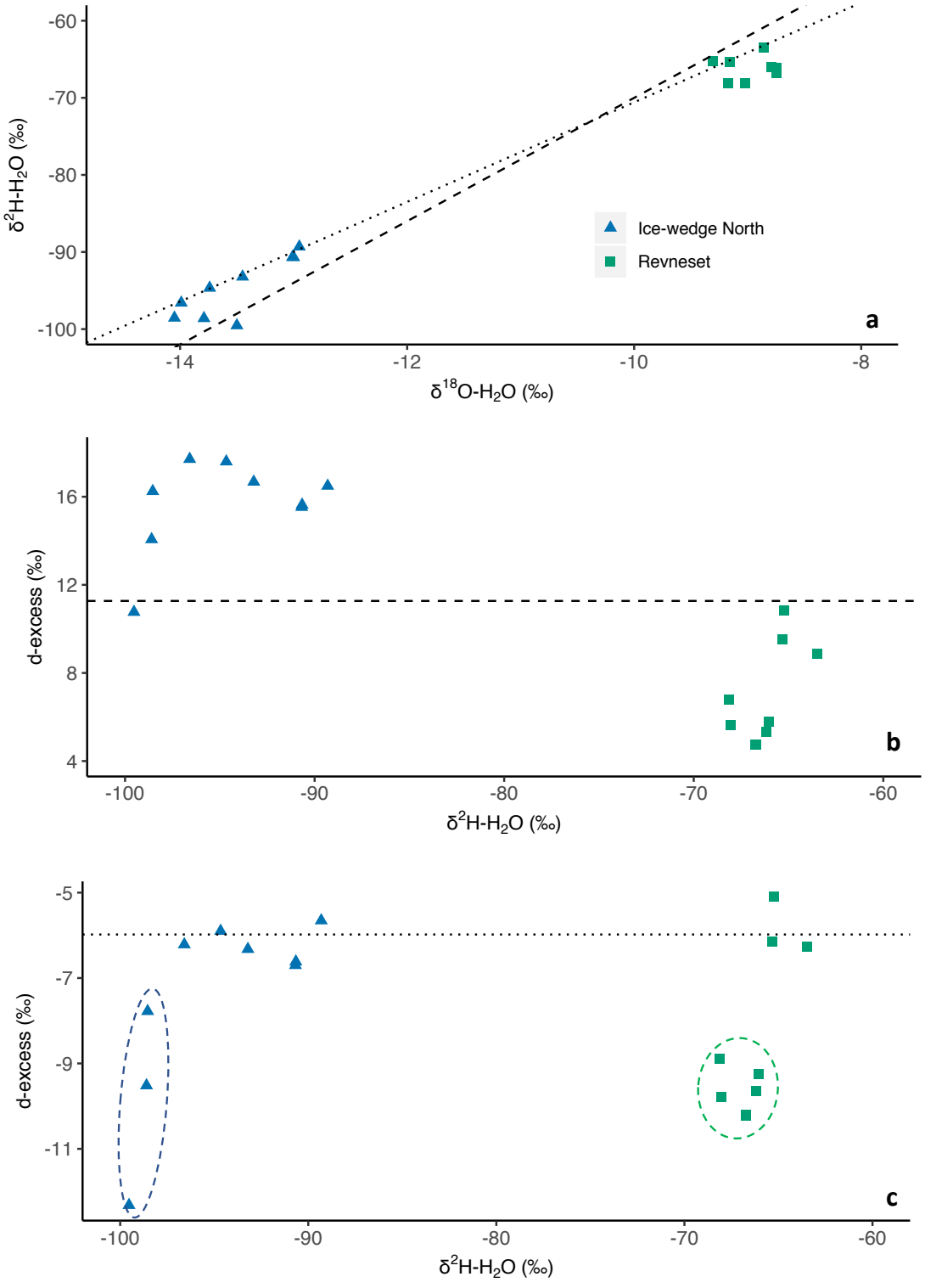

Figure 4.2 Water from the active layer of Ice-wedge North and Revneset: a) δ^{18}O-H2O and δ^{2}H-H2O, with the Global Meteoric Water Line (GMWL; dashed line) and the Local Meteoric Water Line from Isfjord Radio (LMWL; dotted line), b) deuterium excess (d-excess) based on the GMWL and δ^{2}H-H_2O, with a horizonal dashed line at d-excess = 11.27 (Equation 2.8), and c) deuterium excess (d-excess) based on the LMWL and δ^{2}H-H_2O, with a horizonal dashed line at d-excess = -5.98 (Equation 2.9). The blue dashed line (oval) encompasses samples from 60 cm depth at Ice-wedge North. The green dashed line (oval) encompasses samples from 20 and 30 cm depth at Revneset.

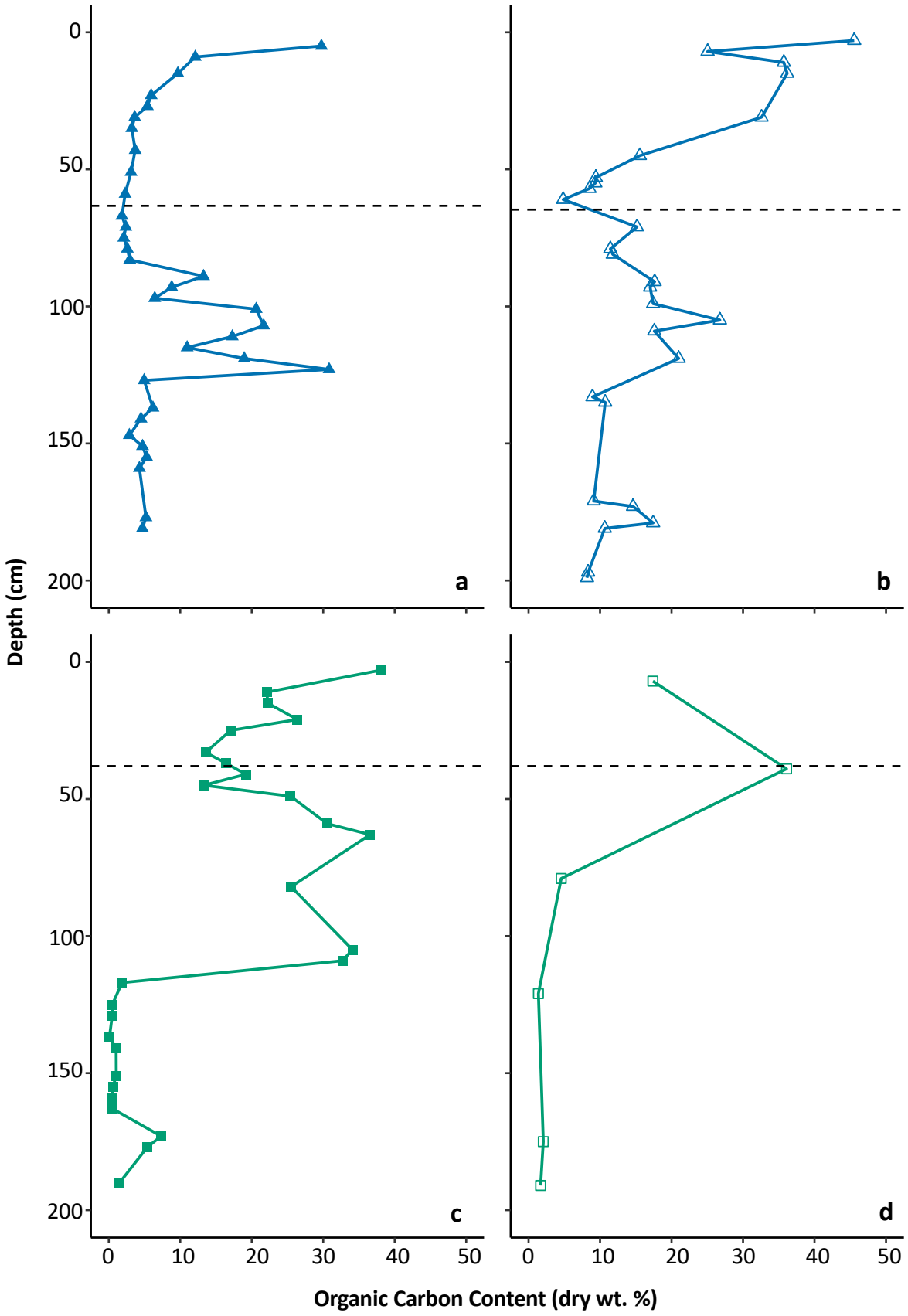

Figure 4.3 Organic carbon content with depth in cores a) N1, b) N2, c) R1a and d) R1b. The horizontal dashed line on each plot shows the active layer depth at the end of the thaw season in 2017.

Table 4.2 shows that the dominant iron phase at Revneset was ferrihydrite (Fe_{ox1}), whereas there were lower amounts of pyrite and siderite (CRS and Fe_{carb}) at this site. In contrast, the sediments at Ice-wedge North contained more pyrite and siderite, but less ferrihydrite (Table 4.2). Revneset contained more crystalline iron (oxyhydr)oxides (Fe_{ox2}) than Ice-wedge North (Table 4.2), and the amounts of magnetite (Fe_{mag}) at both sites were variable, with the Ice-wedge North sediments containing slightly more magnetite overall. Concentrations of acid-volatile sulfur (AVS) were low at both sites (Table 4.2).

Table 4.2 Summary statistics for the solid phase data from Revneset and Ice-wedge North including AVS, CRS, Fe_{ox1}, Fe_{ox2}, Fe_{carb}, Fe_{mag}, and organic carbon.

			Ice-wedge North		Revneset	
Unit			N1	N2	R1a	R1b
AVS	dry wt. %	mean	0.02	na	0.007	na
		(min-max)	*(0.00-0.05)*	na	*(0.00-0.04)*	na
		n	7	na	8	na
CRS	dry wt. %	mean	0.12	na	0.077	na
		(min-max)	*(0.02-0.27)*	na	*(0.017-0.16)*	na
		n	7	na	8	na
Fe_{ox1}	dry wt. %	mean	0.97	na	1.04	na
		(min-max)	*(0.32-1.64)*	na	*(0.18-3.26)*	na
		n	10	na	8	na
Fe_{ox2}	dry wt. %	mean	0.13	na	0.31	na
		(min-max)	*(0.05-0.32)*	na	*(0.05-1.19)*	na
		n	10	na	8	na
Fe_{carb}	dry wt. %	mean	1.00	na	0.42	na
		(min-max)	*(0.38-1.57)*	na	*(0.16-0.81)*	na
		n	10	na	8	na
Fe_{mag}	dry wt. %	mean	1.58	na	0.52	na
		(min-max)	*(0.55-3.43)*	na	*(0.05-2.10)*	na
		n	10	na	8	na
Organic Carbon	dry wt. %	mean	8.55	16.7	14.6	10.5
		(min-max)	*(1.84-30.82)*	*(4.83-45.55)*	*(0.09-38.1)*	*(1.38-36.1)*
		n	33	29	27	6

The concentrations of $Fe_{(aq)}$ in cores R1a and R1b were low (<0.7 mmol l^{-1}; Figure 4.4c and d). In R1a, the concentrations of $Fe_{(aq)}$ were low but variable down to 117 cm, below which $Fe_{(aq)}$ concentrations were negligible until 173 cm, where a small peak in $Fe_{(aq)}$ was detected. The decrease in $Fe_{(aq)}$ occurred at a more shallow depth in R1b (75 cm) and concentrations of $Fe_{(aq)}$ remained low below this depth. The concentrations of $Fe_{(aq)}$ in N1 reached over 1.5 mmol L^{-1}

(~150 cm depth; Figure 4.4a), but many samples contained negligible $Fe_{(aq)}$. N2 had the highest concentrations of $Fe_{(aq)}$, reaching 3 mmol L^{-1} at the base of the core (Figure 4.4b). However, the rest of the core had lower, but variable, $Fe_{(aq)}$ concentrations, with no trend with depth.

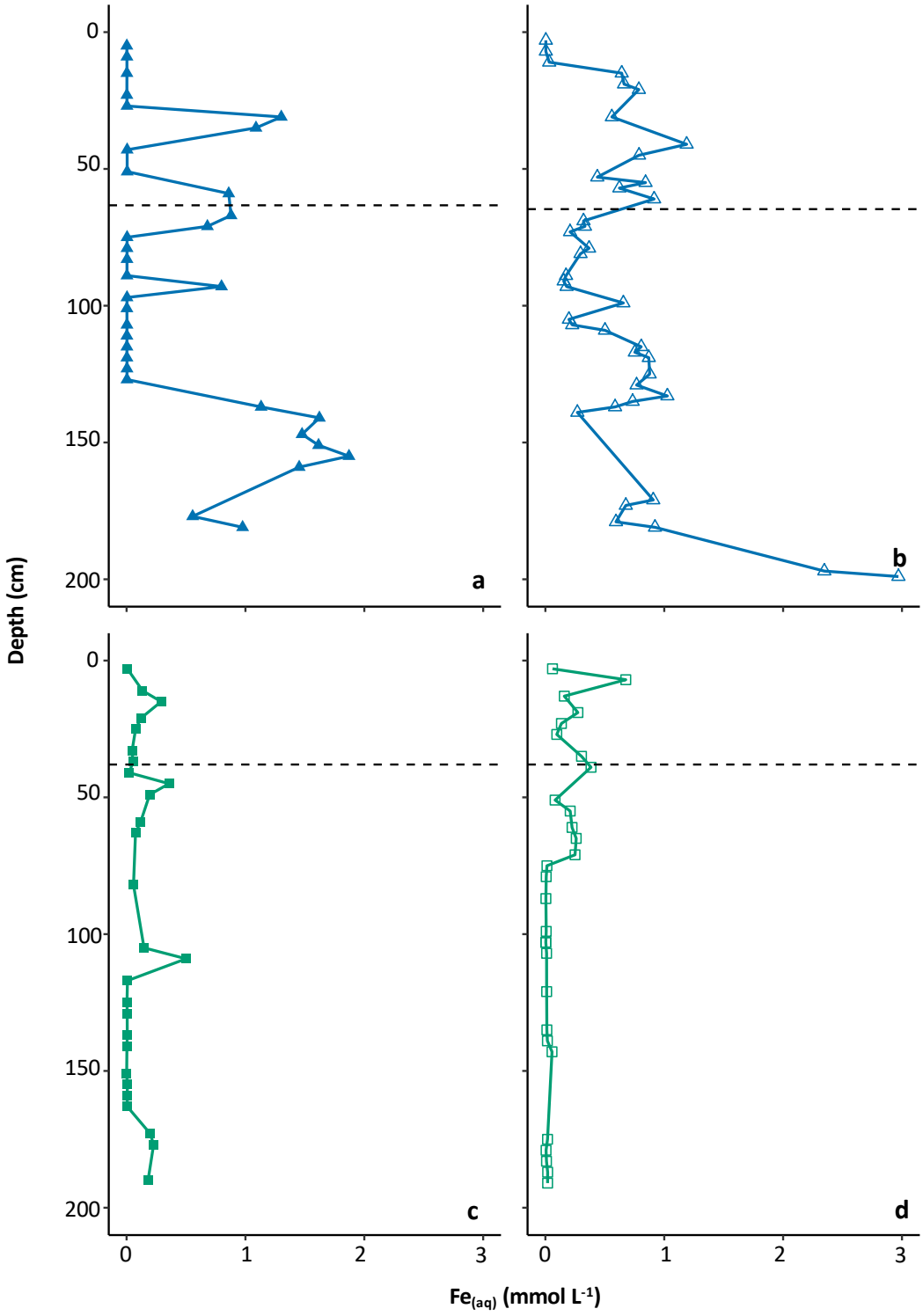

Figure 4.4 Aqueous iron ($Fe_{(aq)}$) with depth in cores **a)** N1, **b)** N2, **c)** R1a and **d)** R1b. The horizontal dashed line on each plot shows the active layer depth at the end of the thaw season in 2017.

The concentrations of $Mn_{(aq)}$ were <0.15 mmol L^{-1} in all the cores from Ice-wedge North and Revneset (Figure 4.4). Notable characteristics of the concentration profiles are that N1 displayed a peak in $Mn_{(aq)}$ at the active layer base (Figure 4.4a), N2 displayed a peak in $Mn_{(aq)}$ close to the ground surface (Figure 4.4b), R1a displayed an increase in $Mn_{(aq)}$ below 100 cm

depth (Figure 4.4c), and R1b displayed a peak in $Mn_{(aq)}$ close to the ground surface (Figure 4.4d).

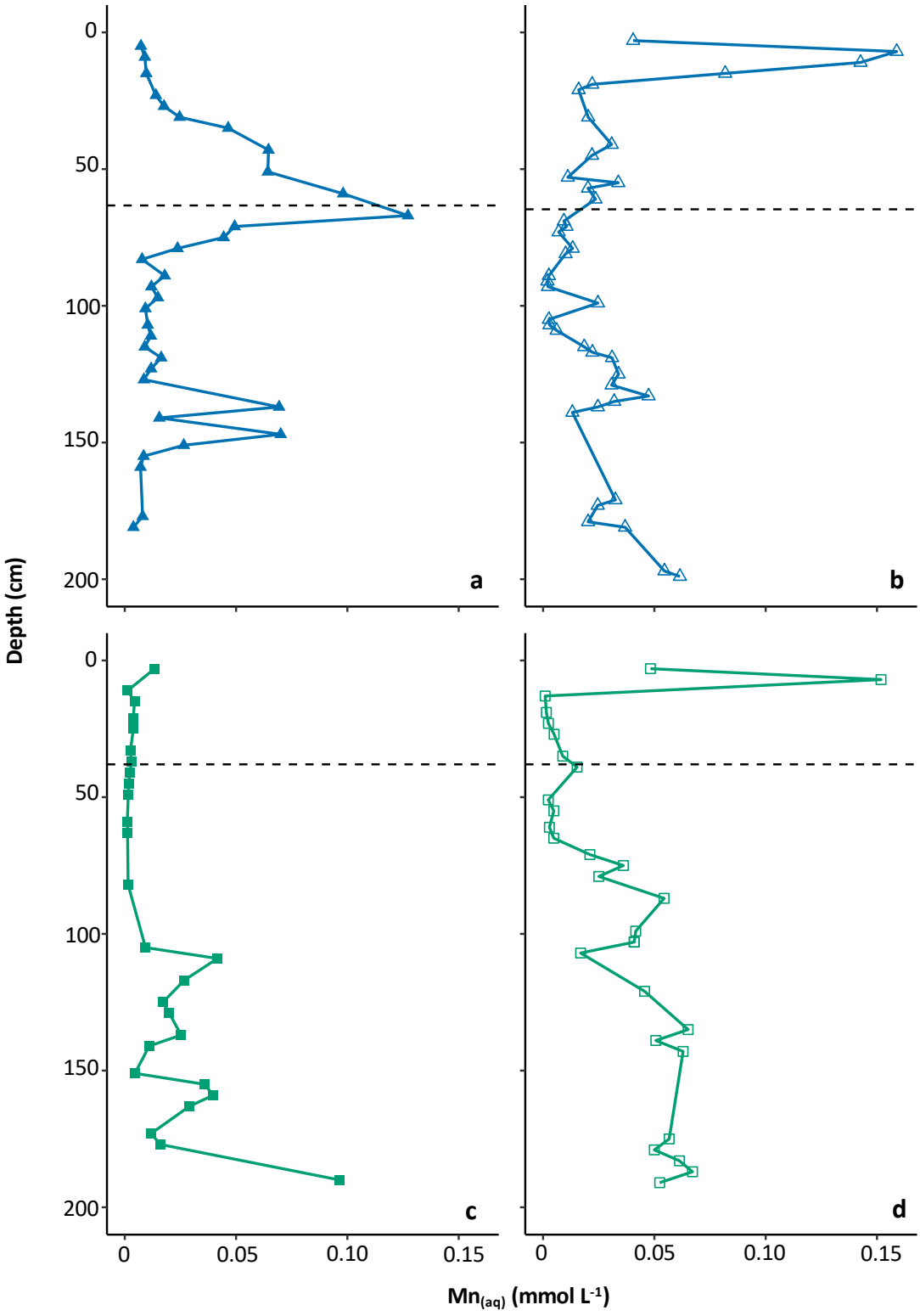

Figure 4.5 Aqueous manganese ($Mn_{(aq)}$) with depth in cores **a)** N1, **b)** N2, **c)** R1a and **d)** R1b. The horizontal dashed line on each plot shows the active layer depth at the end of the thaw season in 2017.

Sulfate concentrations in N1 were generally <2 mmol L^{-1}, but the sulfate concentration peaked at >4 mmol L^{-1} at the base of the active layer (Figure 4.6a). The sulfate concentrations in N2

were the most consistently low of the four cores compared here; the sulfate concentrations only rose above 1 mmol L^{-1} in one sample point (Figure 4.6b). Sulfate concentrations in R1a were <0.30 mmol L^{-1} down to 105 cm depth, below which sulfate concentrations increased, but remained variable, rising over 6 mmol L^{-1} at the core base (Figure 4.6c). Sulfate concentrations in R1b were similarly low in the shallow sediments, but increased below 75 cm, although concentrations in this core were always <4 mmol L^{-1} (Figure 4.6d). Figure 4.7 shows the $\delta^{34}S\text{-}SO_4^{2-}$ and $\delta^{18}O\text{-}SO_4^{2-}$ of water from the active layer of Ice-wedge South, Ice-wedge North and Revneset in $\delta^{34}S\text{-}\delta^{18}O$ isotope space. This figure demonstrates that sulfate reduction occurred in water in the active layer at Ice-wedge North and Revneset.

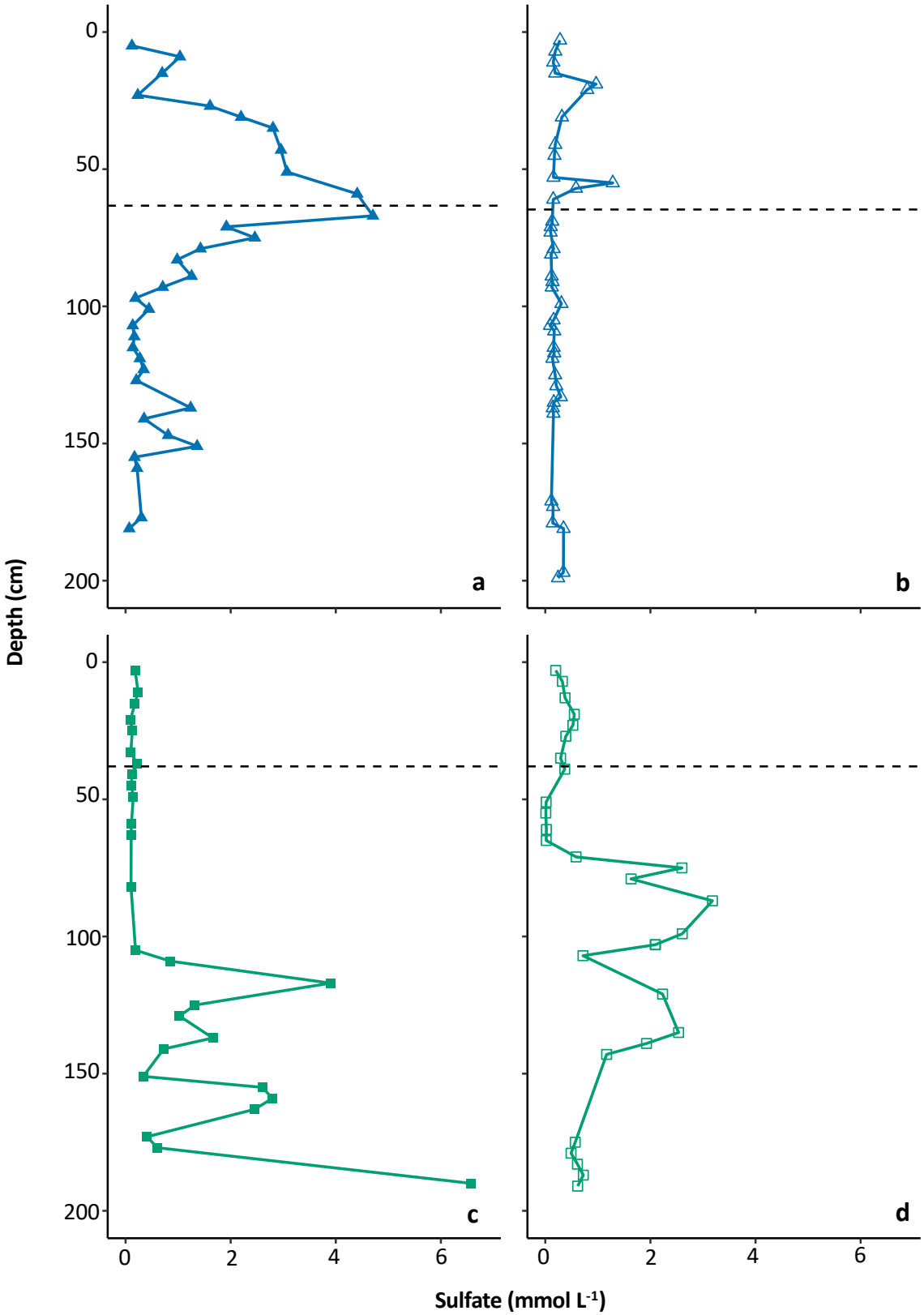

Figure 4.6 Sulfate with depth in cores **a)** N1, **b)** N2, **c)** R1a and **d)** R1b. The horizontal dashed line on each plot shows the active layer depth at the end of the thaw season in 2017.

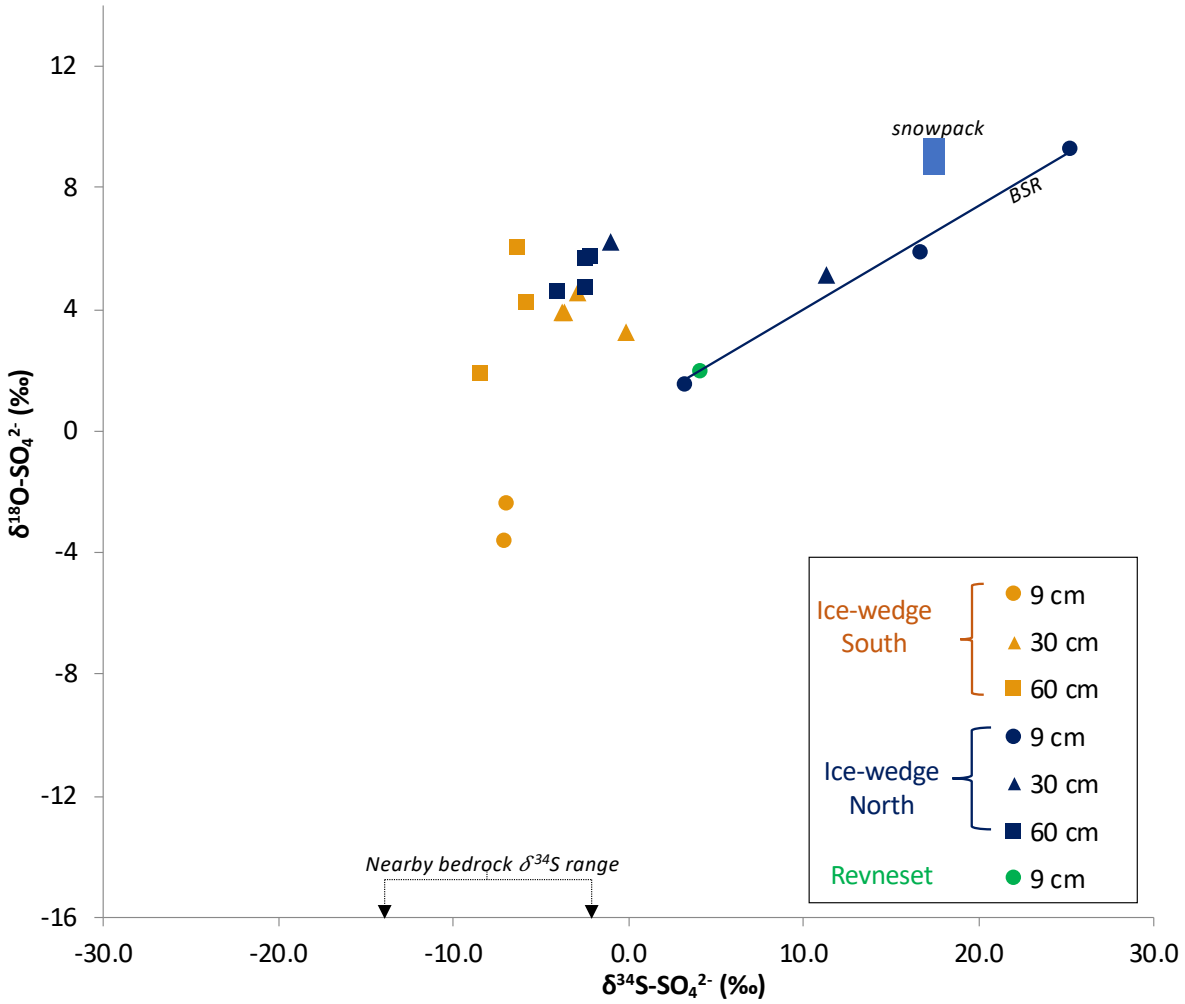

Figure 4.7 Water samples from the active layer of Ice-wedge South, Ice-wedge North and Revneset in $\delta^{18}O\text{-}SO_4$ and $\delta^{34}S\text{-}SO_4$ isotope space. The blue box represents the isotopic range of pre-melt snowpacks in Svalbard at Midtre Lovenbreen (Wynn et al., 2006) and near Ny Ålesund (Tye & Heaton, 2007). The solid blue line is a regression line illustrating BSR (R^2 = 0.98). The nearby bedrock range is of the mass-weighted mean sulfide $\delta^{34}S$ in the Firkanten and Carolinefjellet Formations (Dixon, 2020).

Overall, Figure 4.8 shows that chloride concentrations were low (<3 mmol L^{-1}), except for at the base of N2, where they increased to over 9 mmol L^{-1}. Despite the low concentrations, it is clear from Figure 4.8 that the concentration of chloride varied with depth in the cores. In core N2, the clearest variation was in the core base, where the concentration of chloride increased rapidly with depth (Figure 4.8b). N1 had no such increase in chloride at its base, but concentrations were variable up to 3 mmol L^{-1}, with the highest chloride concentrations in the upper permafrost (Figure 4.8a). R1a had a variable chloride concentration with depth, but no trend in chloride concentration with depth (Figure 4.8c). Table 4.3 shows that R1b had significantly lower chloride concentrations in the permafrost compared to the active layer.

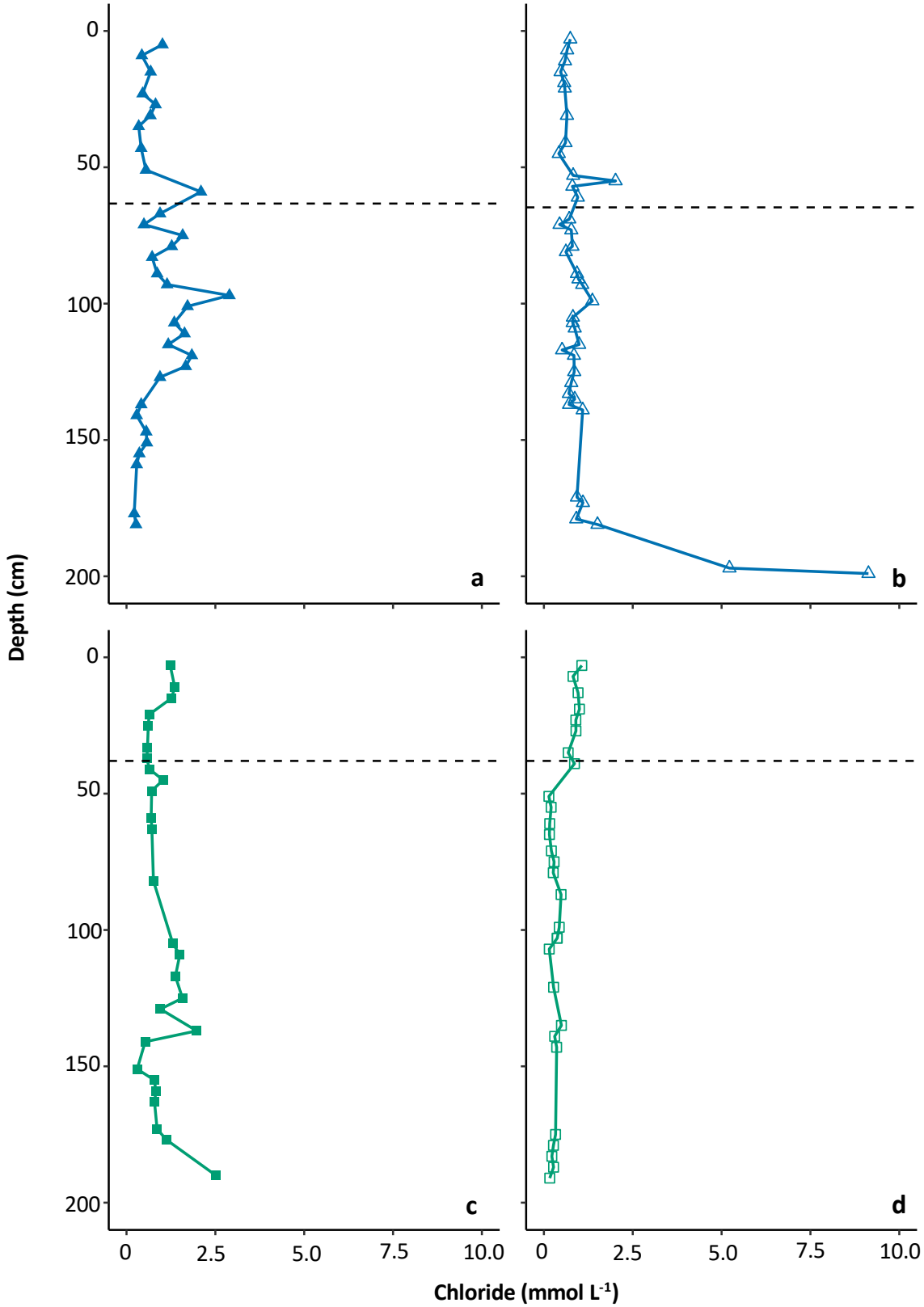

Figure 4.8 Chloride with depth in cores **a)** N1, **b)** N2, **c)** R1a and **d)** R1b. The horizontal dashed line on each plot shows the active layer depth at the end of the thaw season in 2017.

Table 4.3 Results from Welch's t-test, which was used to test whether the concentration of chloride was significantly different for permafrost (PF) versus active layer (AL) in each core. t is the t statistic, df is the degrees of freedom, p is the significance level, S.D. is the standard deviation of the mean and n is the number of samples. Asterisks indicate level of significance: $p < 0.05$ (*); $p < 0.01$ (**); $p < 0.001$ (***); not significant (n.s.).

Core	Variable	t	df	p-value	AL			PF			Units for mean
					mean	S.D.	*n*	mean	S.D.	*n*	
N1	chloride	-1.22	22.15	n.s.	0.75	0.52	10	1.01	0.67	23	mmol L^{-1}
N2	chloride	-1.62	31.10	n.s.	0.76	0.40	13	1.35	1.78	27	mmol L^{-1}
R1a	chloride	-0.66	12.97	n.s.	0.89	0.37	7.00	1.01	0.53	20	mmol L^{-1}
R1b	chloride	9.70	21.7	***	0.91	0.13	7.00	0.33	0.16	22	mmol L^{-1}

4.3 Discussion

4.3.1 Sources of water to the active layer

Figure 4.2a shows that water in the active layer of Revneset was more enriched in ^{2}H and ^{18}O than water in the active layer of Ice-wedge North. This indicates that the primary water source to the active layer of Revneset was summer precipitation, whereas the primary water source to the active layer of Ice-wedge North was winter precipitation (e.g., Ala-aho et al., 2018; Throckmorton et al., 2016). This inference is supported by analysis of the deuterium-excess ("d-excess") in water from the active layer, relative to the GMWL (Equation 2.8). The d-excess in precipitation over Svalbard displays a strong seasonality (Frankenberg et al., 2009). Winter precipitation has high d-excess values, owing to a strong kinetic effect as evaporation occurs from local source regions with contrasting air and sea temperature. In comparison, summer precipitation has a lower d-excess, due to a stronger influence from moisture evaporated from the warmer North Atlantic below 50 °N (Frankenberg et al., 2009). Figure 4.2b shows that all the samples from Ice-wedge North, except one, have a d-excess relative to the GMWL, indicating that they were principally sourced from winter precipitation. This is corroborated by field observations of snowmelt-fed springs providing water to Ice-wedge North from the adjacent mountains. The samples from Revneset generally had a lower d-excess relative to the GMWL, indicating that the principal water source to this site was summer precipitation. This was unexpected because a nivation hollow was observed to cut into the raised beach sediments upslope of the high-centred polygon, leading to the expectation that snowmelt

contributed to water in the active layer. However, the snow accumulation at this site is markedly lower than in the mountains, largely due to wind removal during winter.

Throckmorton et al. (2016) argue that snowmelt is unlikely to be an important contributor to water in the active layer, as during peak snowmelt, the active layer is poorly developed, so snow melt runs off quickly into larger stream channels. This could be particularly true for a wind-exposed (cold) high-centred ice-wedge polygon, such as that studied at Revneset. Despite the assertion that snowmelt occurred before significant active layer development, the active layers at Ice-wedge North preserve a signature of winter precipitation (snow). This is difficult to reconcile with the paradigm of a poorly-developed active layer during snowmelt, but it may be related both to the continuous supply of snowmelt from the mountains, which would melt later than snow at a (warmer) lower elevation close to the raised beaches and sustain a water supply all summer. The thicker active layer at Ice-wedge North (Table 4.1) may be indicative of more rapid active layer thaw at Ice-wedge North compared to at Revneset, meaning that snowmelt was more likely to percolate into the Ice-wedge North active layer than the Revneset active layer. In addition, water flow through peat typically occurs mainly in the upper, seasonally aerobic layer ("acrotelm"), and in the deeper, permanently anaerobic layer ("carotelm"), there is only a very low thoughflow (Damman, 1986; Kolka et al., 2015). Hence, the rate of water flow through the unsaturated sediments of Revneset may be greater than the water flow through the saturated sediments of Ice-wedge North, meaning that the isotopic signature of snowmelt would be lost more quickly from the water in the active layer of Revneset.

Calculating a d-excess of the samples using the LMWL (Equation 2.9) tests whether modifications have occurred since precipitation (summer or winter) reached the active layer. Water left behind by evaporation is more enriched in the heavy isotopes relative to the LMWL and a d-excess value below -5.98 may indicate that evaporation has affected the sample (Ala-aho et al., 2018). Figure 4.2c shows that some samples from Ice-wedge North and Revneset have d-excess values below -5.98. However, those samples with the most negative d-excess values (blue and green dashed line ovals; Figure 4c) are from deeper in the active layer (60 cm depth at Ice-wedge North and 20 to 30 cm depth at Revneset). It is unlikely that evaporation has a stronger influence on waters from the deeper active layer relative to waters

from the shallow active layer. In addition, studies near Barrow (on the coastal plain of Alaska) found that evaporation effects are more significant in early summer to midsummer, with these effects diminishing after midsummer (Throckmorton et al., 2016; Koch et al., 2014). It is probable that a similar seasonal pattern in evaporation occurs in Adventdalen and Revneset. An alternative explanation to evaporation for those samples with a low d-excess is that seasonal ice melt contributed water to the deeper active layer (e.g., Throckmorton et al., 2016). As water freezes, water molecules containing the heavier isotopes (deuterium and oxygen-18) preferentially freeze out of solution, leaving their lighter isotopic counterparts in the unfrozen water (Throckmorton et al., 2016). This is freeze-out fractionation and results in active layer and shallow permafrost ice enriched in deuterium and oxygen-18, with a d-excess below -5.98. Towards the end of summer, as the active layer deepens, melting of this ice results in water with a low d-excess, such as that observed in the deeper active layers of Ice-wedge North and Revneset. Overall, then, the δ^2H-H_2O and δ^{18}O-H_2O of the water in the active layer of Revneset and Ice-wedge North indicated that the primary water source to Ice-wedge North was winter precipitation, whereas the primary water source to Revneset was summer precipitation, with seasonal ice melt as a secondary water source in the deeper active layers of both sites.

4.3.2 Organic carbon accumulation

A net accumulation of organic matter occurs when the rate of primary production or deposition surpasses the rate of decomposition (Mitsch & Gosselink, 2007). Figure 4.3 shows that cores from both Revneset and Ice-wedge North contained an abundance of organic carbon sequestered in distinct depths of the active layer and permafrost. A high organic carbon content is characteristic of peat formed under anaerobic conditions, as net primary production generally exceeds decomposition under waterlogged conditions (Kolka et al., 2015), implying that the sediments rich in organic carbon were deposited under stagnant conditions. In ice-wedge polygonal tundra, stagnant conditions are more likely in the centres of low-centred polygons because the rims of low-centred polygons tend to block water drainage, whereas the troughs of high-centred polygons facilitate relatively fast and effective drainage of water from the polygonal networks (Liljedahl et al., 2012). Thus, frequently, low-centred polygon centres are flooded with stagnant water during summer. A high organic

carbon content in the cores hence implied sediment deposition under anaerobic conditions in the centre of a low-centred polygon. This is congruent with the ice-wedge polygon morphology at Ice-wedge North, as here, the sampled polygons were low-centred. However, the sampled polygon at Revneset was high-centred, and so a high organic carbon content in the well-drained active layer was unanticipated. The high organic carbon content in the active layer and upper permafrost implied that the polygon has undergone a transformation from low-centred and water-saturated to high-centred and well-drained.

Chapter 3 showed that the organic carbon content and degree of water saturation of the Adventdalen sediments had a strong influence on the biogeochemical processes occurring across the landscape. The organic carbon content was an important factor in determining the consumption of electron acceptors. Revneset presented a different picture, where degradation of an ice-wedge polygon led to a high organic carbon content that was not always matched by the present-day water saturation.

4.3.3 Biogeochemical processes driving carbon dioxide production

In addition to determining the accumulation of organic carbon in the landscape, the hydrologic conditions under which previously frozen organic carbon is decomposed have a strong influence on the type of gaseous products of decomposition. Under drained conditions, organic carbon can be decomposed aerobically, producing carbon dioxide (Elberling et al., 2013; Liljedahl et al., 2012), whereas under water-saturated conditions, organic carbon can be decomposed anaerobically, producing carbon dioxide and/or methane (Lipson et al., 2012). The ratio of carbon dioxide to methane produced under anaerobic conditions is dependent on the availability of alternative electron acceptors, such as nitrate, manganese, iron and sulfate, in the system (Froelich et al., 1978). The final stage in the remineralisation of organic matter in anaerobic systems is methanogenesis (Kiene, 1991). Carbon dioxide production relative to methane production is increased by the use of alternative electron acceptors. Hence, the magnitude of the permafrost carbon feedback is at least partly determined by hydrology and the availability of alternative electron acceptors.

Iron has been shown in many Arctic permafrost locations to exert an influence on methane and carbon dioxide production. For instance, the Barrow basin system, where much of the previous work on interactions between iron and organic carbon in permafrost has been conducted, is particularly well-suited to the study of these interactions because of low or absent nitrate, sulfate and manganese in the porewaters (Lipson et al., 2010; Miller et al., 2015) and a high water table (Liljedahl, 2011). Here, Lipson et al. (2010) showed that the reduction of ferric iron had a function in anaerobic respiration in an Arctic peat soil in Barrow, Alaska. Iron reduction increased carbon dioxide production relative to methane production. Furthermore, the end product of the iron reduction was siderite, which was found in substantial quantities in the sediments; siderite is a store of both reduced iron and carbon, and therefore warrants further research attention. For instance, the $\delta^{13}C$ values in authigenic siderite reflect the biogeochemical processes that yield groundwater dissolved inorganic carbon; methanogenic environments result in positive $\delta^{13}C$ values, whereas methanotrophic environments result in $\delta^{13}C$ values below -40‰ VPDB (Ludvigson et al., 2013; Ludvigson et al., 1998). Additionally, the mineralogy of iron oxides impacts the organic carbon decomposition pathway (Herndon et al., 2017; Herndon et al., 2015). For instance, Herndon et al. (2017) showed that whilst ferrihydrite minerals could suppress methanogenesis by being energetically favourable electron acceptors, the crystalline iron oxides were not as easily-reduced in anaerobic respiration and so did not decrease methane production.

Svalbard presents a different geochemical context from Barrow, on account of the weathering of reactive bedrock and the relatively recent glaciation (Hodson et al., 2016), and so is an ideal environment to study some of the alternative anaerobic respiratory pathways. The substantial quantities of siderite and pyrite at Ice-wedge North were indicative of iron and sulfate reduction. As discussed in Chapter 3, the prevalence of these processes was controlled by the organic carbon content. Iron reduction appeared to be particularly significant at Ice-wedge North, as indicated by the high quantities of siderite. In contrast, iron reduction appeared to be less important at Revneset. The primary indication of this was the relatively low concentrations of siderite and pyrite at Revneset (Table 4.2). Ferrihydrite was the dominant solid iron phase close to the surface at Revneset. Ferrihydrite is an amorphous, poorly crystalline iron oxide mineral that is precipitated as a result of the oxidation of Fe(II) (Megonigal & Hines, 2004). In fact, the most common product of Fe(II) oxidation is ferrihydrite

(Straub et al. 1998). It takes weeks to months for the diagenesis of ferrihydrite to produce crystalline iron oxides such as haematite and goethite. Organic compounds can slow down this transition (Schwertmann & Murad, 1988; Amstaetter et al., 2012). In addition, the association between ferrihydrite and organic compounds can protect the organic compounds from degradation (e.g., Herndon et al., 2017, and references therein). Although the data from Revneset do not provide direct evidence of the stabilising effects of interactions between ferrihydrite and organic carbon, it is likely that such interactions in the shallow sediments of Revneset protected both the ferrihydrite from diagenesis and the organic carbon from degradation. Overall, iron oxidation exceeded iron reduction in the shallow sediments of Revneset.

Despite the dominance of iron oxidation over iron reduction at Revneset, there were low and variable concentrations of $Fe_{(aq)}$ in the active layer and shallow permafrost of Revneset (Figure 4.4), indicating that minor iron reduction occurred. In addition, the amounts of magnetite and crystalline iron oxides increased in the deeper permafrost. The greater amount of magnetite indicates that the bedrock has a stronger influence deeper in the permafrost at Revneset. The increase in crystalline iron oxides with depth may suggest that due to the lower concentrations of organic carbon, the diagenesis of ferrihydrite occurred more rapidly. In contrast, Ice-wedge North had no such increase in magnetite and crystalline iron oxides. Ferrihydrite was also less important here, which may be due to the relative importance of iron reduction over iron oxidation.

Although iron reduction is well-studied in permafrost regions, alternative anaerobic respiratory pathways, such as manganese reduction and sulfate reduction, are less frequently observed in permafrost settings. A study of fjord sediments in Svalbard indicated that high manganese concentrations in the porewaters could be the result of dissimilatory metal reduction of the manganese oxide phases (Wehrmann et al., 2014). If dissimilatory manganese reduction in the cores from Revneset and Ice-wedge North were limited by the organic carbon content, there would be a positive correlation between $Mn_{(aq)}$ and organic carbon content. However, across all cores together, there was a weak negative correlation between $Mn_{(aq)}$ and organic carbon content ($\rho = -0.37$, $p < 0.001$), indicating that on the landscape scale, dissimilatory manganese reduction was not limited by the organic carbon

content. Despite this, in R1b and N2, $Mn_{(aq)}$ concentrations peaked near the ground surface (Figure 4.5). This is similar to a typical marine sediment, where the hypothetical porewater profile shows a depth sequence of electron acceptors used in sedimentary organic carbon oxidation, with $Mn_{(aq)}$ peaking below oxygen and nitrate, but above $Fe_{(aq)}$ and sulfate under steady state conditions (Froelich et al., 1978). Overall, however, manganese reduction had a negligible contribution to the carbon dioxide production in these sediments.

N1 displayed significant negative correlations between $Mn_{(aq)}$ and organic carbon content (ρ =-0.51, $p < 0.01$), as did R1 (ρ = -0.57, $p < 0.01$). These negative correlations suggest that the oxidation of pyrite by manganese oxides contributed $Mn_{(aq)}$ to the pore water of the sediments. The positive and highly significant correlation between $Mn_{(aq)}$ and sulfate across all cores together (ρ = 0.61, $p < 0.001$) supported that manganese reduction coupled to sulfide oxidation was an important contributor of $Mn_{(aq)}$ across the landscape. The oxidation of pyrite by manganese oxides in anoxic sediments was shown by Schippers & Jorgensen (2001) to proceed by the following equation (Equation 4.1):

$$FeS_2 + 7.5\ MnO_2 + 11\ H^+ \rightarrow\ Fe(OH)_3 + 2\ SO_4^{2-} + 7.5\ Mn^{2+} + 4\ H_2O \qquad (4.1)$$

This mechanism of manganese reduction does not produce carbon dioxide because it is not directly linked with the oxidation of organic carbon. The concentration of manganese was substantially lower than the concentration of sulfate in the cores, and this indicates that while the oxidation of pyrite by manganese oxides contributed much of the $Mn_{(aq)}$, there must be other mechanisms that made up the deficit in sulfate. Unlike in Chapter 3, where pyrite oxidation was shown to exert a landscape-scale control over the concentrations of $Fe_{(aq)}$ and SO_4^{2-}, in this site comparison, it is more challenging to determine the importance of pyrite oxidation, due to the generally higher organic carbon content causing iron and sulfate reduction to mask the signatures of pyrite oxidation. Despite this, many samples from Ice-wedge North and Revneset have a sulfate to chloride ratio greater than the snowpack sulfate to chloride ratio (0.11). This indicates that sulfide oxidation has enhanced the sulfate

concentrations, as gypsum is absent from the bedrock and so sulfate cannot be derived from gypsum (Svinth, 2013).

Consistent with deposition under anaerobic conditions, both Revneset and Ice-wedge North displayed strong evidence for sulfate reduction. Sulfate reduction is observed in permafrost settings less often than iron reduction, but Rivkina et al. (1998) detected ferrous iron, acid-soluble sulfide and methane in frozen permafrost sediment samples from northeastern Siberia. The acid-soluble sulfide (greigite and mackinawite) was inferred to have formed in-situ, indicating a role for sulfate reduction in these sediments. Chapter 3 demonstrated that, in the absence of processes removing sulfate, the oxidative weathering of pyrite caused high concentrations of sulfate in the cores from Ice-wedge South. The catchment bedrock geology is the same for all our sites. Therefore, in the absence of processes removing sulfate, we might expect to observe up to 18 mmol L^{-1} sulfate in the porewaters, owing to the oxidation of pyrite (see Chapter 3, Figure 3.2). As the concentrations of sulfate were <7 mmol L^{-1} and <5 mmol L^{-1} at at Revneset and Ice-wedge North respectively (Figure 4.6), this is indicative of sulfate reduction. However, concentrations of sulfate are variable with depth (Figure 4.6) and there was a strong negative correlation between sulfate concentration and organic carbon content for all cores (ρ =-0.66, $p < 0.0001$). This demonstrates that organic carbon content controlled sulfate reduction. Further evidence for sulfate reduction at Ice-wedge North and at Revneset is shown in the sulfate isotopes plot from Chapter 3. It is presented here with an additional point from Revneset, which fits with the points from Ice-wedge North that display evidence of BSR (Figure 4.7), despite an absence of evidence for the active formation of pyrite at Revneset. This may indicate that sulfate reduction occurred at this site, but that the redox conditions were not consistently low enough for much pyrite to form. Alternatively, perhaps the high organic carbon content of the active layer and upper permafrost meant that the proportion of mineral soil was too low for pyrite oxidation to contribute much sulfate to the porewater in the first place, thereby meaning that even under anoxic conditions, sulfate reduction was limited simply by the low concentration of sulfate. Finally, given that only one sampling depth at Revneset yielded sufficient sulfate mass for isotopic analysis, it could be that this one point instead represents mixing between sulfate derived from the OWP via O_2 and sulfate derived from precipitation. Further sampling and analysis are required to

elucidate whether the $\delta^{34}S\text{-}SO_4^{2-}$ and $\delta^{18}O\text{-}SO_4^{2-}$ values in the sample at Revneset are representative of BSR or of mixing between the different sources of sulfate.

4.3.4 Depth variations in pore water geochemistry

The pore water profiles shown in Figure 4.3 to Figure 4.6 and in Figure 4.8 represent the following attributes of both the active layer and the underlying permafrost: (1) the *in situ* distribution of extractable or adsorbed solutes, reactive mineral phases, and gases, and (2) the products of additional rock-water-microorganism interactions following thaw. As discussed in Chapter 3, the variations in pore water geochemistry with depth in the permafrost and the active layer are influenced by multiple factors. These include physical factors, such as hydrological inputs to the active layer (precipitation and ground ice melt; Throckmorten et al., 2016), hydrological outputs from the active layer (evaporation, freezing and advection); and the diffusion of ions. Each process influences the pore water chemistry, and it can prove challenging to gauge the effect of each separate process. Kokelj & Burn, (2003, 2005) suggest that the shallow permafrost may be a sink for soluble materials, relative to the active layer, on account of (1) leaching of soluble materials by advection of water through the active layer, (2) the migration of ions downwards along thermally-induced suction gradients in fine-grained alluvium ("cryosuction"), and (3) solute exclusion by downward freezing in sandy silt alluvium. Here, the approach used in Section 3.3.4 is applied to the cores from Revneset. The cores from Ice-wedge North are discussed briefly as a reference. Assuming that chloride moves conservatively, without participating in dissolution or precipitation reactions, its concentration profile in each core is used to trace the variations in physical processes that concentrate or dilute pore waters (Jessen et al., 2014).

A constant concentration of chloride with depth would indicate that active layer leaching, ion migration and solute exclusion are unimportant in the cores. A variable concentration with depth would indicate that these processes are causing vertical solute transport (Jessen et al. 2014) and presumably causing concentration gradients that induce diffusion. Figure 4.8 shows that the concentrations of chloride did indeed vary with depth in all our cores, indicating that physical processes were removing or concentrating chloride at specific depths. However, none of these profiles are indicative of marine pore waters, in contrast to the

deeper pore waters analysed by Cable et al. (2017). Welch's t-test shows that cores N2, N1, and R1a did not have significantly different concentrations of chloride in the active layer and permafrost (Table 4.3). Welch's t-test shows that the permafrost of core R1b had significantly lower concentrations of chloride than the active layer (Table 4.3), suggesting that the active layer was less leached than the permafrost. However, the difference in chloride concentrations in this core was <1 mmol L^{-1} between the active layer and the permafrost, and so the decrease in leaching has only been small. The absence of a significant difference in chloride concentration between the active layer and the permafrost in the other three cores may indicate that the rate of advection through the active layer has remained unchanged as the permafrost has aggraded. The increased chloride concentration at the base of N2 was discussed in more depth in Chapter 3, but in summary it is highly probable that the enhanced chloride concentrations were due to upward diffusion from the cryopeg or frozen deltaic sediments.

Solute exclusion by downward freezing results in the accumulation of solutes at the base of the active layer (Kokelj & Burn, 2005). N2, R1a and R1b did not display distinctive chloride accumulation at the base of the active layer (Figure 4.8a-c). There was a small accumulation of chloride close to the base of the active layer in N1 (Figure 4.8b). A further possibility is that this accumulation may instead have been caused by the migration of chloride ions downwards along thermally-induced suction gradients. In that case, zones of solute enrichment would correspond to locations of ice enrichment (Kokelj & Burn, 2005). Evaluation of the correlations between chloride concentration and gravimetric water content in N1 reveal that there is no significant correlation between these two variables (ρ = 0.051, p = 0.78). Therefore, it is more likely that this small solute/chloride enrichment at the base of the active layer of N1 is due to solute exclusion by downward freezing, rather than cryosuction.

In summary, the rate of active layer leaching appears to have been largely unchanged during the aggradation of the upper 2 metres of sediment, despite a small decrease in leaching in R2. One core (N1) has experienced solute exclusion by downward freezing of the active layer, and another (N2) shows evidence of chloride sourced from upwards diffusion from a cryopeg or frozen deltaic sediments. In all the cores, there are small variations in the concentration of chloride that are not explained by these tests. This indicates that there were physical

processes occurring that are not explained by active layer leaching, cryosuction, or solute exclusion. Therefore, in this chapter, the focus has been on the broader-scale biogeochemistry of the sites.

4.3.5 Summary and predictions of the impact of permafrost thaw

In Adventdalen, the organic carbon content coupled with the degree of water saturation controlled the prevailing biogeochemical processes (Chapter 3), but the organic carbon content in the cores from Revneset did not have this effect. This difference between Adventdalen and Revneset was due to both the sediment composition and the polygon morphology. Firstly, the high organic carbon content of the active layer and shallow permafrost at Revneset was coupled with a relatively low mineral content of the soil. This was reflected in the lower extracted iron (dry wt. percent) at Revneset compared to Ice-wedge North (Table 4.2). The low mineral content of the organic soil at Revneset limited the supply of iron and sulfate to iron- and sulfate-reducers. In addition, the degradation of the ice-wedge polygon at Revneset resulted in a high-centred polygon with a low or fluctuating water table. The lack of consistent water saturation in the high-centred polygon precluded the maintainance of low redox conditions at Revneset. This was in contrast to Ice-wedge North, where the low redox conditions of the organic-rich sediments in the low-centred polygons were maintained by more consistent water saturation. The low or fluctuating water table of Revneset meant that even with minor iron and sulfate reduction occurring, the products were not preserved in pyrite and siderite to the same degree as at Ice-wedge North.

Permafrost in Svalbard is relatively warm for its northerly latitude (Romanovsky et al., 2010b), and between 1961-1990 and 2000-2011 there has been a 2.95 °C increase in mean annual air temperatures in Adventdalen (Førland et al., 2011; Christiansen et al., 2013; Nordli et al., 2014). Despite this, occurences of extremely high summer temperatures have so far been prevented by the maritime climate on Svalbard (Pirk et al. 2017a). This may explain the absence of dramatic ice-wedge degradation in Adventdalen, as extremely high summer temperatures are a trigger of ice-wedge degradation in Alaska (Jorgenson et al., 2006; Liljedahl et al., 2016; Pirk et al., 2017a). In addition, the topography of Svalbard is influential on the airflow and wind speeds in Svalbard, with acceleration of wind channelised in the

Adventdalen valley cooling the ground (Christiansen et al., 2013). In contrast, data from Longyearbyen Airport, which, like Revneset, is situated in the open outer part of Adventdalen on marine terraces, suggest that there is lower acceleration of the winds and also relatively more wind from the open fjord. This indicates that the permafrost on the marine terraces is likely to be warmer than that in the valley bottom, and could be a reason for the observed ice-wedge polygon degradation at Revneset, compared to Adventdalen.

Pirk et al. (2017a) posit that as temperature increases markedly on Svalbard, this may cause future ice-wedge polygon degradation in Adventdalen. In this case, the biogeochemistry of the Revneset high-centred polygon may be helpful for predicting the future biogeochemistry of the degraded Ice-wedge North polygons. Based on the Revneset high-centred polygon biogeochemistry, polygon degradation at Ice-wedge North could cause oxidation of pyrite and siderite, with resulting increases in carbon dioxide fluxes to the atmosphere. Although, the Adventdalen valley sediments are much thicker than those at Revneset, and hence potentially more concerning for greenhouse gas emissions under future warming and permafrost thaw, the particularly organic-rich sediments are mainly confined to the upper 2 metres (Cable et al., 2017). Hence, future warming and polygon degradation at Ice-wedge North is likely to result in a similar set of biogeochemical processes to those occurring at present-day Revneset.

4.4 Conclusion

Although there were similarly organic-rich sediments at Ice-wedge North and Revneset, the differences in primary water source and hydrology, coupled with degradation of the ice-wedge polygons at Revneset, caused the sites to exhibit different dominant biogeochemical processes. The sediments of the low-centred polygons of Ice-wedge North were water-saturated and anaerobic, with iron and sulfate reduction leading to the precipitation of pyrite and siderite. In contrast, the active layer of the high-centred polygon was not consistently water-saturated, owing to the degradation of the ice-wedge polygon and the probable greater hydraulic conductivity of both the peat and the underlying beach sediments. This led to the more oxidising conditions found in the high-centred polygon, with a dominance of iron oxidation at Revneset; ferrihydrite was the dominant extracted iron phase and there were

much lower levels of pyrite and siderite. The low or fluctuating water table precluded the formation and/or preservation of pyrite, even though isotopic data were indicative of sulfate reduction occurring in the active layer at Revneset. While the concentrations of $Mn_{(aq)}$ at both sites were indicative of the reduction of manganese oxides, this was not coupled to the oxidation of organic carbon, but rather to the oxidation of pyrite. Hence, dissimilatory manganese reduction did not produce substantial quantities of carbon dioxide at either site. The data presented in this chapter demonstrate the profound effect of ice-wedge polygon degradation on the sediment and porewater biogeochemistry: polygon degradation resulted in more oxidising conditions, a decrease in iron reduction, and a decrease in the preservation of the products of iron and sulfate reduction.

Chapter 5. Sources and Sinks of Greenhouse Gases in the Active Layer and Permafrost of a High Arctic Valley

The previous chapters in this thesis focused on the influence of landscape geomorphology upon iron, sulfur and carbon cycling within permafrost pore water and sediment, with discussion of the biogeochemical processes driving carbon dioxide production. This chapter follows with an emphasis on quantifying the methane and carbon dioxide concentrations in the pore water and elucidating the biogeochemical processes that lead to methanogenesis.

5.1 Introduction

5.1.1 The permafrost carbon feedback

As explained in Section 1.1, around half of the global terrestrial belowground organic carbon stocks (1330 to 1580 Pg carbon) are stored in permafrost soils (Hugelius et al., 2014; Tarnocai et al., 2009). This is the largest individual component of the terrestrial carbon pool, and is over double the amount of carbon in the present atmosphere (Tarnocai et al., 2009; McGuire et al., 2012; IPCC, 2013). According to models of the global climate, the mean annual air temperature of the Arctic is predicted to increase by up to 9 °C by the year 2100 (Anisimov et al., 2007). Permafrost ecosystems are predicted to transform from a net *sink* of carbon to a net *source* of carbon in the next decade, due to gradual, top-down thawing of permafrost in response to climate change (Kirschke et al., 2013; Parmentier et al., 2013; Schaefer et al., 2011; Elberling et al., 2013; Lee et al., 2012; Schuur et al., 2015).

The emission of greenhouse gases from permafrost is a feedback from the global carbon cycle to climate change. However, there remains substantial uncertainty pertaining to both the size and the timing of emissions of greenhouse gases and the impact on climate change that will accrue from this climate feedback process (Schuur et al., 2015). This uncertainty is due to numerous factors, which include: problems associated with limited spatial and temporal data due to challenges in data collection from cold, remote areas, which are difficult and expensive to access (Metcalfe et al., 2018; Turetsky et al., 2019); heterogeneous processes including

fine-scale effects such as abrupt thaw (Turetsky et al., 2019); and local soil redox status (Riley et al., 2011; Meng et al., 2012; Xu et al., 2015; Zheng et al., 2019). For instance, recent models of the permafrost methane feedback-to-climate up to the year 2100 do not thoroughly account for microbial responses to permafrost thaw, nor do they include soil pore-scale anaerobic and aerobic niches that are crucial in determining the balance between methane production and methane oxidation (Gao et al., 2013; Lawrence et al., 2015; Schaefer et al., 2014; Ebrahimi & Or, 2017). Ice-wedge polygon degradation, for example, is associated with an overall landscape drying, as low-centred polygons transition to high-centred polygons (Section 4.1, Figure 4.14.1; Liljedahl et al., 2016). The drying of the landscape has implications for methane fluxes from polygons (Lara et al., 2015; Sachs et al., 2010; Wainwright et al., 2015). For instance, numerous studies at the Barrow Environmental Observatory, Alaska, have observed a decrease in methane emissions with permafrost degradation in ice-wedge polygon terrain (Vaughn et al., 2016; Wainwright et al., 2015). While the evidence for decreasing methane emissions with polygon degradation is clear, less is known about whether this degradation impacts methane storage and production within the permafrost. Hence, further work is required, both to extend the spatial and temporal coverage of permafrost data and to incorporate such data into models of the permafrost methane feedback.

5.1.2 Sources and sinks of methane

Across the Arctic, much research attention has been devoted to methane and carbon dioxide emissions from the shallow permafrost and active layer, where relatively modern organic carbon is decomposed by methanogens to produce methane and carbon dioxide (e.g., Knoblauch et al., 2018; Lara et al., 2015; Miller et al., 2015; Sachs et al., 2010; Throckmorton et al., 2015). In addition, biogenic and thermogenic methanogenic processes produce methane beneath permafrost within sedimentary basins (Walter Anthony et al., 2012). In some permafrost areas, permafrost degradation results in the removal of the permafrost ‘cryospheric cap’, which drives methane emissions from beneath the permafrost.

Biogenic methane is primarily produced via two mechanisms: hydrogenotrophic and acetotrophic methanogenesis. Different precursor compounds, kinetic isotope effects and

the high temperatures required for thermogenic generation of hydrocarbons all cause each source to produce methane with a distinct isotopic composition (Whiticar, 1999). Hence, measuring the isotopic composition of methane dissolved in water of the active layer is helpful in elucidating the primary source of methane. *Thermogenic* methane has a $\delta^{13}C$ of approximately -50‰ to -20‰ (Whiticar, 1999). *Biogenic* (or 'bacterial') methane has a $\delta^{13}C$ of -110‰ to -50‰ (Whiticar, 1999). Bacterial methane can be produced via the acetotrophic pathway ($\delta^{13}C$-CH_4 of -60‰ to -50‰) or the hydrogenotrophic pathway ($\delta^{13}C$-CH_4 of -110‰ to -60‰; Whiticar, 1999). Hydrogenotrophic methanogens form methane via the reduction of carbon dioxide with hydrogen, a process also known as "carbonate reduction" (Equation 5.1; Oremland, 1988; Whiticar, 1999):

$$CO_2 + 8H^+ + 8e^- \rightarrow CH_4 + 2H_2O \quad (5.1)$$

Acetotrophic methanogens form methane via acetate fermentation (Equation 5.2; Whiticar, 1999):

$$CH_3COOH \rightarrow CH_4 + CO_2 \quad (5.2)$$

Furthermore, $\delta^{13}C$ values of methane are influenced by numerous other factors, including the $\delta^{13}C$ values in organic matter, the temperature of methanogen growth, the phase of methanogen growth and methanogenesis energetics (Valentine et al., 2004; Penning et al., 2005; Hornibrook, 2009; Chanton et al., 1989; Botz et al., 1996; Whiticar, 1999). Despite these complicating factors, the $\delta^{13}C$ of methane is useful in distinguishing the various methane sources. In addition, methano*trophy*, which is the oxidative consumption of methane by methanotrophs, such as methane-oxidising archaea (Whiticar, 1999; Barbier et al., 2012), has an effect on the $\delta^{13}C$ of the residual methane. During methanotrophy, ^{12}C-CH_4 is consumed preferentially, resulting in an enrichment of ^{13}C in the residual methane (Whiticar, 1999). Finally, δD values of methane are useful as a further constraint on the methane sources, particularly for distinguishing between the two main biogenic methane sources (Whiticar, 1999). However, the analysis of δD values of methane is beyond the scope of this thesis.

$\delta^{13}C\text{-}CH_4$ data from natural systems show that acetotrophic methanogenesis produces around two thirds of methane globally (Oremland, 1988; Ferry, 1992). Atmospheric inversion studies inferring the sources and sinks of atmospheric methane globally make the assumption that methane production from wetlands is dominated by acetotrophic methanogenesis (Bousquet et al., 2006; Kai et al., 2011). The accuracy of this assumption has implications for correctly attributing global methane sources and sinks (McCalley et al., 2014). Acetotrophic methanogenesis was the dominant biogenic source of methane in the active layer waters in Barrow, Alaska, (Throckmorton et al., 2015). In addition, anoxic microcosm experiments with high Arctic peat soil from the active layer in Knudsenheia, in Svalbard, found that the minimum fraction of methane originating from hydrogen and formate was ~35%, and the maximum methane proportion formed by acetotrophic methanogenesis was therefore ~65% (Tveit et al., 2015). In contrast, methane isotope data from the Kara Sea coast had a mean $\delta^{13}C\text{-}CH_4$ of -68.6‰ in the permafrost and a mean $\delta^{13}C\text{-}CH_4$ of -63.6‰ in the active layer, indicating the importance both of hydrogenotrophic methanogenesis in the permafrost and additionally of methanotrophy in the active layer (Streletskaya et al., 2018). Furthermore, incubations of permafrost sediments from Samoylov Island, on the Lena Delta in the Siberian Arctic, showed that amendment with hydrogen at low temperatures (< 0 °C) resulted in 2.5 to 3.5 times more methane production than amendment with acetate, implying a prevalence of hydrogenotrophic methanogenesis (Wagner et al., 2007). It is clear from these studies that the primary pathway of methanogenesis varies across the Arctic, and also depends on whether the methane is produced in the active layer or the permafrost.

5.1.3 Permafrost and greenhouse gases in Adventdalen

Methane emitted from Adventdalen is sourced from both below the permafrost and within the shallow permafrost and active layer (Hodson et al., 2019; Pirk et al., 2017b). As part of an effort to estimate the potential for geological carbon sequestration on Spitsbergen, Huq et al. (2017) measured the $\delta^{13}C$ of methane and carbon dioxide down to a depth of 700 metres in Adventdalen. They established that the dominant sources of methane transition gradually from thermogenic at depth to biogenic in more shallow sediments. In Adventdalen, the thermogenic methane that diffuses from below a depth of 400 metres has $\delta^{13}C$ values ca. -45‰ (Huq et al., 2017). Importantly, these authors determined that although there is some

vertical diffusion of thermogenic methane to shallower sediments, this diffusion is too slow to contribute to the isotopic signatures of methane in the shallow permafrost and active layer. Outgassing of methane produced beneath permafrost in Adventdalen is not necessarily driven by permafrost degradation. Instead methane sourced from both thermogenic and biogenic production may be transported to the surface via sub-permafrost groundwaters emerging from open system pingos (Hodson et al., 2019). Hodson et al. (2019) found high seasonal maximum concentrations of methane (up to 14.5 mg L^{-1} methane) in waters accumulating beneath the winter ice layer on an open system pingo in Adventdalen (Lagoon Pingo). The methane was primarily biogenic, and the authors suggested that it was transported along groundwater flowpaths below the permafrost in fractures within sandstone bedrock. This resulted in a large summer methane emission flux from the pingo pond of 46 $gCH_4C\ m^{-2}$, and an even more substantial annual emission flux of 223 $gCH_4\text{-}C\ m^{-2}$ once the winter emissions were included.

In Adventdalen, previous work by Pirk et al. (2017b) revealed that wetlands in this valley have relatively low methane fluxes, with (median) rates of 1-2 $gCH_4C\ m^{-2}$. In Arctic wetlands, the authors used a statistical description of methane emissions based on three hypothesised mechanisms: i) slow-turnover carbon contained within soil microorganism cells or frost-damaged roots contributed to a peak in methane emissions immediately after thawing (Skogland et al., 1988), ii) fast-turnover carbon of root exudates (Ström et al., 2003) contributed to a wider peak in methane emissions in the middle of the growing season and iii) during the autumnal freeze-in period, there is physical release of stored methane (Mastepanov et al., 2008). Their statistical description was effective in delineating the spatial and temporal patterns in methane fluxes, even in Adventdalen, which did not exhibit an early emission peak and was dominated by the wider peak in the middle of the growing season. The ice-wedge polygons in Adventdalen caused the methane fluxes to vary on small spatial scales, owing to the variable soil moisture. While this work accurately described the spatial and temporal patterns in methane fluxes from the studied site, the datasets did not allow a comprehensive investigation of the mechanisms underlying the methane fluxes.

These previous studies of methanogenesis and methane fluxes in Adventdalen indicate that there are methane sources both below the permafrost and within the shallow permafrost and

active layer (Hodson et al., 2019; Pirk et al., 2017b). While the mechanisms of methanogenesis have been analysed in some detail for the methane sourced from beneath the permafrost, the biogeochemical processes leading to methanogenesis in the shallow permafrost and active layer of Adventdalen are less clearly understood at present. In addition, the scarcity of ice-wedge polygon degradation in the Adventdalen region (Pirk et al., 2017) means that studies of ice-wedge polygons in Svalbard have not yet examined the impact of ice-wedge polygon degradation on methane production. The focus of this chapter, therefore, is on quantifying the methane and carbon dioxide concentrations in the active layer and shallow permafrost in Adventdalen and Revneset, elucidating the biogeochemical processes that lead to methanogenesis, and inferring the methanogenic pathways. This chapter presents and discusses for the first time the concentrations of methane and carbon dioxide in the pore water of the sediment cores, the relative abundance of archaea in the sediment cores, and the $\delta^{13}C\text{-}CH_4$ values and concentrations of acetate in water from the active layer of Adventdalen and Revneset.

5.2 Results

The concentrations of methane were low or negligible in the cores from Ice-wedge South (up to 14.4 µmol L^{-1}; Figure 5.1a-c). In contrast, all cores from Ice-wedge North and Revneset contained substantial concentrations of methane accumulated in specific depths (up to 560 µmol L^{-1}; Figure 5.1d-g). Much of the active layer of core N1 contained low or negligible concentrations of methane (the minimum was 1.07 µmol L^{-1}), except for a peak in concentration at 15 cm depth (126 µmol L^{-1}; Figure 5.1d). Concentrations of methane were consistently higher in the permafrost (Mean = 105 µmol L^{-1}, Range = 3.29-195 µmol L^{-1}) of core N1 relative to the active layer (Mean= 31.6 µmol L^{-1}, Range = 1.07-126 µmol L^{-1}), with substantial variability below 10 cm depth (Figure 5.1d). A large peak in methane was observed in the active layer of core N2 (219 mmol L^{-1} at 53 cm depth; Figure 5.1e); this peak occurred at greater depth than the active layer methane peak in core N1. The concentrations of methane in the permafrost of core N2 were similarly variable to those observed in N1 and reached a maximum of 293 µmol L^{-1} at 109 cm depth (Figure 5.1e). The concentrations of methane in the active layer of cores R1a and R1b were low or negligible (< 1 µmol L^{-1}; Figure

5.1f-g). The shallow permafrost of cores R1a and R1b contained substantially higher concentrations of methane than N1 and N2 (up to 560 μmol L^{-1}). The peak in methane in the shallow permafrost was concentrated in a narrower depth interval, closer to the permafrost table, and reached higher concentrations in core R1b compared to core R1a (Figure 5.1f and g). Below this peak, the methane concentrations decreased in cores R1a and R1b.

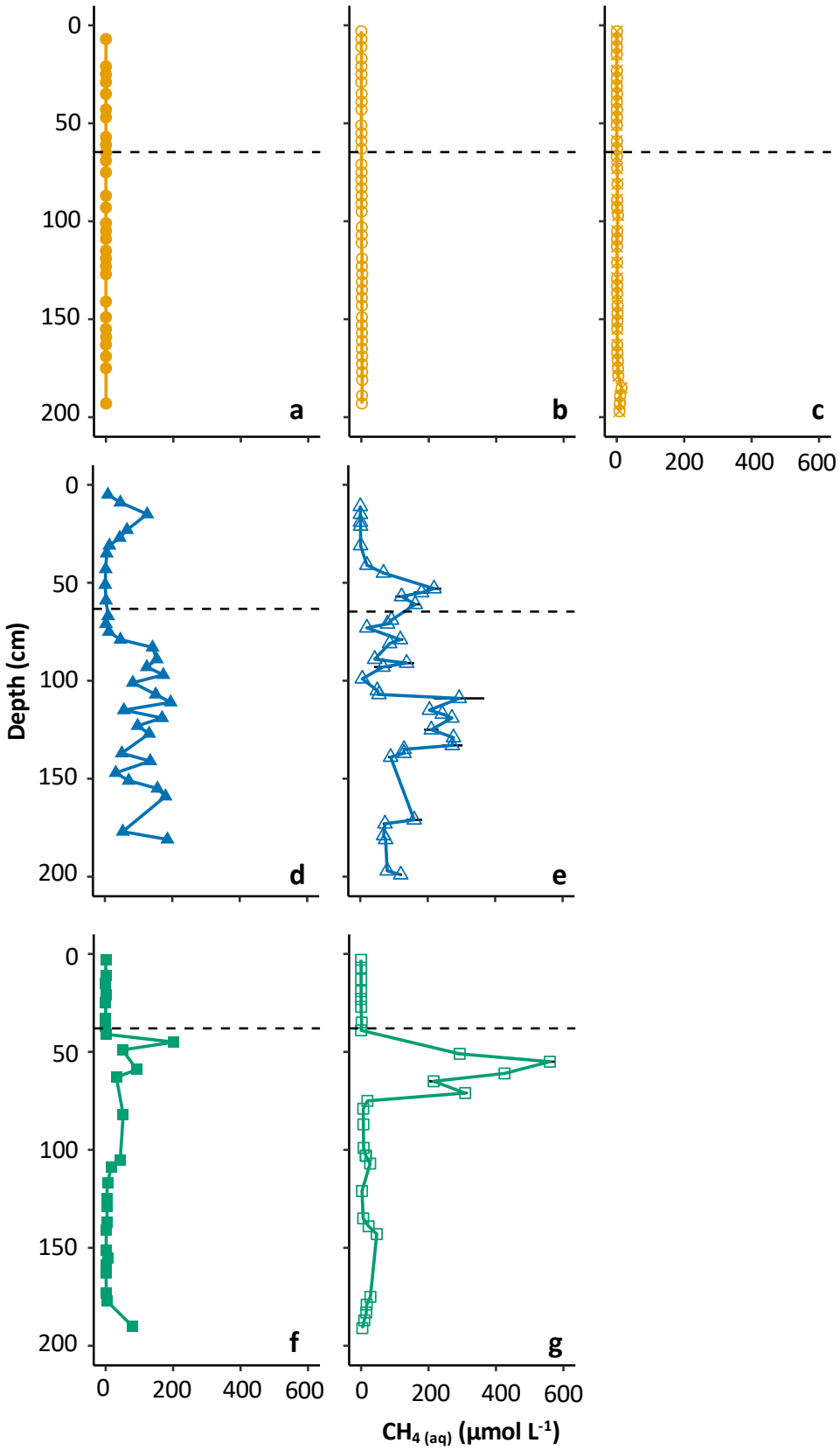

Figure 5.1 Methane ($CH_{4\ (aq)}$) with depth in cores a) S1, b) S2a, c) S2b, d) N1, e) N2, f) R1a and g) R1b. The error bars (black horizontal solid lines that are only rarely wider than the points themselves) represent one standard deviation either side of the mean, calculated from 3 replicate measurements of the same vial. Horizontal dashed lines represent the active layer depths.

In all cores, the concentrations of carbon dioxide far exceeded the concentrations of methane (Figure 5.2a-g). The concentrations of carbon dioxide were highly variable with depth in all cores. The cores from Ice-wedge South did not display consistent trends with depth (Figure 5.2a-c). However, in core S1, the concentrations of carbon dioxide were generally higher in the permafrost than in the active layer, whereas in cores S2a and S2b, the concentration increased slightly from the base of the active layer towards the ground surface. The concentrations of carbon dioxide in core N1 were highest in the deeper active layer and the shallow permafrost (Figure 5.2d). Although an instrumentation failure resulted in no carbon dioxide data from much of the active layer of core N2, it is clear from the limited existing data that the highest concentrations of carbon dioxide were at the base of the active layer, and that the concentrations were lower in the permafrost (Figure 5.2e). In core R1a, the highest concentrations of carbon dioxide were in the active layer and shallow permafrost (Figure 5.2f). Core R1b also displayed higher concentrations in the active layer, but in addition, the concentrations increased into the deeper permafrost (Figure 5.2g).

The relationship between organic carbon content and methane concentration is presented in Figure 5.3a for the Adventdalen cores. A higher organic carbon content was associated with a higher methane concentration ($\rho = 0.75$, $p < 0.001$), although there was variability in this relationship. The relationship between the concentration of sulfate and the organic carbon content is presented in Figure 5.3b for the Adventdalen cores. Samples were either rich in sulfate or in organic carbon, giving a negative monotonic correlation ($\rho = -0.68$, $p<0.001$). The same was true of the relationship between aqueous iron and organic carbon content ($\rho = -0.61$, $p<0.001$; Figure 5.3c). Across Revneset and Adventdalen, the relationship between methane concentration and aqueous iron and sulfate concentrations is presented in Figure 5.4. There was a negative monotonic correlation between methane and sulfate ($\rho = -0.46$, $p < 0.0001$; Figure 5.4a), which was particularly strong in the Adventdalen cores alone (orange points for S1, S2a, S2b and blue points for N1 and N2, $\rho = -0.76$, $p < 0.001$), as well as in water samples from the active layer of Adventdalen (orange points for S3w and blue points for N1w and N2w, $\rho = -0.67$, $p < 0.01$). There was a negative monotonic correlation between methane and aqueous iron in the Adventdalen cores ($\rho = -0.58$, $p < 0.001$; Figure 5.4b). In general, the samples from Ice-wedge South that had varying sulfate and iron concentrations with low

methane concentrations, and the samples from the remaining two sites exhibited low sulfate and iron concentration with varying methane concentration.

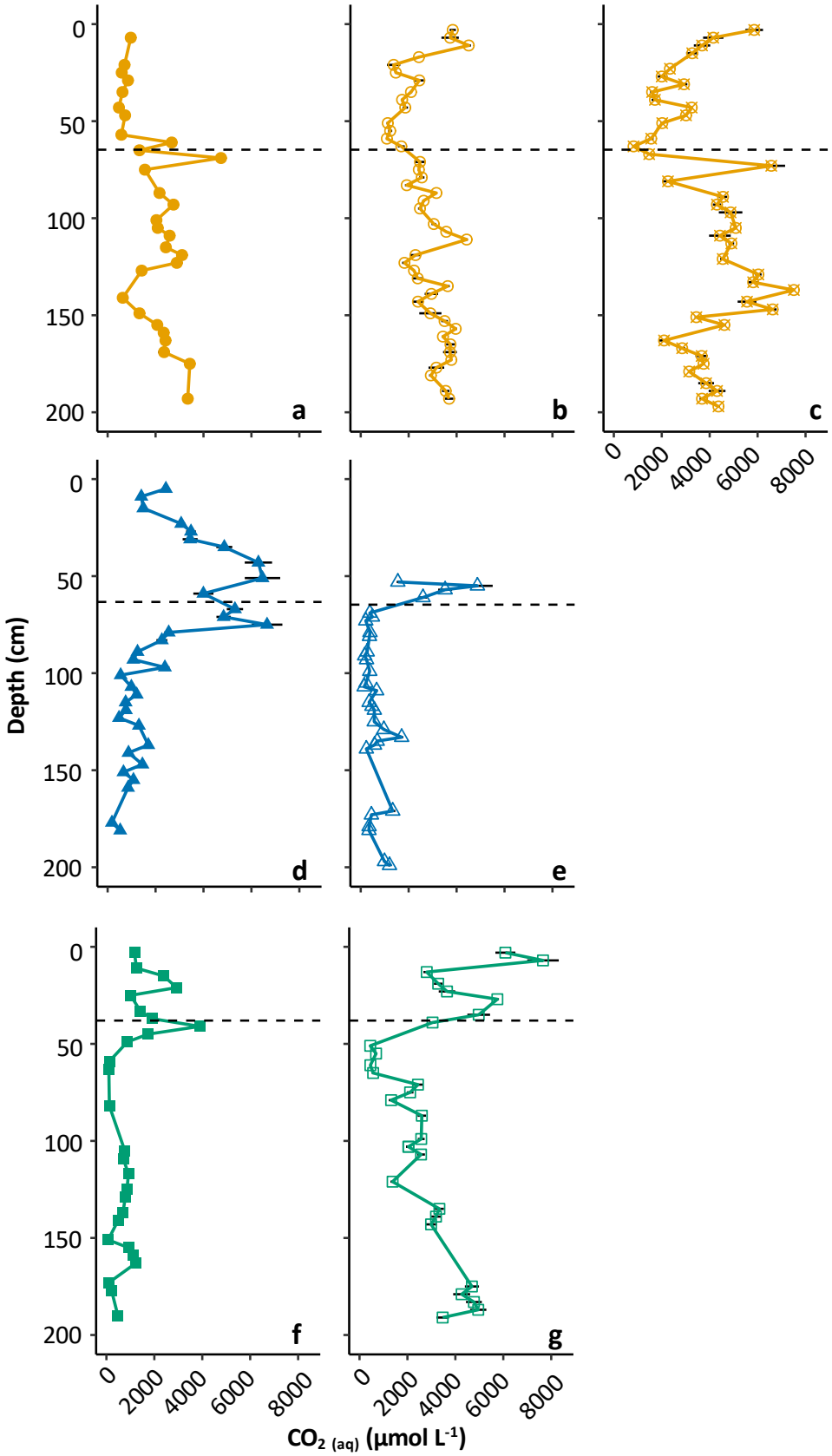

Figure 5.2 $CO_{2\ (aq)}$ with depth in cores a) S1, b) S2a, c) S2b, d) N1, e) N2, f) R1a and g) R1b. Error bars (horizontal solid black lines) represent one standard deviation either side of the mean, calculated from 3 replicate measurements of the same vial. Horizontal dashed lines represent the active layer depths.

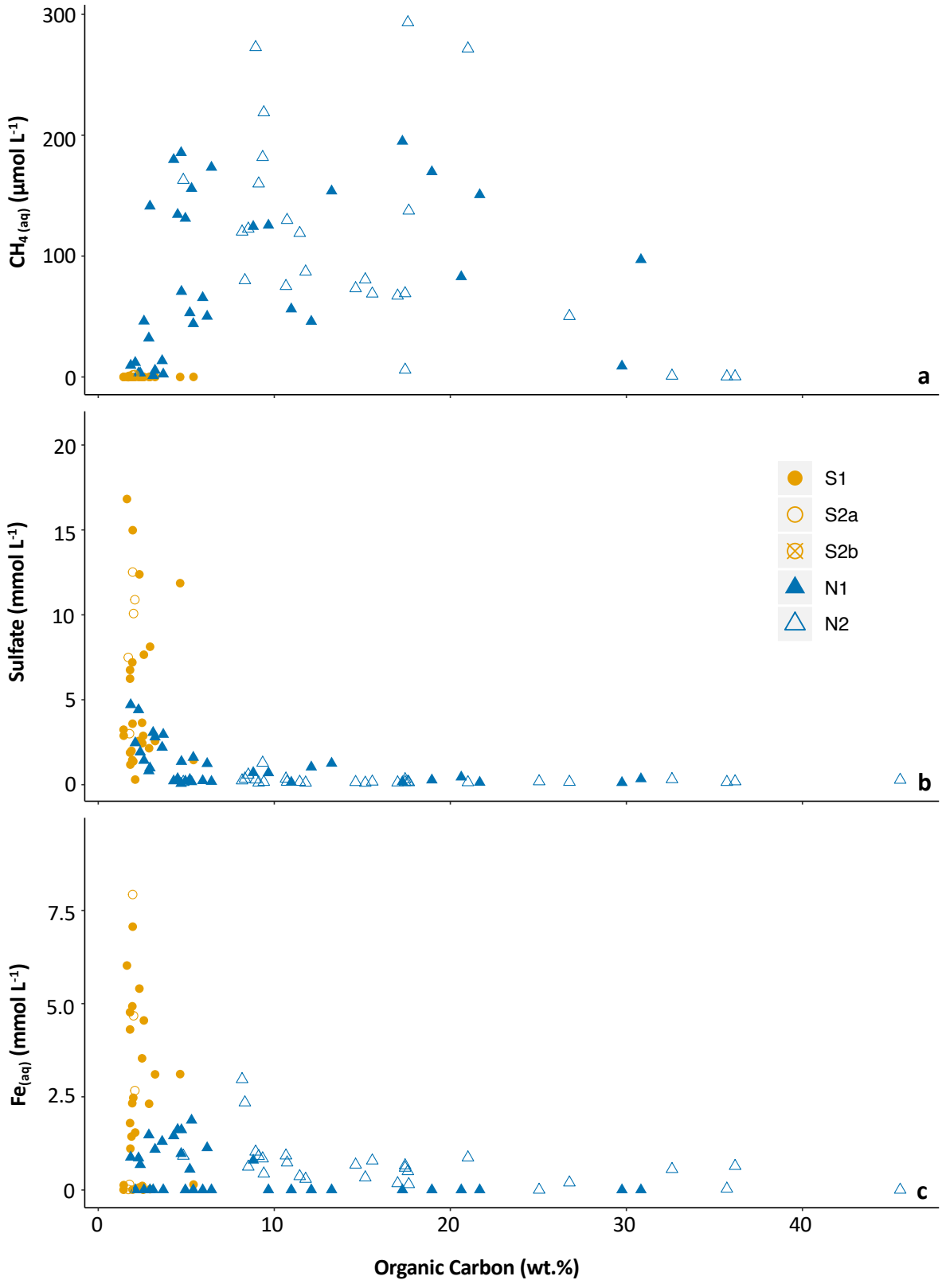

Figure 5.3 a) $CH_{4\,(aq)}$ plotted as a function of the organic carbon content ($\rho = 0.75$, $p < 0.001$), b) SO_4^{2-} plotted as a function of organic carbon content, and c) $Fe_{(aq)}$ plotted as a function of organic carbon content, in cores (S1, S2a, S2b, N1, N2) from Adventdalen.

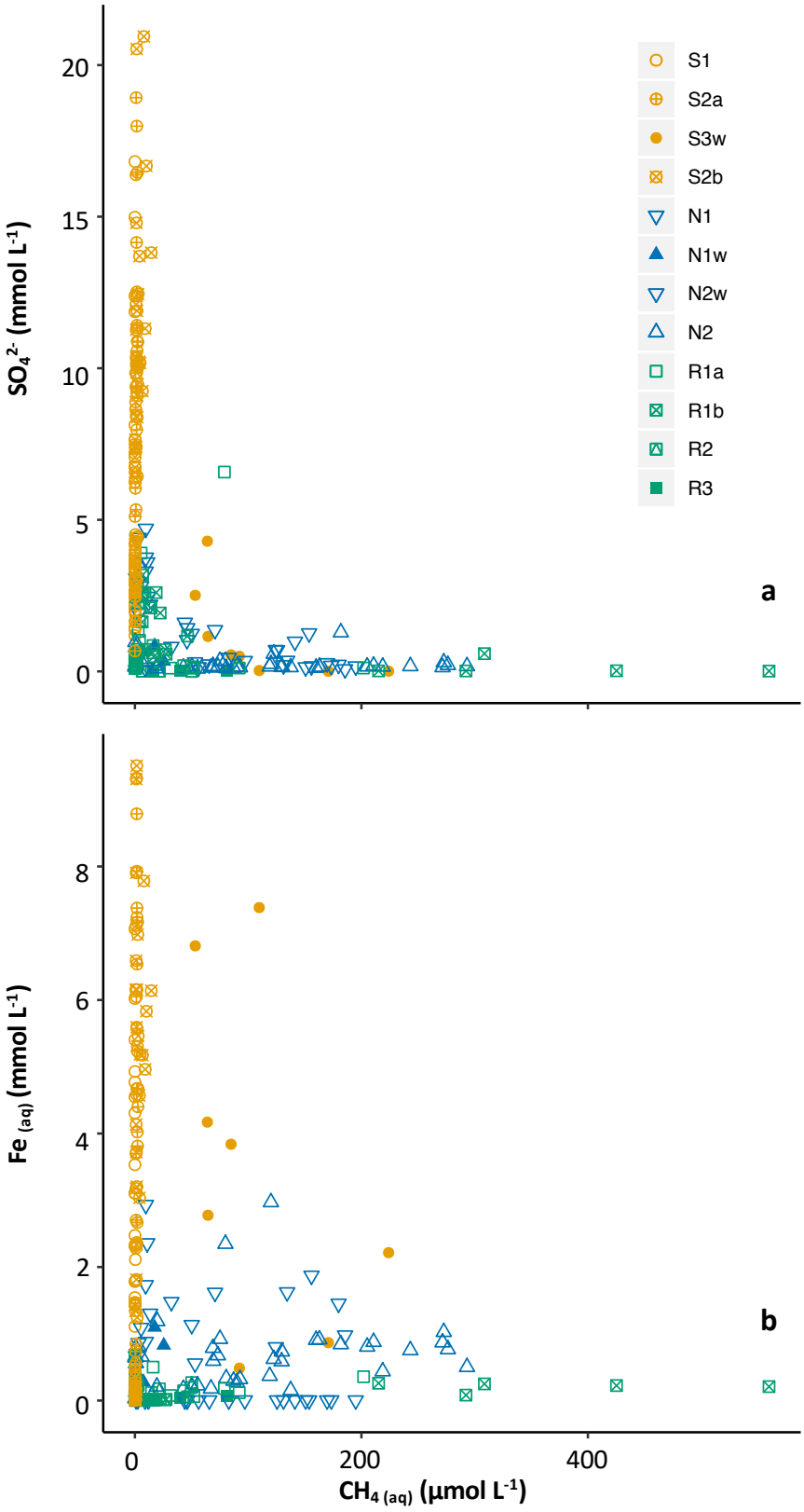

Figure 5.4 a) $CH_{4\ (aq)}$ plotted in relation to SO_4^{2-}, and b) $CH_{4\ (aq)}$ plotted in relation to $Fe_{(aq)}$, in cores (S1, S2a, S2b, N1, N2, R1a and R1b) and water from the active layer (S3w, N1w, N2w, R1a, R1b, R2 and R3) from Adventdalen and Revneset. All samples except those from R2 and R3 are from ice-wedge polygon centres. R2 and R3 are from the water ponding in ice-wedge troughs.

Figure 5.5a shows a large range in the concentration of methane in the water samples from the active layer, with samples from polygon S3 containing the highest concentrations of methane (up to 224 µmol L^{-1}). There was also a large range in $\delta^{13}C\text{-}CH_4$ values, with no statistically significant difference between the sites. Most of the water samples from the active layer contained low or negligible concentrations of acetate (Figure 5.5b). However, some water samples from polygon S3 contained high concentrations of acetate (up to 4400 µmol L^{-1}; Figure 5.5b). These samples also generally contained higher concentrations of methane (Figure 5.5b).

The relative abundance of archaea was recorded as a function of depth for three different sites. There was a relative abundance of hydrogenotrophic methanogens, compared to acetotrophic methanogens (see Table 5.1). In contrast to Ice-wedge North and Revneset, there was a relatively low abundance of methanogens in polygon S1 at Ice-wedge South. The relative abundance of methanotrophs was high in all the sites (Table 5.1). Figure 5.6 shows that Ice-wedge North was dominated by the mainly methanogenic Methanomicrobia at depths below 150 cm and by the methanotrophic Bathyarchaeia nearer the surface (Figure 5.1). Similarly, there was a substantial input from Methanobacteria and Methanomicrobia in the shallow permafrost of Revneset, whereas the methanotrophic Bathyarchaeia dominated in the active layer. Overall, at Ice-wedge North and Revneset, methanogenesis dominated in the deeper permafrost, whereas methanotrophy was more dominant in the shallower permafrost and active layer. The microbial data presented in Table 5.1 and Figure 5.6 were generously provided by Ebbe Norskov Bak (Aarhus University) and are interpreted here for the first time.

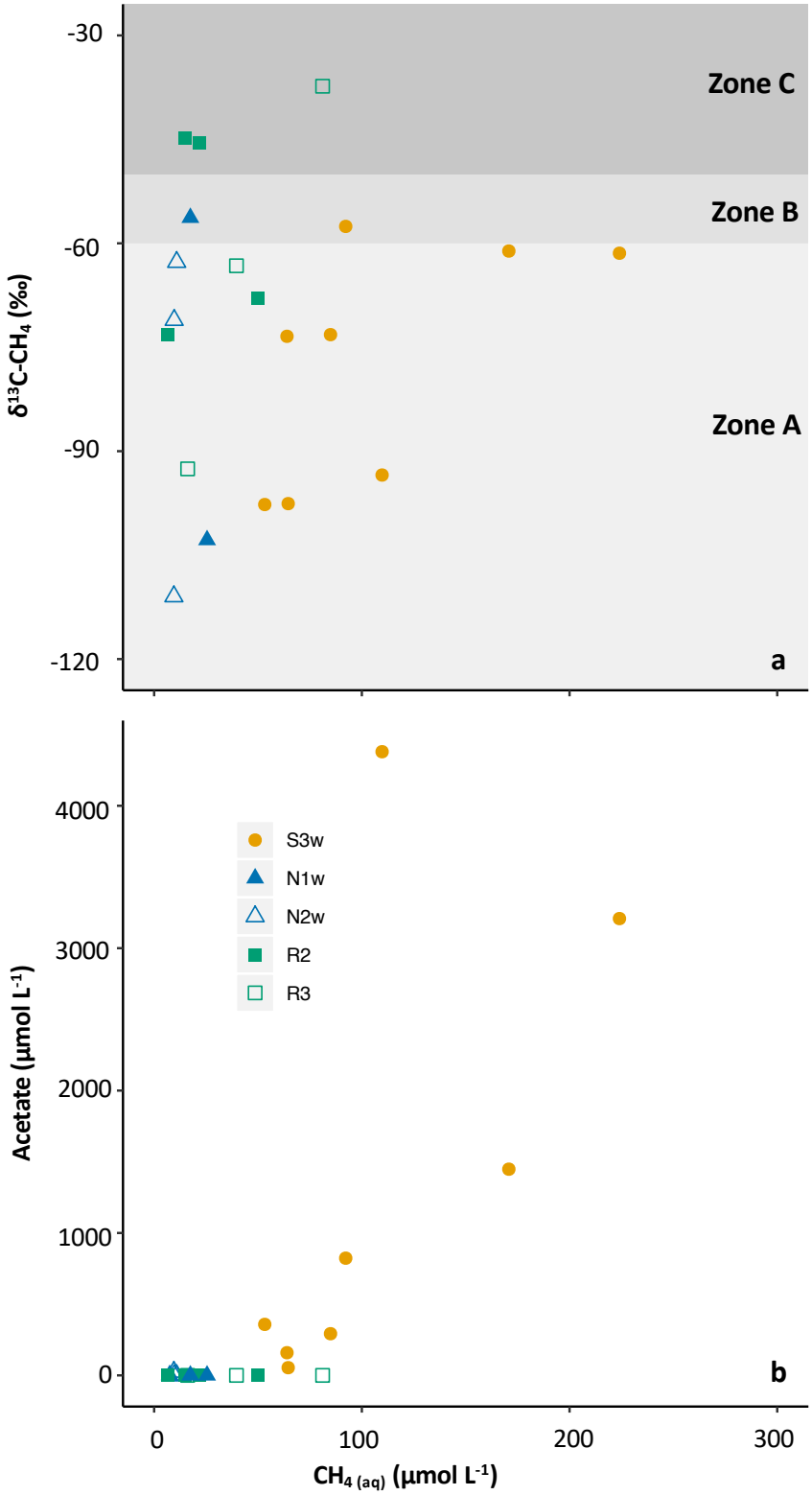

Figure 5.5 a) δ^{13}C-CH_4 plotted as a function of the concentration of $CH_{4\,(aq)}$ in water samples from the active layer, with Zone A representing the isotopic signature of methane produced via the hydrogenotrophic pathway, Zone B representing methane produced via the acetotrophic pathway and Zone C representing *either* thermogenic production of methane *or* isotopic enrichment of methane produced via hydrogenotrophic or acetotrophic methanogenesis and then isotopically enriched by methanotrophy (Whiticar, 1999; Huq et al., 2017), and b) acetate concentration plotted in relation to $CH_{4\,(aq)}$ concentrations in water samples from the active layer.

Table 5.1 Summary table of the relative abundance of archaea involved in producing methane (hydrogenotrophic methanogens, acetoclastic methanogens, and all other methanogens) and consuming methane (methanotrophs) in cores from Ice-wedge North, Ice-wedge South and Revneset. Data provided by Ebbe Norskov Bak (Aarhus University).

Site	Depth (cm)	Relative abundance (%)			
		Hydrogenetrophic methanogens	Acetoclastic methanogens	Methanogens of unclassified metabolic pathway	Methanotrophs
Ice-wedge North	0-25	14	0.0	6.8	79
	25-50	7.9	0.0	11	81
	75-100	13	2.3	11	73
	100-125	6.3	4.6	23	66
	125-150	10	5.2	26	58
	150-175	6.1	2.6	20	71
	175-200	9.1	6.1	24	60
Ice-wedge South	0-25	0.0	0.0	3.0	0.3
	25-50	0.0	0.0	0.8	1.4
	50-75	0.0	0.0	0.0	7.8
	100-125	1.7	0.0	0.0	85
	125-150	0.0	0.0	0.0	0.0
	150-175	0.0	0.0	0.2	98
	175-200	0.0	0.0	0.0	99
	200-225	0.3	0.0	0.0	96
Revneset	0-25	12	5.3	5.3	77
	25-50	12	0.1	29	58
	50-75	11	2.9	59	27
	75-100	57	0.0	0.0	40
	100-125	51	0.0	6.1	43
	125-150	81	0.2	2.1	16

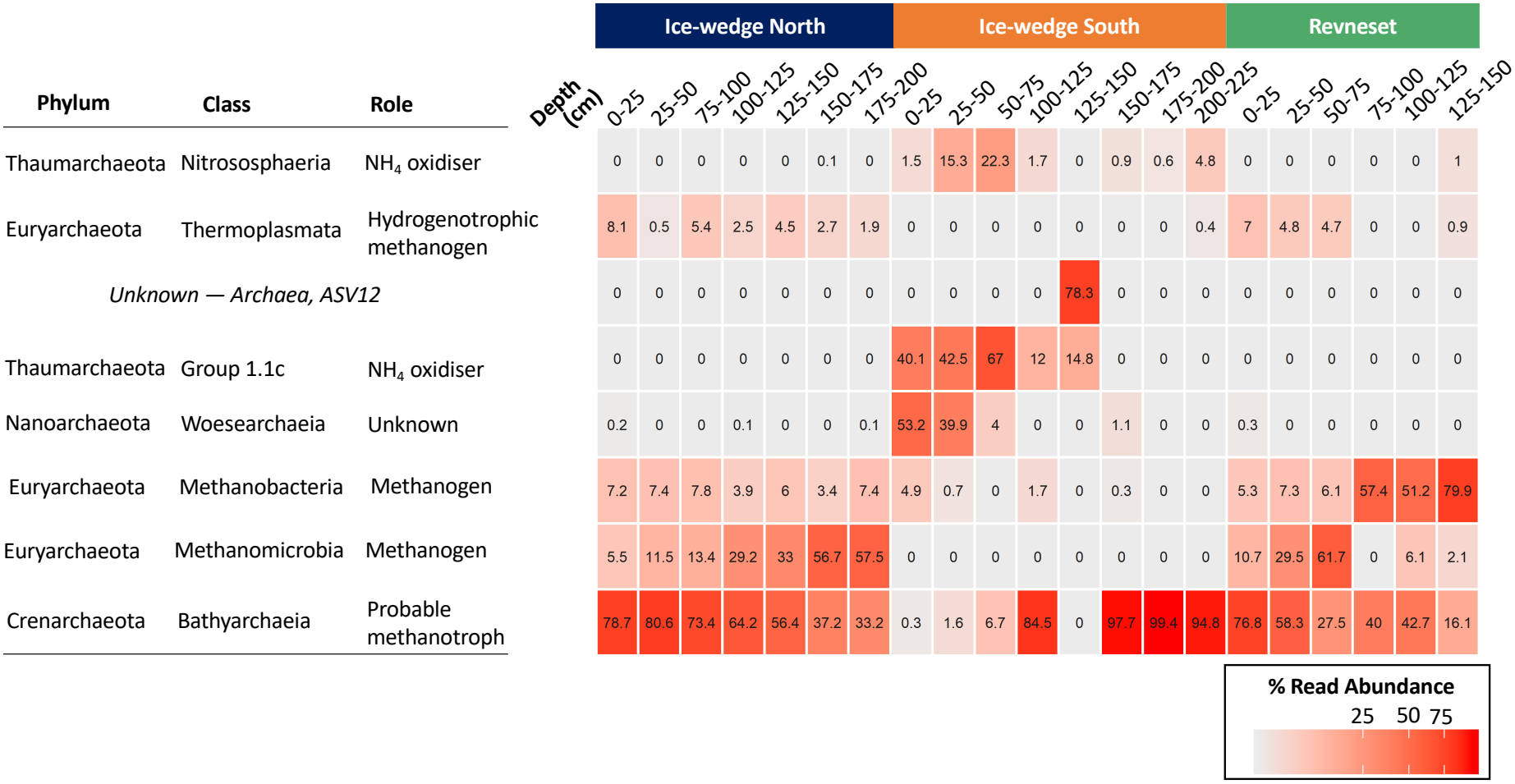

Figure 5.6 Heatmap of the relative abundance (% read abundance) of archaeal classes detected in permafrost cores from Ice-wedge North, Ice-wedge South and Revneset. Functional assignments (where possible) were based on Evans et al. (2015) and Bergey's Manual of Systematics of Archaea and Bacteria (2015). Data provided by Ebbe Norskov Bak (Aarhus University).

5.3 Discussion

The interaction of carbon, iron and sulfur cycling in the permafrost and active layer resulted in higher methane concentrations in organic carbon rich, water-saturated sediments that were undergoing active iron- and sulfate-reduction. However, carbon dioxide concentrations were much higher than methane concentrations, indicating that iron- and sulfate-reduction dominated over methanogenesis. Degradation of an ice-wedge polygon had a substantial impact on biogeochemical cycling and methanogenesis. Isotopic and microbial data from sediments of the shallow permafrost and active layer in Adventdalen and Revneset indicate that the primary mode of methane production was hydrogenotrophic methanogenesis. This is in contrast with atmospheric inversion studies, which assume that methane production from Northern Hemisphere wetlands is dominated by acetotrophic methanogenesis to infer the global sources and sinks of atmospheric methane (Bousquet et al., 2006; Kai et al., 2011). Methane consumption by methanotrophs occurred, particularly in the active layer, resulting in a wide range of $\delta^{13}C\text{-}CH_4$ values within and between sites (Figure 5.5).

5.3.1 Redox and Greenhouse Gases

In cores from Ice-wedge South and Ice-wedge North, the quantity of sediment organic carbon influenced methane production indirectly, by regulating the consumption of alternative electron acceptors, such as iron and sulfate. The negative monotonic correlation between organic carbon content and sulfate concentration (Figure 5.3b), and between organic carbon content and aqueous iron concentration (Figure 5.3c), indicated that generally a higher organic carbon content led to increased iron and sulfate reduction and perhaps also decreased pyrite oxidation (Chapter 3). Both Ice-wedge South and Ice-wedge North displayed evidence of active iron and sulfur cycling, with Ice-wedge North generally displaying more reduced conditions than Ice-wedge South. The reducing conditions at Ice-wedge North were conducive to methanogenesis, with the concentration of methane in the pore water reaching a maximum of 293 µmol L^{-1} (Figure 5.1e). In contrast, methanogenesis appeared to be negligible in most of the core samples from Ice-wedge South, with methane concentrations reaching a maximum of 14.4 µmol L^{-1} (Figure 5.1a-c). A higher organic carbon content was associated with a higher concentration of methane in cores from Adventdalen, although there is variability in this relationship (Figure 5.3a). A positive relationship between the content of organic carbon and the concentration of

methane was also seen in earlier studies in Siberia and in the Western Canadian Arctic (Barbier et al., 2012; Ganzert et al., 2007). The variability in the positive correlation shown in Figure 5.3 is probably the result of diffusion and ebullition of methane, which would cause methane to travel away from the zone of methanogenesis, obscuring the relationship between organic carbon and methane concentration.

Core pore water samples from Adventdalen and Revneset were either rich in methane or in sulfate, resulting in a negative monotonic correlation between methane and sulfate concentration (Figure 5.4a; ρ = -0.46, $p < 0.0001$). In the core pore water samples from Adventdalen alone (Figure 5.4a; cores S1, S2a and S3b), there was a particularly strong relationship between methane and sulfate concentration (ρ = -0.76, $p < 0.001$), and this was true also for water samples from the active layer of Adventdalen (samples S3w, N1w and N2w; ρ = -0.67, $p < 0.01$). In addition, the core pore water samples from Adventdalen displayed a negative monotonic correlation between methane and aqueous iron concentrations (ρ = -0.58, $p < 0.001$; Figure 5.4b). Generally, the samples from Ice-wedge South contained variable sulfate and iron concentrations with low methane concentrations, while samples from Ice-wedge North and Revneset exhibited low sulfate and iron concentrations with variable methane concentrations. Many previous studies have observed the suppression of methanogenesis due to methanogens being outcompeted by sulfate- and iron-reducers for substrates, such as acetate and hydrogen (e.g., Lovley & Phillips, 1987; Lovley & Klug, 1983; Schönheit et al., 1982), and this is a potential factor influencing methanogenesis in the sediments of Adventdalen and Revneset.

Sampling of water from the active layer at the end of summer 2017 revealed intra-site, inter-polygon heterogeneity, with the water-saturated polygon S3 in Ice-wedge South containing the highest concentrations of methane (224 μmol L^{-1}; Figure 5.5) across all the water samples from the active layer. Biased sampling of water from the active layer was necessary in summer 2017 to ensure recovery of water with The Sheffield Spike; this sampling strategy led to sampling the water-saturated polygon S3 in order to recover sufficient water. The advantage of this is that it showed that that the prevailing biogeochemical processes differed dramatically in ice-wedge polygons separated by only ~300 metres. The high degree of heterogeneity in this system is typical of ice-wedge polygons and soils (Coleman et al., 2004; Wainwright et al., 2015; Zona et al., 2011).

Despite the clear indications of methanogenesis at Ice-wedge North, the concentrations of carbon dioxide were much higher, exceeding 6 mmol L^{-1} (Figure 5.2d). In addition, the concentration of carbon dioxide in the pore water exceeded 7 mmol L^{-1} at Ice-wedge South (Figure 5.2a-c). The high concentration of porewater carbon dioxide relative to porewater methane is congruent with previous studies of iron cycling in permafrost, where carbon dioxide was the dominant biogas (Lipson et al., 2012; Miller et al., 2015). In fact, there was a negative correlation between dissolved methane and carbon dioxide in the N1 core ($\rho = -0.69$; $p < 0.001$), with the deeper active layer having most carbon dioxide and least methane. This negative correlation may be indicative of sulfate- and iron-reduction producing more carbon dioxide where there is less methanogenesis occurring. Alternatively, this relationship could be the result of methanotrophs consuming methane and producing carbon dioxide, or of hydrogenotrophic methanogens consuming carbon dioxide during methane production.

Wagner et al. (2007) concluded that methane in the upper permafrost in a core from the Lena Delta in the Siberian Arctic was produced *in-situ* (within the permafrost), rather than being produced in the former active layer and preserved in the permafrost during sedimentation. Their low temperature (< 0 °C) incubations produced methane, and the concentration of methane in the cores was found to correlate well with the biomass of archaea and the activity of methanogens. In fine-textured permafrost soils, liquid water can be present down to -60 °C (Ananyan, 1970). Liquid water, which facilitates the movement of ions and nutrients, is crucial for microorganisms (Ostroumov & Siegert, 1996). The data presented in Figure 5.1 are, unfortunately, not sufficient to discern whether the methane in the shallow permafrost has been preserved during sedimentation and aggradation of permafrost, or whether the methane was produced *in-situ*. However, given that increased methanogenic activity has been found close to the permafrost table and at low temperatures (Ganzert et al., 2007), and that Adventdalen experiences highly variable winter temperatures (-30 °C to slightly above 0 °C) accompanied by episodes of winter rain (Pirk et al., 2016) that would further warm the shallow permafrost, it is likely that at least some of the methane in the shallow permafrost was produced *in-situ*.

5.3.2 Ice-wedge polygon degradation

In Adventdalen, the organic carbon content, coupled with the degree of water saturation, played a critical role in determining the redox conditions and dominant biogeochemical processes

leading to the production of greenhouse gases. It is likely that the water-saturated, low-centred polygons at Ice-wedge North were a net sink of carbon, due to storage of carbon in organic carbon and in siderite (Section 3.3). While the evidence for methanogenesis indicates that these polygons were a methane source, it is possible that this was counteracted by methanotrophy (Section 5.3.3). Flux measurements would be necessary to determine that these polygons are indeed a methane source. The high-centred polygon at Revneset had a low or fluctuating water table, which implied that the active layer was not consistently anaerobic. This meant that, despite the high organic carbon content of the active layer, concentrations of methane in the active layer core pore water were negligible (Figure 5.1f and g). This indicates that the high-centred polygon at Revneset is no longer a methane source. However, the concentration of methane in the water from the active layer of Revneset was up to 81 µmol L^{-1} (Figure 5.1). This could be a result of sampling the Revneset cores from the dry centre of a high centred-polygon, and sampling water from the active layer of nearby ice-wedge polygon troughs (Table 2.1; Figure 2.3). The difference in sampling location (troughs instead of polygon centres) was because water-saturated environments were required for sampling using The Sheffield Spike. Water was ponding in the troughs at the time of sampling, and so the conditions in the troughs were more conducive to methanogenesis (and methanotrophy; Sections 5.3.3 and 5.3.4). In contrast with the active layer in the centre of the ice-wedge polygon, the shallow permafrost, which was rich in organic carbon, contained high concentrations of methane (Figure 5.1f and g). These high concentrations of methane were probably due to a combination of a high content of organic carbon, anaerobic conditions and active methanogens. As discussed in Chapter 4, a high content of organic carbon is characteristic of a water-saturated, low-centred polygon. The high organic carbon content and anaerobic conditions were probably preserved in the permafrost during aggradation of permafrost and were maintained despite subsequent degradation of the polygon. The methane in the shallow permafrost was either produced *in-situ* or was produced in the active layer and preserved during aggradation of the permafrost. The deeper permafrost at Revneset contained lower concentrations of methane, which was most likely to be a result of the lower content of organic carbon at depth. Climate change, which is associated with degradation of ice-wedge polygons in western, coastal permafrost, may therefore already be influencing modern methane biogeochemistry, with the potential for further changes in the future. Thawing and release of methane formerly stored in the permafrost could result in emission of methane to the atmosphere, but this will depend upon the rates of methanotrophy (Sections 5.3.3 and 5.3.4)

5.3.3 Sources and sinks of methane in the active layer

Figure 5.5a shows that most of the methane detected in water from the active layer (locations in Table 2.1) of Adventdalen and Revneset had δ^{13}C-CH_4 values in the range of hydrogenotrophic methanogenesis. The data show no localisation (grouping) around δ^{13}C-CH_4 values in the range of acetotrophic methanogenesis; only two samples contained methane with δ^{13}C-CH_4 values in the relatively narrow range of acetotrophic methanogenesis (-60‰ to -50‰). This is substantiated by evidence from Huq et al. (2017), who found clear evidence of hydrogenotrophic methanogenesis from the δ^{13}C-CO_2 and δ^{13}C-CH_4 of samples from the permafrost and below the permafrost (Figure 5.7). In addition, Table 5.1 indicates that there was a relative abundance of hydrogenotrophic methanogens, compared to acetotrophic methanogens. Hence, there are multiple lines of evidence supporting a mainly hydrogenotrophic source of the methane produced in the permafrost and active layer of Adventdalen and Revneset.

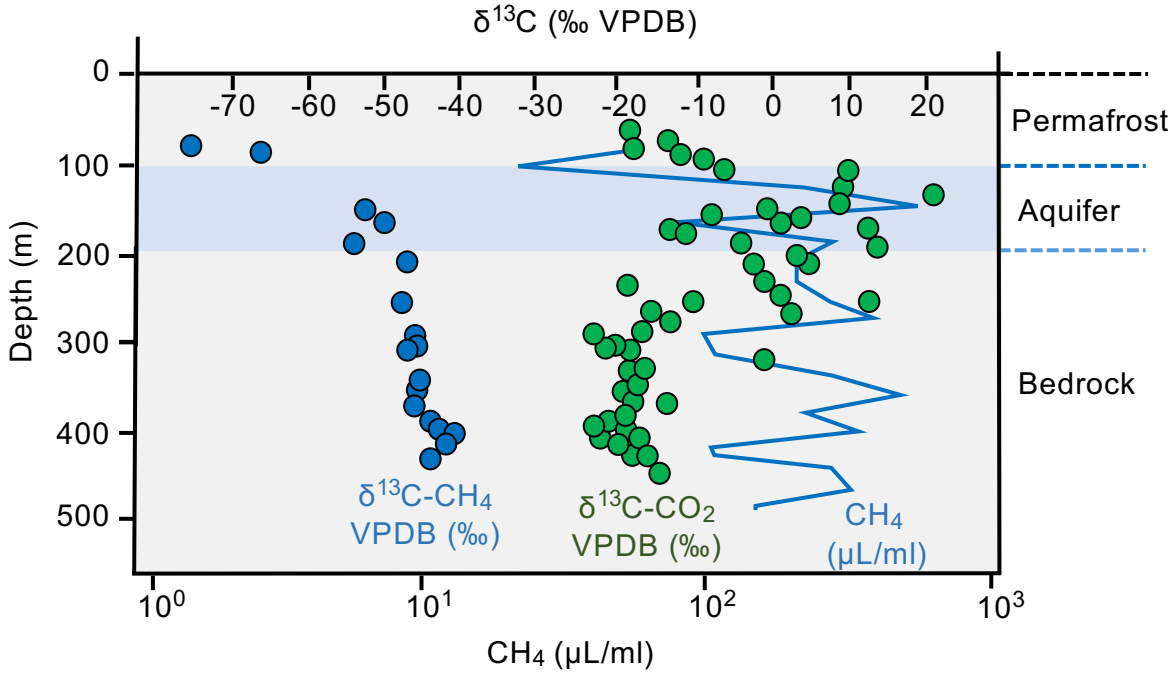

Figure 5.7 Stable isotope characteristics in rock pore gases at different depths. The pore gas analyses are from published results (Huq et al. 2017) from a core collected close to Ice-wedge South. Horizontal dashed lines indicate the approximate permafrost, aquifer and shale boundaries for lower Adventdalen. Figure modified after Hodson et al. (In Review).

The acetate data presented in Figure 5.5b show that acetate rarely accumulated in water from the active layer of Adventdalen and Revneset. Concentrations of acetate were below the limit of detection (4.22 µmol L^{-1}) in 62% of the water samples from the active layer water, all of which

were from Revneset and Ice-wedge North. The low concentrations of acetate may imply either that acetogenesis (the production of acetate via fermentation of low-molecular weight fatty acids and alcohols) was slow, or that the uptake of acetate by bacteria was rapid (e.g., King et al., 1983; Lovley & Klug, 1983). In particular, sulfate- and iron-reducers can outcompete acetotrophic methanogens for acetate (King et al., 1983; Bridgham et al., 2013). Geochemical evidence from the permafrost and active layer presented in Chapters 3 and 4 is indicative of iron- and sulfate-reduction in Ice-wedge North and Revneset. Hence, it could be that, in organic-carbon rich sediments of Ice-wedge North and Revneset, sulfate-reducers kept the acetate concentrations too low for acetotrophic methanogens, resulting in methanogenesis proceeding via the hydrogenotrophic pathway. Dilution by lateral groundwater influx (e.g., Hordijk et al., 1994) is unlikely to have occurred owing to the ice-wedges and polygon rims impeding groundwater flow. Reversible attachment of acetate to the sediment matrix (e.g., Hordijk & Cappenberg, 1983) is also unlikely to have caused the stark difference in acetate concentrations between Ice-wedge North and Ice-wedge South, as both sites are based on similar aeolian sediments.

Samples from polygon S3 at Ice-wedge South contained strikingly high concentrations of acetate (up to 4400 µmol L^{-1}) as well as high concentrations of methane (up to 224 µmol L^{-1}) in the water from the active layer (Figure 5.5b). Furthermore, some water samples from the active layer of Ice-wedge North contained concentrations of acetate (up to 117 µmol L^{-1} in N2) above the detection limit. Clearly, an alternative explanation is required to explain these high concentrations of acetate. The accumulation of acetate is similar to that observed in northern peatlands (Duddleston et al., 2002). In northern peatlands, it appears that acetotrophic methanogens are not capable of utilising acetate as an energy source. Acetate either accumulates or diffuses into oxic peat and is oxidised to carbon dioxide by sulfate or oxygen (Duddleston et al., 2002). This process is “acetate-decoupling” (coined by Hines et al., 2001), and it is not fully understood why the methanogens cannot use the acetate (Bridgham et al., 2013). The samples from Ice-wedge South exhibited a strong, positive correlation between the concentration of acetate and the concentration of methane ($\rho = 0.76$, $p < 0.05$). This strong positive correlation could indicate a lack of acetotrophic methanogens, with methanogenesis instead proceeding via the hydrogenotrophic pathway. This is corroborated by $\delta^{13}C\text{-}CH_4$ values of the samples from Ice-wedge South mainly in the hydrogenotrophic zone (Figure 5.5a). These

isotopic values may imply that hydrogenotrophic methanogenesis was favourable in the environments that were accumulating acetate.

Three of the samples from Revneset had $\delta^{13}C\text{-}CH_4$ values in the range of thermogenic methane (Figure 5.5a). Huq et al. (2017) modelled the diffusion of thermogenic methane from a depth of 800 to 300 metres in Adventdalen. The authors found that thermogenic methane originating from a depth of ~800 metres had been migrating upwards by diffusion over the past 10,000 years. However, they also found that the $\delta^{13}C\text{-}CH_4$ values in the permafrost layer at 100 metres depth were unequivocally biogenic and appeared unaffected by the diffusion of thermogenic methane from the deeper sediments (Figure 5.7). Hence, it is likely that thermogenic methane has not yet reached the permafrost and active layer sediments by diffusion. It is probable, therefore, that the isotopically heavy $\delta^{13}C\text{-}CH_4$ values in water from the active layer of Revneset reflect the influence of methanotrophy, rather than diffusion of thermogenic methane from deeper sediments. Methanotrophy complicates the use of $\delta^{13}C\text{-}CH_4$ values to determine the primary methane source. For instance, if methane produced via the hydrogenotrophic pathway experiences methanotrophy, the enrichment of ^{13}C in the residual methane may cause the $\delta^{13}C$ values of the residual methane to increase and fall in the range of $\delta^{13}C\text{-}CH_4$ values for acetotrophic methanogenesis. Hence, Figure 5.5a alone cannot be used to identify acetotrophic methanogenesis, unless the possibility of methanotrophy can be eliminated. Due to the large spread of $\delta^{13}C\text{-}CH_4$ values within and across sites, the occurrence of methanotrophy is highly probable. Therefore, the low number of samples containing methane appearing in the acetotrophic region (Zone B) of Figure 5.5a could rather be displaying the complex isotopic signature of hydrogenotrophic methanogenesis followed by methanotrophy.

The results presented in Figure 5.5a imply a greater degree of methanotrophy at Revneset (green) compared to Adventdalen (orange and blue). It is possible that this difference is related to degradation of the ice-wedge polygon at Revneset. However, as the water samples from the active layer of Revneset were from ice-wedge polygon troughs and the water samples from the active layer of Adventdalen were from polygon centres, it could be that the isotopic differences reflect the increased methanotrophy in the troughs compared to the centres. Further work, including sampling of the ice-wedge polygon troughs in Adventdalen, would help to discern the reason for the apparently higher rates of methanotrophy at Revneset. In addition, further work is required to determine whether the water from the active layer of Revneset and Adventdalen

was influenced by acetotrophic methanogenesis. It is clear, however, that the $\delta^{13}C$ values of methane show that hydrogenotrophic methanogenesis was the prevalent mechanism of methanogenesis in the water from the active layer of Adventdalen and Revneset.

5.3.4 Molecular approaches to elucidating methane cycling

Table 5.1 shows that there was a relative abundance of hydrogenotrophic methanogens, compared to acetotrophic methanogens. This corroborates the geochemical evidence presented in the previous section of this discussion. Ice Wedge North was dominated by the mainly methanogenic Methanomicrobia at depths below 150 cm, while methanotrophic Bathyarchaeia were dominant at depths above 150 cm (Figure 5.6). This is likely to have resulted in the higher concentrations of methane in the permafrost compared to the active layer (Figure 5.1). A similar microbial trend was evident at Revneset, where in the shallow permafrost, there was a substantial input from Methanobacteria and Methanomicrobia, and the trend from the permafrost into the active layer was towards dominance by the methanotrophic Bathyarchaeia. Overall, methanogenesis dominated in the permafrost and methanotrophy dominated in the active layer of Ice-wedge North and Revneset.

In contrast to Ice-wedge North and Revneset, there was a relatively low abundance of methanogens in Ice-wedge South. It is important to reiterate here that water sampling from the active layer of Ice-wedge South was conducted in a different polygon to coring of permafrost, owing to the biased sampling necessary to achieve recovery of water from the active layer in summer 2017. Water samples of the active layer were obtained from water-saturated polygon S3, whereas molecular analyses were conducted on three cores from a well-drained polygon (S1). Hence, molecular data from Ice-wedge South correspond to geochemical data from the permafrost cores, but are unlikely to explain the geochemistry of water from the active layer of a different polygon. The low relative abundance of methanogens in polygon S1 of Ice-wedge South is in agreement with findings from Müller et al. (2018), who reported low archaeal abundances and found either a very low level or a complete absence of genes involved in methane production. The low relative abundance of methanogens in Ice-wedge South cores could explain the negligible concentrations of methane found in the core from this polygon (S1; Figure 5.1). The composition of the microbial community at Ice-wedge South is likely to vary substantially between polygons. For instance, it could be expected that the high concentrations

of methane detected in polygon S3 would be linked to a higher abundance of methanogens in this water-saturated polygon.

The relative abundance of methanotrophs was high in all the sites (Table 5.15.1). This evidence corroborates the isotopic evidence presented in Figure 5.55.5 and discussed in Section 5.3.3, and may explain why there was such a large spread in $\delta^{13}C\text{-}CH_4$ values observed both within each site and between sites (Figure 5.55.5a). In addition, negligible concentrations of methane in the permafrost cores from Ice-wedge South might be a result both of low rates of methanogenesis and active methanotrophy.

5.4 Conclusions

Concentrations of carbon dioxide were substantially higher than concentrations of methane in the pore water of the cores, due to microbial respiration using ferric iron and sulfate as electron acceptors. The data from the pore water of cores from Ice-wedge South and Ice-wedge North indicated that methanogenesis was controlled by the quantity of organic carbon, coupled with the degree of water saturation (Section 5.3.1). This was linked with the iron and sulfur redox chemistry, as the quantity of organic carbon in these cores regulated the concentrations of alternative electron acceptors via iron and sulfate reduction. In contrast, the degradation of the ice-wedge polygon at Revneset resulted in a decoupling between the concentration of methane and the content of organic carbon (Section 5.3.2). This was exemplified by the absence of methane in the dry, organic carbon-rich active layer of the high-centred ice-wedge polygon. The evidence from the active layer suggests that it is likely that the low-centred, water-saturated ice-wedge polygons were a net sink of carbon, due to storage of carbon in organic carbon and siderite. It is probable that methanotrophy decreased the emissions of methane, or even resulted in the polygons being a net sink of methane. Despite this, the permafrost of the high- and low-centred polygons at Revneset and Ice-wedge North contained high concentrations of methane, which could be released to the atmosphere upon permafrost thawing, depending on the rates of methanotrophy. Quantifying these processes and their influence on greenhouse gas emissions from thawing permafrost would improve the accuracy of predictions of the response of permafrost to climate change.

Hydrogenotrophic methanogenesis was the dominant mode of methanogenesis in the water from the active layer of Adventdalen and Revneset. It is unlikely that thermogenic methane made a substantial contribution to the concentration of methane in the active layer, owing to very slow diffusion of thermogenic methane from depth. Although it is possible that acetotrophic methanogenesis occurred in two samples, consumption of methane by methanotrophs could have produced the same $\delta^{13}C\text{-}CH_4$ signature in the residual methane. The high relative abundance of hydrogenotrophic methanogens and methanotrophs revealed by the microbial data support a conclusion that the $\delta^{13}C\text{-}CH_4$ signatures result from production of methane via the hydrogenotrophic pathway, followed by variable amounts of methane consumption by methanotrophy. The methane data for the water in the active layer were not always directly comparable with that for the pore water in the cores, due to the different timing of the sampling and the slightly different locations of sampling. However, the active layer data are a useful initial indication of the processes producing and consuming methane in Adventdalen and Revneset. Further insights into the modes of methane production and consumption would be gleaned by measuring the $\delta^{13}C\text{-}CH_4$ and $\delta^{13}C$-DIC (dissolved inorganic carbon) of the core pore water. This would be useful because, although the active layer data presented in this chapter indicate that the primary mode of methanogenesis is hydrogenotrophic, it could be that the prevalent pathway of methanogenesis differs between the active layer and the permafrost. Finally, the prevalence of hydrogenotrophic methanogenesis in the data presented in this chapter adds to a body of evidence from Arctic permafrost indicating that the prevalent pathway of methanogenesis varies across the Arctic, and this needs to be accounted for, both in predictions of future climate change, and in atmospheric inversion studies.

Chapter 6. Synthesis and Conclusions

This chapter presents a landscape-scale synthesis of the biogeochemical processes in active layer and shallow permafrost sediments of Adventdalen and Revneset. The thesis aim and objectives are revisited and the work presented in the thesis is discussed in the context of past landscape development and future climate warming. Finally, the limitations of the work are assessed, and recommendations for future research are identified.

6.1 Restatement of Project Aim and Objectives

The motivation for the research presented in this thesis was an appreciation that landscape geomorphology influences biogeochemical processes in permafrost regions, but that this has been frequently overlooked in previous research on permafrost carbon cycling. The key aim of this thesis was to link landscape geomorphology with the biogeochemical processes that lead to the production of methane and carbon dioxide in active layer and shallow permafrost sediments in Adventdalen and Revneset (Svalbard). The specific objectives were to:

1. Assess the variability of biogeochemical processes within two contrasting wetlands in a fjord valley (Adventdalen).

2. Examine the influence of larger-scale landforms (fjord valley, raised beaches) and smaller-scale landforms (ice-wedge polygons) on biogeochemical processes and the concentrations of methane and carbon dioxide in active layer and shallow permafrost sediments in Svalbard.

3. Quantify the sources and sinks of methane in fjord valley (Adventdalen) and intra-beach sediments (Revneset).

6.2 Summary of Findings

The research presented in Chapter 3 follows from hydrological monitoring in the Endalen, Bolterdalen and Longyeardalen catchments, where the oxidation of pyrite exerted a strong control on the composition of fluvial runoff, as evidenced by the presence of high sulfate and

cation concentrations (Hodson et al., 2016; Yde et al., 2008; Rutter et al., 2011). While sulfate reduction and precipitation of pyrite, iron monosulfide and elemental sulfur were inferred from the decreasing concentrations of sulfate and *Fe , these processes were hypothesised to be limited by a paucity of reactive organic matter in the sediments (Hodson et al., 2016; Raiswell & Canfield, 2012). Hence, further work was conducted to test whether the accumulation of organic carbon in such environments led to enhanced rates of iron- and sulfate-reduction. For this, two ice-wedge polygon wetlands (Ice-wedge South and Ice-wedge North) were selected for sampling. Sediment cores from the active layer and shallow permafrost were collected from the sites, pore water was extracted from the sediment cores and was analysed for major ions and metals, while the core sediments were analysed for organic carbon content, iron oxides and iron sulfides. The results from Ice-wedge South indicated that Ca^{2+}, Mg^{2+}, SO_4^{2-} and $Fe_{(aq)}$ in the pore water were primarily sourced from sulfide oxidation coupled to carbonate dissolution. Sulfide oxidation coupled to silicate dissolution was a secondary source of base cations, SO_4^{2-} and $Fe_{(aq)}$. $\delta^{18}O\text{-}SO_4$ and $\delta^{34}S\text{-}SO_4$ values in water from the active layer of Ice-wedge South corroborated these findings, indicating that sulfate in pore water of Ice-wedge South originated from pyrite oxidation via O_2 and pyrite oxidation via Fe^{3+}. These weathering reactions were similar in nature to those reported by Hodson et al. (2016), since both are influenced by the limited availability of organic carbon.

In contrast, the high content of organic carbon in Ice-wedge North caused increased iron- and sulfate-reduction in this water-saturated site. $\delta^{18}O\text{-}SO_4$ and $\delta^{34}S\text{-}SO_4$ values in water from the active layer of Ice-wedge North were indicative of pyrite oxidation via O_2 at depths where the content of organic carbon was low, and of bacterial sulfate reduction (BSR). The products of iron- and sulfate reduction were pyrite (CRS) and siderite (Fe_{carb}), and the quantity of both minerals displayed a positive correlation with the content of organic carbon, supporting the conclusion that enhanced iron- and sulfate-reduction leading to pyrite and siderite precipitation occurred where the content of sediment organic carbon content was high. Finally, Chapter 3 used chloride as a tracer to examine the complex physical processes contributing to variations of geochemical parameters with depth in the pore water profiles. While cryosuction appeared unimportant for vertical migration of ions in both sites, solute exclusion by downward freezing of the active layer was a factor in cores S1, N1 and S2b. Cores S2a and S2b may have been influenced by diffusion of chloride upwards from underlying marine sediments. Overall, however, the physical processes influencing the vertical distribution of ions in the cores were very complex and not well-

constrained by using chloride as a tracer. The key message of Chapter 3 was that the accumulation of organic carbon in water-saturated sediments of a deglaciated high Arctic fjord valley caused a transition from sulfide oxidation coupled to carbonate/silicate dissolution towards enhanced iron-reduction, sulfate-reduction and precipitation of pyrite and siderite. This confirmed the hypothesis of Hodson et al. (2016) that a paucity of organic matter in sediments limited sulfate- and iron-reduction, hence limiting precipitation of pyrite, iron monosulfide and elemental sulfur. It is plausible that precipitation of pyrite, iron monosulfide, elemental sulfur and siderite may result if organic carbon accumulates below the water table of the sediment fans.

Chapter 4 focussed on the effect of landscape geomorphology and ice-wedge polygon degradation on the biogeochemistry of the active layer and shallow permafrost. The aim of this chapter was to compare the biogeochemical processes in intra-beach sediments (Revneset) with water-saturated fjord valley sediments (Ice-wedge North) and to examine the effect of the degradation of an ice-wedge polygon on its biogeochemistry. Two sediment cores from the active layer and shallow permafrost were extracted from a high-centred ice-wedge polygon at Revneset, and the pore water and sediments were analysed in an identical manner to the cores from Ice-wedge South and Ice-wedge North. In addition, water from the active layer was analysed for $\delta^{18}O\text{-}SO_4$, $\delta^{34}S\text{-}SO_4$, $\delta^{18}O\text{-}H_2O$ and $\delta^{2}H\text{-}H_2O$ to determine the primary water sources to Revneset and Ice-wedge North and the sinks for sulfate at Revneset. Finally, active layer and water table depths were measured at the end of summer 2017 to understand the hydrology during the thaw season at these sites. $\delta^{2}H\text{-}H_2O$ and $\delta^{18}O\text{-}H_2O$ values of water from the active layer of Revneset and Ice-wedge North indicated that the primary source of water for Ice-wedge North was winter precipitation, whereas the primary source of water for Revneset was summer precipitation, with evaporation contributing to mask any signature of the input of winter precipitation. The sediments of Ice-wedge North and Revneset were similarly rich in organic carbon, but the ice-wedge polygon at Revneset was much drier, due to a less consistent supply of water and degradation of the ice-wedge polygon. The sites hence exhibited different dominant biogeochemical processes. In the unsaturated active layer of the high-centred ice-wedge polygon at Revneset, iron oxidation resulted in high concentrations of ferrihydrite and low concentrations of pyrite and siderite. The formation of pyrite and siderite in the active layer of Revneset was precluded by the low water table, despite limited isotopic evidence for sulfate reduction. The rate of active layer leaching at Revneset appeared to have remained

approximately constant and there was no evidence of cryosuction or solute exclusion by downward freezing of the active layer. The research in chapter 4 indicated that future degradation of low-centred ice-wedge polygons at Ice-wedge North could lead to more oxidising conditions, with a decrease in iron-reduction and a decreased preservation of pyrite and siderite in the sediments.

Chapter 5 was concerned with quantifying methane and carbon dioxide concentrations in the active layer and shallow permafrost sediments of Ice-wedge South, Ice-wedge North and Revneset, to elucidate the biogeochemical processes leading to methanogenesis and to infer methanogenic metabolic pathways. Sediment cores were analysed in an identical manner to Chapters 3 and 4, with the additional analysis of methane and carbon dioxide concentrations. Water was sampled from the active layer and analysed to determine the concentrations of methane and carbon dioxide, in addition to the $\delta^{13}C$ values of methane. $\delta^{13}C\text{-}CH_4$ values showed that the primary source of methane in the active layer was hydrogenotrophic methanogenesis. In addition, sequencing data showed that hydrogenotrophic methanogens were more abundant than acetotrophic methanogens in cores of the active layer and shallow permafrost. However, there was a high relative abundance of methanotrophs and the detected methane was relatively enriched in ^{13}C, suggesting that methanotrophs in the active layer consumed methane. At Ice-wedge North and Revneset, there was a greater abundance of methanogens in the permafrost compared to the active layer, with a greater abundance of methanotrophs in the active layer compared to the permafrost. This fits with the higher concentrations of methane in the permafrost compared to the active layer. The low relative abundance of methanogens in the cores from Ice-wedge South could explain the low concentrations of methane in the same polygon. However, it is clear from higher methane concentrations in the active layer of a different, water-saturated, polygon from Ice-wedge South that methane production is spatially variable across polygons within this site. Across all the sites, the methane concentration was higher in water-saturated sediments that had higher organic carbon content. A higher concentration of methane was inferred to reflect the removal of iron and sulfate from solution by iron- and sulfate-reduction where there was sufficient organic carbon, which created redox conditions more conducive to methanogenesis. Carbon dioxide concentrations in the sediment cores were substantially higher than methane concentrations, in part due to iron- and sulfate-reduction.

Chapter 5 showed that while the quantity of sediment organic carbon and degree of water saturation controlled methanogenesis in Adventdalen, the degradation of the ice-wedge polygon at Revneset resulted in a decoupling between methane concentration and organic carbon content. It was suggested that the water-saturated, low-centred polygons in Ice-wedge North were a net sink of carbon, due to carbon storage in organic carbon and siderite. Although methanogenesis occurred in these polygons, there was partial consumption of the methane by methanotrophs. The high-centred polygon at Revneset is likely to have become a net carbon source, due to siderite oxidation, sulfate-reduction and perhaps aerobic respiration of peat producing carbon dioxide. However, this polygon is likely to be a methane sink, due to methanotrophy in the active layer. Nonetheless, methane concentrations in the permafrost of Ice-wedge North and Revneset were high, and the release of this methane to the atmosphere upon permafrost thawing will depend on rates of methanotrophy. The prevalence of hydrogenotrophic methanogenesis in Adventdalen and Revneset is in contrast to the assumption made in atmospheric inversion studies that methane produced in wetlands is dominated by acetotrophic methanogenesis (Bousquet et al., 2006; Kai et al., 2011). Atmospheric inversion studies and predictions of future climate change must account for this variability in the dominant methanogenic pathway.

6.3 Synthesis

The essence of this thesis is that post-glacial landscape development, coupled with present and future permafrost degradation, influences carbon, iron and sulfur cycling in Adventdalen and Revneset, and is therefore likely to be important across deglaciated Arctic permafrost regions (Figure 6.1). The aim of this section is to place the present-day biogeochemical processes in active layer and shallow permafrost sediments in Svalbard in a longer-term biogeochemical context. To achieve this, the following section presents an overview of the biogeochemical development of Adventdalen and Revneset over the past 20 ka, culminating in a proposed descriptive conceptual model of probable future biogeochemical changes in Adventdalen and Revneset.

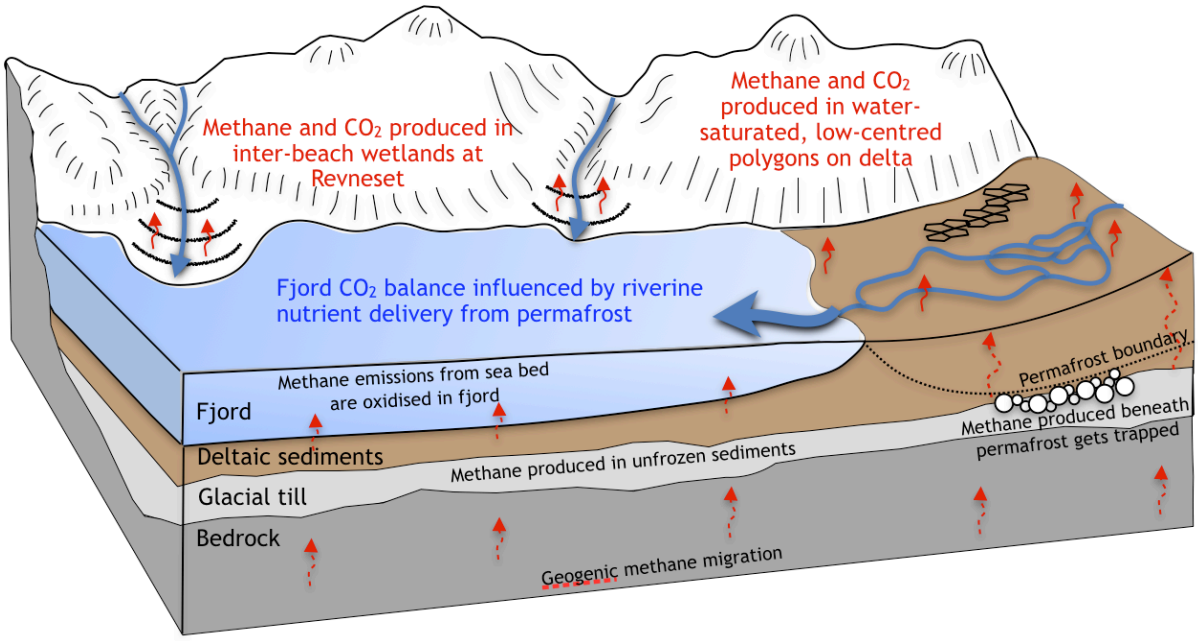

Figure 6.1 A conceptual model of methane and carbon dioxide production in the post-glacial permafrost landscape central to the research in this thesis. Methane seepage from deep, natural (thermogenic) gas occurs in addition to methane associated with continental ice sheet retreat. There is production of carbon dioxide and methane (hydrogenotrophic pathway) in the active layer and shallow permafrost sediments of Adventdalen and Revneset. Figure modified from the LowPerm final project report (A. Hodson, pers. com.).

Chapter 1 introduced the concept that in the most recent glacial advance, the Last Glacial Maximum (LGM; 20 ka), the entire archipelago of Svalbard was covered by the Svalbard-Barents ice sheet (Landvik et al., 1988; Landvik et al., 2005). Previous work on present-day ice sheets has shown that their subglacial environments are highly geochemically reactive (Wadham et al., 2010). Sulfide oxidation coupled to silicate dissolution tends to dominate beneath ice sheets (Wadham et al., 2010). While methane has only rarely been detected in subglacial meltwaters of valley glaciers (Burns et al., 2018), the basal environment of ice sheets may be more conducive to methanogenesis, provided that conditions are anoxic, with sufficient organic carbon and meltwater (Wadham et al., 2008; Wadham et al., 2019). Recently, subglacial runoff from two Greenlandic catchments has been found to be supersaturated with biogenic methane (Dieser et al., 2014; Lamarche-Gagnon et al., 2019). The subglacial biogenic methane source is supplemented by thermogenic methane (Wadham et al., 2012; Crémière et al., 2016). Once the concentration of methane in subglacial sediment pore water reaches saturation, the formation of methane hydrates is favoured by the low temperature and high pressure conditions at the base of ice sheets (Wadham et al., 2012; Weitemeyer & Buffett, 2006; Portnov et al., 2016). As the LGM drew to a close, deglaciation caused methane hydrates to become thermodynamically unstable, resulting in methane release from sea floor pockmarks (submarine fluid escape

features; Smith et al., 2001; Weitemeyer & Buffett, 2006; Crémière et al., 2016). Escape of methane associated with continental ice sheet retreat is still occurring from submarine seepages in Svalbard (Wallmann et al., 2018). However, methanotrophy in the water column above the pockmarks results in only a small fraction of the dissolved methane reaching the atmosphere (Mau et al., 2017). Following deglaciation, uplifted pockmarks can form pingos during permafrost aggradation (Hodson et al., 2019). Pingos provide significant contributions to terrestrial methane emissions because they route groundwater to the ground surface with little opportunity for interaction with methanotrophic water and soil ecosystems (Hodson et al., 2019). Otherwise, thermogenic methane produced at depth only seeps upwards slowly (Huq et al., 2017), owing to the low hydraulic conductivity of the marine infills. In summary, assuming that weathering processes beneath the Svalbard-Barents ice sheet during the LGM were similar to those beneath present-day ice sheets, it is likely that the subglacial environment of the Svalbard-Barents ice sheet was dominated by sulfide oxidation coupled to silicate dissolution. The subglacial environment of the Barents-Svalbard ice sheet facilitated methanogenesis, and the release of the methane initiated by deglaciation is still occurring today (Figure 6.2).

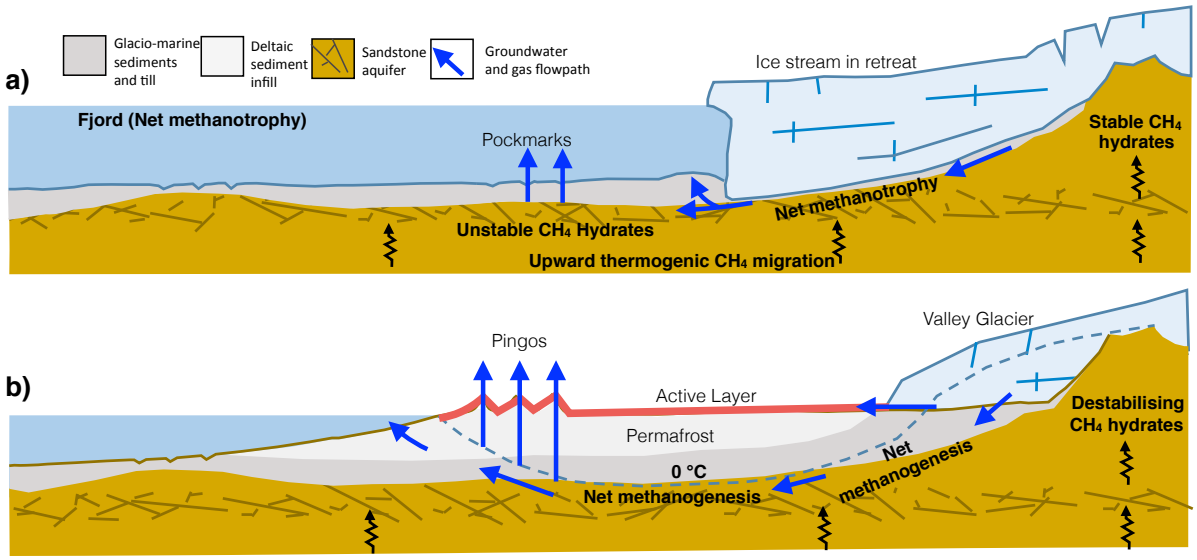

Figure 6.2 Conceptual model of dominant methane sources and sinks a) 11 ka. and b) the present day in Adventdalen. Methane sources include destabilising methane hydrates, deep thermogenic methane and zones of net methanogenesis (e.g., some active layers and permafrost sediments). Methane sinks (zones of net methanotrophy) exist in the fjord and potentially in some active layers and permafrost sediments. Modified after Hodson et al. (2019, In Review).

During deglaciation deltaic sediments were deposited in the fjord and their subsequent uplift by isostatic recovery of the land surface led to permafrost aggradation. Prior to the accumulation of substantial quantities of organic carbon in these sediments, it is likely that the chemical

composition of active layer and permafrost pore water was determined primarily by weathering of reactive, fine-grained sediments. Pyrite oxidation exerts a strong control on the chemical composition of fluvial runoff (Hodson et al., 2016; Yde et al., 2008; Rutter et al., 2011) and Chapter 3 confirmed the importance of this process in the present-day active layer and shallow permafrost sediments and pore water of Ice-wedge South. In these sediments, sulfide oxidation coupled to carbonate weathering was the main source of cations and sulfate, and silicate weathering coupled to sulfide oxidation was a secondary source of cations and sulfate.

Following the retreat of the ice sheet, the recently deglaciated terrain would have lacked vegetation cover (Wietrzyk et al., 2018). Tishkov (1986) studied primary succession on landforms on the west coast of Spitsbergen and found that the total time for primary succession ranged from around 800 to 3500 years. The growth of vegetation in deglaciated terrain is linked to nutrient and water supply (Burga et al., 2010). Following deglaciation, a consistent supply of water to sediments during the thaw season would have induced anoxia, which, combined with low temperatures, would have restricted extensive decomposition of vegetation organic matter, facilitating peat formation. The accumulation of peat would have been influenced by changing site-specific characteristics (such as hydrology) and by climatic variations during the Holocene. Results from Ice-wedge North indicated that in present-day sediments with abundant organic carbon, geochemical signals of weathering were masked by biogeochemical processes such as iron- and sulfate-reduction, which produce carbon dioxide and result in the formation of pyrite and siderite (Chapter 3). The abundance of organic carbon facilitated the maintenance of reducing conditions and hydrogenotrophic methanogenesis occurred with associated methanotrophy at shallower depths (Chapter 5). It is likely that present-day Ice-wedge North is a net sink of atmospheric carbon, due to storage of carbon in organic matter and siderite formation. It is not yet clear how the quantity of methane emitted from shallow active layer sediments in such environments compares to methane emissions from nearby pingos, but release of methane stored in the underlying shallow permafrost sediments could become an additional carbon source under climate warming.

The mean annual air temperature (MAAT) in Longyearbyen, Svalbard, has increased by 1.25 °C per decade in 1989-2011 (Førland et al., 2011) and the rising air temperature has caused a recent increase in permafrost temperature (Isaksen et al., 2007). Degradation of ice-wedge polygons in response to rising air temperatures and thawing ground ice has been observed across the Arctic

(e.g., Sachs et al., 2010; Lara et al., 2015). However, no dramatic degradation of ice-wedge polygons has occurred in Adventdalen (Pirk et al., 2017a). The biogeochemical state of a high-centred polygon at Revneset provides inferences on the future of low-centred polygons at Ice-wedge North. Degradation of an ice-wedge polygon at Revneset resulted in an overall drainage of water and drying of the polygon centre. This has led to oxidising conditions, a decrease in iron-reduction and decreased preservation of pyrite and siderite in the sediments. Degradation has also resulted in an absence of methane in the active layer, and further degradation could cause the release of methane presently stored in permafrost. However, the amount of methane released from the permafrost will depend on rates of methanotrophy. The high hydraulic conductivity of the beach sediments and peat at Revneset are likely to facilitate drainage of water. However, even in fjord valley infill sediments at Ice-wedge North, there is a possibility that lateral drainage of water will occur as a result of the degradation of ice-wedge polygons. If ice-wedge polygons at Ice-wedge North were to follow a similar trajectory to the polygon at Revneset, low-centred polygons would progressively transform to high-centred polygons, with oxidising conditions, a decrease in iron-reduction, and oxidation of pyrite, siderite and methane in the sediments.

Degradation of ice-wedge polygons may have less of an impact on biogeochemical cycling at Ice-wedge South, due to the already drier sediments and lower accumulation of organic carbon. However, conditions within ice-wedge polygons at Ice-wedge South are heterogeneous, with some water-saturated polygons displaying clear indications of methanogenesis. Across the ice-wedge polygonal terrain of Adventdalen and Revneset, it is likely that permafrost will become a sink of methane, due to degradation of ice-wedge polygons and drainage of water from the landscape. It is possible that a transformation to high-centred polygons will result in increased carbon dioxide emissions and that, despite methanotrophy, the polygons will be a net carbon source. As ~250 000 km^2 of the Arctic is covered by polygon tundra (Minke et al., 2007), this transformation could have a substantial impact on the future permafrost carbon feedback. Further work is required to quantify the impact of ice-wedge polygon degradation across Adventdalen on the biogeochemistry of pore water and fluxes of methane and carbon dioxide to the atmosphere.

6.4 Recommendations for Future Research

The limitations of this study inform the following recommendations for future research.

6.4.1 Sources and quality of organic carbon

Accumulation of organic carbon in active layer and shallow permafrost sediments of Adventdalen and Revneset has a substantial impact on the cycling of iron and sulfur, as well as on the production of methane. Further information on the sources and quality of organic carbon would complement this study. There are various typical sources of permafrost carbon, which include undecomposed plant roots, infiltrating dissolved organic carbon and mineral-associated organic matter in loess (Waldrop et al., 2010). Future research should focus on analysing plant macrofossil residues and $\delta^{13}C$ values of organic carbon to reconstruct the history of peat accumulation and changing plant assemblages (e.g., Andersson et al., 2012). These analyses would be complemented by radiocarbon dating peat deposits to determine the time of initiation of peat formation at Revneset and Ice-wedge North and the varying rates of peat accumulation through time. This could provide insight into the rate of accumulation of organic carbon and carbon drawdown in other regions in the high Arctic that either have a shared history of glaciation and glacial isostatic rebound, or that have a probable future of deglaciation (e.g., Greenland). Further valuable research would include linking these analyses with grain size analyses of Ice-wedge North, to ascertain whether the varying location of sediment fans cascading down the steep valley side of Adventdalen was implicated in altering the rate of organic carbon accumulation over time.

Vegetation type influences the rate of organic carbon decomposition and the spatial variability of methane emissions in Arctic tundra (Schuur et al., 2008; Davidson et al., 2016). It is imperative that future research on the biogeochemistry of Adventdalen and Revneset considers the role of vegetation in organic carbon quality, decomposition rate and methane emissions. The quality, or decomposability, of soil organic carbon affects the rate of release of permafrost carbon to the atmosphere (Schädel et al., 2014). There are various approaches to assessing carbon quality, or decomposability. Schädel et al. (2014) constructed a three-pool carbon decomposition model based on the turnover time of organic carbon during incubations. Strauss et al. (2015) used a multiproxy approach, including the analysis of lipid biomarkers, to ascertain permafrost carbon

quality. Waldrop et al. (2010) instead focussed on analysing spectra obtained from solid state ^{13}C nuclear magnetic resonance (NMR) spectroscopy to determine the inherent chemical composition of soil organic matter. It would also be useful to understand changes in microbial community composition and how this influences the regional carbon content of the soil. There is scope for future studies to apply these diverse approaches in Adventdalen and Revneset to refine and extend the information on organic carbon presented in this thesis.

6.4.2 Iron and sulfur cycling

Measurements of $\delta^{13}C$ of siderite and $\delta^{34}S$ in pyrite from Ice-wedge North would provide further evidence for the sources of these mineral phases in the sediments. This could be supplemented with incubations to ascertain the rate of siderite and pyrite formation in the sediments. It is hoped that this would corroborate the results from Chapter 3, which suggest that pyrite and siderite form *in-situ* in sediments of Ice-wedge North. Measuring $\delta^{13}C$ in siderite could confirm that the bicarbonate mainly originates from degradation of organic matter, rather than from sea water (e.g., Mortimer et al., 2011). Furthermore, measuring $\delta^{34}S$ in pyrite could validate the hypothesis that pyrite in sediments of Ice-wedge North is indeed authigenic. Authigenic pyrite would be more enriched in ^{34}S compared to bedrock, owing to fractionation by sulfate-reduction. Furthermore, in Chapter 3, it was noted that the all sulfate was enriched in ^{34}S compared with the bedrock pyrite. The enrichment could result from of the breakdown of humic matter or plant material. This requires testing by measuring $\delta^{34}S$ in carbon-bonded sulfur at the sites.

6.4.3 Methane fluxes

A deeper understanding of the relationship between net surface methane and carbon dioxide fluxes and biogeochemical profiles in Ice-wedge South, Ice-wedge North and Revneset would be valuable. This could be achieved by measuring methane and carbon dioxide fluxes from the study sites, which would also help to discern whether the sites are a sink or a source of carbon to the atmosphere. Such experiments were attempted with manual flux chambers in 2016, but infrequent and temporally variable sampling protocols led to substantial uncertainty in flux estimates. This was compounded by the difficulty of accessing Ice-wedge North during the summer, when there was high discharge through Adventelva. An automatic closed chamber

system to continuously monitor methane and carbon dioxide fluxes, such as that used by Pirk et al. (2017b) near to Ice-wedge South, would be ideal for continuously measuring methane and carbon dioxide fluxes, particularly at Ice-wedge North and Revneset. Further, it would be useful to understand the environmental reasons for the dominance of hydrogenotrophic methanogenesis over acetotrophic methanogenesis, and the scattered accumulation of acetate, at the study sites. This could be addressed by analyses of the δD of methane and δ^{13}C of dissolved organic carbon, as well as amended incubations of sediments to determine geochemical or microbiological factors that limit acetotrophic methanogenesis or enhance hydrogenotrophic methanogenesis.

6.4.4 Replication

The research presented in this thesis was unusual in analysing permafrost cores at such a high depth resolution. This was useful in that it demonstrated that permafrost biogeochemistry is variable with depth and that it would be incorrect to assume that an active layer sample represents the underlying permafrost. However, it was very time-consuming to analyse the permafrost cores at this high depth resolution and this limited the time available for comprehensive replication of the permafrost core analyses. Although some replication in permafrost cores was achieved (2 cores from Ice-wedge North, 3 from Ice-wedge South and 2 from Revneset), a useful future sampling design should focus on measuring features better suited to scaling up the dominant biogeochemical processes for this region. For instance, ice-wedge polygons are commonplace in this landscape and are easily recognisable from readily available aerial photographs, as are fjord valleys and raised beaches. Ascertaining intra-site, inter-polygon and intra-polygon biogeochemical variability would better establish whether particular landscape features are biogeochemically similar. In practice this would mean a sampling at a coarser resolution with depth, in order to allow time and resources for sampling more polygons within each site, and sampling different polygon features (polygon centres, troughs and rims) in each polygon. This would allow future estimates of biogeochemical processes in specific landforms to be based on measuring fewer parameters. For instance, the water in the active layer of polygon S3 at Ice-wedge South was sampled only because it proved difficult to extract water from the drier polygons with The Sheffield Spike. Analyses of water from this polygon showed a remarkable accumulation of acetate and clear evidence of methanogenesis, in contrast to the other polygons sampled at Ice-wedge South. Clearly, this

polygon was overlooked in the permafrost coring sampling design, and it would be useful to ascertain by surface features or indirect measurements which polygons are similar to S3. In addition, it would be helpful to core polygon S3 and study the bioavailability of the organic matter and the conditions that lead to high acetate and methane concentrations.

A limitation of this study is the failure to consider inter-annual variability in active layer and permafrost biogeochemistry. Further extensions to the work presented here would be to study inter-annual variability, development of active layer biogeochemistry with progression of the annual thaw season and connections with active layer hydrology. This would require frequent site visits during the thaw season over a number of years. Hence, this type of work is probably best suited to Ice-wedge South, which is the most accessible site. Ice-wedge South contains both dry and water-saturated polygons. Hence, Ice-wedge South is an ideal site to examine the impact of hydrology on polygon biogeochemistry and the manner in which polygon active layer biogeochemistry develops over the thaw season. It is clear from the results in this thesis that polygons at Ice-wedge South have a large range in their water-saturation, with some polygons being much drier than others, and that this leads to differences in biogeochemistry and methanogenesis. It would be helpful to know whether the quantity of organic carbon varies between polygons within a site, whether some polygons are consistently water-saturated while others remain dry, and whether polygon hydrology varies on an annual or seasonal basis.

6.4.5 Geomorphology of Revneset

Visits to Revneset during this project were limited by time at the site, due to a variety of logistical challenges. There is scope for future research to consider the geomorphology of Revneset in much greater detail. For instance, it is not yet known why or when the lake at Revneset formed, or whether the lake was implicated in the degradation of down-slope ice-wedge polygons. It may yield useful insights to link the formation of the lake with sea level history. For instance, Lønne & Nemec (2004) linked the formation of successive spits as relative sea level fell to the formation of Moskuslaguna (an intertidal lagoon) in Adventdalen. While the lake at Revneset could have formed by a similar mechanism, it could instead have formed by underlying fine-grained bedrock and permafrost impeding the drainage of water from the area. Later, water draining laterally from the lake may have initiated the degradation of ice-wedge polygons downstream by thermal erosion of the ice wedges. It would in addition be beneficial for future

research to quantify the influence that the lake has on water biogeochemistry in the active layer of downstream ice-wedge polygons.

6.4.6 Other deglaciated coastal regions

While the conclusions drawn from this study are specific to Adventdalen and Revneset, it is likely that there are broad similarities to other previously glaciated fjord valleys or coastal regions in continuous permafrost. The history of glaciation and deglaciation is typical across the high Arctic (Gilbert et al., 2018) and so the evidence presented in this study may be broadly applicable to other high Arctic settings. As glaciers retreat, fjord valleys have rapid sedimentation and organic carbon burial rates, forming valley infills that are ideal for methanogenesis (Gilbert et al., 2017; Gilbert et al., 2018; Smith et al., 2015; Syvitski et al., 1986). In fact, over the past 10,000 years, almost one quarter of global marine sedimentation has occurred in fjords (Syvitski et al., 1987). Glacial retreat and postglacial isostatic rebound has occurred across much of the Arctic, uplifting fjord systems (Milne & Shennan, 2007). For instance, following deglaciation, the marine limit in the Canadian high Arctic varies, but reaches as high as >130 metres above sea level (England et al., 2006), and in Greenland it reaches a maximum of 140 metres above sea level (Bennike et al., 2011). The highest marine limit in Novaya Zemlya is 13.5 metres above high tide and 49 metres above high tide in Franz Josef Land, Russia (Forman et al., 2004; Zeeberg et al., 2001; Forman et al., 1996). It would be informative to conduct a similar study to this in coastal sediments that have experienced isostatic rebound and permafrost aggradation following ice sheet retreat. Such future study might be profitably focussed on coastal Greenland or the Canadian high Arctic. If similar processes occur in these locations, it would useful to incorporate some of the biogeochemical mechanisms into models of the permafrost carbon feedback.

Finally, this research on the present state of permafrost biogeochemistry in Svalbard raises further questions about the evolution of the study sites and similar sites in the future. Future changes in in the biogeochemistry of permafrost will be closely linked to changes in hydrology and geomorphology. For instance, the scale and timing of future degradation of ice-wedge polygons will impact their biogeochemistry and emissions of methane; the form, amount and timing of precipitation will regulate hydrology and hence the biogeochemistry of permafrost; and air and ground temperature will influence the thawing of permafrost, rates of weathering and microbial activity. However, the timing and relative importance of these future changes is

not well-known for the study sites and further research is required to constrain this uncertainty. Further uncertainties include, but are not limited to, the rate of decrease in carbon storage in permafrost in these sites, changing grazing patterns, and changing vegetation. Changes in permafrost are coupled to the fjord by runoff and to the atmosphere by greenhouse gas emissions. If ice-wedge polygons remain water-saturated and low-centred, it is likely that this will decrease the adverse impact of permafrost thaw both on the atmosphere and on downstream ecosystems. However, if polygons degrade across Adventdalen and other similar regions in the high Arctic, this could lead to drying of the landscape, rapid loss of carbon as carbon dioxide, and oxidation of pyrite and siderite.

References

Ala-aho, P., Soulsby, C., Pokrovsky, O.S., Kirpotin, S.N., Karlsson, J., Serikova, S., Vorobyev, S.N., Manasypov, R.M., Loiko, S. & Tetzlaff, D., 2018. Using stable isotopes to assess surface water source dynamics and hydrological connectivity in a high-latitude wetland and permafrost influenced landscape. *Journal of Hydrology*, 556, pp. 279–293.

Amstaetter, K., Borch, T. & Kappler, A., 2012. Influence of humic acid imposed changes of ferrihydrite aggregation on microbial Fe(III) reduction. *Geochimica et Cosmochimica Acta*, 85, pp. 326–341.

Ananyan, A.A., 1970. Unfrozen water content in frozen clay at a temperature from 0.6 °C to -40 °C – -60 °C. *Merzlotnye Issledovaniya*, 10, pp. 267-270 (in Russian).

Andersen, K.S., Kirkegaard, R.H., Karst, S.M. & Albertsen, M., 2018. ampvis2: an R package to analyse and visualise 16S rRNA amplicon data. *bioRxiv*.

Andersson, R.A., Meyers, P., Hornibrook, E., Kuhry, P. & Mörth, C.M., 2012. Elemental and isotopic carbon and nitrogen records of organic matter accumulation in a Holocene permafrost peat sequence in the East European Russian Arctic. *Journal of Quaternary Science*, 27(6), pp. 545–552.

Anisimov, O.A., Vaughan, D.G., Callaghan, T., Furgal, C., Merchant, H., Prowse, T., Vilhjálmsson, H. & Walsh, J., 2007. Polar regions (Arctic and Antarctic). In M. L. Parry et al., eds. *Climate Change 2007: Impacts, Adaptation and Vulnerability. Contribution of Working Group II to the Fourth Assessment Report of the Intergovernmental Panel on Climate Change*. Cambridge: Cambridge University Press, pp. 653–685.

Balci, N., Shanks, W.C., Mayer, B. & Mandernack, K.W., 2007. Oxygen and sulfur isotope systematics of sulfate produced by bacterial and abiotic oxidation of pyrite. *Geochimica et Cosmochimica Acta*, 71(15), pp. 3796–3811.

Barbier, B.A., Dziduch, I., Liebner, S., Ganzert, L., Lantuit, H., Pollard, W. & Wagner, D., 2012. Methane-cycling communities in a permafrost-affected soil on Herschel Island, Western Canadian Arctic: Active layer profiling of mcrA and pmoA genes. *FEMS Microbiology Ecology*, 82(2), pp. 287–302.

Bennike, O., Wagner, B. & Richter, A., 2011. Relative sea level changes during the Holocene in the Sisimiut area, south-western Greenland. *Journal of Quaternary Science*, 26(4), pp. 353–361.

Berner, R.A., 1967. Thermodynamic stability of sedimentary iron sulfides. *American Journal of Science*, 265(9), pp. 773–785.

Bethke, C.M., Sanford, R.A., Kirk, M.F., Jin, Q. & Flynn, T.M., 2011. The thermodynamic ladder in geomicrobiology. *American Journal of Science*, 311(3), pp. 183–210.

Bianchi, T.S., Schreiner, K.M., Smith, R.W., Burdige, D.J., Woodard, S. & Conley, D.J., 2016. Redox Effects on Organic Matter Storage in Coastal Sediments During the Holocene: A Biomarker/Proxy Perspective. *Annual Review of Earth and Planetary Sciences,* 44(1), pp. 295-319.

Birks, H.H., 1991. Holocene vegetational history and climatic change in west Spitsbergen - plant macrofossils from Skardtjørna, an Arctic lake. *The Holocene*, 1(3), pp. 209-218.

Blodau, C., Mayer, B., Peiffer, S. & Moore, T.R., 2007. Support for an anaerobic sulfur cycle in two Canadian peatland soils. *Journal of Geophysical Research: Biogeosciences*, 112(2), p.G02004.

Bloom, A.A., Palmer, P.I., Fraser, A., David, S.R. & Frankenberg, C., 2010. Large-scale controls of methanogenesis inferred from methane and gravity spaceborne data. *Science*, 44(1), pp. 295-319.

Blum, J.D., Gazis, C.A., Jacobson, A.D. & Chamberlain, C.P., 1998. Carbonate versus silicate weathering in the Raikhot watershed within the High Himalayan Crystalline Series. *Geology*, 26(5), pp. 411.

Boden, T.A., Marland, G. & Andres, R.J., 2011. Global, Regional, and National Fossil-Fuel CO_2 Emissions. *Carbon Dioxide Information Analysis Center, Oak Ridge National Laboratory, U.S. Department of Energy, Oak Ridge, Tenn., U.S.A.*, pp.1981–1982.

Bottrell, S.H. & Tranter, M., 2002. Sulphide oxidation under partially anoxic conditions at the bed of the Haut Glacier d'Arolla, Switzerland. *Hydrological Processes*, 16, pp. 2363-2368.

Bottrell, S.H., Hatfield, D., Bartlett, R., Spence, M.J., Bartle, K.D. & Mortimer, R.J.G., 2010. Concentrations, sulfur isotopic compositions and origin of organosulfur compounds in pore waters of a highly polluted raised peatland. *Organic Geochemistry*, 41(1), pp. 55–62.

Botz, R., Pokojski, H.-D., Schmitt, M. & Thomm, M., 1996. Carbon isotope fractionation during bacterial methanogenesis by CO_2 reduction. *Organic Geochemistry*, 25(3–4), pp. 255–262.

Bousquet, P., Ciais, P., Miller, J.B., Dlugokencky, E.J., Hauglustaine, D.A., Prigent, C., Van der Werf, G.R., Peylin, P., Brunke, E.-G., Carouge, C., Langenfelds, R.L., Lathière, J., Papa, F., Ramonet, M., Schmidt, M., Steele, L.P., Tyler, S.C. & White, J., 2006. Contribution of anthropogenic and natural sources to atmospheric methane variability. *Nature*, 443(7110), pp. 439–443.

Bridgham, S.D., Cadillo-Quiroz, H., Keller, J.K. & Zhuang, Q., 2013. Methane emissions from wetlands: Biogeochemical, microbial, and modeling perspectives from local to global scales. *Global Change Biology*, 19(5), pp. 1325–1346.

Brown, J., 1965. Radiocarbon Dating, Barrow, Alaska. *Arctic*, 18(1), pp. 37–48.

Brown, J., Ferrians, O.J. Jr., Heginbottom, J.A. & Melnikov, E.S., 1997. Circum-Arctic Map of Permafrost and Ground-Ice Conditions. *U.S. Geological Survey, Map CP-45, U.S. Department of the Interior.*

Brunner, B., Yu, J.-Y., Mielke, R.E., MacAskill, J.A., Madzunkov, S., McGenity, T.J. & Coleman, M., 2008. Different isotope and chemical patterns of pyrite oxidation related to lag and exponential growth phases of Acidithiobacillus ferrooxidans reveal a microbial growth strategy. *Earth and Planetary Science Letters*, 270(1–2), pp. 63–72.

Bryant, I.D., 1982. Loess deposits In Lower Adventdalen, Spitsbergen. *Polar Research*, 1982(2), pp. 93–103.

Burdige, D.J., 1993. The biogeochemistry of manganese and iron reduction in marine sediments. *Earth Science Reviews*, 35, pp. 249–284.

Burga, C.A., Krüsi, B., Egli, M., Wernli, M., Elsener, S., Ziefle, M., Fischer, T. & Mavris, C., 2010. Plant succession and soil development on the foreland of the Morteratsch glacier (Pontresina, Switzerland): Straight forward or chaotic? *Flora: Morphology, Distribution, Functional Ecology of Plants*, 205(9), pp. 561-576.

Burns, R., Wynn, P.M., Barker, P., McNamara, N., Oakley, S., Ostle, N., Stott, A.W., Tuffen, H., Zhou, Z., Tweed, F.S., Chesler, A. & Stuart, M., 2018. Direct isotopic evidence of biogenic methane production and efflux from beneath a temperate glacier. *Scientific Reports*, 8(1), pp. 17118.

Cable, S., Elberling, B. & Kroon, A., 2017. Holocene permafrost history and cryostratigraphy in the High-Arctic Adventdalen Valley, central Svalbard. *Boreas*, 47(2), pp. 423–442.

Callahan, B.J., McMurdie, P.J., Rosen, M.J., Han, A.W., Johnson, A.J.A. & Holmes, S.P., 2016. DADA2: High-resolution sample inference from Illumina amplicon data. *Nature Methods*, 13(7), pp. 581-583.

Calmels, D., Gaillardet, J., Brenot, A. & France-Lanord, C., 2007. Sustained sulfide oxidation by physical erosion processes in the Mackenzie River basin: Climatic perspectives. *Geology*, 35(11), pp. 1003–1006.

Canfield, D.E., Raiswell, R., Westrich, J.T., Reaves, C.M. & Berner, R.A., 1986. The use of chromium reduction in the analysis of reduced inorganic sulfur in sediments and shales. *Chemical Geology*, 54(1–2), pp. 149–155.

Carleton, T.A. & Hsiang, S.M., 2016. Social and economic impacts of climate. *Science (New York, N.Y.)*, 353(6304), pp.aad9837.

Chanton, J., Crill, P., Bartlett, K. & Martens, C., 1989. Amazon Capims (floating grassmats): A source of 13C enriched methane to the troposphere. *Geophysical Research Letters*, 16(8), pp. 799-802.

Chesworth, W. ed., 2008. Encyclopedia of Soil Science, *Springer,* Dordrecht.

Christiansen, H.H., 2005. Thermal regime of ice-wedge cracking in Adventdalen, Svalbard. *Permafrost and Periglacial Processes*, 16(1), pp. 87–98.

Christiansen, H.H., Etzelmüller, B., Isaksen, K., Juliussen, H., Farbrot, H., Humlum, O., Johansson, M., Ingeman-Nielsen, T., Kristensen, L., Hjort, J., Holmlund, P., Sannel, A.B.K., Sigsgaard, C., Åkerman, H.J., Foged, N., Blikra, L.H., Pernosky, M.A. & Ødegård, R.S., 2010. The thermal state of permafrost in the nordic area during the international polar year 2007-2009. *Permafrost and Periglacial Processes*, 21(2), pp. 156–181.

Christiansen, H.H., Humlum, O. & Eckerstorfer, M., 2013. Central Svalbard 2000–2011 Meteorological Dynamics and Periglacial Landscape Response. *Arctic, Antarctic, and Alpine Research*, 45(1), pp. 6–18.

Christiansen, H.H., Matsuoka, N. & Watanabe, T., 2016. Progress in Understanding the Dynamics, Internal Structure and Palaeoenvironmental Potential of Ice Wedges and Sand Wedges. *Permafrost and Periglacial Processes*, 27(4), pp. 365–376.

Coleman, D.C., Callaham, M.A. & Crossley, D.A., 2004. Fundamentals of soil ecology 2nd ed. D. Cella & K. Sonnack, eds., *Elsevier*.

Cowtan, K. & Way, R.G., 2014. Coverage bias in the HadCRUT4 temperature series and its impact on recent temperature trends. *Quarterly Journal of the Royal Meteorological Society*, 140(683), pp.1935–1944.

Crémière, A., Lepland, A., Chand, S., Sahy, D., Condon, D.J., Noble, S.R., Martma, T., Thorsnes, T., Sauer, S. & Brunstad, H., 2016. Timescales of methane seepage on the Norwegian margin following collapse of the Scandinavian Ice Sheet. *Nature Communications*, 7, 11, 509.

Dallmann, W.K., Midbø, P.S., Nøttvedt, A. & Steel, R.J., 1999. *Lithostratigraphic lexicon of Svalbard : review and recommendations for nomenclature use : Upper Palaeozoic to Quaternary bedrock*, Norsk Polarinstitutt, pp. 318.

Damman, A.W.H., 1986. Hydrology, development, and biogeochemistry of ombrogenous peat bogs with special reference to nutrient relocation in a western Newfoundland bog. *Canadian Journal of Botany*, 64(2), pp. 384–394.

Davidson, S.J., Sloan, V.L., Phoenix, G.K., Wagner, R., Fisher, J.P., Oechel, W.C. & Zona, D., 2016. Vegetation Type Dominates the Spatial Variability in CH4 Emissions Across Multiple Arctic Tundra Landscapes. *Ecosystems*, 19(6), pp. 1116-1132.

Dean, J.F., Middelburg, J.J., Röckmann, T., Aerts, R., Blauw, L.G., Egger, M., Jetten, M.S.M., de Jong, A.E.E., Meisel, O.H., Rasigraf, O., Slomp, C.P., in't Zandt, M.H. & Dolman, A.J., 2018. Methane Feedbacks to the Global Climate System in a Warmer World. *Reviews of Geophysics*, 56(1), pp. 207–250.

Dieser, M., Broemsen, E.L.J.E., Cameron, K.A., King, G.M., Achberger, A., Choquette, K., Hagedorn, B., Sletten, R., Junge, K. & Christner, B.C., 2014. Molecular and biogeochemical evidence for methane cycling beneath the western margin of the Greenland Ice Sheet. *ISME Journal*, 8(11), pp. 2305–2316.

Dise, N.B. & Verry, E.S., 2001. Suppression of peatland methane emission by cumulative sulfate deposition in simulated acid rain. *Biogeochemistry*, 53, pp. 143-160.

Dixon, T., 2020. Geogenic nitrogen as a nutrient source to subglacial microbial ecosystems, *PhD Thesis, School of Earth and Environment, University of Leeds*.

Duddleston, K.N., Kinney, M.A., Kiene, R.P. & Hines, M.E., 2002. Anaerobic microbial biogeochemistry in a northern bog: Acetate as a dominant metabolic end product. *Global Biogeochemical Cycles*, 16(4), pp. 1-9.

Dyke, A.S., England, J., Reimnitz, E. & Jetté, H., 1997. Changes in driftwood delivery to the Canadian Arctic Archipelago: The hypothesis of postglacial oscillations of the transpolar drift. *Arctic*, 50(1), pp. 1–16.

Ebrahimi, A. & Or, D., 2017. Mechanistic modeling of microbial interactions at pore to profile scale resolve methane emission dynamics from permafrost soil. *Journal of Geophysical Research: Biogeosciences*, 122(5), pp. 1216–1238.

Elberling, B., Michelsen, A., Schädel, C., Schuur, E.A.G., Christiansen, H.H., Berg, L., Tamstorf, M.P. & Sigsgaard, C., 2013. Long-term CO2 production following permafrost thaw. *Nature Climate Change*, 3(October), pp. 890–894.

England, J., Atkinson, N., Bednarski, J., Dyke, A.S., Hodgson, D.A. & Ó Cofaigh, C., 2006. The Innuitian Ice Sheet: configuration, dynamics and chronology. *Quaternary Science Reviews*, 25(7–8), pp. 689–703.

Ernakovich, J.G., Lynch, L.M., Brewer, P.E., Calderon, F.J. & Wallenstein, M.D., 2017. Redox and temperature-sensitive changes in microbial communities and soil chemistry dictate greenhouse gas loss from thawed permafrost. *Biogeochemistry*, 134(1–2), pp.183–200.

Evans, P.N., Parks, D.H., Chadwick, G.L., Robbins, S.J., Orphan, V.J., Golding, S.D. & Tyson, G.W., 2015. Methane metabolism in the archaeal phylum Bathyarchaeota revealed by genome-centric metagenomics. *Science*, 350(6259), pp. 434-438.

van Everdingen, R.O., 2005. Multi-language glossary of permafrost and related ground ice terms. *International Permafrost Association*.

Fairbanks, R.G., 1989. A 17,000-year glacio-eustatic sea level record: Influence of glacial melting rates on the Younger Dryas event and deep-ocean circulation. *Nature*, 342(6250), pp. 637-642.

Ferry, J.G., 1992. Methane from acetate. *Journal of bacteriology*, 174(17), pp. 5489–95.

Førland, E.J., Benestad, R., Hanssen-Bauer, I., Haugen, J.E. & Skaugen, T.E., 2011. Temperature and Precipitation Development at Svalbard 1900–2100. *Advances in Meteorology*, 2011, pp. 1–14.

Forman, S.L., Lubinski, D.J., Ingólfsson, Ó., Zeeberg, J.J., Snyder, J.A., Siegert, M.J. & Matishov, G.G., 2004. A review of postglacial emergence on Svalbard, Franz Josef Land and Novaya Zemlya, northern Eurasia. *Quaternary Science Reviews*, 23(11–13), pp. 1391–1434.

Forman, S.L. & Miller, G., 1984. Arctic and Alpine Research Time-Dependent Soil Morphologies and Pedogenic Processes on Raised Beaches, Bröggerhalvöya, Spitsbergen, Svalbard Archipelago. *Arctic and Alpine Research*, 16(4), pp. 381–394.

Forman, S.L., Lubinski, D., Miller, G.H., Matishov, G.G., Korsun, S., Snyder, J., Herlihy, F., Weihe, R. & Myslivets, V., 1996. Postglacial emergence of western Franz Josef Land, Russian, and retreat of the barents sea ice sheet. *Quaternary Science Reviews*, 15(1), pp. 77–90.

Fossing, H. & Barker Jørgensen, B., 1989. Measurement of Bacterial Sulfate Reduction in Sediments: Evaluation of a Single-Step Chromium Reduction Method. *Biogeochemistry*, 8(3), pp. 205–222.

Frankenberg, C., Yoshimura, K., Warneke, T., Aben, I., Butz, A., Deutscher, N., Griffith, D., Hase, F., Notholt, J., Schneider, M., Schrijver, H. & Röckmann, T., 2009. Dynamic processes governing lower-tropospheric HDO/H_2O ratios as observed from space and ground. *Science (New York, N.Y.)*, 325(5946), pp. 1374–7.

French, H.M., 2013. The periglacial environment, Third edition, *John Wiley and Sons*.

Froelich, P.N., Klinkhammer, G.P., Bender, M.L., Luedtke, N.A., Heath, G.R., Cullen, D., Dauphin, P., Hammond, D., Hartman, B. & Maynard, V., 1978. Early oxidation of organic matter in pelagic sediments of the eastern equatorial Atlantic : suhoxic diagenesis. *Geochimica et Cosmochimica Acta*, 43, pp. 1075–1090.

Froese, D.G., Westgate, J.A., Reyes, A. V., Enkin, R.J. & Preece, S.J., 2008. Ancient permafrost and a future, warmer arctic. *Science*, 321(5896), p. 1648.

Funder, S., Jepsen, H., Goosse, H., Moller, P., Olsen, J., Willerslev, E., Kjaer, K.H., Kaas, E., Larsen, N.K., Linderson, H., Lysa, A. & Korsgaard, N.J., 2011. A 10,000-Year Record of Arctic Ocean Sea-Ice Variability--View from the Beach. *Science*, 333(6043), pp. 747–750.

Ganzert, L., Jurgens, G., Münster, U. & Wagner, D., 2007. Methanogenic communities in permafrost-affected soils of the Laptev Sea coast, Siberian Arctic, characterized by 16S rRNA gene fingerprints. *FEMS Microbiology Ecology*, 59(2), pp. 476–488.

Gao, X., Adam Schlosser, C., Sokolov, A., Anthony, K.W., Zhuang, Q. & Kicklighter, D., 2013. Permafrost degradation and methane: low risk of biogeochemical climate-warming feedback. *Environmental Research Letters*, 8(3), p.035014.

Gilbert, G.L., Cable, S., Thiel, C., Christiansen, H.H. & Elberling, B., 2017. Cryostratigraphy, sedimentology, and the late Quaternary evolution of the Zackenberg River delta, northeast Greenland. *The Cryosphere*, 11(3), pp. 1265–1282.

Gilbert, G.L., O'Neill, H.B., Nemec, W., Thiel, C., Christiansen, H.H. & Buylaert, J.-P., 2018. Late Quaternary sedimentation and permafrost development in a Svalbard fjord-valley, Norwegian high Arctic. *Sedimentology*, 65(7), pp. 2531–2558.

Godin, E., Fortier, D. & Lévesque, E., 2016. Nonlinear thermal and moisture response of ice-wedge polygons to permafrost disturbance increases heterogeneity of high Arctic wetland. *Biogeosciences*, 13, pp. 1439–1452.

Grubbs, F.E., 1950. Sample Criteria for Testing Outlying Observations. *The Annals of Mathematical Statistics*, 21(1), pp. 27–58.

Gubin, V. & Lupachev, A. V, 2008. Soil Formation and the Underlying Permafrost. *Eurasian Soil Science*, 41(6), pp. 655–667.

Hald, M., Ebbesen, H., Forwick, M., Godtliebsen, F., Khomenko, L., Korsun, S., Ringstad Olsen, L. & Vorren, T.O., 2004. Holocene paleoceanography and glacial history of the West Spitsbergen area, Euro-Arctic margin. *Quaternary Science Reviews*, 23(20-22 SPEC. ISS.), pp. 2075–2088.

Haldorsen, S., Heim, M., Dale, B., Landvik, J.Y., van der Ploeg, M., Leijnse, A., Salvigsen, O., Hagen, J.O. & Banks, D., 2010. Sensitivity to long-term climate change of subpermafrost groundwater systems in Svalbard. *Quaternary Research*, 73(2), pp. 393–402.

Herndon, E.M., Yang, Z., Bargar, J., Janot, N., Regier, T.Z., Graham, D.E., Wullschleger, S.D., Gu, B. & Liang, L., 2015. Geochemical drivers of organic matter decomposition in arctic tundra soils. *Biogeochemistry*, 126(3), pp. 397–414.

Herndon, E., AlBashaireh, A., Singer, D., Roy Chowdhury, T., Gu, B. & Graham, D., 2017. Influence of iron redox cycling on organo-mineral associations in Arctic tundra soil. *Geochimica et Cosmochimica Acta*, 207, pp. 210–231.

Hindshaw, R.S., Heaton, T.H.E., Boyd, E.S., Lindsay, M.R. & Tipper, E.T., 2016. Influence of glaciation on mechanisms of mineral weathering in two high Arctic catchments. *Chemical Geology*, 420, pp. 37–50.

Hines, M.E., Duddleston, K.N. & Kiene, R.P., 2001. Carbon flow to acetate and C_1 compounds in northern wetlands. *Geophysical Research Letters*, 28(22), pp. 4251–4254.

Hinzman, L.D., Deal, C.J., Mcguire, A.D., Mernild, S.H., Polyakov, I. V. & Walsh, J.E., 2013. Trajectory of the Arctic as an integrated system. *Ecological Applications*, 23(8), pp. 1837–1868.

Hodgkins, R., Tranter, M. & Dowdeswell, J.A., 1997. Solute provenance, transport and denudation in a high Arctic glacierized catchment. *Hydrological Processes*, 11, 1813-1832.

Hodson, A., Nowak, A. & Christiansen, H., 2016. Glacial and periglacial floodplain sediments regulate hydrologic transfer of reactive iron to a high arctic fjord. *Hydrological Processes*, 30(8), pp. 1219–1229.

Hodson, A.J., Nowak, A., Redeker, K.R., Holmlund, E.S., Christiansen, H.H. & Turchyn, A. V., 2019. Seasonal Dynamics of Methane and Carbon Dioxide Evasion From an Open System Pingo: Lagoon Pingo, Svalbard. *Frontiers in Earth Science*, 7.

Hordijk, K.A. & Cappenberg, T.E., 1983. Quantitative high-pressure liquid chromatography-fluorescence determination of some important lower Fatty acids in lake sediments. *Applied and environmental microbiology*, 46(2), pp. 361–9.

Hordijk, C.A., Kamminga, H. & Cappenberg, T.E., 1994. Kinetic studies of acetate in freshwater sediments: Use of stable isotopic tracers. *Geochimica et Cosmochimica Acta*, 58(2), pp. 683–694.

Hornibrook, E.R.C., 2009. The Stable Carbon Isotope Composition of Methane Produced and Emitted from Northern Peatlands. *Carbon Cycling in Northern Peatlands*. A. J. Baird et al., eds., American Geophysical Union.

Horton, T.W., Chamberlain, C.P., Fantle, M. & Blum, J.D., 1999. Chemical weathering and lithologic controls of water chemistry in a high-elevation river system: Clark's Fork of the Yellowstone river, Wyoming and Montana. *Water Resources Research*, 35(5), pp. 1643–1655.

Hugelius, G., Strauss, J., Zubrzycki, S., Harden, J.W., Schuur, E.A.G., Ping, C.-L., Schirrmeister, L., Grosse, G., Michaelson, G.J., Koven, C.D., O 'donnell, J.A., Elberling, B., Mishra, U., Camill, P., Yu, Z., Palmtag, J. & Kuhry, P., 2014. Estimated stocks of circumpolar permafrost carbon with quantified uncertainty ranges and identified data gaps. *Biogeosciences*, 11, pp. 6573–6593.

Humlum, O., Instanes, A. & Sollid, J.L., 2003. Permafrost in Svalbard: A review of research history, climatic background and engineering challenges. *Polar Research*, 22(2), pp. 191–215.

Humlum, O., 2005. Holocene permafrost aggradation in Svalbard. *Geological Society, London, Special Publications*, 242(1), pp. 119–129.

Humlum, O., Christiansen, H.H. & Juliussen, H., 2007. Avalanche-derived Rock Glaciers in Svalbard. *Permafrost and Periglacial Processes*, 18, pp.75–88.

Huq, F., Smalley, P.C., Mørkved, P.T., Johansen, H., Johansen, I. & Yarushina, V., 2017. The Longyearbyen CO_2 Lab : Fluid communication in reservoir and caprock. *International Journal of Greenhouse Gas Control*, 63(May), pp. 59–76.

IPCC, 2013: *Climate Change 2013: The Physical Science Basis. Contribution of Working Group I to the Fifth Assessment Report of the Intergovernmental Panel on Climate Change* [Stocker, T.F., D. Qin, G.-K. Plattner, M. Tignor, S.K. Allen, J. Boschung, A. Nauels, Y. Xia, V. Bex and P.M. Midgley (eds.)]. Cambridge University Press, Cambridge, United Kingdom and New York, NY, USA, 1535 pp.

Isaksen, K., Sollid, J.L., Holmlund, P. & Harris, C., 2007. Recent warming of mountain permafrost in Svalbard and Scandinavia. *Journal of Geophysical Research*, 112(F2), p.F02S04.

Jakobsson, M., Ingólfsson, Ó., Long, A.J. & Spielhagen, R.F., 2014. The dynamic Arctic. *Quaternary Science Reviews*, 92, pp. 1–8.

Jessen, S., Holmslykke, H.D., Rasmussen, K., Richardt, N. & Holm, P.E., 2014. Hydrology and pore water chemistry in a permafrost weland, Ilulissat, Greenland. *Water Resources Research*, 50, pp. 1–15.

Johnston, S.G., Burton, E.D., Aaso, T. & Tuckerman, G., 2014. Sulfur, iron and carbon cycling following hydrological restoration of acidic freshwater wetlands. *Chemical Geology*, 371, pp. 9–26.

Jorgenson, M.T., Kanevskiy, M., Shur, Y., Moskalenko, N., Brown, D.R.N., Wickland, K., Striegl, R. & Koch, J., 2015. Role of ground ice dynamics and ecological feedbacks in recent ice wedge degradation and stabilization. *Journal of Geophysical Research: Earth Surface*, 120(11), pp. 2280–2297.

Jorgenson, M.T., Shur, Y.L. & Pullman, E.R., 2006. Abrupt increase in permafrost degradation in Arctic Alaska. *Geophysical Research Letters*, 33(2), p.L02503.

Kai, F.M., Tyler, S.., Randerson, J., T. & Blake, D.R., 2011. Reduced methane growth rate explained by decreased Northern Hemisphere microbial sources. *Nature*, 476, pp. 194–197.

Kaiser, C., Meyer, H., Biasi, C., Rusalimova, O., Barsukov, P. & Richter, A., 2007. Conservation of soil organic matter through cryoturbation in arctic soils in Siberia. *Journal of Geophysical Research*, 112(G2), p.G02017.

Kanevskiy, M., Shur, Y., Fortier, D., Jorgenson, M.T. & Stephani, E., 2011. Cryostratigraphy of late Pleistocene syngenetic permafrost (yedoma) in northern Alaska, Itkillik River exposure. *Quaternary Research*, 75(3), pp. 584–596.

Kanevskiy, M., Jorgenson, T., Shur, Y., O'Donnell, J.A., Harden, J.W., Zhuang, Q. & Fortier, D., 2014. Cryostratigraphy and Permafrost Evolution in the Lacustrine Lowlands of West-Central Alaska. *Permafrost and Periglacial Processes*, 25(1), pp. 14–34.

Kaufman, D.S. & Manley, W.F., 2004. Pleistocene Maximum and Late Wisconsinan glacier extents across Alaska, U.S.A. *Developments in Quaternary Sciences*, 2, pp. 9–27.

King, G.M., Klug, M.J. & Lovley, D.R., 1983. Metabolism of acetate, methanol, and methylated amines in intertidal sediments of lowes cove, maine. *Applied and environmental microbiology*, 45(6), pp. 1848–53.

Kirschke, S., Bousquet, P., Ciais, P., Saunois, M., Canadell, J.G., Dlugokencky, E.J., Bergamaschi, P., Bergmann, D., Blake, D.R., Bruhwiler, L., Cameron-Smith, P., Castaldi, S., Chevallier, F., Feng, L., Fraser, A., Heimann, M., Hodson, E.L., Houweling, S., Josse, B. et al., 2013. Three decades of global methane sources and sinks. *Nature Geoscience*, 6(10), pp. 813–823.

Knoblauch, C., Beer, C., Liebner, S., Grigoriev, M.N. & Pfeiffer, E.-M., 2018. Methane production as key to the greenhouse gas budget of thawing permafrost. *Nature Climate Change*, 8(4), pp. 309–312.

Koc, N., Jansen, E. & Haflidason, H., 1993. Paleoceanographic reconstructions of surface ocean conditions in the Greenland, Iceland and Norwegian seas through the last 14 ka based on diatoms. *Quaternary Science Reviews*, 12(2), pp. 115–140.

Koch, J.C., Gurney, K. & Wipfli, M.S., 2014. Morphology-dependent water budgets and nutrient fluxes in arctic thaw ponds. *Permafrost and Periglacial Processes*, 25, pp. 79-93.

Kokelj, S. V. & Burn, C.R., 2003. Ground ice and soluble cations in near-surface permafrost, Inuvik, Northwest Territories, Canada. *Permafrost and Periglacial Processes*, 14(3), pp. 275–289.

Kokelj, S. V & Burn, C.R., 2005. Geochemistry of the active layer and near-surface permafrost, Mackenzie delta region, Northwest Territories, Canada. *Canadian Journal of Earth Sciences*, 42(1), pp. 37–48.

Kolka, R., Bridgham, S. & Ping, C.-L., 2015. Soils of Peatlands: Histosols and Gelisols. In *Wetland Soils*. pp. 277–310.

Kottek, M., Grieser, J., Beck, C., Rudolf, B. & Rubel, F., 2006. World Map of the Köppen-Geiger climate classification updated. *Meteorologische Zeitschrift*, 15(3), pp. 259–263.

Koven, C.D., Ringeval, B., Friedlingstein, P., Ciais, P., Cadule, P., Khvorostyanov, D., Krinner, G. & Tarnocai, C., 2011. Permafrost carbon-climate feedbacks accelerate global warming. *Proceedings of the National Academy of Sciences of the United States of America*, 108(36), pp. 14769–74.

Kristjansson, J.K. & Schönheit, P., 1983. Why do sulfate-reducing bacteria outcompete methanogenic bacteria for substrates? *Oecologia*, 60, pp. 264-266.

Kuhry, P., Dorrepaal, E., Hugelius, G., Schuur, E.A.G. & Tarnocai, C., 2010. Potential remobilization of belowground permafrost carbon under future global warming. *Permafrost and Periglacial Processes*, 21(2), pp. 208–214.

Lachenbruch, A.H., 1962. Mechanics of Thermal Contraction Cracks and Ice-Wedge Polygons in Permafrost. *Special Paper of the Geological Society of America*, 70, pp. 1-65.

Lamarche-Gagnon, G., Wadham, J.L., Sherwood Lollar, B., Arndt, S., Fietzek, P., Beaton, A.D., Tedstone, A.J., Telling, J., Bagshaw, E.A., Hawkings, J.R., Kohler, T.J., Zarsky, J.D., Mowlem, M.C., Anesio, A.M. & Stibal, M., 2019. Greenland melt drives continuous export of methane from the ice-sheet bed. *Nature*, 565(7737), pp. 73–77.

Landvik, J., Mangerud, J. & Salvigsen, O., 1988. Glacial history and Permafrost in the Svalbard area. *International Conference on Permafrost,* pp. 194–198.

Landvik, J.Y., Ingólfsson, Ó., Mienert, J., Lehman, S.J., Solheim, A., Elverhøi, A. & Ottesen, D., 2005. Rethinking Late Weichselian ice-sheet dynamics in coastal NW Svalbard. *Boreas*, 34(1), pp. 7–24.

Lara, M.J., Mcguire, A.D., Euskirchen, E.S., Tweedie, C.E., Hinkel, K.M., Skurikhin, A.N., Romanovsky, V.E., Grosse, G., Bolton, W.R. & Genet, H., 2015. Polygonal tundra geomorphological change in response to warming alters future CO_2 and CH_4 flux on the Barrow Peninsula. *Global Change Biology*, 21(4), pp. 1634–1651.

Lawrence, D.M., Koven, C.D., Swenson, S.C., Riley, W.J. & Slater, A.G., 2015. Permafrost thaw and resulting soil moisture changes regulate projected high-latitude CO_2 and CH_4 emissions. *Environmental Research Letters*, 10(9), p.094011.

Lee, H., Schuur, E.A.G., Inglett, K.S., Lavoie, M. & Chanton, J.P., 2012. The rate of permafrost carbon release under aerobic and anaerobic conditions and its potential effects on climate. *Global Change Biology*, 18(2), pp. 515–527.

Leffingwell, E. de K., 1915. Ground-Ice Wedges: The Dominant Form of Ground-Ice on the North Coast of Alaska. *The Journal of Geology*, 23(7), pp. 635–654.

Liljedahl, A.K., 2011. The hydrological regime at sub-arctic and arctic watersheds: present and projected. *PhD Thesis*. University of Alaska, Fairbanks.

Liljedahl, A.K., Boike, J., Daanen, R.P., Fedorov, A.N., Frost, G.V., Grosse, G., Hinzman, L.D., Iijma, Y., Jorgenson, J.C., Matveyeva, N., Necsoiu, M., Raynolds, M.K., Romanovsky, V., Schulla, J., Tape, K.D., Walker, D.A., Wilson, C., Yabuki, H. & Zona, D., 2016. Pan-Arctic ice-wedge degradation in warming permafrost and influence on tundra hydrology. *Nature Geoscience*, (March), pp.1–8.

Liljedahl, A., Hinzman, L.D. & Schulla, J., 2012. Ice-Wedge Polygon Type Controls Low-Gradient Watershed-Scale Hydrology. *Tenth International Conference on Permafrost,* pp. 231-236.

Lipson, D.A., Jha, M., Raab, T.K. & Oechel, W.C., 2010. Reduction of iron (III) and humic substances plays a major role in anaerobic respiration in an Arctic peat soil. *Journal of Geophysical Research: Biogeosciences*, 115(4).

Lipson, D.A., Zona, D., Raab, T.K., Bozzolo, F., Mauritz, M. & Oechel, W.C., 2012. Water-table height and microtopography control biogeochemical cycling in an Arctic coastal tundra ecosystem. *Biogeosciences*, 9(1), pp. 577–591.

Lønne, I., 2005. Faint traces of high Arctic glaciations: An early Holocene ice-front fluctuation in Bolterdalen, Svalbard. *Boreas*, 34(3), pp. 308–323.

Lønne, I. & Nemec, W., 2004. High-arctic fan delta recording deglaciation and environment disequilibrium. *Sedimentology*, 51(3), pp. 553–589.

Lovley, D.R. & Chapelle, F.H., 1995. Deep subsurface microbial processes. *Reviews of Geophysics*, 33(3), pp. 365-381.

Lovley, D.R. & Klug, M.J., 1983. Methanogenesis from Methanol and Methylamines and Acetogenesis from Hydrogen and Carbon Dioxide in the Sediments of a Eutrophic Lake. *Applied and Environmental Microbiology*, 45(4), pp. 1310-1315.

Lovley, D.R. & Phillips, E.J., 1987. Competitive mechanisms for inhibition of sulfate reduction and methane production in the zone of ferric iron reduction in sediments. *Applied and environmental microbiology*, 53(11), pp. 2636–2641.

Lloyd, R.M., 1968. Oxygen isotope behaviour in the Sulfate-Water System. *Journal of Geophysical Research*, 73(18), pp. 6099-6110.

Ludvigson, G.A., González, L.A., Metzger, R.A., Witzke, B.J., Brenner, R.L., Murillo, A.P. & White, T.S., 1998. Meteoric sphaerosiderite lines and their use for paleohydrology and paleoclimatology. *Geology*, 26(11), pp. 1039-1042.

Ludvigson, G.A., González, L.A., Fowle, D.A., Roberts, J.A., Driese, S.G., Villarreal, M.A., Smith, J.J. & Suarez, M.B., 2013. Paleoclimatic Applications and Modern Process Studies of Pedogenic Siderite. In *New Frontiers in Paleopedology and Terrestrial Paleoclimatology: Paleosols and Soil Surface Analog Systems*. pp. 79–87.

Mackay, J.R., 1984. The direction of ice-wedge cracking in permafrost: downward or upward? *Canadian Journal of Earth Sciences*, 21(5), pp. 516–524.

Mandernack, K.W., Krouse, H.R. & Skei, J.M., 2003. A stable sulfur and oxygen isotopic investigation of sulfur cycling in an anoxic marine basin, Framvaren Fjord, Norway. *Chemical Geology*, 195(1–4), pp. 181–200.

Mangerud, J., Dokken, T., Hebbeln, D., Heggen, B., Ingólfsson, Ó., Landvik, J.Y., Mejdahl, V., Svendsen, J.I. & Vorren, T.O., 1998. Fluctuations of the Svalbard-Barents sea ice sheet during the last 150 000 years. *Quaternary Science Reviews*, 17, pp. 11–42.

Martínez-Botí, M.A., Foster, G.L., Chalk, T.B., Rohling, E.J., Sexton, P.F., Lunt, D.J., Pancost, R.D., Badger, M.P.S. & Schmidt, D.N., 2015. Plio-Pleistocene climate sensitivity evaluated using high-resolution CO2 records. *Nature*, 518(7537), pp. 49–54.

Martini, I.P. & Glooschenko, W.A., 1985. Cold climate peat formation in Canada, and its relevance to Lower Permian coal measures of Australia. *Earth-Science Reviews*, 22(2), pp. 107–140.

Mastepanov, M., Sigsgaard, C., Dlugokencky, E.J., Houweling, S., Ström, L., Tamstorf, M.P. & Christensen, T.R., 2008. Large tundra methane burst during onset of freezing. *Nature*, 456(7222), pp. 628–30.

Mau, S., Römer, M., Torres, M.E., Bussmann, I., Pape, T., Damm, E., Geprägs, P., Wintersteller, P., Hsu, C.W., Loher, M. & Bohrmann, G., 2017. Widespread methane seepage along the continental margin off Svalbard-from Bjørnøya to Kongsfjorden. *Scientific Reports*, 7.

McCalley, C.K., Woodcroft, B.J., Hodgkins, S.B., Wehr, R.A., Kim, E.H., Mondav, R., Crill, P.M., Chanton, J.P., Rich, V.I., Tyson, G.W. & Saleska, S.R., 2014. Methane dynamics regulated by microbial community response to permafrost thaw. *Nature*, 514(7253), pp. 478–481.

McGuire, A.D., Christensen, T.R., Hayes, D., Heroult, A., Euskirchen, E., Kimball, J.S., Koven, C., Lafleur, P., Miller, P.A., Oechel, W., Peylin, P., Williams, M. & Yi, Y., 2012. An assessment of the carbon balance of Arctic tundra: Comparisons among observations, process models, and atmospheric inversions. *Biogeosciences*, 9(8), pp. 3185–3204.

McMurdie, P.J. & Holmes, S., 2013. Phyloseq: An R Package for Reproducible Interactive Analysis and Graphics of Microbiome Census Data. *PLoS ONE*, 8(4).

Megonigal, J.P. & Hines, M.E., 2004. Anaerobic Metabolism : Linkages to Trace Gases and Aerobic Processes. In *Treatise on GeochemistryBiogeochemistry*, 8, pp. 317–424.

Meng, L., Hess, P.G.M., Mahowald, N.M., Yavitt, J.B., Riley, W.J., Subin, Z.M., Lawrence, D.M., Swenson, S.C., Jauhiainen, J. & Fuka, D.R., 2012. Sensitivity of wetland methane emissions to model assumptions: application and model testing against site observations. *Biogeosciences*, 9, pp. 2793–2819.

Metcalfe, D.B., Hermans, T.D.G., Ahlstrand, J., Becker, M., Berggren, M., Björk, R.G., Björkman, M.P., Blok, D., Chaudhary, N., Chisholm, C., Classen, A.T., Hasselquist, N.J., Jonsson, M., Kristensen, J.A., Kumordzi, B.B., Lee, H., Mayor, J.R., Prevéy, J., Pantazatou, K. et al., 2018. Patchy field sampling biases understanding of climate change impacts across the Arctic. *Nature Ecology & Evolution*, 2(9), pp.1443-1448.

Meyer, H., Schirrmeister, L., Andreev, A., Wagner, D., Hubberten, H.-W., Yoshikawa, K., Bobrov, A., Wetterich, S., Opel, T., Kandiano, E. & Brown, J., 2010. Lateglacial and Holocene isotopic and environmental history of northern coastal Alaska – Results from a buried ice-wedge system at Barrow. *Quaternary Science Reviews*, 29(27–28), pp. 3720–3735.

Miller, K.E., Lai, C.T., Friedman, E.S., Angenent, L.T. & Lipson, D.A., 2015. Methane suppression by iron and humic acids in soils of the Arctic Coastal Plain. *Soil Biology and Biochemistry*, 83, pp. 176–183.

Milne, G. & Shennan, I., 2007. SEA LEVEL STUDIES | Isostasy. In: *Encyclopedia of Quaternary Science*, pp. 3043–3051.

Milner, A.M., Brown, L.E. & Hannah, D.M., 2009. Hydroecological response of river systems to shrinking glaciers. *Hydrological Processes*, 23(1), pp. 62–77.

Minke, M., Donner, N., Karpov, N.S., De Klerk, P. & Joosten, H., 2007. Distribution, diversity, development and dynamics of polygon mires: examples from NE Yakutia (NE Siberia). *Peatlands International*, 1, pp. 36-40.

Mitsch, W.J. & Gosselink, J.G., 2007. *Wetlands*, 5th Edition, Wiley.

Mortimer, R.J.G., Galsworthy, A.M.J., Bottrell, S.H., Wilmot, L.E. & Newton, R.J., 2011. Experimental evidence for rapid biotic and abiotic reduction of Fe (III) at low temperatures in salt marsh sediments: A possible mechanism for formation of modern sedimentary siderite concretions. *Sedimentology*, 58(6), pp. 1514–1529.

Müller, O., Bang-Andreasen, T., White, R.A., Elberling, B., Taş, N., Kneafsey, T., Jansson, J.K. & Øvreås, L., 2018. Disentangling the complexity of permafrost soil by using high resolution profiling of microbial community composition, key functions and respiration rates. *Environmental Microbiology*, 20, pp. 4328-4342.

Murali, A., Bhargava, A. & Wright, E.S., 2018. IDTAXA: A novel approach for accurate taxonomic classification of microbiome sequences. *Microbiome*, 6(1), pp. 140.

Myhre, G., Shindell, D., Bréon, F.M., Collins, W., Fuglestvedt, J., Huang, J., Koch, D., Lamarque, J.-F., Lee, D., Mendoza, B., Nakajima, T., Robock, A., Stephens, G., Takemura, T. & Zhang, H., 2013. Anthropogenic and Natural Radiative Forcing. *In: Climate Change 2013: The Physical Science Basis. Contribution of Working Group I to the Fifth Assessment Report of the Intergovernmental Panel on Climate Change*, pp. 659-740.

Nielsen, L., Bendixen, M., Kroon, A., Hede, M.U., Clemmensen, L.B., Weling, R. & Elberling, B., 2017. Sea-level proxies in Holocene raised beach ridge deposits (Greenland) revealed by ground-penetrating radar. *Scientific Reports*, 7(1), pp. 46460.

Nordli, Ø., Przybylak, R., Ogilvie, A.E.J. & Isaksen, K., 2014. Long-term temperature trends and variability on Spitsbergen: the extended Svalbard Airport temperature series, 1898–2012. *Polar Research*, 33(1), pp. 21349.

Olefeldt, D., Turetsky, M.R., Crill, P.M. & Mcguire, A.D., 2013. Environmental and physical controls on northern terrestrial methane emissions across permafrost zones. *Global Change Biology*, 19(2), pp. 589–603.

Oremland, R.S., 1988. Biogeochemistry of Methanogenic Bacteria. In: *Biology of anaerobic microrganisms,* Zehnder, A.J.B., ed., New York: John Wiley, pp. 641-705.

Osterkamp, T.E., 2007. Characteristics of the recent warming of permafrost in Alaska. *Journal of Geophysical Research*, 112(F2), pp. F02S02.

Ostroumov, V.. & Siegert, C., 1996. Exobiological aspects of mass transfer in microzones of permafrost deposits. *Advances in Space Research*, 18(12), pp. 79–86.

Parmentier, F.-J.W., Christensen, T.R., Sørensen, L.L., Rysgaard, S., McGuire, A.D., Miller, P.A. & Walker, D.A., 2013. The impact of lower sea-ice extent on Arctic greenhouse-gas exchange. *Nature Climate Change*, 3(3), pp.195–202.

Penning, H., Plugge, C.M., Galand, P.E. & Conrad, R., 2005. Variation of carbon isotope fractionation in hydrogenotrophic methanogenic microbial cultures and environmental samples at different energy status. *Global Change Biology*, 11(12), pp. 2103–2113.

Pester, M., Knorr, K.-H., Friedrich, M.W., Wagner, M. & Loy, A., 2012. Sulfate-reducing microorganisms in wetlands – fameless actors in carbon cycling and climate change. *Frontiers in Microbiology*, 3(Feb), pp.72.

Péwé, T.L., 1975. Quaternary geology of Alaska, *Professional Paper*, *USGS Numbered* Series, 835, p. 145.

Pirk, N., Tamstorf, M.P., Lund, M., Mastepanov, M., Pedersen, S.H., Mylius, M.R., Parmentier, F.-J.W., Christiansen, H.H. & Christensen, T.R., 2016. Snowpack fluxes of methane and carbon dioxide from high Arctic tundra. *Journal of Geophysical Research: Biogeosciences*, 121(11), pp. 2886–2900.

Pirk, N., Sievers, J., Mertes, J., Parmentier, F.J.W., Mastepanov, M. & Christensen, T.R., 2017a. Spatial variability of CO_2 uptake in polygonal tundra: Assessing low-frequency disturbances in eddy covariance flux estimates. *Biogeosciences*, 14(12), pp. 3157–3169.

Pirk, N., Mastepanov, M., López-Blanco, E., Christensen, L.H., Christiansen, H.H., Hansen, B.U., Lund, M., Parmentier, F.J.W., Skov, K. & Christensen, T.R., 2017b. Toward a statistical description of methane emissions from arctic wetlands. *Ambio*, 46(S1), pp. 70–80.

Pisapia, C., Chaussidon, M., Mustin, C. & Humbert, B., 2007. O and S isotopic composition of dissolved and attached oxidation products of pyrite by Acidithiobacillus ferrooxidans: Comparison with abiotic oxidations. *Geochimica et Cosmochimica Acta*, 71(10), pp. 2474–2490.

Portnov, A., Vadakkepuliyambatta, S., Mienert, J. & Hubbard, A., 2016. Ice-sheet-driven methane storage and release in the Arctic. *Nature Communications*, 7.

Poulton, S.W. & Canfield, D.E., 2005. Development of a sequential extraction procedure for iron: implications for iron partitioning in continentally derived particulates. *Chemical Geology*, 214(3–4), pp. 209–221.

du Prel, J.-B., Röhrig, B., Hommel, G. & Blettner, M., 2010. Choosing statistical tests: part 12 of a series on evaluation of scientific publications. *Deutsches Arzteblatt international*, 107(19), pp. 343–8.

Price, J.S. & Woo, M.-K., 1988. Studies of a subarctic coastal marsh, I. Hydrology. *Journal of Hydrology*, 103(3–4), pp. 275–292.

R Core Team, 2017. a language and environment for statistical computing. Vienna, Austria: R Foundation for Statistical Computing, 2017. Available at: http://www.R-project.org/.

Raiswell, R. & Canfield, D.E., 2012. The Iron Biogeochemical Cycle Past and Present. *Geochemical Perspectives*, 1(1), pp. 1–220.

Raiswell, R., Benning, L.G., Tranter, M. & Tulaczyk, S., 2008. Bioavailable iron in the Southern Ocean: The significance of the iceberg conveyor belt. *Geochemical Transactions*, 9, pp. 1–9.

Raynolds, M.K., Walker, D.A., Ambrosius, K.J., Brown, J., Everett, K.R., Kanevskiy, M., Kofinas, G.P., Romanovsky, V.E., Shur, Y. & Webber, P.J., 2014. Cumulative geoecological effects of 62 years of infrastructure and climate change in ice-rich permafrost landscapes, Prudhoe Bay Oilfield, Alaska. *Global Change Biology*, 20(4), pp. 1211–1224.

Reyes, A. V., Froese, D.G. & Jensen, B.J.L., 2010. Permafrost response to last interglacial warming: field evidence from non-glaciated Yukon and Alaska. *Quaternary Science Reviews*, 29(23–24), pp. 3256–3274.

Riber, L. & Lars, 2009. Paleogene depositional conditions and climatic changes of the Frysjaodden Formation in central Spitsbergen (sedimentology and mineralogy). *Unpublished University of Oslo MSc thesis*.

Riley, W.J., Subin, Z.M., Lawrence, D.M., Swenson, S.C., Torn, M.S., Meng, L., Mahowald, N.M. & Hess, P., 2011. Barriers to predicting changes in global terrestrial methane fluxes: Analyses using CLM4Me, a methane biogeochemistry model integrated in CESM. *Biogeosciences*, 8(7), pp. 1925–1953.

Rivkina, E., Gilichinsky, D., Wagener, S., Tiedje, J. & McGrath, J., 1998. Biogeochemical activity of anaerobic microorganisms from buried permafrost sediments. *Geomicrobiology Journal*, 15(3), pp. 187–193.

Rodionov, A., Flessa, H., Grabe, M., Kazansky, O.A., Shibistova, O. & Guggenberger, G., 2007. Organic carbon and total nitrogen variability in permafrost-affected soils in a forest tundra ecotone. *European Journal of Soil Science*, 58(6), pp. 1260–1272.

Rohling, E., 2013. Oxygen Isotope Composition of Seawater. *Encyclopedia of Quaternary Science*, 2nd edition, pp. 915-922.

Romanovsky, V.E., Drozdov, D.S., Oberman, N.G., Malkova, G.V., Kholodov, A.L., Marchenko, S.S., Moskalenko, N.G., Sergeev, D.O., Ukraintseva, N.G., Abramov, A.A., Gilichinsky, D.A & Vasiliev, A.A., 2010a. Thermal State of Permafrost in Russia. *Permafrost and Periglacial Processes*, 21(2), pp. 136-155.

Romanovsky, V.E., Smith, S.L. & Christiansen, H.H., 2010b. Permafrost thermal state in the polar northern hemisphere during the international polar year 2007-2009: A synthesis. *Permafrost and Periglacial Processes*, 21(2), pp. 106–116.

Rotty, R.M., 1983. Distribution of and changes in industrial carbon dioxide production. *Journal of Geophysical Research*, 88(C2), pp. 1301-1308.

Rozanski, K., Araguás-Araguás, L. & Gonfiantini, R., 1993. Isotopic Patterns in Modern Global Precipitation. *Climate Change in Continental Isotopic Records, Geophysical Monograph 78,* American Geophysical Union, pp. 1–36.

Rozema, J., Boelen, P., Doorenbosch, M., Bohncke, S., Blokker, P., Boekel, C., Broekman, R.A. & Konert, M., 2006. A vegetation, climate and environment reconstruction based on palynological analyses of high arctic tundra peat cores (5000–6000 years BP) from Svalbard. *Plant Ecology*, 182(1–2), pp. 155–173.

Rutter, N., Hodson, A., Irvine-Fynn, T. & Solås, M.K., 2011. Hydrology and hydrochemistry of a deglaciating high-Arctic catchment, Svalbard. *Journal of Hydrology*, 410(1–2), pp. 39–50.

Sachs, T., Giebels, M., Boike, J. & Kutzbach, L., 2010. Environmental controls on CH4 emission from polygonal tundra on the microsite scale in the Lena river delta, Siberia. *Global Change Biology*, 16(11), pp. 3096–3110.

Salvigsen, O., 1984. Occurrence of pumice on raised beaches and Holocene shoreline displacement in the inner Isfjorden area, Svalbard. *Polar Research*, 2(1), pp. 107–113.

Salvigsen, Otto, Høgvard, K. & Salvigsen, O, 2005. Glacial history, Holocene shoreline displacement and palaeoclimate based on radiocarbon ages in the area of Bockfjorden, north-western Spitsbergen, Svalbard. *Polar Research*, 25(1), pp. 15-24.

Sannel, A.B.K. & Kuhry, P., 2009. Holocene peat growth and decay dynamics in sub-arctic peat plateaus, west-central Canada. *Boreas*, 38(1), pp. 13–24.

Saunois, M., Bousquet, P., Poulter, B., Peregon, A., Ciais, P., Canadell, J.G., Dlugokencky, E.J., Etiope, G., Bastviken, D., Houweling, S., Janssens-Maenhout, G., Tubiello, F.N., Castaldi, S., Jackson, R.B., Alexe, M., Arora, V.K., Beerling, D.J., Bergamaschi, P., Blake, D.R. et al., 2016. The global methane budget 2000-2012. *Earth System Science Data*, 8(2), pp. 697–751.

Schädel, C., Schuur, E.A.G., Bracho, R., Elberling, B., Knoblauch, C., Lee, H., Luo, Y., Shaver, G.R. & Turetsky, M.R., 2014. Circumpolar assessment of permafrost C quality and its vulnerability over time using long-term incubation data. *Global Change Biology*, 20(2), pp. 641–652.

Schaefer, K., Zhang, T., Bruhwiler, L. & Barrett, A.P., 2011. Amount and timing of permafrost carbon release in response to climate warming. *Tellus, Series B: Chemical and Physical Meteorology*, 63(2), pp. 165–180.

Schaefer, K., Lantuit, H., Romanovsky, V.E., Schuur, E.A.G. & Witt, R., 2014. The impact of the permafrost carbon feedback on global climate. *Environmental Research Letters*, 9(8).

Schippers, A. & Jorgensen, B.B., 2001. Oxidation of pyrite and iron sulfide by manganese dioxide in marine sediments. *Geochimica et Cosmochimica Acta*, 65(6), pp. 915–922.

Schirrmeister, L., Grosse, G., Wetterich, S., Overduin, P.P., Strauss, J., Schuur, E.A.G. & Hubberten, H.W., 2011a. Fossil organic matter characteristics in permafrost deposits of the northeast Siberian Arctic. *Journal of Geophysical Research: Biogeosciences*, 116(3), p.G00M02.

Schirrmeister, L., Kunitsky, V., Grosse, G., Wetterich, S., Meyer, H., Schwamborn, G., Babiy, O., Derevyagin, A. & Siegert, C., 2011b. Sedimentary characteristics and origin of the Late Pleistocene Ice Complex on north-east Siberian Arctic coastal lowlands and islands – A review. *Quaternary International*, 241(1–2), pp. 3–25.

Schönheit, P., Kristjansson, J.K. & Thauer, R.K., 1982. Kinetic mechanism for the ability of sulfate reducers to out-compete methanogens for acetate. *Archives of Microbiology*, 132(3), pp. 285–288.

Schuur, E.A.G., McGuire, A.D., Schädel, C., Grosse, G., Harden, J.W., Hayes, D.J., Hugelius, G., Koven, C.D., Kuhry, P., Lawrence, D.M., Natali, S.M., Olefeldt, D., Romanovsky, V.E., Schaefer, K., Turetsky, M.R., Treat, C.C. & Vonk, J.E., 2015. Climate change and the permafrost carbon feedback. *Nature*, 520(7546), pp. 171–179.

Schuur, E.A.G., Bockheim, J., Canadell, J.G., Euskirchen, E., Field, C.B., Goryachkin, S. V., Hagemann, S., Kuhry, P., Lafleur, P.M., Lee, H., Mazhitova, G., Nelson, F.E., Rinke, A., Romanovsky, V.E., Shiklomanov, N., Tarnocai, C., Venevsky, S., Vogel, J.G. & Zimov, S.A., 2008. Vulnerability of Permafrost Carbon to Climate Change: Implications for the Global Carbon Cycle. *BioScience*, 58(8), pp. 701–714.

Schwertmann, U. & Murad, E., 1988. The Nature of an Iron Oxide—Organic Iron Association in a Peaty Environment. *Clay Minerals*, 23, pp. 291–299.

Screen, J.A. & Simmonds, I., 2010. The central role of diminishing sea ice in recent Arctic temperature amplification. *Nature*, 464(7293), pp. 1334–1337.

Serrano-Silva, N., Sarria-Guzmán, Y., Dendooven, L. & Luna-Guido, M., 2014. Methanogenesis and Methanotrophy in Soil: A Review. *Pedosphere*, 24(3), pp. 291–307.

Serreze, M.C., Barrett, A.P., Stroeve, J.C., Kindig, D.N. & Holland, M.M., 2009. The emergence of surface-based Arctic amplification. *The Cryosphere*, 3(1), pp. 11–19.

Sjögersten, S., Van Der Wal, R. & Woodin, S.J., 2006. Small-scale hydrological variation determines landscape CO_2 fluxes in the high Arctic. *Biogeochemistry*, 80(3), pp. 205–216.

Skogland, T., Lomeland, S. & Goksøyr, J., 1988. Respiratory burst after freezing and thawing of soil: Experiments with soil bacteria. *Soil Biology and Biochemistry*, 20(6), pp. 851–856.

Smith, L.M., Sachs, J.P., Jennings, A.E., Anderson, D.M. & deVernal, A., 2001. Light $\delta^{13}C$ events during deglaciation of the East Greenland continental shelf attributed to methane release from gas hydrate. *Geophysical Research Letters*, 28(11), pp. 2217-2220.

Smith, R.W., Bianchi, T.S., Allison, M., Savage, C. & Galy, V., 2015. High rates of organic carbon burial in fjord sediments globally. *Nature Geoscience*, 8(6), pp.450–453.

Smith, S.L., Burgess, M.M., Riseborough, D. & Nixon, F.M., 2005. Recent trends from Canadian permafrost thermal monitoring network sites. *Permafrost and Periglacial Processes*, 16(1), pp. 19–30.

Smith, S.L., Romanovsky, V.E., Lewkowicz, A.G., Burn, C.R., Allard, M., Clow, G.D., Yoshikawa, K. & Throop, J., 2010. Thermal state of permafrost in North America: A contribution to the international polar year. *Permafrost and Periglacial Processes*, 21(2), pp. 117–135.

Sørbel, L. & Tolgensbakk, J., 2002. Ice-wedge polygons and solifluction in the Adventdalen area, Spitsbergen, Svalbard. *Norsk Geografisk Tidsskrift - Norwegian Journal of Geography*, 56(2), pp. 62–66.

Spence, M.J., Thornton, S.F., Bottrell, S.H. & Spence, K.H., 2005. Determination of interstitial water chemistry and porosity in consolidated aquifer materials by diffusion equilibrium-exchange. *Environmental Science and Technology*, 39(4), pp. 1158–1166.

Spratt, H.G. & Morgan, M.D., 1990. Sulfur cycling in a cedar-dominated, freshwater wetland. *Limnology and Oceanography*, 35(7), pp. 1586–1593.

Straub, K.L., Hanzlik, M. & Buchholz-Cleven, B.E.E., 1998. The Use of Biologically Produced Ferrihydrite for the Isolation of Novel Iron-Reducing Bacteria. *Systematic and Applied Microbiology*, 21(3), pp. 442–449.

Strauss, J., Schirrmeister, L., Mangelsdorf, K., Eichhorn, L., Wetterich, S. & Herzschuh, U., 2015. Organic-matter quality of deep permafrost carbon - A study from Arctic Siberia. *Biogeosciences*, 12(7), pp. 2227–2245.

Streletskaya, I., Vasiliev, A., Oblogov, G., Streletskiy, D., Streletskaya, I.D., Vasiliev, A.A., Oblogov, G.E. & Streletskiy, D.A., 2018. Methane Content in Ground Ice and Sediments of the Kara Sea Coast. *Geosciences*, 8(12), p. 434.

Ström, L., Ekberg, A., Mastepanov, M. & Christensen, T.R., 2003. The effect of vascular plants on carbon turnover and methane emissions from a tundra wetland. *Global Change Biology*, 9(8), pp. 1185–1192.

Stumm, W. & Morgan, J.J., 1996. *Aquatic chemistry: chemical equilibria and rates in natural waters*, Wiley.

Svinth, A.A.G., 2013. A Sedimentological and Petrographical Investigation of the Todalen Member and the Boundary Beds of the Endalen Member.: Within the Firkanten Formation (Paleocene) in the Central Basin of Spitsbergen, Svalbard. *Unpublished Masters Thesis,* Norwegian University.

Syvitski, J.P.M., Burrell, D.C. & Skei, J.M., 1987. *Fjords : processes and products*, Springer-Verlag New York Inc.

Tarnocai, C., Canadell, J.G., Schuur, E.A.G., Kuhry, P., Mazhitova, G. & Zimov, S., 2009. Soil organic carbon pools in the northern circumpolar permafrost region. *Global Biogeochemical Cycles*, 23(GB2023).

Thamdrup, B., Fossing, H. & Barker Jørgensen, B., 1994. Manganese, iron, and sulfur cycling in a coastal marine sediment, Aarhus Bay, Denmark. *Geochimica et Cosmochimica Acta*, 58(23), pp. 5515-5129.

Thompson, A., Chadwick, O.A., Rancourt, D.G. & Chorover, J., 2006. Iron-oxide crystallinity increases during soil redox oscillations. *Geochimica et Cosmochimica Acta*, 70(7), pp. 1710–1727.

Throckmorton, H.M., Heikoop, J.M., Newman, B.D., Altmann, G.L., Conrad, M.S., Muss, J.D., Perkins, G.B., Smith, L.J., Torn, M.S., Wullschleger, S.D. & Wilson, C.J., 2015. Pathways and transformations of dissolved methane and dissolved inorganic carbon in Arctic tundra watersheds: Evidence from analysis of stable isotopes. *Global Biogeochemical Cycles*, 29(11), pp. 1893–1910.

Throckmorton, H.M., Newman, B.D., Heikoop, J.M., Perkins, G.B., Feng, X., Graham, D.E., O'Malley, D., Vesselinov, V. V., Young, J., Wullschleger, S.D. & Wilson, C.J., 2016. Active layer hydrology in an arctic tundra ecosystem: quantifying water sources and cycling using water stable isotopes. *Hydrological Processes*, 30(26), pp. 4972–4986.

Tishkov, A.A., 1986. Primary succession in arctic tundra on the west coast of spitsbergen (svalbard). *Polar Geography and Geology*, 10(2), pp. 148–156.

Tostevin, R. & Poulton, S.W., 2019. Suboxic Sediments. In *Encyclopedia of Astrobiology*, pp. 1-4.

Tranter, M., Sharp, M.J., Lamb, H.R., Brown, G.H., Hubbard, B.P. & Willis, I.C., 2002. Geochemical weathering at the bed of Haut Glacier d'Arolla, Switzerland—a new model. *Hydrological Processes*, 16(5), pp. 959–993.

Turchyn, A. V., Tipper, E.T., Galy, A., Lo, J.K. & Bickle, M.J., 2013. Isotope evidence for secondary sulfide precipitation along the Marsyandi River, Nepal, Himalayas. *Earth and Planetary Science Letters*, 374, pp. 36–46.

Turetsky, M.R., Treat, C.C., Waldrop, M.P., Waddington, J.M., Harden, J.W. & McGuire, A.D., 2008. Short-term response of methane fluxes and methanogen activity to water table and soil warming manipulations in an Alaskan peatland. *Journal of Geophysical Research*, 113(G3), p.G00A10.

Turetsky, M.R., Abbott, B.W., Jones, M.C., Walter Anthony, K., Olefeldt, D., Schuur, E.A.G., Koven, C., McGuire, A.D., Grosse, G., Kuhry, P., Hugelius, G., Lawrence, D.M., Gibson, C. & Sannel, A.B.K., 2019. Permafrost collapse is accelerating carbon release. *Nature*, 569(7754), pp. 32–34.

Tveit, A.T., Urich, T., Frenzel, P. & Svenning, M.M., 2015. Metabolic and trophic interactions modulate methane production by Arctic peat microbiota in response to warming. *Proceedings of the National Academy of Sciences*, 112(19), pp. E2507–E2516.

Tye, A.M. & Heaton, T.H.E., 2007. Chemical and isotopic characteristics of weathering and nitrogen release in non-glacial drainage waters on Arctic tundra. *Geochimica et Cosmochimica Acta*, 71(17), pp. 4188–4205.

Valentine, D.L., Chidthaisong, A., Rice, A., Reeburgh, W.S. & Tyler, S.C., 2004. Carbon and hydrogen isotope fractionation by moderately thermophilic methanogens. *Geochimica et Cosmochimica Acta*, 68(7), pp. 1571–1590.

Vaughn, L.J.S., Conrad, M.E., Bill, M. & Torn, M.S., 2016. Isotopic insights into methane production, oxidation, and emissions in Arctic polygon tundra. *Global Change Biology*, 22(10), pp. 3487–3502.

Wadham, J.L., Bottrell, S., Tranter, M. & Raiswell, R., 2004. Stable isotope evidence for microbial sulphate reduction at the bed of a polythermal high Arctic glacier. *Earth and Planetary Science Letters*, 219(3–4), pp. 341–355.

Wadham, J.L., Tranter, M., Tulaczyk, S. & Sharp, M., 2008. Subglacial methanogenesis: A potential climatic amplifier? *Global Biogeochemical Cycles*, 22(2), pp. 1–16.

Wadham, J.L., Tranter, M., Skidmore, M., Hodson, A.J., Priscu, J., Lyons, W.B., Sharp, M., Wynn, P. & Jackson, M., 2010. Biogeochemical weathering under ice: Size matters. *Global Biogeochemical Cycles*, 24(3).

Wadham, J.L., Arndt, S., Tulaczyk, S., Stibal, M., Tranter, M., Telling, J., Lis, G.P., Lawson, E., Ridgwell, A., Dubnick, A., Sharp, M.J., Anesio, A.M. & Butler, C.E.H., 2012. Potential methane reservoirs beneath Antarctica. *Nature*, 488(7413), pp. 633–637.

Wadham, J.L., Hawkings, J.R., Tarasov, L., Gregoire, L.J., Spencer, R.G.M., Gutjahr, M., Ridgwell, A. & Kohfeld, K.E., 2019. Ice sheets matter for the global carbon cycle. *Nature Communications*, 10(1), p.3567.

Wagner, D., Gattinger, A., Embacher, A., Pfeiffer, E.M., Schloter, M. & Lipski, A., 2007. Methanogenic activity and biomass in Holocene permafrost deposits of the Lena Delta, Siberian Arctic and its implication for the global methane budget. *Global Change Biology*, 13(5), pp. 1089–1099.

Wainwright, H.M., Dafflon, B., Smith, L.J., Hahn, M.S., Curtis, J.B., Wu, Y., Ulrich, C., Peterson, J.E., Torn, M.S. & Hubbard, S.S., 2015. Identifying multiscale zonation and assessing the relative importance of polygons geomorphology on carbon fluxes in an Arctic tundra ecosystem. *Journal of Geophysical Research: Biogeosciences*, pp. 707–723.

Waldrop, M.P., Wickland, K.P., White, R., Berhe, A.A., Harden, J.W. & Romanovsky, V.E., 2010. Molecular investigations into a globally important carbon pool: Permafrost-protected carbon in Alaskan soils. *Global Change Biology*, 16(9), pp. 2543–2554.

Walker, D.A., Raynolds, M.K., Daniëls, F.J.A., Einarsson, E., Elvebakk, A., Gould, W.A., Katenin, A.E., Kholod, S.S., Markon, C.J., Melnikov, E.S., Moskalenko, N.G., Talbot, S.S., Yurtsev, B.A.. & The other members of the CAVM Team, T. other members of the C., 2005. The Circumpolar Arctic vegetation map. *Journal of Vegetation Science*, 16(3), pp. 267–282.

Wallmann, K., Riedel, M., Hong, W.L., Patton, H., Hubbard, A., Pape, T., Hsu, C.W., Schmidt, C., Johnson, J.E., Torres, M.E., Andreassen, K., Berndt, C. & Bohrmann, G., 2018. Gas hydrate dissociation off Svalbard induced by isostatic rebound rather than global warming. *Nature Communications*, 9(83), p. 1.

Walter Anthony, K.M., Anthony, P., Grosse, G. & Chanton, J., 2012. Geologic methane seeps along boundaries of Arctic permafrost thaw and melting glaciers. *Nature Geoscience*, 5(6), pp. 419–426.

Wang, Z., 1996. Methane emissions from natural wetlands. *Environmental Monitoring and Assessment*, pp. 143-161.

Wehrmann, L.M., Formolo, M.J., Owens, J.D., Raiswell, R., Ferdelman, T.G., Riedinger, N., Lyons, Timothy W & Lyons, T W, 2014. Iron and manganese speciation and cycling in glacially influenced high-latitude fjord sediments (West Spitsbergen, Svalbard): Evidence for a benthic recycling-transport mechanism. *Geochimica et Cosmochimica Acta*, 141, pp. 628–655.

Weitemeyer, K.A. & Buffett, B.A., 2006. Accumulation and release of methane from clathrates below the Laurentide and Cordilleran ice sheets. *Global and Planetary Change*, 53(3), pp. 176-187.

Whiticar, M.J., 1999. Carbon and hydrogen isotope systematics of bacterial formation and oxidation of methane. *Chemical Geology*, 161(1), pp. 291–314.

Whitman, W.B., 2015. *Bergey's Manual of Systematics of Archaea and Bacteria*. John Wiley and Sons, Inc.

Wiesenburg, D.A. & Guinasso, N.L., 1979. Equilibrium Solubilities of Methane, Carbon Monoxide, and Hydrogen in Water and Sea Water. *Journal of Chemical and Engineering Data,* 24(1), pp. 356-360.

Wietrzyk, P., Rola, K., Osyczka, P., Nicia, P., Szymański, W. & Węgrzyn, M., 2018. The relationships between soil chemical properties and vegetation succession in the aspect of changes of distance from the glacier forehead and time elapsed after glacier retreat in the Irenebreen foreland (NW Svalbard). *Plant and Soil*, 428(1–2), pp. 195–211.

Woo, M. & Young, K.L., 2006. High Arctic wetlands: Their occurrence, hydrological characteristics and sustainability. *Journal of Hydrology*, 320(3–4), pp. 432–450.

Wynn, P.M., Morrell, D.J., Tuffen, H., Barker, P., Tweed, F.S. & Burns, R., 2015. Seasonal release of anoxic geothermal meltwater from the Katla volcanic system at Sólheimajökull, Iceland. *Chemical Geology*, 396, pp. 228–238.

Wynn, P.M., Hodson, A. & Heaton, T., 2006. Chemical and isotopic switching within the subglacial environment of a High Arctic glacier. *Biogeochemistry*, 78(2), pp. 173–193.

Xu, X., Elias, D.A., Graham, D.E., Phelps, T.J., Carroll, S.L., Wullschleger, S.D. & Thornton, P.E., 2015. A microbial functional group-based module for simulating methane production and consumption: Application to an incubated permafrost soil. *Journal of Geophysical Research: Biogeosciences*, 120(7), pp. 1315–1333.

Yde, J.C., Riger-Kusk, M., Christiansen, H.H., Knudsen, N.T. & Humlum, O., 2008. Hydrochemical characteristics of bulk meltwater from an entire ablation season, Longyearbreen, Svalbard. *Journal of Glaciology*, 54(185), pp. 259–272.

Zeeberg, J., Lubinski, D.J. & Forman, S.L., 2001. Holocene Relative Sea-Level History of Novaya Zemlya, Russia, and Implications for Late Weichselian Ice-Sheet Loading. *Quaternary Research*, 56(2), pp. 218–230.

Zhang, T., Barry, R.G., Knowles, K., Heginbottom, J.A. & Brown, J., 2008. Statistics and characteristics of permafrost and ground-ice distribution in the Northern Hemisphere. *Polar Geography*, 31(1–2), pp. 47–68.

Zheng, J., Thornton, P.E., Painter, S.L., Gu, B., Wullschleger, S.D. & Graham, D.E., 2019. Modeling anaerobic soil organic carbon decomposition in Arctic polygon tundra: insights into soil geochemical influences on carbon mineralization. *Biogeosciences*, 16, pp. 663–680.

Zimov, S.A., Schuur, E.A.G. & Chapin III, F.S., 2006. Permafrost and the Global Carbon Budget. *Science*, 312(5780), pp. 1612–1613.

Zona, D., Lipson, D.A., Zulueta, R.C., Oberbauer, S.F. & Oechel, W.C., 2011. Microtopographic controls on ecosystem functioning in the Arctic Coastal Plain. *Journal of Geophysical Research*, 116(G4), p. G00I08.